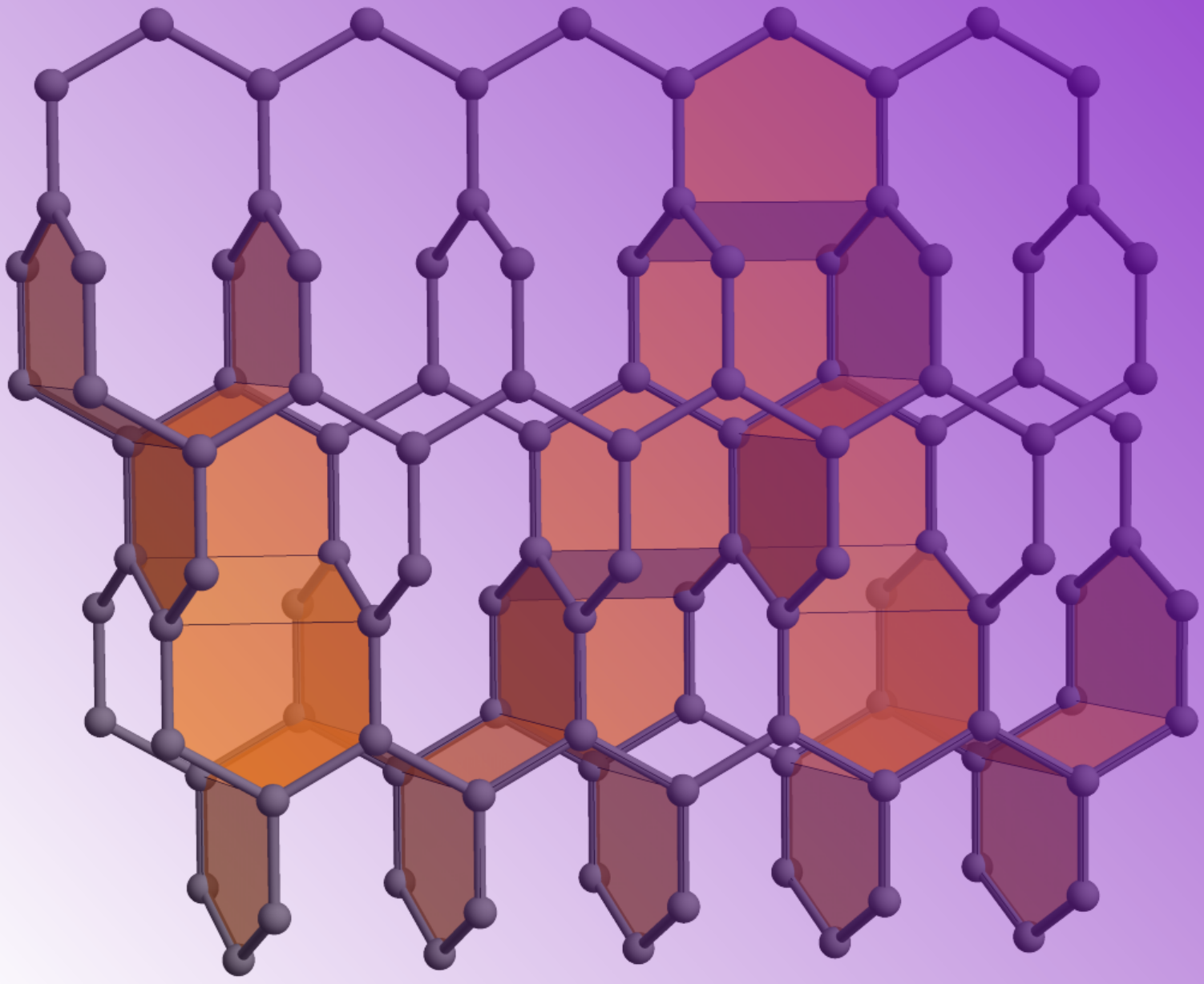

Thermodynamics of Kitaev Spin Liquids

Tim Eschmann

Dissertation

Thermodynamics of Kitaev Spin Liquids

Inaugural-Dissertation

zur

Erlangung des Doktorgrades

der Mathematisch-Naturwissenschaftlichen Fakultät

der Universität zu Köln

vorgelegt von

Tim Christian Eschmann

aus Wuppertal

Köln 2020

Berichterstatter:	Prof. Dr. Simon Trebst
	Prof. Dr. Achim Rosch
Tag der mündlichen Prüfung:	30.06.2020

Abstract

In the field of frustrated magnetism, Kitaev models provide prototypical examples of exactly solvable quantum spin liquids, in which the spin degrees of freedom fractionalize into Majorana fermions coupled to an emergent $\mathbb{Z}_2$ gauge field. While the ground states of these models are already well understood as exhibiting different kinds of Majorana (semi)metals, it has still been an open task to achieve a detailed understanding of the thermodynamics, and, namely, the low-temperature ordering of the gauge field into different $\mathbb{Z}_2$ flux configurations.

In this thesis, we investigate the thermodynamics of Kitaev systems in two and three spatial dimensions with sign-problem-free quantum Monte Carlo simulations. In a first study of elementary 3D Kitaev models, we verify that the ground state $\mathbb{Z}_2$ flux sectors of these systems are entirely determined by their elementary plaquette length – a result which shows the validity of Lieb's theorem for lattice geometries which lack the geometric requirements for its proof. We closely investigate the low-temperature phase transition associated with gauge-ordering, which is a particular realization of an inverted Ising phase transition, as it occurs in general lattice $\mathbb{Z}_2$ gauge theories. Our results corroborate the understanding of this transition as separating different regimes in terms of vison-loop excitations, by showing a clear correlation between the critical temperature and the vison gap. We also introduce the concept of "gauge frustration", which, for a particular 3D Kitaev model, leads to the suppression of the phase transition and a more complex physical behavior at low temperatures.

A second quantum Monte Carlo study focuses on a generalized 2D Kitaev model on a five-coordinated lattice system. Here, the gauge ordering is accompanied by the spontaneous breaking of time-reversal symmetry, a scenario which not only allows for a variety of topological ground states, but also for the occurrence of a phase transition in two spatial dimensions. We show that this model exhibits such a transition at a particularly high temperature scale. Moreover, the system possesses a number of phases where the $\mathbb{Z}_2$ fluxes are only partially ordered.

Kurzzusammenfassung

Auf dem Gebiet des frustrierten Magnetismus stellen Kitaev-Modelle prototypische Beispiele für exakt lösbare Quanten-Spinflüssigkeiten dar, in denen die Spin-Freiheitsgrade in Majorana-Fermionen fraktionalisieren, die an ein emergentes $\mathbb{Z}_2$-Eichfeld gekoppelt sind. Während die Grundzustände dieser Modelle als Träger verschiedener Majorana-(Halb)metalle bereits gut verstanden sind, bleibt es eine offene Aufgabe, ein detailliertes Verständnis ihres Verhaltens bei endlichen Temperaturen zu erzielen, und insbesondere darüber, wie das Eichfeld in verschiedene $\mathbb{Z}_2$-Flusskonfigurationen ordnet.

In dieser Arbeit untersuchen wir die Thermodynamik von Kitaev-Systemen in zwei und drei räumlichen Dimensionen mit Quanten-Monte-Carlo-Simulationen ohne Vorzeichenproblem. In einer ersten Untersuchung von einfachen 3D Kitaev-Modellen verifizieren wir, dass die $\mathbb{Z}_2$-Flusssektoren der Grundzustände dieser Systeme vollständig von deren elementarer Plakettenlänge bestimmt werden – ein Ergebnis, dass die Gültigkeit des Lieb-Theorems für solche Gitter zeigt, die nicht über die geometrischen Voraussetzungen für dessen Beweisbarkeit verfügen. Wir untersuchen den Phasenübergang bei niedrigen Temperaturen, der mit dem Ordnen des Eichfelds verknüpft ist und ein besonderes Beispiel für einen invertierten Ising-Phasenübergang darstellt, wie er in allgemeinen $\mathbb{Z}_2$-Gittereichtheorien vorkommt. Unsere Ergebnisse bestätigen das Verständnis dieses Übergangs als eines Übergangs zwischen zwei verschiedenen Vison-Schleifen-Regimes, indem sie eine deutliche Korrelation zwischen der kritischen Temperatur und der Vison-Bandlücke zeigen. Wir führen außerdem den Begriff der "Eichfrustration" ein, die auf einem bestimmten 3D-Kitaev-Modell zur Unterdrückung des Phasenübergangs, und einem komplexeren physikalischen Verhalten bei niedrigen Temperaturen führt.

Eine zweite Quanten-Monte-Carlo-Untersuchung konzentriert sich auf ein verallgemeinertes 2D-Kitaev-Modell auf einem Gittersystem mit Koordinationszahl 5. Hier ist die Eich-Ordnung von einer spontanen Brechung der Zeitumkehrsymmetrie begleitet, ein Szenario, das nicht nur verschiedene topologische Grundzustände erlaubt, sondern auch das Auftreten eines Phasenübergangs in zwei räumlichen Dimensionen. Wir zeigen, dass dieses Modell solch einen Übergang bei

einer besonders hohen Temperatur aufweist. Außerdem besitzt es eine Reihe von Phasen, in denen die $\mathbb{Z}_2$-Flüsse nur teilweise geordnet sind.

Contents

Outline

This thesis presents numerical studies of Kitaev spin liquids at finite temperatures, which are performed with sign-problem-free quantum Monte Carlo simulations. The Kitaev model is an exactly solvable quantum spin liquid model, the low-temperature behavior of which is described by a system of (itinerant) Majorana fermions coupled to a (static) $\mathbb{Z}_2$ gauge field.

In the introductory **Chapter 1**, we start with a general discussion of the concept of quantum spin liquids, and their inherent relation with lattice gauge theories. Here, close attention is paid to lattice $\mathbb{Z}_2$ gauge theory, which applies to Kitaev systems. **Chapter 2** introduces the Kitaev model for lattice systems in two and three spatial dimensions and gives a detailed presentation of its exact solution. It also presents the generalization of the model to a five-coordinated, non-bipartite lattice geometry, the Shastry-Sutherland lattice, which is shown to host different topological ground state phases. A brief review on experimental realizations is given. In **Chapter 3**, we introduce the quantum Monte Carlo method applied in this work. This includes a detailed discussion on how the quantum partition function of Kitaev systems can be mapped to classical probabilities, a problem which underlies every quantum Monte Carlo approach.

In the remainder of the thesis, we present our numerical results: **Chapter 4** discusses the simulations we have performed on a family of elementary, tricoordinated lattice systems in three spatial dimensions. The numerical results establish the ground state flux sectors of these Kitaev models, and corroborate the understanding of the thermal transitions in these systems, in particular the inverted Ising phase transition at low temperature scales, which is a general feature in lattice $\mathbb{Z}_2$ gauge theories and associated with $\mathbb{Z}_2$ flux ordering. In addition, the concept of "gauge frustration" is introduced at the example of a particular 3D lattice system with specific geometric properties, which lead to a deviating phase transition mechanism.

Chapter 5 presents the numerical results for the 2D Kitaev Shastry-Sutherland model, for which simulations have been performed in different topological regimes. Here, the focus is also on the thermal phase transition. Other than in three dimensions, this transition only occurs in 2D if the ground state spontaneously breaks

time-reversal symmetry. In the stated model, this happens at a particularly high temperature scale. In addition, the system is shown to possess several phases with only a partial ordering of the $\mathbb{Z}_2$ fluxes.

In the final **Chapter 6**, we summarize our results and give an outlook on different lines for a future research on the topic.

Chapter 1

Introduction: Quantum Spin Liquids and Lattice Gauge Theories

In condensed matter physics, quantum spin liquids have been an intensive field of research for almost five decades, starting with Anderson's proposal of the *resonating valence bond* (RVB) state in a frustrated spin-$1/2$ Heisenberg antiferromagnet in 1973 [1, 2]. Since then, numerous theoretical models for the realization of this exotic state of strongly correlated electron systems have been proposed and studied, which has been complemented by an immense experimental effort to produce and verify their realizations in various materials [3–8]. The practical relevance of quantum spin liquids spans a topical range that reaches from high-temperature superconductivity [9, 10] to modern approaches for fault-tolerant quantum computing [11, 12].

There has been an ongoing debate among researchers about the precise definition of what, at the core, constitutes this phase of matter. Clearly, quantum spin liquids (QSLs) occur as the collective ground states of certain highly-correlated spin systems, in which the emergence of a magnetic long-range order at temperatures $T \to 0$ is prevented by strong quantum fluctuations, and the latter typically arise as a consequence of frustration effects in the system. For a long time, the dominant point of view has been to focus on the analogy of this phase to classical liquids - to which also the name quantum spin *liquid* is owed - and define the QSL phase merely by the *absence* of ordering in the sense of Landau theory [13–15]. However, this negative definition has been broadly regarded as unsatisfying, and, in recent years, this standpoint has been more and more superseded by approaches to move forward to a positive QSL definition. Such a modern point of view is provided by regarding the QSL as a magnetic phase of matter that is characterized by a *macroscopic amount of quantum entanglement* between the degrees of freedom

in the system [7]. In this sense, the wave function of the QSL is a quantum superposition state which cannot be smoothly connected to a product state in terms of its single particle constituents, a fact which implies its ability to support non-local excitations [7]. Quantum spin liquids may occur both as gapped or gapless states, and can show different kinds of *quantum order* [16, 17]. This includes gapped states that possess a *topological order* [18–20], such as *chiral* spin liquids, which are the bosonic analogues of fractional quantum Hall states [21].

A typical common feature of QSLs is the phenomenon of *fractionalization*, i.e., the existence of a low-temperature description of the system in terms of quasiparticles with "fractional" quantum numbers, i.e, quantum numbers that cannot be constructed by any combination of the quantum numbers of the system's original degrees of freedom. These quasiparticles are most generally denoted by the name of *partons*, and often, the parton description comprises a system of itinerant fermionic *spinon* degrees of freedom coupled to an emergent bosonic *gauge field*. This makes it possible to deduce important physical properties of the quantum spin liquid from the corresponding *lattice gauge theory* [22–24]. Concretely, the QSL phase, in which the fractionalized degrees of freedom behave as independent quasiparticles, turns out to be described by the *deconfined* regime in such lattice gauge theories. The latter are specified by their elementary symmetry, and serve to classify different quantum spin liquids accordingly as $U(1)$ spin liquids [1], $\mathbb{Z}_2$ spin liquids [20, 25, 26], and others. Notably, it is the nature of the underlying lattice gauge theory that has been shown also to determine the stability of the QSL state to quantum fluctuations, which can be seen when the corresponding models are treated with mean-field theory [16, 20]. In particular, the $\mathbb{Z}_2$ spin liquid is known to possess only gapped gauge excitations, which are insensitive to low-energy fluctuations [20, 26]. In addition, we see later that certain $\mathbb{Z}_2$ spin liquids may, depending on their dimensionality, also be stable to thermal fluctuations up to some finite temperature, and therefore exist as an extended phase in the thermal phase diagram of the underlying models.

In fact, spin models in more than one dimension which possess an exact QSL ground state are rather scarce. Therefore, it has been a fundamental theoretical breakthrough when in 2006, Alexei Kitaev proposed a spin-$1/2$ model on the two-dimensional honeycomb lattice that is an exactly solvable $\mathbb{Z}_2$ quantum spin liquid [27], in which the original spin degrees of freedom fractionalize into itinerant Majorana fermions, which are coupled to an emergent (static) $\mathbb{Z}_2$ gauge field. This $\mathbb{Z}_2$ spin liquid possesses gapless and gapped phases in terms of the Majorana fermions, while the *vison* excitations of the gauge field are always gapped. Soon, the *Kitaev model* has been established not only as generalizable to other lattice geometries in two and three spatial dimensions [28–36], but also as being realized in certain Mott-insulating materials [8, 37–43]. Later on, Nasu and Motome have shown with quantum Monte Carlo simulations on different lattice systems [44,

45] that the QSL phase in 3D is thermally stable and separated from the high-temperature paramagnet by a phase transition, while in 2D, the occurrence of a thermal phase transition depends on whether the ground state is stabilized by the spontaneous breaking of time-reversal symmetry by the (gauge-invariant) $\mathbb{Z}_2$ plaquette fluxes [46, 47]. In parallel, O'Brien et al. have used the *projective symmetry group* approach by Wen [16, 20] to classify the gapless and gapped $\mathbb{Z}_2$ spin liquids which occur in a family of elementary 3D Kitaev systems, and have shown that these systems host a variety of different Majorana (semi)metals with characteristic features, such as topological Fermi surfaces, nodal lines and Weyl nodes [35, 36, 48].

Both the thermodynamic results of Nasu and Motome, and the classification of gapless $\mathbb{Z}_2$ spin liquids by O'Brien et al. constitute the starting point for the work which is presented in this thesis. In a first project, we have adapted the quantum Monte Carlo method introduced in Ref. [44] to perform large-scale numerical studies on the thermodynamics of elementary 3D Kitaev systems, as they are classified in Ref. [36] (Chapter 4). A second project has extended these quantum Monte Carlo studies to a generalized Kitaev system, which shows spin liquid ground states with different kinds of topological order (Chapter 5).

In the remainder of this introductory chapter, we present a brief review on the general theoretical foundation of our work by, first, discussing the role of lattice gauge theories in the realm of quantum spin liquid physics. In particular, we introduce the notion of a $\mathbb{Z}_2$ spin liquid and how it relates to other spin liquid versions. Also, we take a glimpse at the question of stability of spin liquids. Finally, we comment on where our work is located in the broader field of studies on quantum spin liquids. There is an abundance of literature on the subject [3–8, 20, 49–51]. The presentation in this chapter is primarily based on Refs. [7, 49–51].

1.1 Lattice gauge theories

Originally, lattice gauge theories have been developed as discretized versions of gauge theories in quantum field theory, which allow for the study of strongly interacting particles beyond perturbative approaches, and have a special relevance for the description of quarks in quantum chromodynamics [52]. It has been soon discovered that there is a natural connection to statistical mechanics, and, in particular, quantum magnets, where systems of spins on lattices can be treated with lattice gauge theories [22].

In the context of quantum spin liquids, the low-temperature description of a spin system in terms of *parton* degrees of freedom is usually accompanied by the emergence of a *gauge field* on the underlying lattice. Hence, it is possible to use

the corresponding lattice gauge theory to deduce important physical properties of the QSL state, such as the gapless or gapped nature of the gauge excitations, the existence of short-ranged or long-ranged interactions between quasiparticles, and the stability of the QSL state with respect to quantum and thermal fluctuations. As it turns out, a lot of these fundamental properties can already be extracted from the elementary symmetry of the gauge theory, such as the (continuous) $U(1)$ or the (discrete) $\mathbb{Z}_2$ symmetry. For instance, in $\mathbb{Z}_2$ spin liquids like the Kitaev model, the parton description of the system is usually based on two different excitations, namely fermionic *spinons*, i.e., charge-neutral spin-$1/2$ quasiparticles, and bosonic *visons*, which are topological vortex excitations of the $\mathbb{Z}_2$ gauge field [43]. The vison excitations in $\mathbb{Z}_2$ gauge theory are generically gapped. This implies that they can only mediate short-ranged interactions between the spinons, which are renormalization-group-irrelevant and therefore do not affect the spin liquid state in the (0^{th}-order) mean-field approximation [20, 49, 53]. In this sense, the $\mathbb{Z}_2$ spin liquid is stable to quantum fluctuations.

Following the introduction in the textbook by Wen [49], we use the term *gauge theory* to denote a theory where more than one label is used to describe the same quantum state. In spin liquids, this redundancy occurs when more than one gauge field configuration describes the same physical state of the system. In this sense, a *gauge transformation* is a mapping from one "gauge field label" of the same physical state to another such label. Physical quantities are invariant under such gauge transformations, hence, in order to describe the Hilbert space of the system and, for instance, find its ground state, it is necessary to identify the relevant gauge-invariant quantities.

1.1.1 Lattice $U(1)$ gauge theory

An intuitive approach to a number of basic concepts in lattice gauge theory is provided by first looking at the (compact) lattice $U(1)$ gauge theory, which is a discretized version of electromagnetism [7, 49]. Here, the vector potential $\mathbf{A}$ translates to discrete field variables A_{ij}, which are defined on the bonds of a three-dimensional cubic lattice, and for which $A_{ij} = -A_{ji}$. The scalar potential ϕ, on the other hand, translates to field variables ϕ_i on the lattice sites i. In this setup, physical observables can be defined by the (integer-valued) electric field e_{ij} on the bonds,

$$\begin{aligned} e_{ij} &= \frac{d}{dt} A_{ij}(t) + \phi_i(t) - \phi_j(t), \\ [A_{ij}, e_{ij}] &= i, \end{aligned} \tag{1.1}$$

and the magnetic $U(1)$ flux through the square plaquettes p of the lattice,

$$\Phi_p = \sum_{\langle i,j\rangle \in p} A_{ij}, \tag{1.2}$$

where the notation $\langle i, j\rangle$ describes the summation over lattice bonds. A simple Hamiltonian for this lattice gauge theory can be formulated as [49]

$$\mathcal{H}_{U(1)} = \frac{J}{2} \sum_{\langle i,j\rangle} e_{ij}^2 - g \sum_p \cos(\Phi_p), \tag{1.3}$$

where J and g are coupling parameters. This Hamiltonian is periodic with respect to the fields A_{ij}, with periodicity 2π, so the equivalence relation $A_{ij} \sim A_{ij} + 2\pi$ defines the compactness of the theory. In addition, $\mathcal{H}_{U(1)}$ is compatible with the presence of charges on the lattice sites, which are the eigenvalues of the field-divergence operator

$$q_i = \sum_{j \in \mathrm{nn(i)}} e_{ij}, \tag{1.4}$$

where the summation is over the nearest-neighbor sites of i [7]. The $U(1)$ nature of this lattice gauge theory can be best seen when we go over to the exponentiated flux definition

$$e^{i\Phi_p} = \prod_{\langle i,j\rangle \in p} u_{ij} = \prod_{\langle i,j\rangle \in p} e^{iA_{ij}}. \tag{1.5}$$

As it is known from electromagnetism, a redundant labelling of the field variables can be introduced in terms of an arbitrary scalar field $\chi(t)$. The lattice $U(1)$ gauge transformation is given by

$$\begin{aligned} A_{ij}(t) &\to A_{ij}(t) + \chi_j(t) - \chi_i(t), \\ \phi_i(t) &\to \phi_i(t) + \dot{\chi}_i(t), \end{aligned} \tag{1.6}$$

and leaves the Hamiltonian $\mathcal{H}_{U(1)}$ invariant. Also, the electric field e_{ij} and plaquette flux variables Φ_p are gauge-invariant.

Conceptually, it is insightful to regard the ground state regimes of the Hamiltonian in Eq. (1.3), which occur in the different coupling limits. For the limit $g \gg J$, the dominant flux term in the Hamiltonian can be Taylor-expanded as

$$-g \sum_p \cos(\Phi_p) \to \frac{g}{2} \sum_p \Phi_p^2 + \mathcal{O}(\Phi_p^3), \tag{1.7}$$

and the exact solution of the theory for all $q_i = 0$ is just standard vacuum electromagnetism, which can be shown to possess *gapless* photon excitations [49]. In this limit, the theory (in 3D) is said to be in the *deconfined* or *Coulomb phase*.

In the limit $g \ll J$, on the other hand, the elementary excitations are loops, which are defined by the nonzero electric field variables e_{ij} on the lattice bonds. These loops have a finite energy gap, and in the presence of a pair of charges $q_i = +1$, $q_j = -1$, the electric field generates a potential that grows linearly with the number of bonds between those charges. Hence, the energy that is necessary to separate such a pair of charges diverges for the infinite lattice system. Such a linear potential is called a *confining* potential, and therefore, the phase is denoted as the *confined* phase of lattice $U(1)$ gauge theory.

If we go from three to two spatial dimensions, the compact lattice $U(1)$ gauge theory can be shown to always be in the confined phase, because the regime defined by $g \gg J$ is destabilized by the occurrence of *instanton* excitations, which lead to additional interaction terms in the gauge theory, and create a gap for the photons [7, 49, 54].

1.1.2 Lattice $\mathbb{Z}_2$ gauge theory

Definition

The lattice $\mathbb{Z}_2$ gauge theory [49–51] can be obtained in a similar way. Here, we start only from the (exponentiated) link variables u_{ij} on a square (or cubic) lattice, as are defined in Eq. (1.5), and restrict them to ± 1. This is equivalent to choosing the vector potential $A_{ij} \in \{0, \pi\}$. Again, we have the relation $u_{ij} = -u_{ji}$. If we formulated a Hamiltonian as a direct function of these link variables $\mathcal{H} = -J \sum u_{ij}$, it would just be the classical Ising model (which can be seen by replacing $u_{ij} = s_i s_j$, with $s_{i/j} = \pm 1$). In this case, every configuration $|\{u_{ij}\}\rangle$ would label a different state in the Hilbert space.

In contrast with that, a general d-dimensional lattice $\mathbb{Z}_2$ or *Ising* gauge theory, here denoted by M_{dn}, takes the product of spins around n-dimensional objects, such as lines ($n = 1$), plaquettes ($n = 2$), volumes ($n = 3$), etc., and formulates a Hamiltonian in terms of these products [50]. In this notation, the lattice $\mathbb{Z}_2$ gauge theory M_{d1} is the standard d-dimensional Ising Model, and M_{d2} is the d-dimensional Ising gauge theory, where the most general, classical Hamiltonian is expressed in terms of $\mathbb{Z}_2$ plaquette flux operators W_p (see Fig. 1.1),

$$\begin{aligned} \mathcal{H}_{\mathbb{Z}_2,\text{class.}} &= -g \sum_p W_p, \\ W_p &= \prod_{\langle i,j \rangle \in p} u_{ij}. \end{aligned} \tag{1.8}$$

The definition of W_p can be naturally extended to arbitrary closed loops in the system. In this case, the operator is known as *Wilson* or *Wegner-Wilson* loop W_l, and defines a $\mathbb{Z}_2$ flux ± 1 through the lattice region that is enclosed by the loop.

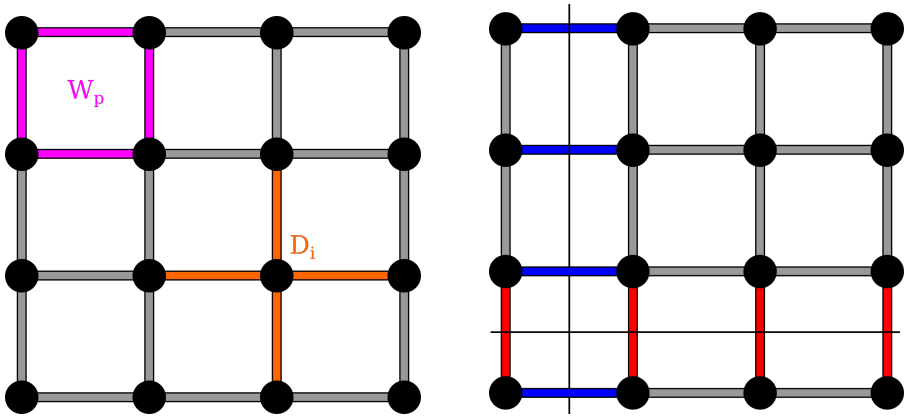

(a) Plaquette flux operator W_p and gauge transformation operator D_i

(b) Sign flips to change between degenerate plaquette flux ground states

Figure 1.1: Lattice $\mathbb{Z}_2$ gauge theory on the square lattice. Fig. (a) shows the definition of the plaquette flux operators W_p and the gauge transformation D_i. In Fig. (b), the colored links indicate the sign flips σ_{ij} along the vertical (blue) and horizontal axis (red) that have to be performed on the link variables u_{ij}, in order to construct the 4-fold degenerate plaquette flux ground states.

In the following, we consider the model M_{22} on the (two-dimensional) square lattice. In this lattice model, the configurations $|\{u_{ij}\}\rangle$ are a redundant labelling of physical states, and hence, deserve the name *gauge* configurations. The physical states are, for the square lattice with open boundary conditions, defined by the plaquette flux states $\{W_p\}$, which can be seen by defining the gauge transformation [49]

$$u'_{ij} = D_i u_{ij} D_j^{-1}, \tag{1.9}$$

where the operators D_i are arbitrary ± 1-valued functions acting on the lattice sites. A useful explicit definition of D_i is provided by introducing the spin flip operator σ_{ij}, which changes the sign of a link variable as $u_{ij} \to -u_{ij}$, and making it act on all nearest neighbors of the site i [1] [51],

$$D_i = \prod_{j \in \mathrm{nn(i)}} \sigma_{ij}. \tag{1.10}$$

Clearly, $[W_p, D_i] = 0$ for all sites i and plaquettes p, so the physical states of the open system can be labelled in a one-to-one manner by the flux states $\{W_p\}$.

For the square lattice with periodic boundary conditions, things are slightly more complicated. Here, the product of all plaquette flux operators is constrained as

$$\prod_p W_p = 1. \tag{1.11}$$

[1] Adding a term $-K \sum_i D_i$ to $\mathcal{H}_{\mathbb{Z}_2,\mathrm{class.}}$ yields exactly the Hamiltonian of Kitaev's Toric Code model [11].

Therefore, from the 2^N plaquette flux states in the periodic 2D square lattice with N sites, only 2^{N-1} are linearly independent. In the Ising gauge model M_{22}, there are, in total, 2^{N+1} states (equivalence classes under the gauge transformation), which follows from dividing the 2^{2N} gauge configurations $|\{u_{ij}\}\rangle$ by 2^{N-1} (which corresponds to 2^N gauge transformations, divided by 2 elements of the $\mathbb{Z}_2$ gauge group). Hence, for each plaquette flux configuration, there are four physical states. From a gauge configuration $|\{u_{ij}\}\rangle$, the other three states that give the same plaquette flux configuration can be constructed by

1. flipping the sign of all link variables u_{ij} that cross a defined horizontal line
2. flipping the sign of all link variables u_{ij} that cross a defined vertical line
3. doing both steps 1. and 2.

This is visualized in Fig. 1.1.

Confined and deconfined phase

A *quantum* version of the lattice $\mathbb{Z}_2$ gauge theory M_{22} (and, likewise, for any d-dimensional gauge theory M_{d2}) is provided by adding a term to the Hamiltonian that contains the sum over all spin-flip operators σ_{ij},

$$\mathcal{H}_{\mathbb{Z}_2} = -g \sum_p W_p - t \sum_{ij} \sigma_{ij}. \tag{1.12}$$

This extended definition introduces a hopping in terms of the $\mathbb{Z}_2$ fluxes, and any state $|\{u_{ij}\}\rangle$ is, under $\mathcal{H}_{\mathbb{Z}_2}$, converted into a highly-entangled superposition state. At the same time, the Hamiltonian $\mathcal{H}_{\mathbb{Z}_2}$ is gauge-invariant with respect to the transformation in Eq. (1.9) [49].

In close analogy to the lattice $U(1)$ gauge theory, we can now distinguish a *deconfined* and *confined* phase for $\mathcal{H}_{\mathbb{Z}_2}$:

For $g \gg t$, the ground states of the Hamiltonian are defined by the homogeneous plaquette flux configuration $\{W_p = 1\}$ and are, as shown above, four-fold degenerate. The gauge-invariant wavefunction for each such ground state is provided by symmetrizing the corresponding gauge configuration $|\{u_{ij}\}\rangle$ over all gauge transformations D_i,

$$|\psi_0^d\rangle = \prod_i (1 + D_i) \, |\{u_{ij}\}\rangle \, , \tag{1.13}$$

and is macroscopically entangled. The four-fold degeneracy of the ground state is called *topological*, as it cannot be lifted by any local perturbations to the Hamiltonian [49]. One degenerate state can only be converted into another by applying a number of gauge flip operators σ_{ij} that corresponds to the linear system size L.

Flipping a single link variable u_{ij}, on the other hand, creates a pair of (bosonic) $\mathbb{Z}_2$ flux excitations, which are called *vortices* or *visons*. The creation of isolated visons is only possible by generating a vison pair, and then applying a non-local string of operators σ_{ij} to separate them – which causes no further energy cost. Hence, they are non-local excitations. The vison excitations in $\mathbb{Z}_2$ gauge theories are always gapped, and the gap Δ is of the order g.

This phase is called the $\mathbb{Z}_2$ *deconfined phase*, and its low-energy properties are determined by the topological degeneracy ($\mathbb{Z}_2$ topological order) and the existence of non-local, gapped vison excitations.

In contrast, for $g \ll t$, there is a unique ground state $|\psi_0^c\rangle = \sum_{\{u_{ij}\}} |\{u_{ij}\}\rangle$, which seems highly entangled at first sight, but simply corresponds to an Ising state with all spins pointing in the x-direction,

$$|\psi_0^c\rangle = \bigotimes_i |{\rightarrow}\rangle_i \,. \tag{1.14}$$

This can be seen by mapping the link variables u_{ij} to Pauli operators, $u_{ij} \rightarrow \sigma_{ij}^z$, and using that the eigenstates $|{\rightarrow}\rangle$, $|{\leftarrow}\rangle$ of σ^x and the eigenstates $|{\uparrow}\rangle$, $|{\downarrow}\rangle$ of σ^z are related as

$$\begin{aligned} |{\rightarrow}\rangle &= \frac{1}{2}(|{\uparrow}\rangle + |{\downarrow}\rangle), \\ |{\leftarrow}\rangle &= \frac{1}{2}(|{\uparrow}\rangle - |{\downarrow}\rangle). \end{aligned} \tag{1.15}$$

This phase is the $\mathbb{Z}_2$ *confined* phase. It doesn't have a topological order, and the elementary excitations are local, as they can be simply created by applying operators σ_{ij}^z to individual lattice bonds.

Ising duality and inverted phase transitions

There is also a well-developed knowledge about the thermodynamics of lattice $\mathbb{Z}_2$ gauge theories. In Ref. [50], Wegner has shown that the lattice $\mathbb{Z}_2$ gauge theories M_{dn} and $M_{d(d-n)}$ are always connected by a duality relation. This implies that the partition function $\mathcal{Z}$ (and all derived thermodynamic quantities) of a model at temperature T is related to the partition function of its dual at the temperature T^*, which is a decreasing function of T. Accordingly, the high-temperature and low-temperature phase of the dual $M_{d(d-n)}$ are inverted with respect to the original model M_{dn}. In particular, the three-dimensional lattice $\mathbb{Z}_2$ gauge theory M_{32} of the form given above is the dual of the three-dimensional Ising model, and exhibits a (continuous) *thermal phase transition*, which is inverted with respect to the Ising phase transition [55]. Therefore, it is called an *inverted Ising transition*.

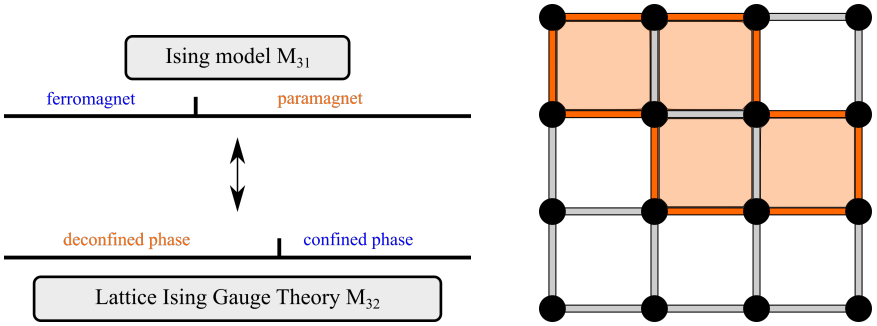

(a) Ising duality **(b)** Wegner-Wilson loop

Figure 1.2: Ising duality and Wegner-Wilson loop. Ising gauge theories M_{dn} and $M_{d(d-n)}$ are connected by a duality relation [50], which holds in particular for the three-dimensional Ising model M_{31} and the lattice Ising gauge theory M_{32} (a). Here, the low-temperature deconfined phase of M_{d2} is the dual of the Ising paramagnet, and separated from the confined phase by a continuous phase transition (inverted Ising phase transition). For $1 < n < d$, this phase transition does not possess a local order parameter. However, both phases can be distinguished by the scaling behavior of the Wegner-Wilson loop $W_l = \prod_{\langle i,j\rangle \in l} u_{ij}$ (b). For the deconfined phase, $\langle W_l \rangle$ scales with the perimeter of the enclosed area, and, for the confined phase, with its area [51].

The phase transition of the d-dimensional Ising model and the corresponding dual lattice gauge theory belong to the same universality class [56–58]. However, Wegner proves that for the lattice $\mathbb{Z}_2$ gauge theory M_{dn} with $1 < n < d$, the phase transition deviates from the conventional Ginzburg-Landau paradigm [13–15], in the sense that it does not require a broken symmetry in terms of any local order parameter. For M_{d2} and $d > 2$, it instead separates the topologically non-trivial, low-temperature *deconfined* and a high-temperature *confined* phase. Instead of a local order parameter, both phases can be distinguished in terms of the average Wegner-Wilson loop $\langle W_l \rangle$ (see Fig. 1.2): In the confined phase, it is expected that $\langle W_l \rangle$ obeys an (extensive) *area law* in terms of the area A_l enclosed by the contour l, such that $\langle W_l \rangle \sim \exp(-aA_l)$, which is a consequence of heavily fluctuating fluxes in this phase. In the *deconfined* phase, on the other hand, vortex excitations are suppressed and $\langle W_l \rangle$ is expected to decay only (subextensively) with the *perimeter* P_l of the enclosed area as $\langle W_l \rangle \sim \exp(-bP_l)$. In correspondence to the scheme of inverted Ising transitions, the deconfined phase, where the plaquettes are *ordered*, is the dual of the *disordered* Ising phase, and the (high-temperature) confined phase is the dual of the *ordered* Ising phase [51].

1.1.3 Emergence of gauge fields in spin liquids

We have seen that the lattice $U(1)$ gauge theory is a discretized version of electromagnetism, and contains gapless excitations in the deconfined phase. The bosonic vortex excitations in lattice $\mathbb{Z}_2$ gauge theory, on the other hand, are always gapped.

For both lattice gauge theories, we have distinguished the deconfined and confined phase. At the example of the lattice $\mathbb{Z}_2$ gauge theory, we have seen that the deconfined phase is a non-trivial phase, which is characterized by topological order, non-local excitations and a ground state wavefunction with macroscopic entanglement. The question is now how all this knowledge can be used for understanding quantum spin liquids.

As it turns out, lattice gauge theories generically emerge in the description of spin liquids, when the latter are represented using a *parton* approach. Such an approach can be realized in terms of a slave-boson (projective construction) [26, 59–61] or slave-fermion ansatz [62, 63], and is necessary to enable the treatment of spin liquid models with mean-field methods. This is seen when considering, for example, a Heisenberg model on the two-dimensional square lattice,

$$\mathcal{H} = \sum_{\langle i,j \rangle} J_{ij} \ \mathbf{S_i} \cdot \mathbf{S_j}, \tag{1.16}$$

which, in the mean-field approximation, is decoupled as

$$\mathcal{H}_{\mathrm{MF}} = \sum_{\langle i,j \rangle} J_{ij} \left(\langle \mathbf{S_i} \rangle \cdot \mathbf{S_j} + \mathbf{S_i} \cdot \langle \mathbf{S_j} \rangle - \langle \mathbf{S_i} \rangle \cdot \langle \mathbf{S_j}, \rangle \right). \tag{1.17}$$

Usually, the ground state $|\psi_{\mathrm{MF}}\rangle$ of $\mathcal{H}_{\mathrm{MF}}$ can be calculated by choosing an adequate ansatz for $\langle \mathbf{S_i} \rangle$, such that the self-consistency equation $\langle \mathbf{S_i} \rangle = \langle \psi_{\mathrm{MF}} | \, \mathbf{S_i} \, | \psi_{\mathrm{MF}} \rangle$ is fulfilled [49].

Clearly, such an approach is only well-suited for ordered spin states, where $\langle \mathbf{S_i} \rangle$ is expected to be finite, but not for spin liquids, which are interesting precisely because $\langle \mathbf{S_i} \rangle = 0$ in the ground state. However, an alternative strategy to perform the mean-field analysis on spin liquids can be pursued by first replacing the spins with parton operators. One (but not the only) possible ansatz is provided by introducing spin-$1/2$ charge neutral *spinon* operators $f_{i\alpha}$ ($\alpha = 1, 2$) as [49, 59]

$$\mathbf{S_i} = \frac{1}{2} f^\dagger_{i\alpha} \sigma_{\alpha\beta} f_{i\beta}, \tag{1.18}$$

which leads to a Hamiltonian that is quartic in the spinons,

$$\mathcal{H} = -\sum_{\langle i,j \rangle} \frac{1}{2} J_{ij} f^\dagger_{i\alpha} f_{j\alpha} f^\dagger_{j\beta} f_{i\beta} + \mathrm{const.} \tag{1.19}$$

With the transformation in Eq. (1.18), the local Hilbert space of the system is artificially extended from dimension 2 to 4, which produces unphysical states, and has to be remedied by introducing a half-filling constraint $f^\dagger_{i\alpha} f_{i\alpha} = 1$ on the fermions. The (0^{th} order) mean-field approximation is then implemented by

1. replacing the operator $f^\dagger_{i\alpha} f_{j\alpha}$ by its ground-state expectation value,

$$\chi_{ij} = \langle f^\dagger_{i\alpha} f_{j\alpha} \rangle, \tag{1.20}$$

and

2. loosening the half-filling constraint, and let it be fulfilled only on average, $\langle f^\dagger_{i\alpha} f_{i\alpha} \rangle = 1$, which is done by adding the site- and time-dependent Lagrange-multiplier term,

$$a_0(i)(f^\dagger_{i\alpha} f_{i\alpha} - 1), \tag{1.21}$$

to the Hamiltonian.

Choosing an ansatz $(\overline{\chi}_{ij}, \overline{a}_0(i))$ for both quantities, the ground-state expectation value χ_{ij} and the Lagrange multiplier $a_0(i)$, the mean-field Hamiltonian assumes the form

$$\mathcal{H}^0_{\mathrm{MF}} = -\sum_{\langle i,j \rangle} \frac{1}{2} J_{ij} \left(\left(f^\dagger_{i\alpha} f_{j\alpha} \overline{\chi}_{ij} + \mathrm{h.c.} \right) - |\overline{\chi}_{ij}|^2 \right) + \sum_i \overline{a}_0(i)(f^\dagger_{i\alpha} f_{i\alpha} - 1), \tag{1.22}$$

and the self-consistency equation is given by $\overline{\chi}_{ij} = \langle f^\dagger_{i\alpha} f_{j\alpha} \rangle$ [49]. Likewise, the ansatz for the Lagrange multiplier $\overline{a}_0(i)$ has to fulfill the relaxed half-filling constraint $\langle f^\dagger_{i\alpha} f_{i\alpha} \rangle = 1$.

Now, the 0^{th} order mean-field Hamiltonian in Eq. (1.22) describes a system of free fermions, but this description is clearly *qualitatively* wrong, as the ansatz has changed not only the Hamiltonian, but also the Hilbert space of the Heisenberg model by allowing individual sites to violate the half-filling constraint. Thus, it looks as if nothing was gained from the entire procedure. However, it is possible to fix this issue and recover the original Hilbert space by introducing (massless) phase fluctuations $(\overline{\chi} e^{-iA_{ij}}, a_0(i))$ around the mean-field state (which can be shown to enforce the half-filling constraint for all sites [49, 59]). In this *first-order* mean-field approximation, the Hamiltonian becomes

$$\mathcal{H}^1_{\mathrm{MF}} = \sum_{\langle i,j \rangle} -J_{ij} \left(f^\dagger_{i\alpha} f_{j\alpha} \overline{\chi}_{ij} e^{-iA_{ij}} + \mathrm{h.c.} \right) + \sum_i a_0(i)(f^\dagger_{i\alpha} f_{i\alpha} - 1), \tag{1.23}$$

and is invariant under the lattice $U(1)$ gauge transformation

$$\begin{aligned} A_{ij} &\to A_{ij} + \chi_j - \chi_i, \\ f_i &\to f_i e^{i\chi_i}. \end{aligned} \tag{1.24}$$

So, instead of a system of free fermions, the Hamiltonian $\mathcal{H}^1_{\mathrm{MF}}$ now describes fermions, which are coupled to an emergent $U(1)$ gauge field [49]. Notably, it is

precisely the introduction of gauge fluctuations which has recovered the original Hilbert space of the system, so it can be concluded that the emergent gauge field is a necessary ingredient for the valid parton description of the spin system (in the words of Wen, the gauge field is required to "glue" the spinons "back together" [49]). Remarkably, the question if the parton description is only a formal rewriting of the spin system, or if it gives access to physical properties that would otherwise stay unrevealed, now depends on the phase of the emergent gauge field. For the *confined* phase of the gauge field, the parton description is just a reformulation of the spin system, which does not provide any physical insight, as the system is still fully governed by the fluctuations of spins. In the *deconfined* phase, on the other hand, the spinons and the emergent gauge field truly behave as independent quasiparticles, and it is exactly this scenario which characterizes the spin liquid state. In this sense, the knowledge about confined and deconfined phases in lattice gauge theories directly translates to the understanding of spin liquids.

There are alternative ways to perform the mean-field approximation for the spinon approach in Eq. (1.18), which essentially distinguish themselves by the pairing channels that are chosen for the spinon operators $f_{i\alpha}$. All these approaches first lead to a qualitatively wrong 0^{th} order mean-field description of the spin system, as any such mean-field ansatz artificially expands the Hilbert space and, on a more fundamental level, breaks the local symmetry of the original Hamiltonian. However, it is always possible to find a global gauge symmetry which the 0^{th} order mean-field Hamiltonian still preserves. This global gauge symmetry is called the *invariant gauge group (IGG)*, and it is converted into a local gauge symmetry in the first-order mean-field approximation by introducing IGG-fluctuations. Generically, it can be shown that a mean-field ansatz which is invariant under the invariant gauge group IGG leads to a low-energy description of the corresponding spin liquid in terms of fermionic spinons, which are coupled to an IGG gauge field. The question if the first-order mean-field solution allows for mass terms in the fluctuations then reflects the nature of excitations of the corresponding spin liquid, and, in consequence, its stability [20, 53]:

- The $U(1)$ spin liquid possesses a gapless gauge boson beside further gapped excitations. The $U(1)$ gauge bosons always mediate long-ranged interactions between the fermionic spinons. For certain systems, these interactions do not affect the stability of the spin liquid regime, which can be shown with renormalization group methods. Such systems are, due to the power-law decay of correlations between the gauge bosons, called algebraic spin liquids. Generically, however, RG-relevant long-range interactions or the instanton effect makes the $U(1)$ spin liquid unstable.

- In contrast, all bosonic gauge excitations in the $\mathbb{Z}_2$ spin liquid are gapped,

and can only mediate short-ranged interactions. These interactions are generically RG-irrelevant and do not affect the stability of the spin liquid. Therefore, it is also called a *rigid spin liquid*.

- A rigid spin liquid can also be realized if the invariant gauge group is $SU(2)$, but the $SU(2)$ fluctuations are suppressed by a Chern-Simons term in the underlying action, which is needed if the filled spinon band has a finite Hall conductance [10, 21]. Such *chiral spin liquids* are quantum spin liquids with broken time-reversal symmetry. They are the spin version of Chern insulators [64–68], i.e., systems with a gapped bulk and gapless (chiral) edge states, which are topologically protected by the bulk gap. The existence of such edge modes can be tracked by a topological $\mathbb{Z}$-invariant, the *Chern number* which is given by the integral of the Berry curvature over the first Brillouin zone.

Parton approaches to spin liquids are not restricted to mean-field treatments, and the emergence of a gauge field is a generic feature of these approaches. In the end, a valid description of the spin system is achieved when the algebra of spin operators is faithfully reproduced by the parton ansatz, which often requires the introduction of additional constraints, in order to reproject the parton system to its physical subspace. We see in Chapter 2 that the Kitaev model, which is in the focus of this thesis, can be solved by a parton ansatz which introduces real (Majorana) fermions as spinons, which are coupled to a $\mathbb{Z}_2$ gauge field. In this basis, the system is even exactly solvable and renders the application of mean-field methods obsolete in many situations. However, it is also possible (and, for some purposes, even more insightful) to study the Kitaev model with an ansatz that uses complex fermions [36, 53].

1.2 Thermodynamics of quantum spin liquids

The common understanding of the quantum spin liquid state in an earlier period of discussion has been focused on the absence of long-range ordering, and the analogy of this state to classical liquids. According to this point of view, it is natural to expect that the QSL state is only well defined at exactly $T = 0$, and for any finite temperature destabilized by thermal fluctuations. With this understanding, it is presumed that the spin *liquid* phase is adiabatically connected to the paramagnetic *gas* phase of the spin system, as is the case for classical liquids [44]. But also from the modern point of view, which defines the QSL phase as a macroscopically entangled quantum many-body state, one can argue that it might be only realized for $T = 0$. Here, it is usually pointed out that any system at finite temperature shows an extensive (volume law) entanglement, and therefore acquires classical

correlations [7]. Hence, it is also expected that a generic QSL state is not protected by a thermal phase transition, and the transition to the high-temperature phase is realized as a smooth crossover.

However, considering that the low-temperature physics of spin liquid systems can be captured in terms of partons coupled to gauge fields, it is the general knowledge about lattice gauge theories that provides us with classes of systems which deviate from this generally assumed behavior. Specifically, it can be argued that spin liquids with *gapped* gauge excitations, such as $\mathbb{Z}_2$ spin liquids, which are stable against quantum fluctuations, are also candidates for a thermally stable phase, which persists up to some finite temperature T_c. In this thesis, we discuss that this is indeed the case for Kitaev systems, which are either defined in three spatial dimensions, or which possess a ground state that is topologically protected by the breaking of time-reversal symmetry. In the case of three-dimensional Kitaev $\mathbb{Z}_2$ spin liquids, Wegner's studies on lattice $\mathbb{Z}_2$ gauge theories even equip us with the universality class of the phase transition. For most 3D Kitaev systems, the spin liquid ground state phase is separated from the paramagnetic state by an inverted Ising phase transition, which is described in terms of loop-like vison excitations. Later on, we see that the paramagnetic phase is further subdivided into an intermediate regime, where the physics is still essentially described by fractionalized degrees of freedom – this phase may also be considered as a *proximate* $\mathbb{Z}_2$ spin liquid [69] – and the true paramagnetic phase, that is merely a spin gas.

1.3 Summary

Lattice gauge theories are discretized versions of gauge theories from quantum field theory, which are useful for the description of spin systems. They are characterized by the symmetry of their underlying gauge transformation as $U(1)$, $\mathbb{Z}_2$ etc., which also determines the gapless or gapped nature of their elementary excitations. Lattice $\mathbb{Z}_2$ gauge theories always possess gapped vison excitations. The three-dimensional lattice $\mathbb{Z}_2$ gauge theory is the dual of the three-dimensional Ising model, and its deconfinement-confinement transition is inverted with respect to the Ising phase transition. In quantum spin liquids, lattice gauge theories arise in the context of the parton description of the spin model. The low-temperature behavior of spin liquid systems is, in this approach, described by fractionalized spinon degrees of freedom, which are coupled to an emergent gauge field. Here, the symmetry of the underlying lattice gauge theory allows for conclusions about the stability of the spin liquid state.

Chapter 2

Kitaev Model

The Kitaev model is the prototypical example of a quantum spin liquid model that possesses an exact solution. Introduced and solved by Kitaev in his seminal paper of 2006 [27], this particular version of a quantum compass model [70, 71] has ever since become a research field of vast interest in both theoretical and experimental condensed matter physics [8, 38–43]. The experimental enthusiasm for the model has been triggered in 2009 by Jackeli's and Khaliullin's proposal for a real material mechanism that leads to the occurrence of Kitaev interactions in certain Mott insulators with strong spin-orbit coupling, such as $\mathrm{Na_2IrO_3}$, $\mathrm{Li_2IrO_3}$ and α-$\mathrm{RuCl_3}$ [37, 72]. Since then, not only have various experimental groups joined in the race to detect signatures of the quantum spin liquid phase in those Kitaev materials [38, 43], but also, there has been an ongoing search for potential alternative realization mechanisms [73]. A fundamental breakthrough in the hunt for signatures of the spin fractionalization in Kitaev magnets has been the recent measurement of the half-integer thermal quantum Hall effect in α-$\mathrm{RuCl_3}$ [74, 75].

In this chapter, we give a detailed introduction of the Kitaev model and its solution, which is the foundation for our numerical studies on the thermodynamics of various 2D and 3D Kitaev systems. We start by explaining the solution ansatz that is used in the original paper by Kitaev [27], which is based on the local transformation of the original spin degrees of freedom to Majorana fermions coupled to an emergent $\mathbb{Z}_2$ gauge field. Here, a close look is given to Lieb's theorem, which makes a statement about the ground state configuration of the corresponding gauge-invariant quantity, the $\mathbb{Z}_2$ plaquette flux. Fixing the gauge field to the ground state plaquette flux configuration, we are able to calculate Majorana band structures and resolve their topological features, such as the graphene-like Dirac cones that the Kitaev honeycomb model exhibits at zero temperature. With this exact solution figured out, we explain how it can be obtained in an alternative way, namely by a non-local Jordan-Wigner transformation of the spins [76–80]. The latter becomes important in the context of developing a numerically exact, sign-

problem-free quantum Monte Carlo algorithm for Kitaev systems (Chapter 3). In this first part, the presentation is based on Refs. [27, 77, 78].

After that, we present how the Kitaev model can be extended to lattice systems in three spatial dimensions, and review the Majorana (semi)metals that are found in these systems. Here, the ground state plaquette flux is harder to determine, since most of these systems lack the geometric requirements for the rigorous applicability of Lieb's theorem. This section is followed by a discussion of the elementary excitations of the $\mathbb{Z}_2$ gauge field, the so-called *visons*, which have a fundamentally different nature in two and three spatial dimensions. In a section on the thermodynamics of Kitaev systems, we see that the loop-like nature of the vison excitations in 3D is the basis for the occurrence of an inverted Ising phase transition in these systems. The presentation in this part is based in particular on Refs. [36, 44, 50, 51, 81].

We also discuss that Kitaev systems with broken time-reversal symmetry can host topologically non-trivial ground states. In particular, this is the case for non-bipartite Kitaev systems in two spatial dimensions, where the ground state breaks time-reversal symmetry spontaneously. In this context, we introduce a generalized version of the Kitaev model for arbitrary odd-coordinated lattice systems, which can be defined in terms of Γ-matrices [82, 83]. The presentation here relies in particular on Refs. [27, 30, 47, 83].

Finally, we close this chapter by giving a brief overview on the material realizations of the Kitaev model, which is mainly based on Refs. [37, 38, 73].

2.1 Definition and solution

2.1.1 Spin model and fractionalization

The Kitaev model is defined on three-coordinated lattice systems. It describes spin-1/2 degrees of freedom, which exist on the lattice sites and interact via bond-dependent Ising interactions. The Hamiltonian is given by [27]

$$\mathcal{H}_{\text{Kitaev}} = \sum_{\langle i,j \rangle_\gamma} J_\gamma \, \sigma_i^\gamma \sigma_j^\gamma \,, \tag{2.1}$$

where the σ_i are the Pauli matrices and the index γ labels the three subclasses of x-, y- and z-bonds (Fig. 2.1). For each of these subclasses, the spins interact only via the respective γ-component. This way, each spin ends up with three competing interactions, which cannot be satisfied at the same time. This phenomenon is called *exchange frustration*. In the classical version of the Kitaev model, where the $SU(2)$ spins σ_i are replaced with $O(3)$ vectors $\mathbf{S_i}$, the exchange frustration leads to a macroscopically degenerate ground state manifold of the system, which

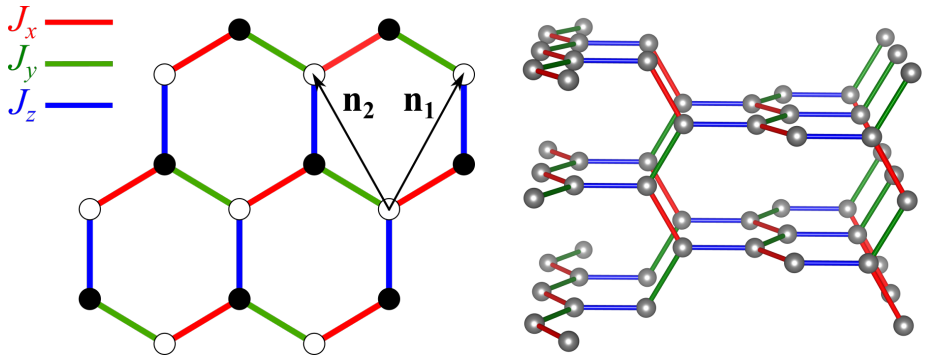

(a) Kitaev honeycomb model **(b)** Kitaev hyperhoneycomb model

Figure 2.1: Kitaev model on the honeycomb (a) and hyperhoneycomb lattice (b) [27, 34, 36]. The Kitaev model is an exactly solvable quantum spin liquid model, which can be defined on three-coordinated lattices. Spin-1/2 degrees of freedom on the lattice sites interact via bond-dependent Ising interactions $-J\sigma_i^\gamma\sigma_j^\gamma$.

has been shown to be equivalent to the full set of dimer coverings on the underlying lattice [84]. Here, in the quantum version, the ground state is instead given by a single wave function with macroscopic entanglement, which constitutes a quantum spin liquid.

Local Majorana transformation

The latter can be derived by applying a parton approach to the system, in which the spins are locally transformed to Majorana fermions. For this, each spin operator σ_i is replaced by four Majorana fermion operators c_i, b_i^x,b_i^y, b_i^z via [27]

$$\sigma_i^\gamma = ib_i^\gamma c_i. \tag{2.2}$$

The Majorana operators b_i^γ, c_i fulfill the canonical commutation relations

$$\begin{aligned} \{b_i^\alpha, b_j^\beta\} &= 2\delta_{ij}\delta_{\alpha\beta}, \\ \{c_i, c_j\} &= 2\delta_{ij}, \\ \{c_i, b_j\} &= 0, \end{aligned} \tag{2.3}$$

and reproduce two of the fundamental relations of the Pauli matrices,

$$\begin{aligned} (\sigma^\gamma)^2 &= 1, \\ (\sigma^\gamma)^\dagger &= \sigma^\gamma. \end{aligned} \tag{2.4}$$

However, reproducing the full spin algebra,

$$\begin{aligned} [\sigma^\alpha, \sigma^\beta] &= 2i\epsilon_{\alpha\beta\gamma}\sigma^\gamma, \\ \{\sigma^\alpha, \sigma^\beta\} &= 2\delta_{\alpha\beta}, \end{aligned} \tag{2.5}$$

requires the introduction of an additional constraint to the Majorana operators. The reason behind this is a change in dimensionality that is typical for parton approaches: The local Hilbert space in the Majorana basis is 4-dimensional ($= (\sqrt{2})^4$), while in the spin basis, it only has dimension 2. The transformation in Eq. (2.2) thus artificially increases the local Hilbert space of each spin. Only a subspace reproduces the spin algebra, though, and can therefore be considered as physical. This physical subspace is obtained by introducing a $\mathbb{Z}_2$ gauge transformation [27],

$$D_i = b_i^x b_i^y b_i^z c_i, \tag{2.6}$$

and consists of all states $|\xi\rangle$ which are $\mathbb{Z}_2$ gauge-invariant, i.e., for which

$$D_i |\xi\rangle = |\xi\rangle . \tag{2.7}$$

The transformation in Eq. (2.2) replaces the Ising terms in the Hamiltonian according to $\sigma_i^\gamma \sigma_j^\gamma = -i(ib_i^\gamma b_j^\gamma)c_i c_j$, i.e., it reveals an interaction that is quadratic in the Majorana fermions c_i. The operators b^γ in the interaction term can, on the other hand, be combined to *bond operators* [27],

$$\hat{u}_{ij}^\gamma = ib_i^\gamma b_j^\gamma, \tag{2.8}$$

with $\hat{u}_{ji} = -\hat{u}_{ij}$. They commute with each other and with the Hamiltonian and have eigenvalues ± 1. Therefore, they can be replaced by their eigenvalues u_{ij} in the Hamiltonian, which then assumes the form [27]

$$\mathcal{H}(\{u_{ij}\}) = \frac{1}{4} \sum_{i,j} iA_{ij} c_i c_j, \tag{2.9}$$

with the matrix A defined by

$$A_{ij} = 2J^\gamma u_{ij}^\gamma, \tag{2.10}$$

for connected sites i,j (otherwise, A_{ij} = 0).

Physically, we now have the paradigmatic scenario for quantum spin liquids, where the original spin degrees of freedom are *fractionalized*, and the fractionalized version of the system includes the description in terms of a lattice gauge theory. Here, the spinon degrees of freedom are given by the non-interacting Majorana fermions c_i, which are coupled to the emergent $\mathbb{Z}_2$ gauge field $\{u_{ij} = \pm 1\}$ on the lattice bonds (Fig. 2.2). Since the bond operators $\hat{u}_{ij}$ commute with $\mathcal{H}$, the $\mathbb{Z}_2$ gauge field is *static*. Hence, if a configuration $\{u_{ij}\}$ is fixed, the model is exactly solvable by diagonalizing the Majorana fermion system, i.e., the complex tight-binding matrix iA in Eq. (2.9). Since iA is Hermitian, its eigenvalues come in (real) pairs $\pm\epsilon_\lambda$. These are the single-particle energy levels of the Majorana fermions.

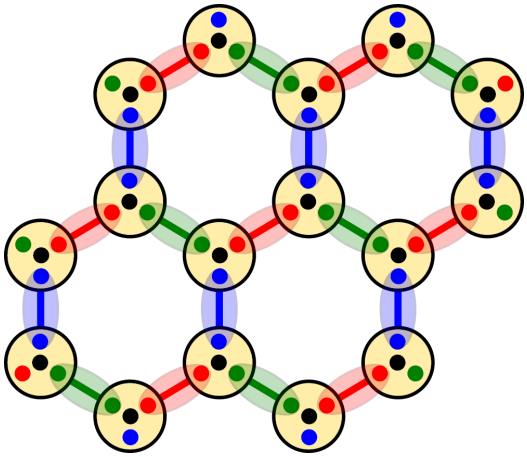

Figure 2.2: Kitaev honeycomb model in the Majorana basis. In this representation, the original spin degrees of freedom are fractionalized to (itinerant) Majorana fermions situated on the lattice sites (black), which are coupled to an emergent (static) $\mathbb{Z}_2$ gauge field on the bonds (red, green, blue) [27].

Vacuum state

The Majorana basis is, however, unsuited to determine a ground state (vacuum state) of the system, because here, the creation and annihilation of a particle are the same, $c^\dagger = c$. Therefore, the system has to be rewritten in terms of complex (Dirac) fermions $a_\lambda^\dagger$. Such a canonical diagonal description is achieved by a pairwise recombination of the Majoranas. For this, we first apply a basis transformation of the operators c_i to normal modes [27],

$$(b'_1, b''_1, ..., b'_m, b''_m) = (c_1, c_2, ..., c_{2m-1}, c_{2m})Q, \tag{2.11}$$

where Q is a transformation matrix consisting of the real (imaginary) parts of the eigenvectors of iA in their odd (even) columns. The matrix A and the eigenvalues ϵ_i of iA are related with the transformation matrix Q by

$$A = Q \begin{pmatrix} 0 & \epsilon_1 & & & \\ -\epsilon_1 & 0 & & & \\ & & \ddots & & \\ & & & 0 & \epsilon_m \\ & & & -\epsilon_m & 0 \end{pmatrix} Q^T. \tag{2.12}$$

After this basis transformation, the spinless fermionic operators a_λ, $a_\lambda^\dagger$ are introduced as [27]

$$\begin{aligned} a_\lambda^\dagger &= (b'_\lambda - ib''_\lambda)/2, \\ a_\lambda &= (b'_\lambda + ib''_\lambda)/2. \end{aligned} \tag{2.13}$$

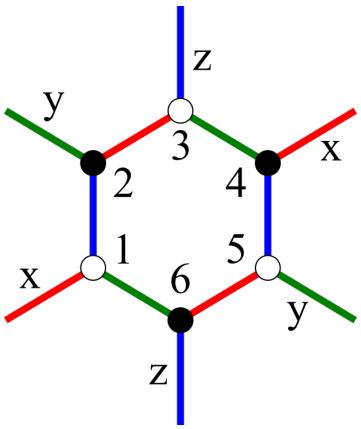

Figure 2.3: Elementary plaquette of size $|p| = 6$ in the honeycomb lattice [27]. Taking the product of the $\mathbb{Z}_2$ gauge variables u_{ij} along the plaquette yields the gauge-invariant $\mathbb{Z}_2$ plaquette flux $W_p = \prod(-iu_{ij}^{\gamma}) = \pm 1$.

Thus, the N Majorana operators are mapped to $N/2$ spinless fermions $a_\lambda^\dagger$, and the final diagonal representation of the Kitaev Hamiltonian in a fixed $\mathbb{Z}_2$ gauge field configuration $\{u_{ij}\}$ reads

$$\mathcal{H}\left(\{u_{ij}\}\right) = \sum_{\lambda=1}^{N/2} \epsilon_\lambda \left(a_\lambda^\dagger a_\lambda - \frac{1}{2}\right). \tag{2.14}$$

The ground state energy of the Majoranas in the gauge field configuration $\{u_{ij}\}$ is now obtained simply by setting the fermionic counting operators $\hat{n}_\lambda = a_\lambda^\dagger a_\lambda = 0$ for all λ,

$$E\left(\{u_{ij}\}\right) = -\frac{1}{2}\sum_{\lambda=1}^{N/2} \epsilon_\lambda. \tag{2.15}$$

2.1.2 Lieb's Theorem

$\mathbb{Z}_2$ plaquette flux

As a result of the described transformations, the problem of obtaining the ground state of the full spin system is reduced to finding the $\mathbb{Z}_2$ gauge field configuration $\{u_{ij}\}$ which minimizes the energy (2.15). The bond operators $\hat{u}_{ij}$ are clearly not gauge-invariant, because they change their sign under any gauge transformation D_i that is applied to one of their adjacent sites i,

$$D_i \hat{u}_{ij} = -\hat{u}_{ij}, \tag{2.16}$$

Thus, it is necessary to find the corresponding gauge-invariant quantity for the $\mathbb{Z}_2$ gauge field $\{u_{ij}\}$, which is expected to be associated with some physical observable.

Reminding ourselves of the general formulation of the lattice $\mathbb{Z}_2$ gauge theory in Sec. 1.1.2, we find that this gauge-invariant quantity is already well known as the plaquette flux, which has been written in terms of the operator W_p, Eq. (1.8). There is an interesting mathematical-physics perspective on this quantity, which relates it to the energy spectrum of arbitrary tight-binding electron Hamiltonians with nearest-neighbor hopping $t_{ij} = |t_{ij}|e^{i\phi_{ij}}$. As it turns out, for a fixed configuration of coupling parameters t_{ij}, this spectrum only depends on the phase variables ϕ_{ij} through the flux Φ around the elementary plaquettes p, i.e., the loops of shortest length of the corresponding lattice [85–87]. This flux Φ is, in the most general version, defined by

$$e^{i\Phi} = \frac{\prod_{\langle i,j\rangle\in p} t_{ij}}{\prod_{\langle i,j\rangle\in p} |t_{ij}|}, \tag{2.17}$$

and corresponds to the plaquette flux that is defined in Sec. 1.1.2 for the lattice $\mathbb{Z}_2$ gauge theory M_{d2}. In Kitaev systems, the plaquette flux operator $e^{i\Phi}$ in Eq. (2.17) is usually also denoted by W_p. We obtain it by taking the product of the Kitaev bond terms around the plaquettes, where, as a standard, we multiply the bond terms in a clockwise manner. Thus, in the spin and Majorana basis, the $\mathbb{Z}_2$ plaquette flux operator reads [27]

$$\begin{aligned} W_p &= \prod_{\langle i,j\rangle_\gamma\in p} \sigma_i^\gamma \sigma_j^\gamma \\ &= \prod_{\langle i,j\rangle_\gamma\in p} (-iu_{ij}^\gamma). \end{aligned} \tag{2.18}$$

The eigenvalues of W_p are ± 1 for plaquettes with even and $\pm i$ for plaquettes with odd length, and the (clock- or counterclockwise) direction of measurement only affects the sign of the odd-length plaquettes. We use the convention that an eigenvalue $W_p = +1 = e^{i0}$ is identified with the *absence* of a $\mathbb{Z}_2$ plaquette flux ($\hat{=}$ 0-flux), while an eigenvalue $-1 = e^{i\pi}$ signifies the *presence* of a $\mathbb{Z}_2$ plaquette flux ($\hat{=}$ π-flux) [1].

W_p is clearly invariant under the gauge transformation D_i, since, for any plaquette, the latter always changes the sign of two $\mathbb{Z}_2$ gauge variables u_{ij} within that plaquette. But this is not all. W_p also commutes with the Hamiltonian $\mathcal{H}(\{u_{ij}\})$, and therefore provides an extensive set of conserved quantities $\{W_p\}$ for the Kitaev model. In consequence, the Hilbert space H of the system is divided into

[1] In the remainder of this thesis, we often use the convention to denote the flux operator eigenvalue W_p also by the name "plaquette flux".

$\mathbb{Z}_2$ gauge-invariant subspaces $H_{\{W_p\}}$, which are given by the eigenspaces of the plaquette flux operators W_p, and called *flux sectors*,

$$H = \bigoplus_{\{W_p\}} H_{\{W_p\}}. \tag{2.19}$$

Thus, in the sense of the general gauge theory definition that is given in Chapter 1, the $\mathbb{Z}_2$ gauge configurations $\{u_{ij}\}$ are redundant labellings of the $\mathbb{Z}_2$ flux configurations $\{W_p\}$, and likewise, different *gauge sectors* $H_{\{u_{ij}\}}$ of the Hilbert space provide a redundant description of the physical flux sectors.

Ground state flux sector

Having this gauge-invariant quantity W_p defined, the remaining problem is to find the plaquette flux configuration $\{W_p\}$ which gives a minimal energy. This problem has been the subject of numerous studies in mathematical physics [85–87] (Appendix A.1). The most striking result is a theorem by Lieb [86], which states that the flux ground state for an arbitrary half-filled band system of hopping electrons and a bipartite lattice with (at least) semi-periodicity is determined by the elementary plaquette length $|p|$ of the lattice. If $|p| \mod 4 = 0$ (e.g., in the square lattice), the energy of the system is minimized by a plaquette flux $\Phi = \pi$. Quite remarkably, this means that the presence of a magnetic flux *lowers* the energy, a phenomenon which can only occur for systems with high electron density. On the other hand, if $|p| \mod 4 = 2$ (e.g., in the honeycomb lattice), the ground state plaquette flux is $\Phi = 0$. A general formula for the plaquette flux is thus given by

$$\Phi = \frac{\pi(|p| - 2)}{2}. \tag{2.20}$$

However, Lieb's theorem is not universally applicable. In non-bipartite lattice systems, we have seen that the odd-length elementary plaquettes have direction-dependent loop operator eigenvalues $W_p = \pm i$. Here, the nature of the flux ground state is fundamentally different from bipartite systems, since there is no energetic selection of one distinguished flux state. Instead, the two possible flux states are connected by time-reversal symmetry, and the ground state spontaneously breaks TR symmetry by selecting either of the two states for all plaquettes.

Also for bipartite lattice systems, Lieb's theorem is only rigorously proven for systems with a specific geometric condition. The whole lattice (i.e. the sites and bonds, along with the configuration of coupling constants J_γ), and the individual plaquettes, for which the flux is minimized, have to be invariant under reflection symmetry. Moreover, the corresponding mirror plane must not cut through any vertices of the lattice. This condition is fulfilled for the honeycomb lattice. Going

over to Kitaev systems in three spatial dimensions, on the other hand, we see that the mirror plane condition is only fulfilled for one of the elementary systems. We discuss this issue in Sec. 2.2.3.

QSL wave function

In the Majorana basis of the Kitaev system, a particular flux configuration $\{W_p\}$ is adjusted by choosing the adequate $\mathbb{Z}_2$ gauge field configuration $\{u_{ij}\}$. Is the ground state plaquette flux configuration known and the gauge configuration $\{u_{ij}\}$ chosen accordingly, we obtain the ground state wave function of the model by symmetrization over all gauge transformations D_j, i.e.

$$|\Psi_w\rangle = \prod_{j=1}^{N} \left(\frac{1 + D_j}{2} \right) |\Psi_u\rangle \,, \tag{2.21}$$

where $|\Psi_u\rangle = |u\rangle \otimes |m\rangle$ consists of the gauge part $|u\rangle$ and the Majorana (matter) part $|m\rangle$ [27]. The symmetrization operation amounts to reprojecting the system to the physical subspace (see the discussion in Sec. 3.4.2), and the resulting ground state wavefunction in Eq. (2.21) obviously contains a macroscopic degree of entanglement, which determines its quantum spin liquid nature.

2.1.3 Majorana (semi)metal

With the plaquette flux configuration $\{W_p\}$ of the quantum spin liquid ground state fixed, we can calculate the band structure of the Majorana fermions. Describing physical energy levels $\epsilon_n(\mathbf{k})$, the band structure is not affected by the gauge transformations D_i. Therefore, it is sufficient to fix the $\mathbb{Z}_2$ gauge field to any configuration $\{u_{ij}\}$ that produces the ground state plaquette flux $\{W_p\}$, and to diagonalize the Majorana Hamiltonian in this gauge sector. For that, we go over to the reciprocal space by Fourier-transforming the Majorana operators,

$$c_{\mathbf{n},i} = \frac{1}{\sqrt{N}} \sum_{\mathbf{k}} \left(c_{\mathbf{k},i} e^{i\mathbf{kn}} + c^{\dagger}_{\mathbf{k},i} e^{-i\mathbf{kn}} \right) , \tag{2.22}$$

with the vectors $\mathbf{n}$ labelling the unit cells, and the indices $i = 1, \ldots, n$ labelling the site positions inside the unit cell. Applying the condition $c^{\dagger}_{\mathbf{k}} = c_{-\mathbf{k}}$ for the Majorana operators, the Hamiltonian, Eq. (2.9), takes the k-space form

$$\mathcal{H}_{\mathbf{k}} = \frac{1}{2} \sum_{k} \left(c_{-\mathbf{k},1} \ldots c_{-\mathbf{k},n} \right) \left(i A_{\mathbf{k}} \right) \left(c_{\mathbf{k},1} \ldots c_{\mathbf{k},n} \right) , \tag{2.23}$$

and the band structure can be calculated by diagonalizing the Bloch matrix $iA_{\mathbf{k}}$. For example, in the case of the Kitaev honeycomb model, we get [27]

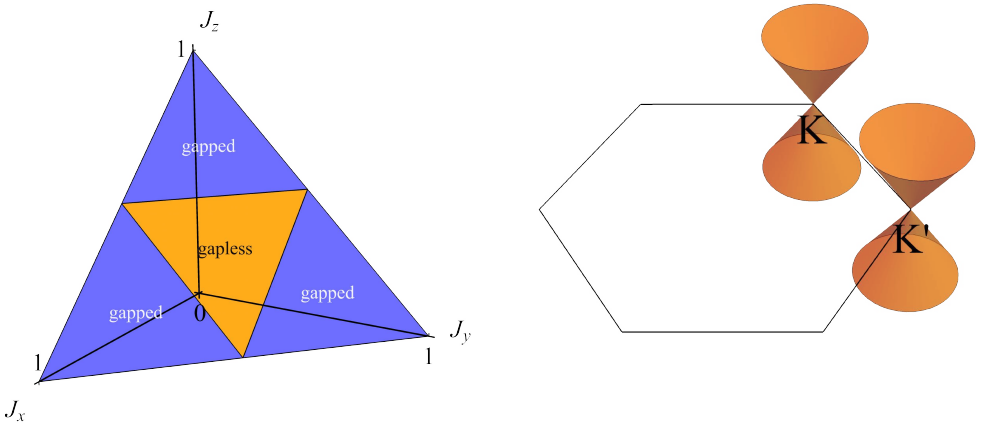

(a) Ground state phase diagram

(b) Dirac cones

Figure 2.4: Majorana semimetal ground state for the Kitaev honeycomb model. For the choice of bond couplings $J_x + J_y + J_z = 1$, the ground state phase diagram in (a) is obtained. The Majorana system is gapless for the triangular region where $|J_{\gamma_1}| \leq |J_{\gamma_2}| + |J_{\gamma_3}|$. Here, it possesses Dirac cones at the symmetry points K, K' of the Brillouin zone [27].

$$iA_{\mathbf{k}} = \begin{pmatrix} 0 & if(\mathbf{k}) \\ -if(\mathbf{k})^* & 0 \end{pmatrix}, \tag{2.24}$$

where

$$f(\mathbf{k}) = 2\left(J_x e^{i\mathbf{k}\mathbf{n_1}} + J_y e^{i\mathbf{k}\mathbf{n_2}} + J_z\right), \tag{2.25}$$

with the lattice vectors $\mathbf{n_1} = \left(\frac{1}{2}, \frac{\sqrt{3}}{2}\right)^T$ and $\mathbf{n_2} = \left(-\frac{1}{2}, \frac{\sqrt{3}}{2}\right)^T$ (Fig. 2.1).

The energy bands are given by

$$\epsilon(\mathbf{k}) = \pm|f(\mathbf{k})|, \tag{2.26}$$

and possess gapless points, $\epsilon(\mathbf{k}) = 0$, if one of the couplings $|J_\gamma|$ is lesser or equal than the sum of the other two,

$$|J_{\gamma_1}| \leq |J_{\gamma_2}| + |J_{\gamma_3}|. \tag{2.27}$$

With these conditions, the ground phase diagram assumes the form that is shown in Fig. 2.4 a, with a triangular gapless region around the point of isotropic coupling ($J_x = J_y = J_z$), and gapped phases beyond this region.

Concerning the nature of the gapless phase, it is shown in Ref. [27] that the latter is a Majorana semimetal, whose band structure possesses two Dirac cones at

the symmetry points K, K' of the Brillouin zone (Fig. 2.4 b). This feature makes the band structure of the Kitaev honeycomb model similar to graphene [88].

As it turns out, the occurrence of gapless spin liquid phases is a generic phenomenon for Kitaev models both in two and three spatial dimensions. We see later that the elementary 3D Kitaev systems that are in the focus of our numerical studies also exhibit a variety of Majorana (semi)metal ground states, where, depending on the underlying lattice geometry, the band structures show different topological features, such as (topological) Fermi surfaces, nodal lines and Weyl nodes. Before we enter the discussion of these models, however, we make a short detour by taking a look at an alternative solution approach for the Kitaev model.

2.1.4 Jordan-Wigner transformation

In the last sections, we have seen how to get from the Kitaev spin model, Eq. (2.1), to its quantum spin liquid ground state in a straightforward manner, by applying the local transformation ansatz introduced in Eq. (2.2) and deriving the Majorana Hamiltonian for a fixed $\mathbb{Z}_2$ gauge sector, Eq. (2.9). However, there are alternative solution approaches, a couple of which have been reviewed in Ref. [89]. One of these alternative approaches is to use a non-local *Jordan Wigner transformation* to transform the original spin operators into Majorana fermions [76–80], and has been applied in earlier quantum Monte Carlo studies of Kitaev systems. [44–47, 90]. We discuss it in the following.

The basic idea of the Jordan-Wigner transformation is to replace the spin operators in a one-dimensional chain of lattice sites $i = 1, \ldots, N$ with fermions, and to maintain the spin algebra by introducing non-local phase factors. The most general form of the transformation is

$$\begin{aligned} \sigma_j^+ &= a_j^\dagger e^{-i\pi \sum_{i<j} \hat{n}_i}, \\ \sigma_j^- &= a_j e^{i\pi \sum_{i<j} \hat{n}_i}, \\ \sigma_j^z &= 2a_j^\dagger a_j - 1, \end{aligned} \tag{2.28}$$

where the $\hat{n}_j$ are fermionic counting operators. The phase terms $e^{\pm i\pi \sum_{i<j} \hat{n}_j}$ always give a ± 1 and depend on the fermionic parity along the chain, between the first and the j-th site.

The Kitaev systems we are interested in are two- or three-dimensional. However, they can be regarded as being composed of one-dimensional *Jordan-Wigner strings* of bonds. Concretely, we choose the Jordan-Wigner strings as bond chains, where the bonds only belong to two of the three subclasses γ. This way, the Jordan-Wigner strings are connected by the bonds of the third subclass. A convenient way to visualize this in two-dimensional systems is to transform the underlying lattice to a bricklayer geometry (Fig. 2.5). In this geometry, where rows

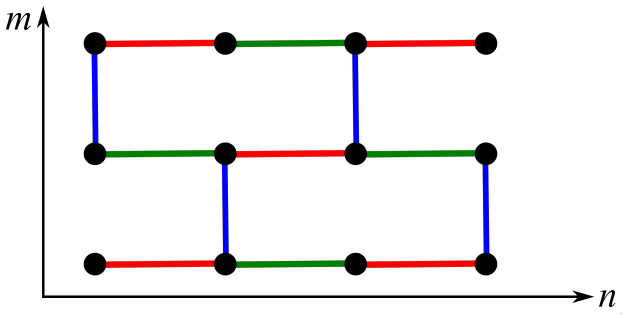

Figure 2.5: Honeycomb lattice in bricklayer geometry. Rows (columns) of sites are labeled by the coordinates m (n). The JW strings are defined along rows of x- and y-bonds (red and green). The z-bonds (blue) host the $\mathbb{Z}_2$ gauge variables η [44].

and columns of sites can be labeled by the two coordinates m and n, the Kitaev Hamiltonian is rewritten as [44]

$$\mathcal{H} = \sum_{\text{m+n even}} -J_x \sigma^x_{m,n}\sigma^x_{m,n+1} - J_y \sigma^y_{m,n-1}\sigma^y_{m,n} - J_z \sigma^z_{m,n}\sigma^z_{m+1,n}. \tag{2.29}$$

In the following, we choose the Jordan-Wigner strings along the x- and y-bonds. With this choice, the spin operators are replaced with spinless fermion operators $a^\dagger, a$ via [44]

$$\begin{aligned}
\sigma^x_{m,n}\sigma^x_{m,n+1} &= \left(\sigma^+_{m,n} + \sigma^-_{m,n}\right)\left(\sigma^+_{m,n+1} + \sigma^-_{m,n+1}\right) \\
&= \left(a^\dagger_{m,n} e^{-i\pi\sum_{j<n}\hat{n}_j} + a_{m,n} e^{i\pi\sum_{j<n}\hat{n}_j}\right) \\
&\quad \cdot \left(a^\dagger_{m,n+1} e^{-i\pi\sum_{j<n+1}\hat{n}_j} + a_{m,n+1} e^{i\pi\sum_{j<n+1}\hat{n}_j}\right) \\
&= a^\dagger_{m,n} e^{-i\pi\hat{n}_n} a^\dagger_{m,n+1} \underbrace{e^{-i\pi(2\hat{n}_1+\cdots+2\hat{n}_{n-1})}}_{=1} + a^\dagger_{m,n} e^{i\pi\hat{n}_n} a_{m,n+1} \\
&\quad + a_{m,n} e^{-i\pi\hat{n}_n} a^\dagger_{m,n+1} + a_{m,n} e^{i\pi\hat{n}_n} a_{m,n+1} \underbrace{e^{i\pi(2\hat{n}_1+\cdots+2\hat{n}_{n-1})}}_{=1} \\
&= -(a_{m,n} - a^\dagger_{m,n})(a_{m,n+1} + a^\dagger_{m,n+1}),
\end{aligned} \tag{2.30}$$

and, likewise,

$$\begin{aligned}
\sigma^y_{m,n}\sigma^y_{m,n+1} &= (a_{m,n} + a^\dagger_{m,n})(a_{m,n+1} - a^\dagger_{m,n+1}), \\
\sigma^z_{m,n}\sigma^z_{m+1,n} &= (2n_{m,n} - 1)(2n_{m+1,n} - 1).
\end{aligned} \tag{2.31}$$

We see that all the parity terms $e^{-i\pi(2\hat{n}_1+2\hat{n}_{n-1})}$ cancel each other to 1, since, due to the multiplication, each fermionic counting operator $\hat{n}_j$ in the exponent carries

a multiple of 2. The Hamiltonian now reads [44]

$$\begin{aligned}\mathcal{H} = \sum_{\text{m+n even}} & J_x(a_{m,n} - a^\dagger_{m,n})(a_{m,n+1} + a^\dagger_{m,n+1}) \\ & + J_y(a_{m,n-1} + a^\dagger_{m,n-1})(a_{m,n} - a^\dagger_{m,n}) \\ & - J_z(2n_{m,n} - 1)(2n_{m+1,n} - 1).\end{aligned} \tag{2.32}$$

On bipartite lattices, the two sublattices can be distinguished by the labels A,B. With these labels, different Majorana operators $c_{A/B}$ for the two sublattices can be defined via [44]

$$\begin{aligned} c_A &= -i(a_A - a^\dagger_A), \\ c_B &= a_B + a^\dagger_B, \\ \bar{c}_A &= a_A + a^\dagger_A, \\ \bar{c}_B &= -i(a_B - a^\dagger_B). \end{aligned} \tag{2.33}$$

With these Majorana operators, the Hamiltonian in Eq. (2.32) is finally rewritten as [44]

$$H = \sum_{\text{m+n even}} iJ_x c_{m,n}c_{m,n+1} - iJ_y c_{m,n-1}c_{m,n} - iJ_z\eta_{m,m+1}c_{m,n}c_{m+1,n}, \tag{2.34}$$

where $\eta_{m,m+1} = i\bar{c}_{m,n}\bar{c}_{m+1,n}$ is the $\mathbb{Z}_2$ gauge variable that is defined on all z-bonds. Structurally, the Hamiltonian now has the same form as Eq. (2.9), with the difference that the $\mathbb{Z}_2$ gauge field is, here, only defined on the z-bonds, and the signs of all other matrix entries are fixed. Hence, the ground state is again obtained by adjusting the $\mathbb{Z}_2$ gauge field $\{\eta\}$ to produce the energy-minimizing plaquette flux configuration, and by diagonalizing the Majorana Hamiltonian in analogy to the procedure that is outlined above.

While the ground state calculation is, thus, almost the same for both approaches, there is a highly non-trivial difference, which, as we see later, has a significant effect on the execution of finite-temperature calculations. In contrast with the local ansatz, there is no artificial Hilbert space expansion necessary within the Jordan-Wigner approach. Thus, all states are naturally physical, and there is no need to introduce a gauge transformation in order to map states to a physical subspace.

Although this seems very satisfying, there is still a caveat. The Jordan-Wigner transformation only gives a Hamiltonian of the easy-to-handle form in Eq. (2.34) for systems with open boundary conditions in the direction of the JW strings. If the boundary conditions are chosen periodic, the phase factors that nicely cancel in Eq. (2.30) remain, leaving the Hamiltonian with parity-terms of the form

$$e^{i\pi\sum_{j<N}\hat{n}_j}, \tag{2.35}$$

which are difficult to handle.

The discussion on this matter is continued in Sec. 3.4.2, in the context of presenting the quantum Monte Carlo method for Kitaev systems.

2.2 3D Kitaev Models

The Kitaev model has originally been introduced on the honeycomb lattice, yet it can be generalized and defined for arbitrary lattices that possess a coordination number $c = 3$. A number of examples have been presented in two spatial dimensions, such as for the square-octagon [28, 29] and the decorated honeycomb lattice [30]. In three spatial dimensions, after a number of early generalization attempts [31–33], a direct version of the Kitaev model has first been presented for the hyperhoneycomb lattice [34], which, later on, has even been shown to possess material realizations [91, 92]. Interestingly, the Kitaev spin liquid on the hyperhoneycomb lattice is also gapless for isotropic coupling parameters, its ground state phase diagram looks the same as for the honeycomb lattice (Fig. 2.4), and it hosts a Majorana semimetal with a nodal line band structure [34], i.e., a one-dimensional manifold of gapless points, which shares the codimension 2 with the zero-dimensional gapless points in the Kitaev honeycomb model. In this sense, the Kitaev hyperhoneycomb model is a straightforward generalization of the honeycomb model. This discovery has been followed by similar studies on the hyperoctagon lattice, where the ground state is shown to exhibit a topological Fermi surface [35], and the Kitaev hyperhoneycomb model with broken time-reversal symmetry, where the Majorana fermions form a Weyl superconductor [48]. These analytical studies have finally led to a comprehensive classification of gapless $\mathbb{Z}_2$ spin liquids in elementary, three-dimensional Kitaev systems [36], and to an extension of this classification to Kitaev systems on lattice geometries with non-symmorphic symmetries [2] [93].

In our thermodynamic studies, we simulate a collection of elementary three-dimensional Kitaev systems that have formerly been presented in the two aforementioned works, in particular Ref. [36]. Therefore, we present this selection of lattice systems in the following. In this context, we also discuss some important geometric differences that arise when going over to Kitaev systems in three spatial dimensions. In particular, the plaquette flux operators generically become subject to volume constraints in 3D, which make them linearly dependent. We also discuss the applicability of Lieb's theorem to these systems. Finally, we give a brief overview on the $\mathbb{Z}_2$ spin liquid ground states that these models exhibit.

[2] Space groups are called *symmorphic* if they possess one point which is invariant under all symmetry operations except translation.

Lattice	Alternative names	Sites in unit cell	Majorana metal	TRS breaking
(10,3)a	hyperoctagon [35]	4	Fermi surface	Fermi surface
(10,3)b	hyperhoneycomb [91]	4	Nodal line	Weyl nodes
(10,3)c		6	Nodal line	Fermi surfaces
(10,3)d		8	Nodal line	Nodal line
(8,3)a		6	Fermi surface	Fermi surface
(8,3)b	hyperhexagon [94]	6	Weyl nodes	Weyl nodes
(8,3)n		16	Gapped	Weyl nodes
(8,3)c*		8	Nodal line	Weyl nodes
(9,3)a*	hypernonagon [95]	12	Weyl nodes	Weyl nodes

Table 2.1: Overview of the elementary three-dimensional, tricoordinated lattices and their Majorana band structures as given in Refs. [36, 93]. The occurrence of Majorana (semi)metals with different topological features is based on distinct projective time-reversal and inversion symmetries of the underlying lattice geometry.

2.2.1 Elementary tricoordinated lattice systems

A comprehensive geometric classification of three-dimensional lattice systems with coordination number $c = 3$ has been presented in 1977 by Wells [96]. For a systematic study of 3D Kitaev systems, the authors of Ref. [36] select a family of these lattice geometries which fulfill a number of prequisites that are considered as *elementary*, namely (i) they have elementary loops of only one fixed length, (ii) they possess equidistant bonds, and (iii) all bond angles have approximately 120 degrees.

A notation which provides a systematic way of labelling these lattices is given by the *Schläfli convention*. According to this notation, a lattice is denoted by $(|p|, c)x$, where $|p|$ is the elementary plaquette length, c the coordination number, and $x = a, b, \ldots$ a letter that serves for numbering.

An overview on the so-obtained three-dimensional lattice systems is given in Table 2.1, which also summarizes the nodal structures that the Majorana metals on these lattice systems exhibit, namely for the Kitaev model with and without a time-reversal symmetry breaking term (see the discussion in Sec. 2.2.4). Details on the lattice definitions (unit cell and basis vectors) and the assignment of Kitaev couplings are documented in Appendix C.1.

2.2.2 Volume constraint

A fundamental geometric difference that arises when the Kitaev model is extended to three spatial dimensions is the appearance of volume constraints for the loop operators, which causes them to be linearly dependent. In the simplest case, when plaquettes form the boundary of a closed volume, the product of their loop opera-

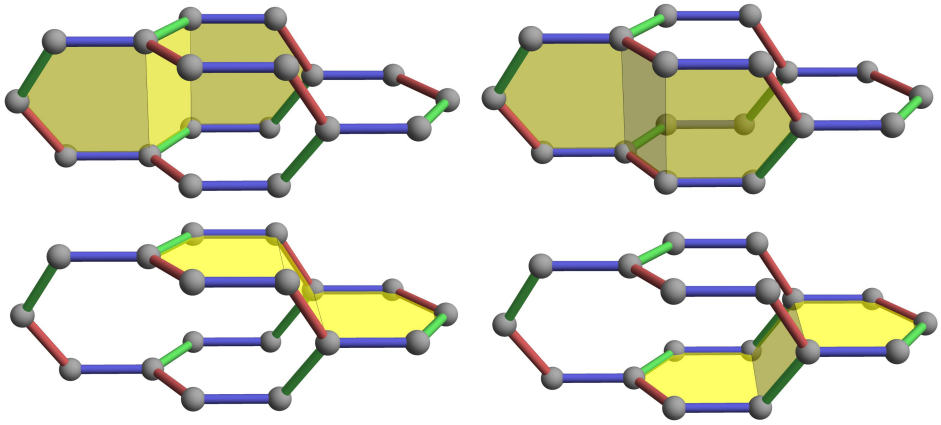

Figure 2.6: Volume enclosed by loop operators in the (10,3)b lattice. The product of plaquette flux operators W_p is constrained to $\prod_p W_p = 1$, if the plaquettes form the boundary of a closed volume. Hence, the plaquette flux operators in 3D are linearly dependent [34, 36].

tors W_p is constrained to be 1,

$$\prod_{p \in \text{vol}} W_p = 1. \tag{2.36}$$

The appearance of such volumes is visualized in Fig. 2.6 for the example of the (10,3)b (hyperhoneycomb) lattice. The volume constraint arises *by construction* of the plaquette flux operators, but possesses an intuitive physical picture, which is explained in the discussion of the elementary excitations of the gauge field (Sec. 2.2.5). In particular, the volume constraint becomes of tremendous significance for the emergent $\mathbb{Z}_2$ plaquette flux ground state in the (8,3)c Kitaev model, which is extensively discussed in Chapter 4.

All 3D lattice systems that are considered in this thesis possess $N/2$ linearly independent plaquette flux operators per unit cell, N being the number of sites per unit cell.

2.2.3 Applicability of Lieb's theorem

We have seen that Lieb's theorem is (i) only applicable to bipartite lattice systems, and (ii) among those only to lattice geometries which possess specific mirror symmetry conditions: The entire lattice system and its plaquettes must be invariant under mirror symmetry, and the corresponding mirror planes must not cut through any lattice sites. Among the 3D Kitaev systems, only (8,3)b and (8,3)n possess mirror planes which fulfill this geometric condition (Fig. 2.7). In the latter case, this is, moreover, only true for seven of the eight elementary plaquettes.

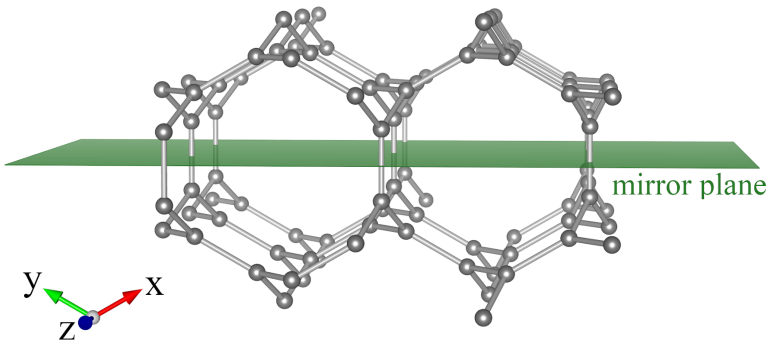

Figure 2.7: Geometric condition for Lieb's theorem [36]. (8,3)b is the only elementary, tricoordinated 3D lattice that possesses a global mirror symmetry for which the mirror plane (green) does not cut through any lattice vertices. Two other mirror planes are obtained by 120-degree rotations around the z-axis (blue).

For this reason, there is no strict mathematical argument to predict the ground state flux sectors for the other lattice systems. In Ref. [36], Lieb's theorem is therefore only considered as a guideline. All lattice systems with elementary plaquette length $|p| = 8$ are assumed to have flux operator eigenvalues $W_p = -1$ in the ground state (with the only exception of (8,3)c, where a specific volume constraint has to be taken into account). The lattice systems with $|p| = 10$ are supposed to have an energy minimum if $W_p = 1$ for all plaquettes p. These assumptions are backed by showing that the predicted flux configurations preserve the lattice symmetries, and by explicit calculations on periodic flux configurations with small unit cells. We verify the correctness of these ground state flux configurations with results from quantum Monte Carlo simulations (Chapter 4).

2.2.4 Majorana band structures

The classification of 3D Kitaev models in Ref. [36] generalizes earlier works on the hyperhoneycomb [34, 48] and hyperoctagon lattice [35]. It shows that all 3D Kitaev systems – except (8,3)n – possess a gapless $\mathbb{Z}_2$ spin liquid ground state for isotropic coupling parameters, and gapped phases beyond a finite-parameter region with small anisotropy. In these systems, the itinerant Majorana fermions form different kinds of (semi)metals, the band structures of which possess distinct topological features, such as (Majorana) Fermi surfaces, nodal lines and Weyl nodes. The occurrence of these topological features depends on the underlying lattice geometry, and, more specifically, its fundamental symmetries. The latter result has been extracted from an analysis of the projective time-reversal and inversion symmetries for all lattices. Also, it is shown how these topological features evolve if a time-reversal symmetry breaking term is added to the Kitaev

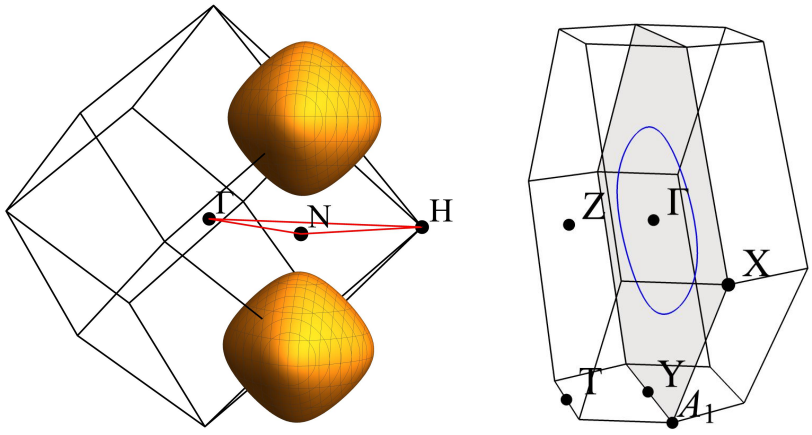

(a) (10,3)a, Fermi surfaces **(b)** (10,3)b, nodal line

Figure 2.8: Nodal structures of the Majorana metals in (10,3)a and (10,3)b. In (10,3)a, the combination of a nontrivial sublattice symmetry and the lack of inversion symmetry leads to the existence of Weyl points at finite energy, which are encapsuled by topological Fermi surfaces. The nodal line in (10,3)b emerges due to a trivial sublattice symmetry [36].

Hamiltonian. Furthermore, the vison gaps Δ are presented for each system.

The results for the Majorana (semi)metals from Ref. [36] are summarized for the different 3D Kitaev systems, with and without broken time-reversal symmetry, in Tab. 2.1. We have also reproduced the calculation of the Fermi surface for (10,3)a, Fig. 2.8 a, and the nodal line for (10,3)b, Fig. 2.8 b.

The analysis of projective symmetries shows that the occurrence of the topological features in the Majorana band structures can be related to the interplay between *(non)trivial sublattice symmetry*, *time-reversal* and *inversion symmetry*. A short summary of the argumentation is given in the following.

The Kitaev Hamiltonian $\mathcal{H}(\mathbf{k})$ is always particle-hole-symmetric, which is a consequence of the description in terms of Majorana operators c with $c^\dagger = c$. In addition, all the considered elementary 3D lattices except (9,3)a are bipartite, i.e., they possess a sublattice symmetry. The distinction between a *trivial* and a *non-trivial* sublattice symmetry amounts to the question if the sublattices have the same translation vectors as the full lattice or not. If not, the two sublattices are connected by the translation vectors, and a non-vanishing reciprocal lattice vector $\mathbf{k_0}$ has to be considered when applying the unitary sublattice transformation matrix U_{SLS} to $\mathcal{H}(\mathbf{k})$,

$$\mathcal{H}(\mathbf{k}) = -U_{\mathrm{SLS}}\, \mathcal{H}(\mathbf{k}+\mathbf{k_0})\, U_{\mathrm{SLS}}^{-1}. \tag{2.37}$$

The vector $\mathbf{k_0}$ also shifts the band structure as

$$\epsilon(\mathbf{k}) = -\epsilon(\mathbf{k}+\mathbf{k_0}). \tag{2.38}$$

For the implementation of the time-reversal symmetry operation T and the inversion symmetry operation U_I, the sublattice transformation, Eq. (2.37), has an important consequence: Both these operations have to be supplemented by a gauge transformation, in order to keep the $\mathbb{Z}_2$ gauge sector of the Hamiltonian fixed. We can make this clear at the example of the time-reversal symmetry transformation. On spin operators, the time-reversal operator T acts as

$$T\sigma_i^\gamma T^{-1} = -\sigma_i^\gamma, \tag{2.39}$$

thus, a naive transformation into the Majorana language yields $Tc_jT^{-1} = c_j$, respectively $Tb_jT^{-1} = b_j$. Unfortunately, this would imply that T flips the $\mathbb{Z}_2$ gauge field, $T\hat{u}_{jk}T^{-1} = -\hat{u}_{jk}$. This, however, can be remedied by introducing a gauge-transformed version $\tilde{T}$ of the time-reversal operation [36] ,

$$\begin{aligned} \tilde{T}c_j\tilde{T}^{-1} &= \mu c_j, \\ \tilde{T}b_j\tilde{T}^{-1} &= \mu b_j, \end{aligned} \tag{2.40}$$

where $\mu = 1$ if site j is in sublattice A, and $\mu = -1$ is site j is in sublattice B. Thus, for the time-reversal operation, the gauge transformation is simply provided by the sublattice transformation U_{SLS}. In consequence, this means that also the time-reversal symmetry operation relates points $\mathbf{k}$ to $-\mathbf{k} + \mathbf{k_0}$ (instead of $\mathbf{k} \to -\mathbf{k}$).

For the inversion symmetry operation, the exact form of the gauge transformation depends on the details of the lattice and the flux configuration, and, in general, relates the points $\mathbf{k}$ to $-\mathbf{k} + \tilde{\mathbf{k}}_\mathbf{0}$, where $\tilde{\mathbf{k}}_\mathbf{0}$ is either half a reciprocal lattice vector or zero.

As it turns out, it follows from these projective symmetries which topological structure the gapless points $\epsilon(\mathbf{k}) = 0$ assume in the Majorana band structure, namely if they exist as isolated Weyl points, one-dimensional lines or two-dimensional surfaces. Concretely, it has been shown that [36]

- the lattice systems (10,3)b, (10,3)c and (8,3)c, which all possess a trivial sublattice and projective time-reversal symmetry, exhibit *nodal lines*.
- from the lattices with a nontrivial sublattice symmetry, (8,3)b is the only one which is also inversion-symmetric. This combination of symmetries determines the emergence of isolated Weyl points, which are constrained to lie exactly at the Fermi energy.
- in contrast, for (10,3)a and (8,3)a, which possess a nontrivial sublattice symmetry, but no inversion symmetry, the Weyl nodes are shifted to finite energy, where they are enclosed by Fermi surfaces – which are topologically protected by the existence of the Weyl points.

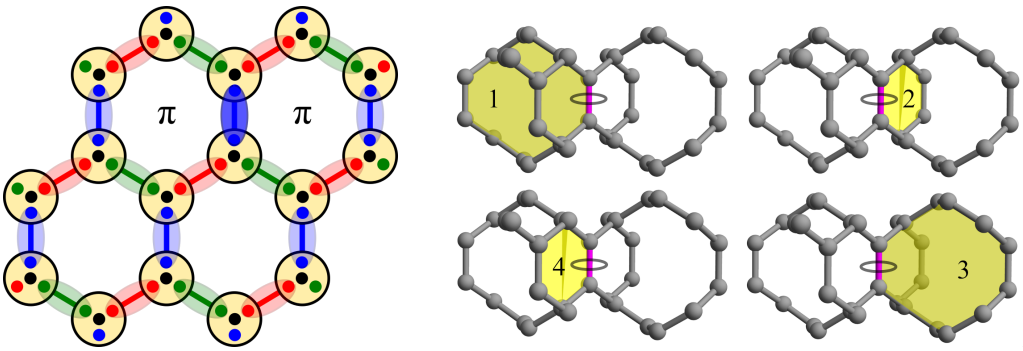

(a) Point-like visons (2D)

(b) Vison loop (3D)

Figure 2.9: Vison excitations in two and three spatial dimensions. On 2D lattices, flipping the $\mathbb{Z}_2$ gauge variable on a single bond creates a pair of point-like vison excitations (a). In 3D, flipping a bond creates a loop-like excitation (b) – here shown for (8,3)b – which is a consequence of the volume constraint on the loop operators [36].

In addition to these results for the unperturbed Kitaev systems, it is shown that adding a magnetic field term, which breaks time-reversal symmetry, generically preserves the gapless spin liquid, but might alter its topological structure. While Weyl nodes and Fermi surfaces remain principally intact upon TR breaking, although the Fermi surfaces are usually deformed and the Weyl nodes moved in k-space, the nodal lines either gap out to a finite number of isolated Weyl points – which is the case on the (10,3)b lattice – or vanish in favor of a topological Fermi surface structure – which is the case for the inversion-symmetric (10,3)c lattice.

The (10,3)d lattice is the only system considered here that is not treated in Ref. [36], but in a separate study on 3D Kitaev systems with non-symmorphic symmetries [93]. In this lattice, the latter appear as a glide mirror symmetry, which keeps the nodal line structure of the isotropic ground state fixed, even if a magnetic field perturbation is applied.

The outlined lattice symmetries also have influence on the occurence of thermodynamic signatures, which is discussed in Appendix C.

2.2.5 $\mathbb{Z}_2$ flux excitations

We have seen that the Majorana excitations are, in general, gapless for 3D Kitaev systems with isotropic coupling parameters. In contrast with that, the *vison* excitations of the $\mathbb{Z}_2$ gauge field are always gapped, which is a generic feature of lattice $\mathbb{Z}_2$ gauge theories. The visons are plaquette flux excitations that are created by flipping $\mathbb{Z}_2$ gauge variables u_{ij}. As it turns out, their nature strongly depends on the dimensionality of the underlying lattice.

In *two* spatial dimensions (e.g. on the honeycomb lattice), flipping a $\mathbb{Z}_2$ gauge

variable creates a pair of $\mathbb{Z}_2$ plaquette flux excitations on the adjacent bonds. These vison excitations are *point-like*. It is not possible to create a single vison, except on lattice systems with an open boundary, if the $\mathbb{Z}_2$ gauge variable on an edge bond is flipped. Of course, a pair of visons can be separated from each other by subsequent bond flips.

Contrasting with two dimensional systems, we have seen that the elementary plaquettes in 3D lattices are characterized by volume constraints. If a number of plaquettes forms the boundary of a closed volume, the product of their loop operators is restricted to $\prod_p W_p = 1$. Due to this volume constraint, the flip of a single $\mathbb{Z}_2$ gauge variable changes the flux on all the surrounding plaquettes of the bond, which always results in a closed, *loop-like* vison excitation. Thus, we can think of the volume constraint as putting a divergence-free condition on the (magnetic) visons: Whenever a flux enters a closed volume by one plaquette, it has to leave through another. There are no magnetic monopoles allowed in the $\mathbb{Z}_2$ gauge field of the Kitaev systems.

The different nature of the $\mathbb{Z}_2$ gauge excitations in two and three spatial dimensions determines an entirely different thermodynamic behaviour of these systems at low temperatures.

2.2.6 Thermodynamics

Another breakthrough for the understanding of Kitaev models has been reached in 2014, when the publication of a numerical finite-temperature study for the Kitaev hyperhoneycomb model [44] has initialized a number of similar works on 3D [45] and 2D lattice systems [46, 47]. All these numerical works have been built on the development of a sign-problem-free quantum Monte Carlo method [44], which allows for unbiased, large-scale studies of real space Kitaev models. This technique is also the foundation for the studies presented in this thesis.

Before the thermodynamic behavior of the Kitaev hyperhoneycomb model was known, it had been widely believed that the quantum spin liquid could not exist as a stable phase at temperatures $T > 0$. Based on the understanding of the quantum spin liquid as a state that is predominantly characterized by the *absence* of long-range order, it was expected that there would always exist an adiabatic connection of this state to the paramagnetic phase, as is the case for other liquid-gas transitions. Accordingly, many experimental approaches to identify quantum spin liquids had been focused on probing the absence of a phase transition [44].

At the example of the Kitaev hyperhoneycomb model, this general belief has been proven wrong by verifying the existence of a low-temperature phase transition [44, 97]. At $T \sim J/100$, the system undergoes an inverted Ising transition [50, 55], which is accompanied by the ordering of $\mathbb{Z}_2$ fluxes. This phase transition manifests itself in one of two characteristic peaks in the specific heat C_v,

which shows a diverging behavior in the thermodynamic limit. A second peak at $T \sim J$, on the other hand, is insensitive to the system size, and indicates a thermal crossover. The latter is identified as the signature for the fractionalization of spins, which occurs at this temperature scale, and which manifests itself in the fact that the kinetic energy of the (itinerant) Majorana fermions – a quantity equivalent to the spin correlator S_{zz} – assumes a finite plateau value here.

In Ref. [44], the occurrence of the low-temperature phase transition is proven for the full range of (an)isotropies in the bond coupling parameters J_γ, which shows that there is no adiabatic connection between the quantum spin liquid state and the paramagnetic phase. Moreover, it is shown that the value for the critical temperature T_c is the largest at the isotropic coupling point, which signifies that the quantum spin liquid phase is stabilized by the exchange frustration. The study further supports a conceptual understanding of the phase transition mechanism which has formerly been discussed in Ref. [81] and is explained in the following.

Deconfinement-confinement transition

As an inverted Ising transition, the phase transition in the Kitaev hyperhoneycomb model lacks a local order parameter [50], and, in this sense, deviates from the conventional Ginzburg-Landau paradigm [13–15]. Instead, it can be explained as a *deconfinement-confinement* transition in terms of the loop-like vison excitations in 3D Kitaev systems [50, 51]. In this picture, the deconfined phase is destabilized by destructive interference of the itinerant Majorana fermions, when the latter encircle the magnetic flux excitations and thereby pick up a phase π. In three spatial dimensions, this only happens with a non-vanishing probability if the loop-like flux excitations have an extension comparable to the system size. The creation of such extended loop excitations, however, requires an amount of energy which is proportional to the loop length L and a temperature-dependent *loop tension* (energy per length) $\tau(T)$. This quantity can be written in the form [81]

$$\tau(T) = \tau(T = 0) + \delta\tau(T), \tag{2.41}$$

where the zero-temperature loop tension $\tau(T = 0)$ is presumably a function of the vison gap Δ, and the finite-temperature contribution $\delta\tau(T)$ is caused by effective flux interactions, which are mediated by the Majorana fermions. Thus, in the thermodynamic limit, the energy required for the creation of macroscopic loops diverges as $E \propto L$, implying a vanishing density of such loops. However, configurations with extended loops also come with a large entropy S, so the relevant quantity to estimate the probability for the creation of extended loops at finite temperatures is given by an *effective loop tension* (free energy per length) $\tilde{\tau}$, which contains an additional term that depends on the entropy per length s [81],

$$\tilde{\tau}(T) = \tau(T) - sT. \tag{2.42}$$

For large vison loops, the entropy per length s is expected to be a constant, which is roughly estimated by the logarithm of the coordination number c_d of the dual lattice (lattice of plaquette fluxes), $s \sim \log(c_d)$. Therefore, the effective loop tension $\tilde{\tau}(T)$ is renormalized to lower values when T is increased, and expected to become negative at a critical temperature T_c. Thus, at T_c, the free energy F is *lowered* by the proliferation of macroscopic loops through the effective loop tension $\tilde{\tau}$. With the picture of destructive interference that is given above, the proliferating system-spanning vison loops at $T > T_c$ then constitute a confining potential for the itinerant Majorana fermions, and destroy the quantum spin liquid phase.

Going back to the point of view of lattice $\mathbb{Z}_2$ gauge theory, we can interpret the vison loops also as domain boundaries of the Ising system which is defined on the dual lattice of plaquette fluxes. In this picture, we can see why the low-temperature and high-temperature phases are *inverted* with respect to the conventional 3D Ising model. Here, the phase with system-spanning domain walls (vison loops) is the high-temperature phase, while in the Ising model, system-spanning domain walls are characteristic for the (ferromagnetic) low-temperature phase. Thus, the transition between two "loop regimes" confirms the general understanding of inverted Ising transitions (Sec. 1.1.2).

It is outlined in Ref. [44] that this, in some sense, non-conventional phase transition mechanism also corresponds to a prediction from mean-field approximation results for three-dimensional $\mathbb{Z}_2$ quantum spin liquids that have formerly been presented in Refs. [16, 26]. The occurrence of the thermal phase transition has also been verified in another 3D Kitaev system on the hyperoctagon lattice [45], and a comparison of the critical temperatures T_c and vison gaps Δ for these systems suggest a correlation between both quantities, which is expected from the described mechanism. Quantum Monte Carlo results for a family of elementary 3D Kitaev systems verify this correlation (Chapter 4).

Thermal crossover in 2D Kitaev systems

A similar quantum Monte Carlo study on Kitaev's original honeycomb model [46] has shown that, in this two-dimensional model, no thermal phase transition occurs. On the one hand, the specific heat curve C_v also shows a double peak structure for this system, and the thermal crossover at $T \sim J$ still indicates the temperature scale of spin fractionalization (Fig. 2.10). On the other hand, the low-temperature peak, which displays the temperature scale of gauge ordering, is now *also* insensitive to the system size.

This thermodynamic behavior can be explained with the same arguments that are given above for the 3D phase transition. There, the creation of extended vison loops is necessary to cause destructive interference of the Majorana fermions,

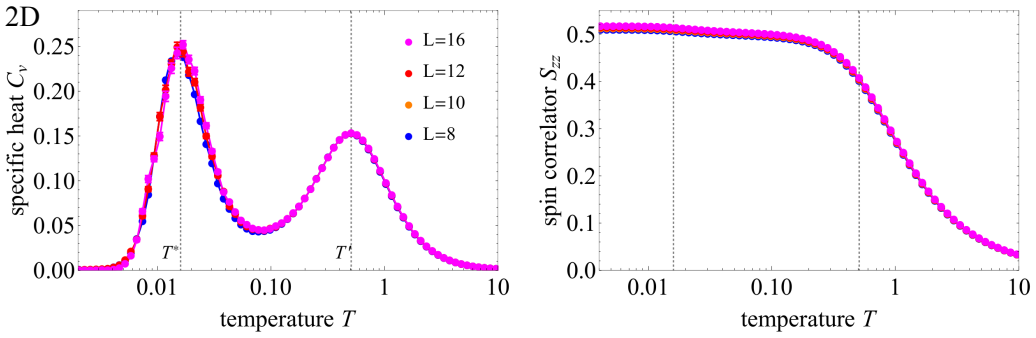

(a) Specific heat C_v

(b) Spin correlator S_{zz}

Figure 2.10: Specific heat C_v and spin correlator S_{zz} for the Kitaev honeycomb model. The specific heat plot (a) shows a two-peak structure, which is characteristic for all Kitaev systems. In 2D, both peaks show no divergence for increased system sizes, and therefore indicate thermal crossovers. The high-temperature peak at T' is a signature of spin fractionalization, which is indicated by the spin correlator S_{zz} assuming a finite low-T value (b). The low-temperature peak at T^* is associated with the proliferation of point-like $\mathbb{Z}_2$ flux excitations, which, in contrast to the flux ordering in 3D systems, is an entirely local phenomenon [46, 69].

which requires an energy that scales with the loop length L. Therefore, a vanishing density of extended loops is expected at low temperatures $T < T_c$, before the effective loop tension $\tilde{\tau}$ assumes negative values as an effect of entropy. In 2D, on the other hand, the creation of point-like visons suffices to destabilize the deconfined phase, and comes with a constant energy cost Δ. Therefore, a finite density of point-like visons exists at any temperature $T > 0$ [81]. In this scenario, the gauge-ordering transition is an entirely local phenomenon, which constitutes a smooth crossover at a temperature T^*.

An exception from this paradigm is realized for two-dimensional Kitaev systems where the ground state is protected by the spontaneous breaking of time-reversal symmetry. This is the case for the Kitaev model defined on the non-bipartite decorated honeycomb lattice (Yao-Kivelson model) [30]. In another QMC study, it has been shown that here, the $\mathbb{Z}_2$ gauge ordering is accompanied by a thermal phase transition [47].

2.3 Chiral Kitaev spin liquids

We have seen that Kitaev models in two and three spatial dimensions host $\mathbb{Z}_2$ spin liquids with both gapless and gapped Majorana fermions. A particular class of spin liquids, which is likewise realized in certain Kitaev systems, is characterized by a broken time-reversal symmetry, and may, under certain circumstances, host topologically non-trivial phases. In such a topological regime, the bulk band

structure is gapped, but, at the same time, the system possesses gapless boundary modes, which cannot be destroyed by any continuous deformation of the Hamiltonian that leaves the bulk gap open [98]. The existence of such boundary modes manifests itself in a finite value of the *Chern number* ν (Sec. 5.1.4). Here and in the following, we denote this particular topological phase, which is the spin version of a Chern insulator [99], as a *chiral spin liquid*, and add the remark that in another broadly used nomenclature, this term is assigned to the class of spin liquids with broken time-reversal symmetry as a whole [1, 2, 9, 10, 21, 100–102].

We consider a conjugate-linear time-reversal operator T with $T^2 = -1$. There are, in principal, two different ways to construct Kitaev systems with broken T-symmetry. Since the Kitaev Hamiltonian $\mathcal{H}_{\mathrm{Kitaev}}$ is, per se, always time-reversal symmetric, the first way is to add an extra term to $\mathcal{H}_{\mathrm{Kitaev}}$ which does not commute with T. In the simplest version, the latter can be realized by a magnetic field. This way, Kitaev systems on bipartite lattice geometries, which belong to symmetry class BDI, are moved to class D [103].

An alternative scenario for broken T-symmetry without an external magnetic field is realized on non-bipartite lattice systems. Here, we have seen that the elementary lattice plaquettes have odd length $|p|$, and the corresponding loop operators $W_p = \pm i$ are connected by the time-reversal operator T due to the complex conjugation inherent in T. While the Kitaev Hamiltonian itself remains T-symmetric on these systems, their flux ground state breaks T-symmetry spontaneously by selecting one of the two fluxes for the entire plaquette set. Therefore, these systems also belong to symmetry class D.

From the classification tables in Refs. [103, 104], we know that symmetry class D allows for the existence of a non-trivial topological phase in two spatial dimensions, but not in three. Hence, it is expected to find chiral spin liquids either in 2D Kitaev systems on bipartite lattices with a magnetic field, or on non-bipartite lattice systems. Since non-bipartite Kitaev systems in 2D are rather scarce, a third option is provided by *generalizing* the Kitaev model to arbitrary lattice geometries, which possess an odd coordination number. Such a generalization can be realized by replacing the spin operators σ_i^γ with higher-dimensional Gamma matrices Γ_i^γ. As it turns out, such models can be likewise solved by a Majorana ansatz, and treated with the same quantum Monte Carlo method as the original, three-coordinated Kitaev model.

In the following, we take a closer look at those different ways to realize chiral spin liquids.

2.3.1 Applying a magnetic field

In the discussion of the classification of three-dimensional Kitaev systems [36], we have seen that the time-reversal symmetry operation on bipartite lattices has to

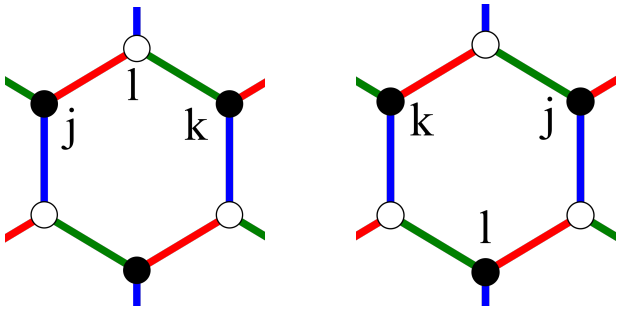

Figure 2.11: Two different kinds of three-spin interactions $\sigma_j^x \sigma_k^y \sigma_l^z$ arise when the Kitaev honeycomb model is perturbed by a weak magnetic field [27].

be supplemented by a sublattice transformation, $T \to \tilde{T}$, in order to achieve gauge invariance, Eq. (2.40). There, we have also seen that the gapless spin liquids in 3D Kitaev models are generically not destroyed if a time-reversal symmetry breaking term is added to the Hamiltonian. However, the situation is different for the two-dimensional Kitaev honeycomb model [27]. Here, it is shown that, if a weak magnetic field is applied along the 111 direction, the Dirac cone singularities in the Majorana band structure gap out into a massive chiral spin liquid phase, which possesses non-Abelian anyonic excitations.

As a matter of fact, with an arbitrary magnetic field term $V = -\sum_j (h_x \sigma_j^x + h_y \sigma_j^y + h_z \sigma_j^z)$, the Kitaev Hamiltonian loses its exact solvability, since the $\mathbb{Z}_2$ gauge field becomes dynamic in this case. However, it is possible to treat the magnetic field h perturbatively, if it is kept smaller than the excitation energy of the visons, $h < \Delta$. In this case, the third-order perturbation term is the first term to break time-reversal symmetry. It introduces a three-spin interaction [27]

$$\mathcal{H}_{\text{eff}}^{(3)} \sim -\frac{h_x h_y h_z}{J^2} \sum_{j,k,l} \sigma_j^x \sigma_k^y \sigma_l^z, \tag{2.43}$$

from which it directly follows that $\tilde{T} \mathcal{H}_{\text{eff}}^{(3)} \tilde{T}^{-1} = -\mathcal{H}_{\text{eff}}^{(3)}$. There are two different versions of the three-spin interaction, which are shown in Fig. 2.11. In the Majorana language, the first variant (a) transforms to a next-nearest neighbor Majorana interaction, which is mediated by the $\mathbb{Z}_2$ gauge field on the two bonds that connect the Majoranas [27],

$$\sigma_j^x \sigma_k^y \sigma_l^z = -i D_l \hat{u}_{jl} \hat{u}_{kl} c_j c_k. \tag{2.44}$$

The second variant (b), on the other hand, transforms into a four-fermion interaction term, which does not alter the energy spectrum and can be ignored [27].

It is shown in Ref. [27] that the magnetic field terms converts the tight-binding

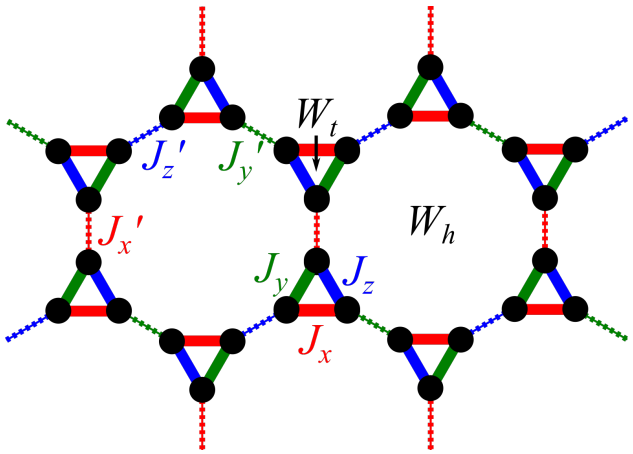

Figure 2.12: Yao-Kivelson model. The two possible plaquette fluxes $W_t = \pm i$ on the triangles are connected by time-reversal symmetry, and the ground state spontaneously breaks TR-symmetry by selecting either of the two fluxes for all plaquettes [30, 47].

matrix $iA_{\mathbf{k}}$ in Eq. (2.24) into [27]

$$i\tilde{A}_{\mathbf{k}} = \begin{pmatrix} \Delta(\mathbf{k}) & if(\mathbf{k}) \\ -if(\mathbf{k})^* & -\Delta(\mathbf{k}) \end{pmatrix}, \tag{2.45}$$

with

$$\Delta(\mathbf{k}) = 4\frac{h_x h_y h_z}{J^2}\left(\sin(\mathbf{k}, \mathbf{n_1}) + \sin(\mathbf{k}, -\mathbf{n_2}) + \sin(\mathbf{k}, \mathbf{n_1} - \mathbf{n_2})\right). \tag{2.46}$$

In particular, this leads to an energy gap $\Delta \sim (h_x h_y h_z)/J^2$ at the positions of the Dirac cones K, K'.

The gapped ground state possesses a nonzero Chern number $\nu = \pm 1$, which corresponds to left- (right-) moving gapless edge modes for systems with open boundary conditions. In Ref. [27], it is also shown that the gapped fermionic bulk excitations behave as non-Abelian anyons.

2.3.2 Yao-Kivelson model

Spontaneous breaking of time-reversal symmetry requires the definition of the Kitaev model on a non-bipartite lattice geometry. In two spatial dimensions, such a geometry can be obtained by taking a honeycomb lattice and replacing the sites with triangles (Fig. 2.12). The "triangle" or "decorated" honeycomb lattice has first been mentioned as a possible stage for a chiral spin liquid ground state in a side remark in Kitaev's original paper [27], and has been studied in detail one year later by Yao and Kivelson [30]. Afterwards, the model has also become known

by the name *Yao-Kivelson model*. Yao and Kivelson use the coupling parameters $J_x = J_y = J_z = J$ ($J'_x = J'_y = J'_z = J'$) on the bonds within (between) the triangles, and map out the ground state phase diagram for the Kitaev system as a function of the coupling ratio $\alpha = J'/J$. Here, it is seen that the system possesses two topologically distinct ground state phases, which are separated by a quantum critical point $\alpha_c = \sqrt{3}$. A chiral spin liquid phase, characterized by a finite Chern number $\nu = \pm 1$ is realized for $\alpha < \alpha_c$. Here, the existence of a gapless edge state corresponds to the non-vanishing Chern number, and the anyon excitations in the system obey non-Abelian statistics. It is not possible to destroy the gapless edge state unless the bulk gap is closed, which is what happens at the quantum critical point. For $\alpha > \alpha_c$, the system enters a topologically trivial ground state phase, with $\nu = 0$, and without gapless edge modes. In this phase, the excitations are Abelian anyons.

In another study of the system in question, Nasu and Motome elucidate how the ground state phase diagram translates into the realm of finite temperatures [47]. With quantum Monte Carlo simulations, they show that, in contrast to the 2D Kitaev honeycomb model, the Yao-Kivelson model undergoes a low-temperature thermal phase transition for all values of α. This thermal phase transition is accompanied by the spontaneous breaking of time-reversal symmetry, which can be measured in terms of the chirality $\kappa = \frac{1}{N_t}\sum_t W_t$, where $W_t = \pm i$ denotes the flux operator eigenvalue for the triangular lattice plaquettes, and N_t is the number of triangles in the lattice. Below T_c, the mean square of the chirality assumes a finite value $\langle \kappa^2 \rangle = 1$ for both quantum regimes. Thus, the phase transition is again related with flux ordering. However, it is also shown that the nature of the thermal phase transition differs, depending on whether α belongs to the chiral or the trivial ground state regime. In the chiral regime $\alpha < \alpha_c$, the phase transition is first-order, and it becomes second-order in the trivial regime. This result, which is obtained from analyzing energy histograms, has been further corroborated by comparing a finite-temperature version of the Chern number $\nu(T)$ and the thermal Hall conductivity $\kappa^{ab}(T)$ for both quantum regimes. While both quantities remain strictly zero for all temperatures in the trivial phase, they obtain finite ground state values in the non-trivial regime. The critical temperature T_c changes continuously as a function of the coupling anisotropy.

In addition to these results, the thermal phase diagram of the system shows various thermal crossovers, which, again, depend on the topological phase. In the trivial phase, the thermal crossover associated with spin fractionalization and the thermal phase transition are accompanied by another crossover at intermediate temperatures, which corresponds to the classical ordering of the length-12 plaquette fluxes. In the chiral phase, the system also shows three transitions. While again, the thermal phase transition at lowest temperatures is explained by the spontaneous breaking of T-symmetry, the occurrence of two thermal crossovers at

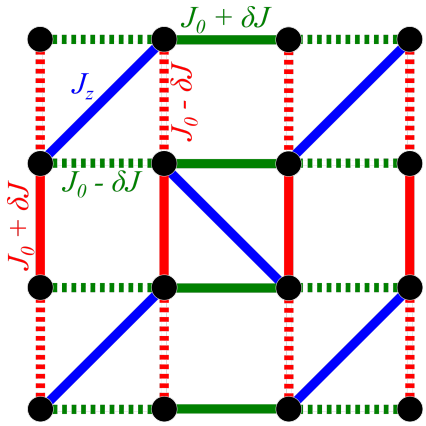

Figure 2.13: Shastry-Sutherland lattice [82, 83, 105]. On this five-coordinated lattice, a generalized version of the Kitaev model can be defined, where anticommuting 4×4 Γ-matrices on the lattice sites represent spin-$\frac{3}{2}$ degrees of freedom. We introduce staggered coupling constants on the horizontal and vertical bonds. The blue bonds carry a coupling J_z, all (red and green) dashed bonds have a coupling $J_0 - \delta J$, and all solid bonds a coupling $J_0 + \delta J$. For a suitable choice of parameters, this model is shown to possess a topologically non-trivial ground state.

higher temperatures requires here a more subtle explanation in terms of subsequent levels of spin fractionalization. The original spins σ_i are first fractionalized into pseudospins τ and triangular plaquette fluxes W_t, before the pseudospins τ further decompose into two Majorana fermions [47].

2.3.3 Generalized Kitaev models

Another realization of a topologically non-trivial quantum spin liquid can be obtained by generalizing the Kitaev model to lattice geometries with a higher coordination number c. For $c = 5$, we can define such a generalization for the Shastry-Sutherland lattice [82, 83] (Fig. 2.13). This lattice is best known as the host for the orthogonal dimer model, which has been solved by Shastry and Sutherland [105] and serves as an effective low-temperature model for the transition-metal oxide $SrCu_2(BO_3)_2$.

A well-defined generalization of the Kitaev model for lattices with an arbitrary odd coordination number $c = 2n - 1$ can be formulated in terms of Γ-matrices [82, 83]. The latter satisfy the anticommutation relation $\{\Gamma_j, \Gamma_k\} = 2\delta_{jk}$, and therefore define a *Clifford algebra*. In fact, the Pauli matrices σ_i^γ, which represent the spins in the Kitaev model, are only a special case of these Γ-matrices. In the generalized version, the Hamiltonian reads

$$\mathcal{H}_{\text{Kitaev}} = -\sum_{\langle j,k \rangle_\gamma} J^\gamma \Gamma_j^\gamma \Gamma_k^\gamma, \tag{2.47}$$

where the index γ again labels the bond direction. On the Shastry-Sutherland lattice, the coordination number is $c = 5$, $\gamma = 1, \ldots, 5$, and the Γ-matrices can be expressed by the 4×4 anticommutating matrices [83]

$$\begin{aligned}
\Gamma^1 &= \tau^x \otimes \mathbb{I}, \\
\Gamma^2 &= \tau^y \otimes \mathbb{I}, \\
\Gamma^3 &= \tau^z \otimes \sigma^x, \\
\Gamma^4 &= \tau^z \otimes \sigma^y, \\
\Gamma^5 &= \tau^z \otimes \sigma^z.
\end{aligned} \tag{2.48}$$

Physically, the Γ-matrices can be interpreted as either $j = \frac{3}{2}$ spins or two coupled spin-$\frac{1}{2}$ degrees of freedom, such as spin and orbital degrees of freedom, which are situated on the lattice sites. In close analogy to the spin-$\frac{1}{2}$ model, the Γ^γ can be replaced on each site i by $c + 1 = 6$ Majorana fermion operators c_i and $\{b_i^\gamma\}$ according to

$$\Gamma_i^\gamma = i b_i^\gamma c_i, \tag{2.49}$$

where the Majorana operators are the same as in the standard case, and, in particular, fulfill the (anti)commutation relations in Eq. 2.3. We again face the issue that the Majorana operators artificially expand the Hilbert space and therefore have to be supplemented by a gauge transformation

$$\Lambda_i = i c_i b_i^1 b_i^2 \ldots b_i^{c=5}, \tag{2.50}$$

which defines the physical subsector as the set of states $|\psi\rangle$ for which

$$\Lambda |\psi\rangle = \lambda |\psi\rangle , \tag{2.51}$$

with $\lambda = i^{n-1} = i^2 = -1$.

In analogy to the solution of the Kitaev model, the Majorana operators $\{b_i\}$ are recombined to bond operators $\hat{u}_{jk} = i b_j^\gamma b_k^\gamma$, which commute with the Hamiltonian, possess eigenvalues $u_{jk} = \pm 1$, and can be interpreted as a (static) $\mathbb{Z}_2$ gauge field, to which the non-interacting, itinerant Majorana fermions $\{c_i\}$ are coupled. Therefore, the Majorana Hamiltonian in a fixed $\mathbb{Z}_2$ gauge configuration $\{u_{jk}\}$ is again given by

$$\begin{aligned}
\mathcal{H}_{\text{Kitaev}} &= \frac{1}{4} \sum_{j,k} i A_{jk} c_j c_k, \\
A_{jk} &= 2 J^\gamma u_{jk}^\gamma,
\end{aligned} \tag{2.52}$$

and the solution for a fixed gauge sector is the same as before.

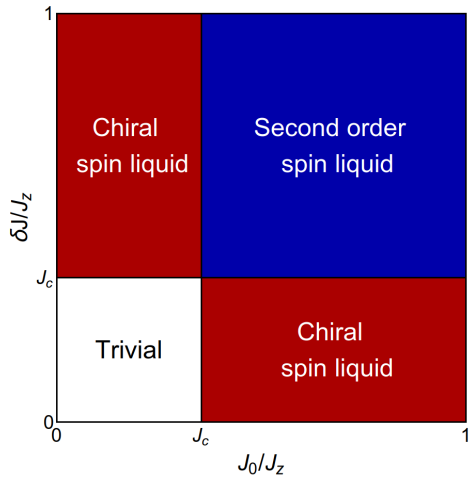

Figure 2.14: Ground state phase diagram of the Kitaev Shastry-Sutherland model with staggered couplings [83]. Fixing the diagonal coupling at $J_z = 1$, we obtain a ground state phase diagram with two chiral spin liquid regimes by varying the parameters $J_0, \delta J$ (with phase transitions at $J_c = 1/(2\sqrt{2})$). In addition, a second order spin liquid phase is realized if both parameters $J_0, \delta J$ are larger than J_c.

The Shastry-Sutherland lattice is non-bipartite, which implies elementary plaquettes with an odd length. Since it is a square lattice, where a diagonal bond is added to every second square plaquette, there are two types of elementary plaquettes, namely triangles and squares. Although Lieb's theorem is not applicable on non-bipartite lattices, the flux ground state is expected to be $W_s = -1$ (π-fluxes) on all squares, and either $W_t = +i$ or $-i$ on all triangles, which we confirm with QMC simulations. Since the sign of W_t depends on the direction in which the product $W_t = \prod(-iu_{jk})$ is taken, we use the convention to take the product with clockwise orientation. Under the conjugate-linear time-reversal operation T, the triangular plaquette flux operator obtains a sign,

$$TW_tT^{-1} = W_t^* = -W_t. \tag{2.53}$$

The flux ground state therefore breaks T-symmetry spontaneously by uniformly selecting a $\pm\pi/2$ flux for all plaquettes. In combination with the lack of sublattice symmetry and the particle-hole symmetry of the Majorana fermions, this sets the symmetry class of the spin-$\frac{3}{2}$ Kitaev model to D, which, in two spatial dimensions, allows for the occurrence of a topologically non-trivial ground state phase [103, 106].

Ground state phase diagram

A ground state phase diagram of the spin-$\frac{3}{2}$ Kitaev-Shastry-Sutherland model has first been presented in Ref. [82], where the occurence of a chiral spin liquid phase

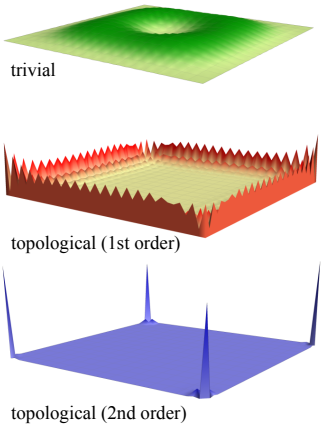

(a) Ground state Majorana wavefunctions[3]

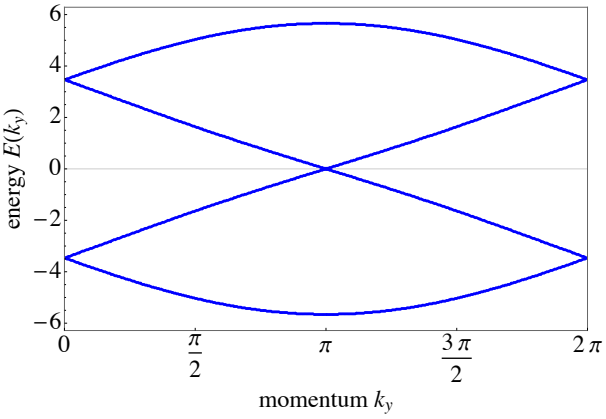

(b) Band structure at $J_z/J_0 = J_c^{-1} = 2\sqrt{2}$

Figure 2.15: Topological band structures of the Kitaev Shastry-Sutherland model [82, 83]. At the quantum critical point $J_z/J_0 = J_c$, the band structure of the system is gapless. Here, the chiral spin liquid phase with a first-order topology, which exhibits edge modes, is separated from the topologically trivial ground state. If an additional staggering δJ is added to the coupling parameters, the system also possesses a ground state phase with a second-order topology, showing gapless corner modes.

is verified. However, a later study on the model shows that this is not the end of the story with respect to topological phases [83]. As a matter of fact, the Shastry-Sutherland lattice possesses additional lattice symmetries in the form of mirror symmetries, where the mirror lines are straight lines through the diagonal bonds. Due to this lattice symmetry, the Kitaev Hamiltonian anticommutes with the mirror operators [83]

$$\mathcal{M}_{11} = \begin{pmatrix} 0 & 0 & 1 & 0 \\ 0 & 1 & 0 & 0 \\ 1 & 0 & 0 & 0 \\ 0 & 0 & 0 & -1 \end{pmatrix}, \quad \mathcal{M}_{1\bar{1}} = \begin{pmatrix} -1 & 0 & 0 & 0 \\ 0 & 0 & 0 & 1 \\ 0 & 0 & 1 & 0 \\ 0 & 1 & 0 & 0 \end{pmatrix}. \tag{2.54}$$

In symmetry class D, such *higher-order* lattice symmetries allow for the existence of an additional *higher-order topological insulator* phase [83, 107–110]. In this nomenclature, an n-th-order topological insulator (TI) is a d-dimensional insulator which possesses topologically protected gapless modes only in $d - n$ dimensions. These gapless modes exist at the intersection of n boundary planes, and the boundaries that have a codimension $< n$ remain gapped [109–111]. In the

[3]The Majorana wavefunctions for the Kitaev Shastry-Sutherland model have been calculated and plotted by Dr. Vatsal Dwivedi.

case of our model, this translates to a second-order topological insulator (SOTI) phase, whose characteristic features in two spatial dimensions are gapless corner modes (see Fig. 2.15 a). We dub such a phase in a (generalized) Kitaev model a *second-order Kitaev spin liquid*.

A suitable choice of bond couplings for the realization of both the chiral spin liquid and SOTI phase is provided by staggered parameters $J_x = J_y = J_0 + \delta J$ and $J'_x = J'_y = J_0 - \delta J$ for the vertical and horizontal bonds (Fig. 2.13), which is inspired by the model in Ref. [110]. Here, δJ denotes the staggering parameter, and J_z is the coupling on the diagonal bonds. With this choice for the couplings, the ground state phase diagram for the system is shown in Fig. 2.14, where the topological phases are drawn for the parameter space spanned up by the ratios J_0/J_z and $\delta J/J_z$. The phase diagram contains four gapped ground state phases, which are divided by a vertical line at the quantum critical points $J_0 = J_c = \pm\frac{J_z}{2\sqrt{2}}$, and a horizontal line at $\delta J = J_c = \pm\frac{J_z}{2\sqrt{2}}$ (see Fig. 2.15 b for the gapless band structure at $J_z/J_0 = J_c^{-1}$). For these parameters, the system is gapless. Within the region $J_0 < J_c$, $\delta J < J_c$, we encounter a topologically trivial ground state phase with Chern number $\nu = 0$. For either $J_0 > J_c$ or $\delta J > 0$, the ground state is a chiral spin liquid (Chern insulator) with a non-vanishing Chern number and a gapless edge mode. The second-order spin liquid phase is realized for both $J_0 > J_c$ and $\delta J > J_c$. Here, the Chern number is likewise $\nu = 0$, but the spectrum of the real space Hamiltonian for a system with open boundary conditions shows four zero-energy states, which are situated at the corners of the system (Fig. 2.15 a).

Based on these results for the ground state phase diagram, we study the thermodynamics of the spin-$\frac{3}{2}$ Kitaev-Shastry-Sutherland model with QMC simulations. The results are presented in Chapter 5.

2.4 Experimental Realizations

In the final section of this chapter, we give a short overview of material realizations for the Kitaev model. In particular, we discuss a physical mechanism for the formation of $j = 1/2$ Mott insulators with bond-dependent interactions, which is encountered in certain transition-metal oxides, and has first been presented in 2009 by Jackeli and Khaliullin [37].

2.4.1 Spin-orbit entangled Mott insulators

Transition metals are characterized by atoms with partially filled d-subshells. According to their number of filled energy levels, they are subdivided into $3d$ - $6d$ transition metals. A mechanism for the formation of effective $j = 1/2$ Mott

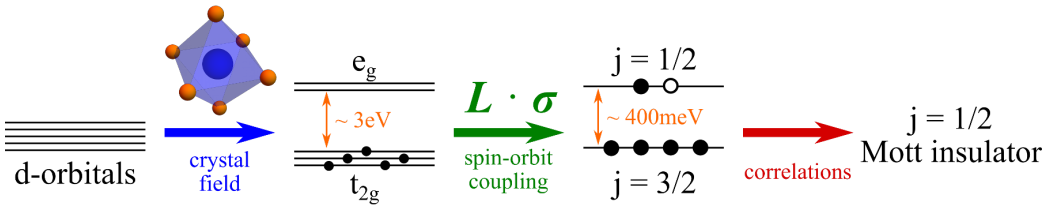

Figure 2.16: Spin-orbit entangled Mott insulators. The interplay of crystal-field effects, spin-orbit coupling and strong electron correlations causes the formation of $j = 1/2$ Mott insulators in d^5 electron configurations, which appear for example in certain iridates (Ir^{4+}) and ruthenates (Ru^{3+}) [38].

insulators can be realized when certain materials of this class form compounds with oxygen, the so-called *transition-metal oxides* [112]. In this case, the Mott insulator formation can be understood as a consequence of the interplay between crystal-field effects, spin-orbit coupling and electron correlations. This mechanism in certain materials with d^5 electronic configurations, such as a number of *iridates* and *ruthenates*, may, under certain conditions, allow for the occurrence of a dominant Kitaev exchange between the effective $j = 1/2$ magnetic moments. The way this is realized is outlined in the following.

Mott insulator formation

The atomic structure of a number of $4d^5$ and $5d^5$ transition-metal oxides (such as the $5d^5$-iridates with Ir^{4+} valence and the $4d^5$-ruthenates with Ru^{3+} valence) is characterized by the localization of transition-metal ions in the centers of octahedral cages of oxygen ions. In this case, the fivefold degeneracy of the d-subshell is partially lifted by the (cubic) crystal electric field of the oxygen octahedra, and the result is the transformation of the d-orbitals into three t_{2g}-orbitals with lower and two e_g-orbitals with higher energy, with an energy difference of ~ 3 eV.

The five electrons corresponding to the d^5-configuration now occupy the t_{2g}-orbitals, and there, constitute an effective orbital moment $l = -1$, while the e_g-orbitals remain empty. In this setting, the $l = -1$ orbital moments couple with the spins $s = 1/2$ of the electrons, and produce another degeneracy lifting, namely of the (sixfold) degeneracy of the t_{2g}-orbitals. These split up into two energy levels with a (much smaller) difference of ~ 400 meV. The new energy levels correspond to the effective magnetic moments $j = l \pm s$: A lower-energy $j = 3/2$ quartet state, and a higher-energy $j = 1/2$ doublet. The quartet state is then occupied by four electrons, and the $j = 1/2$ doublet is filled with one electron.

Due to the relatively small bandwidth between the two j-levels, the Coulomb

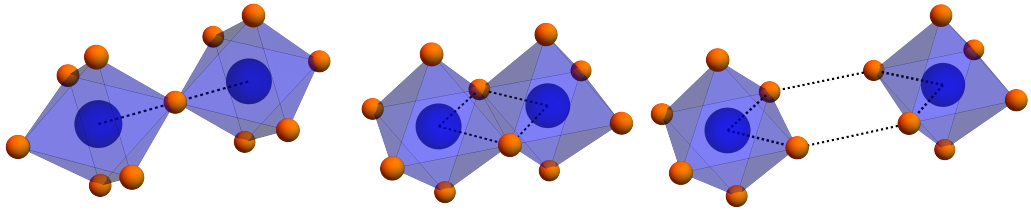

(a) Corner-sharing octahedra **(b)** Edge-sharing octahedra **(c)** Parallel edge-sharing octahedra

Figure 2.17: Orientations of neighbouring IrO_6 octahedra and corresponding Ir-O-Ir exchange paths. The single exchange path for corner-sharing octahedra leads to a dominant Heisenberg coupling between neighbouring $j = 1/2$ moments (a), while the existence of two exchange paths in edge-sharing configurations (b,c) causes a destructive interference of the Heisenberg exchange, and allows for a dominant bond-directional Kitaev exchange [37, 38].

repulsion U between the electrons leads to the opening of a Mott gap and prevents the double occupation of the $j = 1/2$ doublets with electrons from neighboring ions. Thus, the system becomes effectively governed by the *localized* $j = 1/2$ magnetic moments of the holes at each iridium ion. Such a system is called a *Mott insulator* [38]. The described mechanism which leads to its formation is visually summarized in Fig. 2.16.

Bond-directional interactions

The occurrence of *bond-directional* interactions in such systems now depends on the geometric configuration which the oxygen octahedra assume in the material, and the corresponding emergence of superexchange paths for the hopping of holes between the iridium ions. This hopping is realized via the oxygen ions [37, 113], and, for the IrO_6 octahedra that appear in a number of relevant iridates, there are two qualitatively different situations (see Fig. 2.17): If the octahedra share a *corner* (Fig. 2.17 a), there is only one Ir-O-Ir exchange path (180° bond) which allows the holes to hop between the $j = 1/2$ doublets of neighboring ions. This hopping between the $j = 1/2$ orbitals corresponds to a symmetric Heisenberg interaction between the magnetic moments. This scenario is realized for perovskite iridates like Sr_2IrO_4.

On the other hand, if two neighboring IrO_6 octahedra share an *edge* (Fig. 2.17 b), the existence of two different Ir-O-Ir exchange paths (90° bonds) results in the suppression of the symmetric exchanges between the $j = 1/2$ doublets by destructive interference. The remaining, dominant exchange is a bond-directional, ferromagnetic Ising interaction produced by the exchange between the $j = 1/2$ doublet of one iridium ion with the $j = 3/2$ multiplet at the neighboring ion

(Hund's coupling), which is described by a term

$$-\frac{8t^2 J_H}{3U^2} S_1^\gamma S_2^\gamma, \tag{2.55}$$

with a hopping parameter t, a Hund's coupling strength J_H and the electronic correlation strength U [38]. This process only couples the γ-components of the magnetic moments for a bond in the $\alpha\beta$-plane (perpendicular to the γ-axis), and therefore constitutes what we know as the *Kitaev interaction*. The reason for the occurrence of this bond-directional coupling lies in the spatial orientation of the t_{2g}-orbitals, namely in the xy-, yz- and xz-direction [37, 113]. For each bond, only two orbitals participate in the exchange process. These are for example the d_{xz}- and d_{yz}-orbital of neighboring iridium ions, which are "active" in the xy-plane and exchange holes via the p_z-orbitals of the two adjacent oxygen ions. In this example, the Hund's coupling manifests itself in the interaction of the z-components of the magnetic moments.

The same mechanism leads to the suppression of the Heisenberg exchange and a dominant Kitaev interaction for materials with *"parallel edge"-sharing octahedra* (Fig. 2.17 c). Bond-directional interactions have been experimentally verified for α-$\mathrm{RuCl_3}$, as well as the honeycomb iridates $\mathrm{Na_2IrO_3}$ and α-$\mathrm{Li_2IrO_3}$ [39, 114, 115]. The mechanism based on edge-sharing octahedra is also realized in the hyperhoneycomb material β-$\mathrm{Li_2IrO_3}$ and the stripy-honeycomb material γ-$\mathrm{Li_2IrO_3}$ [38], whereas the scenario of parallel edges can be found in so-called *triangular Kitaev materials* ($\mathrm{Ba_3Ir_xTi_{3-x}O_9}$).

Kitaev-Heisenberg-Gamma model

In a realistic material, however, the interaction between $j = 1/2$ moments is never *purely* Kitaev, and a full description of the system requires to consider a remaining Heisenberg exchange, as well as an off-diagonal exchange of the orthogonal spin components $\alpha, \beta \perp \gamma$. A more realistic effective Hamiltonian for the considered systems is therefore given by [115, 116]

$$\mathcal{H} = -\sum_{\langle i,j \rangle_\gamma} J_H \mathbf{S}_i \mathbf{S}_j + J_K S_i^\gamma S_j^\gamma + \Gamma(S_i^\alpha S_j^\beta + S_i^\beta S_j^\alpha), \tag{2.56}$$

and, in the limit $\Gamma = 0$, reduces to the *Kitaev-Honeycomb model* [72].

The residual Heisenberg interaction poses a rather difficult obstacle for the experimental hunt for quantum spin liquids in Kitaev materials, as it notoriously causes magnetic long-range ordering at sufficiently low temperature scales. In fact, magnetic ordering has been detected at temperatures below 7-15 K for the QSL candidates α-$\mathrm{RuCl_3}$, $\mathrm{Na_2IrO_3}$ and α-$\mathrm{Li_2IrO_3}$ [39, 115], while the Kitaev

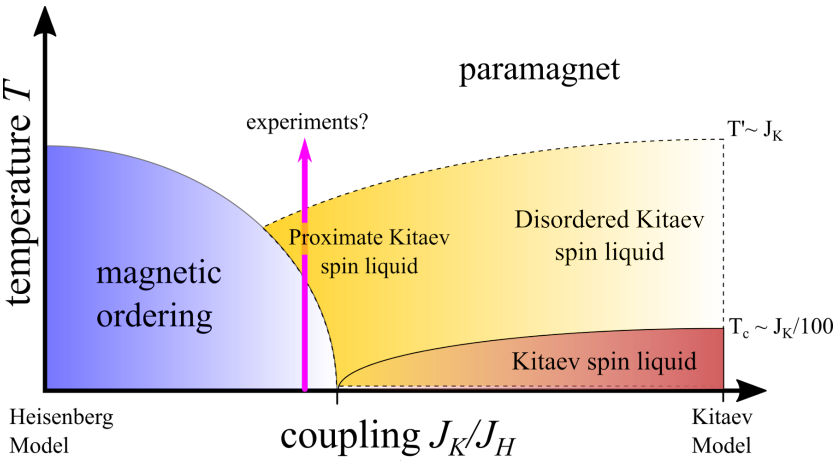

Figure 2.18: Possible phase diagram for the Kitaev-Heisenberg model [69]. Although most Kitaev materials have been shown to possess a magnetically long-range ordered ground state due to a residual Heisenberg coupling between the magnetic $j = 1/2$ moments, it is expected that a proximate spin liquid phase exists above the ordering temperature, where the system is effectively governed by fractionalized degrees of freedom.

exchange for another honeycomb iridate, $H_3LiIr_2O_6$, has at least been shown to remain dominant down to a temperature of 50 mK [117]. State-of-the-art approaches in the experimental search for spin liquids therefore aim on the further suppression of the additional exchange terms by applying a magnetic field [118–125], a route which has already led to the detection of the half-integer thermal quantum Hall effect in α-$RuCl_3$ [74, 75]. Another experimental ansatz is to focus on the *proximate spin liquid* regime, which is expected to exist in Kitaev materials above the long-range ordered phase, and to be effectively governed by the fractionalized degrees of freedom [69]. In the phase diagram of the Kitaev-Heisenberg model, such a proximate spin liquid is considered to be situated in the disordered $\mathbb{Z}_2$ spin liquid phase in three-dimensional Kitaev systems, which might continue to exist above the quantum regime of dominant Heisenberg interactions due to the large configurational entropy arising from system-spanning visons (see Fig. 2.18).

2.4.2 Alternative realizations

Spin-orbit entangled Mott insulators in $4d^5$ and $5d^5$ transition-metal compounds are by now, however, not the only route of research towards the realization of Kitaev spin liquids. In recent years, there has been a number of proposals for Kitaev materials that go beyond the mechanism proposed by Jackeli and Khaliullin. In one of these approaches, systematic ab-initio calculations for various d- and $f-$electron have yielded possible compounds where the occurence of $j = 1/2$ doublets with dominant Kitaev coupling due to interfering exchange

paths is equally obtained. These systems include materials with high-spin d^7 electron configurations (which contain Co^{2+}- and Ni^{3+}-ions) and f^1 configurations (Pr^{4+}), as well as systems with a polar asymmetry in the lattice structure [73]. Another approach aims at the formation of Kitaev honeycomb systems in certain metal-organic frameworks (MOFs), which are also based on ruthenium (Ru^{3+}), or, alternatively, osmium (Os^{3+}) [126]. Here, it is expected that the physical mechanism which determines the bond-directional interaction includes a stronger suppression of the direct exchange, and could therefore realize a Kitaev material that does not suffer from long-range ordering at very low temperatures.

2.5 Summary

The Kitaev model defines an exactly solvable quantum spin liquid, which can be described in terms of (itinerant) Majorana fermions coupled to an emergent (static) $\mathbb{Z}_2$ gauge field. A gauge-invariant quantity is given by the magnetic $\mathbb{Z}_2$ flux through the lattice plaquettes. Originally introduced on the two-dimensional honeycomb lattice, the definition of the Kitaev model can be extended to any tri-coordinated lattice system in two or three spatial dimensions. In addition, there is a generalized version of the model for lattices with higher (odd) coordination numbers. The spin liquid ground state in Kitaev models usually possesses gapless and gapped Majorana phases. In 3D lattice systems, the gapless $\mathbb{Z}_2$ spin liquids form a variety of different Majorana (semi)metals, and the spin liquid ground state is stable up to finite temperatures, where it is typically separated from the (confined) high-temperature phase by an inverted Ising phase transition. This phase transition is described in terms of the proliferation of system-spanning $\mathbb{Z}_2$ flux excitations (visons). In two spatial dimensions, on the other hand, a phase transition is only realized on non-bipartite lattice systems, where the $\mathbb{Z}_2$ fluxes are imaginary, and their ground state spontaneously breaks time-reversal symmetry. Such 2D systems can be shown to host topological ground states. A number of $j = 1/2$ Mott insulating materials, such as certain transition-metal oxides, allow for the occurrence of dominant Kitaev interactions between the magnetic moments and are possible candidates for the realization of Kitaev spin liquids.

Chapter 3

Quantum Monte Carlo simulations of Kitaev systems

In this chapter, we present the quantum Monte Carlo method which is applied in this work. After giving a brief overview of a number of frequently used numerical techniques for studying quantum many-body systems, we review the basics of classical Monte Carlo methods in statistical physics [127, 128]. The emphasis here is on the well-known Metropolis algorithm [129]. Afterwards, we outline the application of Monte Carlo methods to quantum systems – a task which, in the first place, relies on finding an appropriate *quantum-to-classical* mapping of the corresponding partition function [130–138]. We then discuss the analytical and numerical details of our Monte Carlo approach. Based on a similar Monte-Carlo method developed for double-exchange models [139–142], this method has been presented in 2014 by Nasu and Motome [44], and, subsequently, been used to study a number of Kitaev models in two and three spatial dimensions [45–47, 90, 143]. While the original method is based on a (non-local) Jordan-Wigner transformation [76–79] to represent the system in its Majorana basis, the simulations here make use of Kitaev's original, local transformation approach [27]. The problem of the artificial Hilbert space extension, which arises in this approach [27, 144, 145], is discussed in detail. Following that, we introduce the *Green's-function-based Kernel Polynomial Method* (GF-KPM) [45, 146, 147]. We use this method to significantly reduce the computation time in the Monte Carlo sampling, and to enable us to study large systems. In the final section of this chapter, we discuss the data analysis and extrapolation methods used to post-process the quantum Monte Carlo results. These comprise the binning analysis used to treat autocorrelation effects in statistical errors, and the *Ferrenberg-Swendsen reweighting* method with multiple histograms [148–150] for data extrapolation.

The general presentation of classical and quantum Monte Carlo methods, as well as data analysis, is based in particular on a number of well-known textbooks

on the matter [127, 128, 134]. The more specific part on Monte Carlo methods for Kitaev systems relies on Refs. [44, 46, 144, 145], and the presentation of the Green's-function-based Kernel Polynomial method on Refs. [45, 146, 147].

3.1 Numerics for quantum many-body systems

The most straightforward technique to address systems of quantum spins is, arguably, the *exact diagonalization* method (ED) [151]. It is applicable for discrete, finite quantum systems. We consider a many-body system with a single particle basis of dimension d. In the ED method, the Hamiltonian $\mathcal{H}$ is directly applied to the d^N basis states $|\psi_i\rangle$ to compute the Hamiltonian matrix $\langle\psi_i|\,\mathcal{H}\,|\psi_j\rangle$ ($i, j \in \{1, \dots d^N\}$). The Hamiltonian matrix is then diagonalized. Its eigenvalues $\{\epsilon_i\}$ are the energy levels of the system, and the partition function can be calculated from those eigenvalues as $\mathcal{Z} = \sum_{i=1}^{d^N} e^{-\beta\epsilon_i}$, making the expectation values of thermodynamic observables $\mathcal{O}$ directly accessible via $\langle\mathcal{O}\rangle = \mathcal{Z}^{-1}\sum_i \mathcal{O}e^{-\beta\epsilon_i}$. Clearly, the possibility to calculate exact expectation values of thermodynamic observables is the unbeatable advantage of this method.

However, one immediately realizes that the task of setting up the Hamiltonian matrix alone scales, in the worst case (without using symmetries), with $\mathcal{O}(2^N)$. Furthermore, a full matrix diagonalization with the usual divide-and-conquer algorithms [152] scales cubically with the matrix size, leading the computational cost of the calculation to an order of $\sim 2^{3N}$. In many cases, it is possible to reduce it by first transforming the Hamiltonian matrix into some block-diagonal form [153, 154], which is possible if the underlying system possesses symmetries. In practice however, the exponential scaling limits the applicability of the exact diagonalization method to very small clusters. While this might still be sufficient for the treatment of certain quantum many-body systems with negligible finite-size effects, for instance in one or two spatial dimensions, ED is clearly unfit to investigate three-dimensional Kitaev systems, where the unit cells of the lattices alone contain up to 16 vertices.

More advanced diagonalization techniques like the *Lanczos algorithm* [155] may be used if the matrix is sparse, and only the lowest energy levels of the system are required. This is, however, not the case if the calculation of full phase diagrams up to highest temperatures is the objective, where also the higher energy levels are occupied and determine the physical behavior of the system.

Beside ED, there are many powerful numerical techniques for the treatment of quantum many-body systems, and, in particular, frustrated magnets. The *density matrix renormalization group* (DMRG) [156, 157] provides a sophisticated variational method which acts on the matrix-product state [158, 159] representation of many-body wavefunctions. Within this method, the degrees of freedom of

the wavefunction are iteratively reduced to the physically relevant ones by subsequent singular value decompositions, thereby yielding the ground state (or another, moderately excited target state) for a given Hamiltonian. However, being suited essentially for one-dimensional systems and, within those, basically to explore the low-energy physics, it is also not an option for our purpose. The latter restriction also holds for generalizations of the DMRG method to higher dimensions [160], among them the tensor-network-based [161] variational techniques like PEPS [162–165], and MERA [166].

Instead, the twofold purpose of obtaining exact results over a wide range of temperature scales, but also being able to study large systems, suggests the use of *quantum Monte Carlo simulations* (QMC) [127, 128] to treat the Kitaev model. Monte Carlo methods provide an unbiased, numerically exact tool to handle the partition function of large-scale many-body systems with statistical sampling. They are widely used in statistical physics, both on classical and quantum systems, provided a proper configuration sampling technique can be designed for the underlying model. Such a method exists for the Kitaev model, and enables us to investigate Kitaev systems at sizes beyond 1000 sites, which is sufficient to extrapolate the physical behavior of these systems in the thermodynamic limit. Interestingly, it is the Majorana basis of the Kitaev system which allows for a quantum Monte Carlo approach that is free of the infamous *sign problem* [167–170]. Furthermore, it does not require the introduction of an additional imaginary-time dimension to treat the quantum character of the system.

3.2 Classical Monte Carlo

Monte Carlo methods [127, 128] comprise a rather large number of numerical techniques, which are applied in numerous scientific fields, from mathematics and physics to social sciences. The common ground of these methods is the application of *random sampling* techniques. These are used to solve problems which are deterministically unaccessible, usually due to a large computational complexity, or which are just less efficiently solvable with other numerical means. We consider for instance a potentially complicated integral $I = \int_\Omega f(\mathbf{x}) d\mathbf{x}$ in a d-dimensional subspace $\Omega \in \mathbb{R}^d$, which can be calculated with the standard trapezoidal or Simpson rule. Instead, in the *Monte Carlo integration* method, one generates a set of N random abscissa points $\{\mathbf{x_i}\} \in \mathbf{\Omega}$ according to some probability distribution $p(\mathbf{x})$. Then, one can approximate I by summing over the function values $f(\{\mathbf{x_i}\})$,

$$I \approx \frac{1}{N} \sum_{i=1}^{N} \frac{f(\mathbf{x_i})}{p(\mathbf{x_i})}. \tag{3.1}$$

Here, the statistical distribution of abscissa points $p(\mathbf{x})$ is desired to express their

"weight" in the integral. Quite obviously, a set of abscissa points which is used to numerically integrate for example a Gaussian function with given mean μ and standard deviation σ is ideally Gaussian-distributed itself, with the same parameters. Most importantly, the numerical error of the Monte Carlo integral is given by [127]

$$\Delta = \sqrt{\frac{\mathrm{Var}\left(\frac{f(x)}{p(x)}\right)}{N}}, \tag{3.2}$$

and does not depend on the dimensionality of the problem. It is only *statistical*, with a $1/\sqrt{N}$-dependence on the number of samples (abscissa points). This is a major difference to the deterministic trapezoidal and Simpson method, which depend exponentially on the dimension d. Therefore, for high-dimensional integrals, the Monte Carlo method converges faster, for example for $d > 9$ in comparison with the Simpson method. The ability to produce a numerical error which is only statistical is the most important advantage of the Monte Carlo method.

In statistical physics, Monte Carlo methods are frequently used to compute statistical estimates of quantities that are, in practice, impossible to calculate exactly, mostly because the partition function $\mathcal{Z}$ of the underlying system comprises an exponentially large number of states. Instead, in a typical Monte Carlo simulation, one generates random sets of configurations C_i of some (e.g. spin) system, which follow a physically meaningful statistical distribution – usually the Boltzmann distribution – and performs numerical measurements on these configurations. From the data of the numerical measurements, statistical estimates of the desired observables can be calculated.

While the early precursors of Monte Carlo methods had been sophisticated recipes to calculate the irrational number π with the help of sticks and stones in the 18th century [127], the breakthrough of random sampling techniques came with the works of Ulam, Metropolis and von Neumann [129, 171] in the context of their research on nuclear weapons at the Los Alamos National Laboratory [127]. At this time, also the name *Monte Carlo* has been invented to underline the random experiment nature of these methods, reminiscent of the famous gambling places in the district of Monaco that has the same name.

3.2.1 Markov chains

How are Monte Carlo simulations in statistical physics performed in detail? First of all, we consider a many-body system with physical configurations C_i. We can think of these configurations as belonging to some abstract configuration space Ω. The key concept of the Monte Carlo simulation is to generate a computationally accessible and statistically representative subset of the configuration space $\tilde{\Omega} \subset \Omega$,

instead of considering all configurations $C_i \in \Omega$. This means, a finite number M of configurations C_i is *sampled*, such that, for every observable $\mathcal{O}_i = \mathcal{O}(C_i)$, which is measured on the C_i, and for large enough M, the statistical average $\bar{\mathcal{O}}$ converges to the exact expectation value $\langle\mathcal{O}\rangle$, defined by the probability distribution $p_i = p(C_i)$,

$$\bar{\mathcal{O}} = \frac{1}{M}\sum_{i=1}^{M}\mathcal{O}_i \xrightarrow{M\to\infty} \langle\mathcal{O}\rangle, \tag{3.3}$$

$$\langle\mathcal{O}\rangle = \sum_{C_i\in\Omega} p_i \cdot \mathcal{O}_i, \tag{3.4}$$

with $\sum_{C_i\in\Omega} p(C_i) = 1$. Here, we have already assumed that the configuration space Ω is finite (however large) and the configurations C_i are discrete. This corresponds to the case of finite systems with discrete single-particle degrees of freedom. The arguably most prominent example of such a system is the *Ising model* [172], where $\mathbb{Z}_2$ spins $s_i = \pm 1$ are situated on the vertices of a lattice, and the Hamiltonian is, in its simplest version, given by

$$\mathcal{H} = -J\sum_{\langle i,j\rangle} s_i s_j. \tag{3.5}$$

At a given inverse temperature β, the probability distribution for the spin configurations of this model is given by the Boltzmann distribution

$$p(C_i) = \frac{1}{\mathcal{Z}} e^{-\beta\mathcal{H}(C_i)}, \tag{3.6}$$

with the partition function $\mathcal{Z} = \sum_{C_i} e^{-\beta\mathcal{H}(C_i)}$. For the sake of simplicity and its paradigmatic character, we explain the further details of Monte Carlo simulations at the example of the Ising model. We show in the remainder of this chapter that also the QMC simulation for Kitaev models is, on the technical level, *Ising Monte Carlo*.

The crucial part of the Monte Carlo method is to sample the configurations C_i in a way that the statistically representative character of $\tilde{\Omega}$ is ensured, i.e. configurations C_i are drawn from Ω according to the right probability distribution $p(C_i)$. The most common method to do so is to generate a *Markov chain* of configurations. The Markov chain is a sequence

$$C_1 \to C_2 \to \cdots \to C_i \to C_{i+1} \to \cdots \to C_n, \tag{3.7}$$

in which the probability W_{ij} to transit from one state C_i to another state $C_{i+1} = C_j$ only depends on C_i, and not on any previous states,

$$P(C_{i+1} = C_j | C_i \ldots C_1) = P(C_{i+1} = C_j | C_i) =: W_{ij}. \tag{3.8}$$

All transition probabilities W_{ij} taken together (with $W_{ij} \in [0,1] \quad \forall i,j$) form a matrix W, which has to fulfill a number of conditions to ensure that (i) the sequence of configurations C_i really obeys Eq. (3.8), and (ii) the configurations in the sequence follow the desired probability distribution $p(C_i)$. These conditions are the following:

- **Normalization:** Probability is conserved in the Markov process, which means, the probability to reach any state C_j from an initial state C_i is 1,

$$\sum_j W_{ij} = 1. \tag{3.9}$$

  All row vectors of W thus have to add up to 1, which, by definition, makes W a *stochastic matrix*. At the beginning of each Markov process, we "feed" the matrix W with an initial distribution of configurations $p^{(0)}$. For example, if the process is started with a random configuration C_0 of N_{spins} Ising spins, which is drawn from a uniform distribution, all $2^{N_{\mathrm{spins}}}$ elements i of $p^{(0)}$ are $p_i^{(0)} = 1/2^{N_{\mathrm{spins}}}$. In each Markov step $C_i \to C_{i+1}$, the probability distribution is changed as $(p^{(n+1)})^T = (p^{(n)})^T \cdot W$, where p^T is the transposed vector, and $\sum_i p_i^{(n)} = 1 \quad \forall n$. Stochastic matrices can be shown to possess a largest eigenvalue 1, which is equivalent to the statement that there exists an eigenvector p_{eq} of W, which does not change under multiplication with W. The elements of this stationary vector p_{eq} give the equilibrium probability distribution of the configurations C_i. We want the stationary vector of the Markov process to be a specific probability distribution p_{spec} (e.g. the Boltzmann distribution), and the Markov chain to converge against this distribution for long enough simulation times, regardless which initial distribution $p^{(0)}$ it is started with. For that, the normalization condition alone is not sufficient.

- **Ergodicity:** In order to allow the sequence of configurations to converge against the probability distribution p_{spec} from *any* initial state, there has to be a finite probability to reach any configuration C_j from a configuration C_i in a finite amount of steps k, i.e.

$$\forall C_i, C_j \quad \exists k : (W^k)_{ij} \neq 0. \tag{3.10}$$

  In a physical sense, ergodicity is the condition for the Markov chain not to get "trapped" in some limited subregion of the configuration space. In this case, the sampled subset of Ω could never become statistically representative.

- **Detailed balance:** With the first two conditions, it is still not guaranteed that the Markov chain really converges against the desired equilibrium distribution p_{spec}. If the distribution $p_i^{(n)}$ changes in each Markov step by $p_j^{(n+1)} = \sum_i p_i^{(n)} W_{ij}$, there is still the possibility that it could rotate around some set of different values with some periodicity $\tilde{n}$ instead of converging. This unfortunate situation is called a *limit cycle* [127]. It can be shown that such a cycle can be avoided by introducing the additional condition

$$\frac{p(C_j)}{p(C_i)} = \frac{W_{ij}}{W_{ji}}, \tag{3.11}$$

  which is known as *detailed balance*. Detailed balance is thus a sufficient condition for the convergence of the Markov chain, and it is here that the probability distribution p_{spec} is explicitly introduced into the process.

If the sampling method fulfills the outlined conditions, the Markov chain generates configurations that follow the probability distribution p_{spec} by construction and for large enough simulation times. The most common (and probably most powerful) algorithm which generates such a Markov chain is the *Metropolis algorithm* [129], which is discussed in the following.

3.2.2 Metropolis algorithm

In order to generate a Markov chain, an appropiate choice for the transition probabilities W_{ij} has to be made. The Metropolis algorithm uses the *Metropolis weights*

$$W_{ij} = \min\left(1, \frac{p(C_j)}{p(C_i)}\right). \tag{3.12}$$

It can be easily seen that with this choice, the detailed balance condition is fulfilled. If p_{spec} is the Boltzmann distribution, Eq. (3.6), the fraction $p(C_j)/p(C_i)$ reduces to the transition probability

$$e^{-\beta(\mathcal{H}(C_j)-\mathcal{H}(C_i))} = e^{-\beta\Delta E}, \tag{3.13}$$

such that the (numerically expensive) partition function $\mathcal{Z}$ cancels out and the computational task is reduced to finding the energy difference ΔE between the two configurations C_i, C_j. Based on this choice for the transition probabilities, the Metropolis algorithm works as follows:

1. Starting from the initial configuration C_i, an update to another configuration C_j is proposed.

2. The statistical weight for the update $C_i \to C_j$ is calculated,

$$\alpha = W_{ij} = \frac{p(C_j)}{p(C_i)}. \tag{3.14}$$

3. A random number $\gamma \in [0, 1]$ is generated.

4. If $\gamma \leq \alpha$, the update is accepted: $C_{i+1} = C_j$. Otherwise, it is rejected: $C_{i+1} = C_i$.

5. The process is restarted from the configuration C_{i+1}.

For an algorithm that is (quite) universally applicable, this general scheme is remarkably simple. However, we have to make a couple of remarks on details and implementation:

1. Choice of updates: Finding a suitable way to propose configuration updates is, in general, a non-trivial task. The update has to fulfill the ergodicity condition of the Markov process. This is easy for the Ising model, where we can pick a single random spin and propose a local update $\sigma_i \to -\sigma_i$. This way, we can reach any (finite-sized) spin configuration C_j from any initial configuration C_i with a finite amount of local updates. In other systems, there is no such local update that fulfills the ergodicity criterium. In classical dimer systems for example, flipping a pair of neighbouring (parallel) dimers is not ergodic. Instead, more advanced non-local directed loop updates are necessary here [173–175].

2. Equilibration: The choice of the Metropolis weight, Eq. (3.12), ensures that updates are always accepted if the new configuration has a lower energy than the initial one, while configurations with higher energy are accepted with the probability $p(C_j)/p(C_i)$. For the Boltzmann distribution, this corresponds to $e^{-\beta\Delta E}$ – meaning that the acceptance to overcome an energy barrier ΔE is modulated by temperature. It is the thermal fluctuations in a system which allow it to adapt (energetically) unfavorable states during the simulation. This way, it is possible for the system to reach its thermal equilibrium at a given temperature in a (possibly large) number of Monte Carlo steps. Since each simulation is started from some initial configuration C_1 – which can be completely random or ordered – it takes a certain number of Monte Carlo steps before the system reaches the equilibrium. In order to get results that are unbiased by the initial configuration, it is important to let the simulation *thermalize*, i.e. perform a sufficient amount of Monte Carlo updates before taking measurements.

3. Sweeps and autocorrelation: The outlined Metropolis loop only describes a single Monte Carlo update. In practice, a *sweep* of such Monte Carlo updates is performed successively, and measurements are performed after every sweep.

In the case of the Ising model with N spins, a sweep usually consists of N (attempted) local updates. Between each measurement, every spin can therefore be randomly picked and flipped at least once. Nonetheless, subsequent observable measurements $\mathcal{O}_i$, $\mathcal{O}_{i+1}$ are still correlated, which can be measured in terms of the (time-displaced) *autocorrelation* [127]

$$\chi(t) = \int dt' (\mathcal{O}(t')\mathcal{O}(t'+t) - \langle \mathcal{O} \rangle^2), \tag{3.15}$$

a function which typically scales as $\chi(t) \sim e^{-t/\tau}$ [127], with the *autocorrelation time* τ for a given simulation and a given observable. Usually, different observables possess different autocorrelation times.

4. Global updates: Due to the autocorrelation, finding local updates as described in 1. is often not enough. We consider the two-dimensional ferromagnetic Ising model on a square lattice. Here, at a critical temperature $T_c = 2J/\log(1+\sqrt{2})$ [176], a phase transition separates the ordered (ferromagnetic) ground state from the paramagnetic regime. In the temperature region around T_c, Monte Carlo simulations suffer not only from large statistical errors due to the critical fluctuations of the system, but also from *critical slowing down*, the divergence of the autocorrelation time. For temperatures far below T_c, where the Ising system is in one of two configurations with all spins $s_i = +1$ or $s_i = -1$, the generation of a Markov sequence which leads from one configuration to the other is extremely unlikely. Thus, the Monte Carlo simulation is "frozen" in a limited phase space region. Both phenomena, critical slowing down at phase transitions and the freezing of the simulation at very low temperatures, ask for more sophisticated update techniques beyond the single spin-flip scheme, where the degrees of freedom in the system are updated not individually, but domainwise. Finding such *cluster* or *global updates* for general systems is far from trivial. For the (simple) case of the Ising model, such cluster update techniques do exist, the most famous ones being the Swendsen-Wang [177] and the Wolff algorithm [178]. Note that the numerical advantage of these techniques is only given in the region of the phase transition, while at high temperatures, where none or only small domains exist, the Metropolis algorithm with local updates remains more efficient.

5. Parallel tempering: A more general technique for the realization of (a kind of) a cluster update can be implemented in Monte Carlo simulations where a number of Markov processes at different temperature (or other parameter) points are performed in parallel. In the *parallel tempering* or *replica exchange* Monte Carlo simulation [179–183], these parallel simulations communicate with each other and exchange (*swap*) configurations with a certain probability. Thus, within such a simulation, particular configurations are updated in the conventional Metropolis sense and interchanged between the parallel processes of the simulation. One can describe this procedure as a random walk of configurations in temperature space,

while, from the standpoint of a particular Monte Carlo process at a fixed temperature, the swap of configurations with neighboring processes appears as a global update.

3.3 Quantum Monte Carlo

We now present the general approach to address quantum problems with Monte Carlo simulations. Particularly, we discuss the problem of mapping the quantum partition function to a sum over classical probabilities, which is the analytical step that lies at the heart of every quantum Monte Carlo (QMC) flavor. A number of common QMC flavors are outlined in the following. Apart from that, we discuss the *sign problem*[167, 170], which arises in many situations and prevents the numerical investigation of quantum systems at a large-scale. This problem is, in general, dependent on the choice of basis for a given system. A sign-problem-free quantum Monte Carlo method can be constructed for Kitaev systems in their Majorana basis, but not in their spin basis.

3.3.1 Mapping problem

In contrast to classical systems, the states in quantum many-body systems are wavefunctions, which are written as linear superpositions of the (orthonormal) basis states of the corresponding Hilbert space. Here and in the following, we consider systems with a discrete Hilbert space basis, where the basis states can be denoted by $|n\rangle$. These may describe for instance the N individual spin states of the Ising model, $|n\rangle = |\sigma_1 \dots \sigma_N\rangle$. An arbitrary quantum many-body state $|\Psi\rangle$ is given by

$$|\Psi\rangle = \sum_n \alpha_n |n\rangle \,, \tag{3.16}$$

with complex coefficients α_n such that $\sum_n |\alpha_n|^2 = 1$.

The physical observables like energy, momentum, etc. in quantum physics are operators acting on the Hilbert space of a given system. Most of these operators do not commute with each other, and are, therefore, not simultaneously diagonalizable. In particular, the Hamiltonian of a quantum system may contain different terms that are not simultaneously diagonalizable.

In classical systems, the distribution of states C_i in statistical ensembles is described by the function $p(C_i)$. Going over to statistical distributions of quantum states, this translates to the *density operator* [128]

$$\hat{\rho} = \frac{e^{-\beta\mathcal{H}}}{\mathcal{Z}}. \tag{3.17}$$

Here, the partition function $\mathcal{Z}$ is the trace over the matrix-valued operator $e^{-\beta\mathcal{H}}$

$$\begin{aligned}\mathcal{Z} &= \operatorname{tr} e^{-\beta\mathcal{H}} \\ &= \sum_n \langle n| e^{-\beta\mathcal{H}} |n\rangle .\end{aligned} \tag{3.18}$$

In general, the operator $e^{-\beta\mathcal{H}}$ contains non-diagonal elements. Observable expectation values can be calculated with the density operator as

$$\langle A\rangle = \operatorname{tr} \rho A. \tag{3.19}$$

In the simplest scenario, there exists an orthonomal basis of the Hilbert space whose states are eigenstates of the Hamiltonian $\mathcal{H}$. In this case, one can replace the Hamiltonian in the partition function with its eigenvalues $\mathcal{H}|n\rangle = E(n)|n\rangle$, the trace simplifies to $\mathcal{Z} = \sum_n e^{-\beta E(n)}$, and the expectation values of observables $\mathcal{O}$ can be calculated as in classical systems [128],

$$\langle A\rangle = \sum_n A(n) e^{-\beta E(n)}, \tag{3.20}$$

with $A(n) = \langle n| A |n\rangle$. In general, however, the Hamiltonian of a quantum system does not possess an eigenbasis that also forms a basis of the Hilbert space, and therefore consists of different non-commuting terms that do not allow for the simplifications that have led to Eq. (3.20).

A standard example of such a more complex quantum system is the Ising model with a transverse magnetic field [184, 185], which is described by the Hamiltonian

$$\mathcal{H} = -J \sum_{\langle i,j\rangle} \sigma_i^z \sigma_j^z + h \sum_i \sigma_i^x. \tag{3.21}$$

Here, the σ^x-operators in the magnetic field term do not commute with the σ^z-operators, implying they have no common eigenbasis. If one chooses the eigenstates of σ^z as the single-particle basis states, it is readily seen that, once the Hamiltonian is applied to a many body basis state, for example $|n\rangle = |\uparrow \dots \uparrow\rangle$, the σ_i^x in the magnetic field term of $\mathcal{H}$ flip the single spins in $|n\rangle$ subsequently, and the result is a superposition state. In this general case, $\mathcal{Z}$ does not trivially become a sum over classical numbers in the way that is shown above. Instead, the essential task to construct a Monte Carlo algorithm for a particular quantum problem is to find a suitable mapping between the (quantum) partition function and classical probabilities,

$$\operatorname{tr} e^{-\beta\mathcal{H}} \longrightarrow \sum_i p_i. \tag{3.22}$$

In other words, quantum Monte Carlo (QMC) simulations are classical Monte Carlo simulations, in which the quantum system is suitably mapped to a classical configuration space Ω. This general concept is the common ground for all different kinds of QMC *flavors* [128, 134], which, above all, differ in the way the mapping, Eq. (3.22), is designed. In the following, we give a brief review on two common QMC flavors, and look at the way $\mathcal{Z}$ is represented in these approaches.

3.3.2 Common Quantum Monte Carlo techniques

World Line QMC

A commonly used starting point for various quantum Monte Carlo techniques is the *path-integral formulation* of the partition function. Here, the inverse temperature β is identified with an *imaginary time* $\tau = it$, and $\mathcal{Z}$ is rewritten as a product over M small imaginary time steps $\Delta\tau$ [128],

$$\begin{aligned}\mathcal{Z} &= \sum_n \langle n| \, e^{-\tau H} \, |n\rangle \\ &= \sum_n \langle n| \left(e^{-\Delta\tau H}\right)^M |n\rangle \, . \end{aligned} \tag{3.23}$$

Considering a Hamiltonian with different terms $\mathcal{H} = \mathcal{H}_1 + \ldots \mathcal{H}_N$, the corresponding exponential operator for each imaginary time step is then approximated as [128]

$$e^{-\Delta\tau\mathcal{H}} = e^{-\Delta\tau\mathcal{H}_1} e^{-\Delta\tau\mathcal{H}_2} \ldots e^{-\Delta\tau\mathcal{H}_N} + \mathcal{O}((\Delta\tau)^2), \tag{3.24}$$

which is the so-called *Trotter-Suzuki decomposition* with a characteristic error quadratic in $\Delta\tau$. Within this approximation, the partition function becomes

$$\mathcal{Z} = \sum_n \langle n| \left(e^{-\Delta\tau\mathcal{H}_1} e^{-\Delta\tau\mathcal{H}_2} \ldots e^{-\Delta\tau\mathcal{H}_N}\right)^M |n\rangle + \mathcal{O}((\Delta\tau)^2). \tag{3.25}$$

Then, a unity operator $\mathbb{I} = \sum_{i_k} |i_k\rangle \langle i_k|$ is inserted after each exponential term. In each of these unity operators, the $\{|i_k\rangle\}$ denote a complete set of basis states of the corresponding Hilbert space. Hence, there are, in total, $(N \cdot M - 1)$ sets of basis states introduced, and, using the identification $|i_0\rangle := |n\rangle$, we can reexpress the partition function as [128]

$$\begin{aligned}\mathcal{Z} = \sum_{i_0,\ldots,i_{N\cdot M}} & \langle i_0| \, e^{-\Delta\tau\mathcal{H}_1} \, |i_1\rangle \, \langle i_1| \, e^{-\Delta\tau\mathcal{H}_2} \, |i_2\rangle \ldots \langle i_{N-1}| \, e^{-\Delta\tau\mathcal{H}_N} \, |i_N\rangle \\ & \ldots \langle i_{N\cdot M-1}| \, e^{-\Delta\tau\mathcal{H}_{N\cdot M}} \, |i_0\rangle \;\; + \;\; \mathcal{O}((\Delta\tau)^2). \end{aligned} \tag{3.26}$$

Usually, the basis states $|i_k\rangle$ are now expanded in the eigenbasis of one of the Hamiltonian terms $\mathcal{H}_i$. For instance, for the transverse field Ising model, these

can be the tensor products of the eigenstates $|\uparrow\rangle, |\downarrow\rangle$ of σ^z. In addition, the further approximation of the exponentials,

$$e^{-\Delta\tau\mathcal{H}_i} \approx (1 - \Delta\tau\mathcal{H}_i), \tag{3.27}$$

is common for practical calculations [128].

In Eq. (3.26), the partition function of the d-dimensional quantum system is represented as a sum over (d+1)-dimensional classical system configurations with periodicity in the imaginary-time dimension. These configurations are also called *world lines*. A quantum Monte Carlo simulation can be realized as the classical sampling of world line configurations, for which certain requirements, as the continuity of world lines, have to be fulfilled. The probability weights in the Monte Carlo simulaton are given by the matrix elements $\langle i_{N-1}| e^{-\Delta\tau\mathcal{H}_N} |i_N\rangle$. Again, local and non-local updates can be defined [128]. Thus, the mapping 3.22 now has the form

$$\mathrm{tr}\, e^{-\beta\mathcal{H}} \longrightarrow \sum_{C_W} p(C_W), \tag{3.28}$$

where the C_W denote world line configurations.

In other words, within this quantum Monte Carlo approach, the d-dimensional quantum system is mapped to a (d+1)-dimensional classical system, and the quantum information is "encoded" in the additional interactions that arise in the imaginary time dimension. World line Monte Carlo is primarily used for the simulation of bosonic models and quantum spin systems, like different incarnations of the Heisenberg model (e.g. the XXZ-model) [134]. Aside from the simulation algorithm in discretized imaginary-time that is outlined here, there is also a modification for continuous times [186], which rids the algorithm of the discretization error that is introduced with the approximation in Eq. (3.24).

Determinant QMC

There are more QMC methods which are based on the path-integral representation of the partition function. For instance, interacting fermion systems on a lattice are frequently treated with the *Determinant Quantum Monte Carlo* (DQMC) method [128, 134, 187, 188]. Here, a Hubbard-Stratonovich transformation [189, 190] is implemented to map the many-particle Hamiltonian $\mathcal{H}$ (or, alternatively, the action $\mathcal{S}$) of the interacting fermion system to a system of non-interacting fermions. For this, a bosonic auxiliary field ϕ – the Hubbard-Stratonovich field – is introduced, to which the non-interacting fermions couple. We consider as an example the

Hubbard-type Hamiltonian [134]

$$\mathcal{H} = \underbrace{-t \sum_{\langle i,j\rangle,\sigma} (c^\dagger_{i,\sigma} c_{j,\sigma} + \text{h.c.})}_{\mathcal{H}_1} + \underbrace{U \sum_{i=1}^{N} \left(c^\dagger_{i,\uparrow} c_{i,\uparrow} - \frac{1}{2}\right)\left(c^\dagger_{i,\downarrow} c_{i,\downarrow} - \frac{1}{2}\right)}_{\mathcal{H}_2}, \quad (3.29)$$

with $U > 0$. The second term in this Hamiltonian is quartic in the fermionic operators $c_i^\dagger, c_i$, which makes the treatment of $\mathcal{H}$ difficult. In the Trotter-Suzuki decomposed path integral, this quartic term appears in the exponential $e^{-\Delta\tau\mathcal{H}_2}$. It can be transformed away with a Hubbard-Stratonovich transformation [189, 190] of the form [128]

$$e^{-\Delta\tau U\left(n_{i,\uparrow}-\frac{1}{2}\right)\left(n_{i,\downarrow}-\frac{1}{2}\right)} = \frac{1}{2} e^{-\frac{1}{4}\Delta\tau U} \sum_{\phi=\pm 1} e^{\alpha\phi\left(n_{i,\uparrow}-n_{i,\downarrow}\right)}, \quad (3.30)$$

where we use the notation $n_i = c_i^\dagger c_i$, and the parameter α is given by the relation $\cosh(\Delta\tau\alpha) = e^{\Delta\tau U/2}$. We see that the transformed exponential in Eq. (3.30) is now only quadratic in the fermions $c_i^\dagger, c_i$. In return, the auxiliary field $\phi = \pm 1$ has been introduced, and we can interpret the second term of the Hamiltonian as a function of this field, $\mathcal{H}_2 = \mathcal{H}_2(\{\phi\})$.

Structurally, with the introduction of the auxiliary field ϕ, the partition function $\mathcal{Z}$ can be rewritten as a double sum over different field configurations $\{\phi\}_i$ in imaginary time, and the fermions, which are here formally denoted by the wavefunctions ψ [128],

$$\mathcal{Z} = \sum_{\{\phi\}_1 \ldots \{\phi\}_M} \sum_{\psi} \langle\psi| e^{-\beta\mathcal{H}_1} e^{-\beta\mathcal{H}_2(\{\phi\}_M)} \ldots e^{-\beta\mathcal{H}_1} e^{-\beta\mathcal{H}_2(\{\phi\}_1)} |\psi\rangle + \mathcal{O}\left((\Delta\tau)^2\right). \quad (3.31)$$

Now that both terms $\mathcal{H}_1$ and $\mathcal{H}_2$ are quadratic in the fermions, the following identity for free fermion Hamiltonians is used [128, 134]

$$\operatorname{tr} e^{-\beta \sum_{i,j} c_i^\dagger A_{ij} c_j} = \det(\mathbb{I} + e^{-A}), \quad (3.32)$$

where the A_{ij} are the elements of the matrix A. With this identity, Eq. (3.31) is brought into the much simpler form

$$\begin{aligned} \mathcal{Z} &= \sum_{\{\phi\}_1 \ldots \{\phi\}_M} \det\left(M^\uparrow(\Phi)\right) \det\left(M^\downarrow(\Phi)\right), \\ M^\sigma(\Phi) &= \mathbb{I} + e^{-\Delta\tau\mathcal{H}_1^\sigma} e^{-\Delta\tau\mathcal{H}_2^\sigma(\{\phi\}_M)} \ldots e^{-\Delta\tau\mathcal{H}_1^\sigma} e^{-\Delta\tau\mathcal{H}_2^\sigma(\{\phi\}_1)}, \end{aligned} \quad (3.33)$$

where the fermionic sector is integrated out for each configuration $\Phi = \{\phi_{i,j}\}$ of the Hubbard-Stratonovich field, which extends both in space (index i) and imaginary time (index j). The weight of each field configuration Φ is given by the product of the two determinants in Eq. (3.33).

Hence, in the Monte Carlo sampling, the field Φ is sequentially sampled from a starting configuration Φ_0 via local updates $\phi_{i,j} \to \phi'_{i,j} = -\phi_{j,i}$, which are accepted with probability

$$\alpha = \frac{\det(M^{\uparrow}(\Phi'))}{\det(M^{\uparrow}(\Phi))} \frac{\det(M^{\downarrow}(\Phi'))}{\det(M^{\downarrow}(\Phi))}. \tag{3.34}$$

These update weights are usually calculated in terms of Green's functions [128, 134]. In the next section, we see that the Kitaev quantum Monte Carlo simulation has a theoretical foundation with a similar structure, namely with a nested partition function over field configurations and a fermionic sector which is explicitly traced out in each Monte Carlo step. The theory behind the Monte Carlo update scheme is simpler here, because the Kitaev Hamiltonian has no quartic terms.

Aside from the quantum Monte Carlo techniques sketched in this section, there are many more. They comprise methods such as Stochastic Series Expansion [135], variational Monte Carlo [191–196], diagrammatic Monte Carlo [197, 198] and Monte Carlo simulations which apply machine learning techniques [199]. The development and improvement of quantum Monte Carlo techniques remains an active field in computational physics until today.

3.3.3 Sign problem

Quantum Monte Carlo methods provide an unbiased, numerically exact tool to study quantum many-body systems, whenever a suitable mapping of the quantum partition function to a classical configuration space, Eq.(3.22), can be found. If they were applicable on all kinds of quantum systems, one might ask why someone would even bother looking for other techniques.

Unfortunately, QMC methods are not applicable to all quantum systems, due to a phenomenon which is known as the *fermionic sign problem* [167, 168, 170]. The sign problem typically appears in world line Monte Carlo simulations of fermionic systems and frustrated quantum spin systems [168]. In order to capture the problem that arises in these systems, we take a look back at the quantum-to-classical mapping of the partition function,

$$\operatorname{tr} e^{-\beta\mathcal{H}} \to \sum_i p_i.$$

The sign problem is the fact that in this mapping, it is not guaranteed that the numbers p_i, which are treated as classical probabilities, are positive, or even real.

The reason for this lies in the exponential operator $e^{-\beta\mathcal{H}}$. Although $\mathcal{H}$ is Hermitian, making its exponential positive definite, it is not necessary that *all* entries of $e^{-\beta\mathcal{H}}$ are positive or even non-negative [128]. In fact, the property of a matrix to

be positive depends on the choice of basis. If there is a diagonal representation of $e^{-\beta\mathcal{H}}$, it can be brought into a positive form, which directly follows from positive definiteness. However, the existence of such a diagonal representation is not guaranteed. Thus, there may appear negative entries in $e^{-\beta\mathcal{H}}$, and therefore negative probability weights in Eq. (3.22). This is the case for world-line configurations which contain an odd number of fermionic exchanges [170]. Similarly, it happens on frustrated spin systems, where a path through the lattice can be found that consists of an odd number of off-diagonal operations, for example on non-bipartite lattices [168].

The occurrence of negative probability weights has to be avoided in the Monte Carlo sampling. An apparent solution is provided if, instead of the numbers p_i itself, the Monte Carlo sampling is performed with respect to their absolute values $|p_i|$. In this case, in the numerical measurements, the sign $\mathrm{sgn}(p) = p/|p|$ is treated as part of the observable $\mathcal{O}$. In doing so, we get the following expression for the expectation value of $\mathcal{O}$, [170]

$$\langle\mathcal{O}\rangle = \frac{\sum_i \mathcal{O}_i \,\mathrm{sgn}(p_i)|p_i| / \sum_i |p_i|}{\sum_i \mathrm{sgn}(p_i)|p_i| / \sum_i |p_i|} = \frac{\langle\mathcal{O}\,\mathrm{sgn}\rangle_{|p|}}{\langle\mathrm{sgn}\rangle_{|p|}}, \tag{3.35}$$

where $\langle\ldots\rangle_{|p|}$ denotes the expectation value with respect to the probability distribution $|p|$ (instead of p).

Hence, we arrive at an expression for the expectation value of $\mathcal{O}$, where the expectation value of the sign, $\langle\mathrm{sgn}\rangle_{|p|}$, appears in the denominator. Configurations with negative and positive signs nearly cancel each other, which leads to an exponentially small value of $\langle\mathrm{sgn}\rangle_{|p|}$. Concretely, for world line configurations, $\langle\mathrm{sgn}\rangle_{|p|}$ can be shown to exponentially scale with the system volume and the temperature [170],

$$\langle sgn\rangle_{|p|} = \frac{\sum_i p_i}{\sum_i |p_i|} = \frac{\mathcal{Z}}{\mathcal{Z}_{|p|}} = e^{-\beta V(F-F_{|p|})}, \tag{3.36}$$

with β the inverse temperature, V the volume and F the free energy density. This exponentially small expectation value of the sign leads to an exponential growth in the statistical errors [170],

$$\frac{\Delta\,\mathrm{sgn}}{\langle\mathrm{sgn}\rangle} = \frac{\sqrt{\frac{\mathrm{Var(sgn)}}{N}}}{\langle\mathrm{sgn}\rangle} \sim \frac{e^{\beta V\Delta F}}{\sqrt{N}}. \tag{3.37}$$

In other words, in order to get the statistical errors under control in the simulation, exponentially many ($\sim e^{\beta V\Delta F}$) measurements become necessary. This, however, sets this method back to a numerical scaling that is no better than exact diagonalization.

For a specific quantum system, the sign problem might still be overcome if the system can be transformed to a suitable basis, where $e^{-\beta\mathcal{H}}$ becomes an operator

with only positive values. However, the computational effort to find such a basis has been shown to be an NP-hard problem [169].

Thus, the usual quantum Monte Carlo methods turn out to fail for many fermion and frustrated spin systems, including the Kitaev model. Here, the sign problem appears as a consequence of the exchange frustration of the spins [44]. The occurence of negative probabilities becomes apparent when the nonzero matrix elements $\langle i_{N-1}| 1 - \Delta\tau\mathcal{H}_i |i_N\rangle$ for a 2-spin example state $|i_N\rangle = |\uparrow\uparrow\rangle$ (in the σ^z basis) are explicitly written down

$$\begin{aligned}
\langle\downarrow\downarrow| 1 - \Delta\tau J_x\sigma_1^x\sigma_2^x |\uparrow\uparrow\rangle &= -\Delta\tau J_x, \\
\langle\downarrow\downarrow| 1 - \Delta\tau J_y\sigma_1^y\sigma_2^y |\uparrow\uparrow\rangle &= +\Delta\tau J_y, \\
\langle\uparrow\uparrow| 1 - \Delta\tau J_z\sigma_1^z\sigma_2^z |\uparrow\uparrow\rangle &= 1 - \Delta\tau J_z.
\end{aligned} \tag{3.38}$$

We see that for positive couplings $J_\gamma > 0$, the first matrix element leads to negative probability weights.

The fermionic sign problem and its possible solutions are an ongoing field of research [170]. It has been shown that for some fermionic systems, a sign-problem-free quantum Monte Carlo simulation can be realized with determinant quantum Monte Carlo [128, 134, 187, 188] or diagrammatic Monte Carlo methods [197, 198]. A particular branch of research in mathematical physics is concentrated on the formulation of models, which, due to their inherent symmetries – such as Kramer's time-reversal symmetry – are sign-problem-free [200–202]. In particular, it has been shown that it is the Majorana representation of interacting fermion models which allows for their systematic classification with respect to the presence or absence of a sign problem. Here, classification approaches are based on Majorana reflection positivity [203] and Majorana time-reversal symmetry [204]. Another recent approach proposes the usage of the properties of contraction semigroups to identify sign-problem-free fermion models. [205].

3.4 Quantum Monte Carlo for Kitaev systems

3.4.1 Majorana Basis

For the Kitaev model, it is the Majorana basis which allows for a sign-problem-free quantum Monte Carlo approach [44]. To see this, we remind ourselves of the exact solution (Sec. 2.1). The original spin degrees of freedom σ_i^γ are replaced with Majorana operators, $\sigma_i^\gamma \longrightarrow ib_i^\gamma c_i$, and the model is reformulated in terms of non-interacting itinerant Majorana fermions c_i and a (static) $\mathbb{Z}_2$ gauge field $\{u_{ij}^\gamma = \pm 1\}$ [27]. A gauge-invariant quantity is defined by the $\mathbb{Z}_2$ plaquette flux operator W_p, and the ground state is obtained by, first, finding the energy-minimizing $\mathbb{Z}_2$

flux configuration, and, secondly, exactly diagonalizing the Majorana Hamiltonian $\mathcal{H}(\{u_{ij}\})$ in the corresponding $\mathbb{Z}_2$ gauge sector, Eq. (2.9).

Thus, the setup is a system of *free fermions* coupled to field variables, and bears similarity with the scenario for the DQMC method. However, while the DQMC approach starts from a Hamiltonian that is quartic in the fermions, and the quartic terms have to be transformed via Hubbard-Stratonovich transformation, this is not necessary here. Within a given $\mathbb{Z}_2$ gauge field configuration $\{u_{ij}\}$, the Hamiltonian $\mathcal{H} = \mathcal{H}(\{u_{ij}\})$ is quadratic in the Majoranas c_i, and can be directly brought into a diagonal form, Eq. (2.14). Thus, the eigenbasis of $\mathcal{H}(\{u_{ij}\})$ is an eigenbasis of the partial fermionic Hilbert space H_f, and its eigenvalues can be used to calculate observable expectation values in the simple way that is shown in Eq. (3.20). The $\mathbb{Z}_2$ gauge field commutes with the Hamiltonian, and therefore effectively becomes a *classical* variable. This situation of fermionic degrees of freedom coupled to classical variables is known from the *double-exchange model* [139], for which a quantum Monte Carlo approach is known [140–142].

The key idea in the QMC approach for the Kitaev model is the Monte Carlo sampling of the $\mathbb{Z}_2$ gauge field $\{u_{ij}\}$ [44], which can be thought of as a local Ising variable: $u_{ij} = \pm 1$. For each $\mathbb{Z}_2$ gauge field configuration $\{u_{ij}\}$, the tight-binding Majorana Hamiltonian is exactly diagonalized, giving access to the thermodynamic observables needed for the calculation of Metropolis weights and numerical measurements.

More specifically, we rewrite the partition function of the full Kitaev spin system, which is the Boltzmann-weighted trace over all possible spin configurations $\{\sigma\}$, as a double trace over its fractionalized degrees of freedom, namely the $\mathbb{Z}_2$ gauge configurations $\{u_{ij}\}$ and the Majorana degrees of freedom $\{c_i\}$ [44],

$$\begin{aligned} \mathcal{Z} &= tr_{\{\sigma\}} e^{-\beta \mathcal{H}_{\text{Kitaev}}} \\ &= tr_{\{u_{ij}\}} tr_{\{c_i\}} e^{-\beta \mathcal{H}(\{u_{ij}\})}. \end{aligned} \tag{3.39}$$

Here, $\mathrm{tr}_{\{u_{ij}\}}$ is the sum over classical gauge configurations, for which the fermionic solutions can be calculated independently. Therefore, we can replace the trace by the sum

$$\mathrm{tr}_{\{u_{ij}\}} \longrightarrow \sum_{\{u_{ij}\}}. \tag{3.40}$$

Diagonalizing $\mathcal{H}(\{u_{ij}\})$ and transforming the Majorana operators to (spinless) fermions $a_\lambda^\dagger, a_\lambda$, we rewrite the partition function in terms of the fermionic count-

ing operators $\hat{n}_\lambda = a_\lambda^\dagger a_\lambda$ [44],

$$\begin{aligned}\mathcal{Z} &= \sum_{\{u_{ij}\}} \left(tr_{\{\hat{n}_\lambda\}} e^{-\beta \sum_\lambda \epsilon_\lambda (\hat{n}_\lambda - \frac{1}{2})} \right) \\ &= \sum_{\{u_{ij}\}} \left(tr_{\{\hat{n}_\lambda\}} \prod_\lambda e^{-\beta \epsilon_\lambda (\hat{n}_\lambda - \frac{1}{2})} \right). \end{aligned} \tag{3.41}$$

Now, since we are summing over all occupation numbers of the fermionic single particle states λ, we can exchange the trace and the product in the last equation. Subsequently, for each λ, we explicitly perform the partial summation $tr_{\{\hat{n}_\lambda\}}$, i.e. we sum over the fermionic states $n_\lambda \in \{0, 1\}$, which gives an analytic expression $\mathcal{Z}_{\mathrm{Maj}}(\{u_{ij}\})$ for the Majorana partition function in a fixed gauge sector [44],

$$\begin{aligned}\mathcal{Z} &= \sum_{\{u_{ij}\}} \prod_\lambda tr_{\{\hat{n}_\lambda\}} e^{-\beta \epsilon_\lambda (\hat{n}_\lambda - \frac{1}{2})} \\ &= \sum_{\{u_{ij}\}} \prod_\lambda \left(e^{\frac{\beta\epsilon_\lambda}{2}} + e^{-\frac{\beta\epsilon_\lambda}{2}} \right) \\ &= \sum_{\{u_{ij}\}} \underbrace{\prod_\lambda \left(2\cosh\left(\frac{\beta\epsilon_\lambda}{2} \right) \right)}_{=: \mathcal{Z}_{\mathrm{Maj}}(\{u_{ij}\})}. \end{aligned} \tag{3.42}$$

From the Majorana partition function $\mathcal{Z}_{\mathrm{Maj}}(\{u_{ij}\})$, the relevant thermodynamic observables, such as the free energy, internal energy, specific heat and entropy, can be directly derived, using the standard formulas from statistical physics (Appendix B.4). Considering that the Majorana fermions form a many-particle system in the fixed $\mathbb{Z}_2$ gauge sector, where internal energy and entropy are in competition with each other, the statistical weight for a given gauge sector is determined by the Majorana free energy in that gauge sector. The quantum partition function of the Kitaev system is therefore finally expressed as the classical sum,

$$\mathcal{Z} = \sum_{\{u_{ij}\}} e^{-\beta F(\{u_{ij}\})}, \tag{3.43}$$

with

$$\begin{aligned} F(\{u_{ij}\}) &= -T \ln \mathcal{Z}_{\mathrm{Maj}}(\{u_{ij}\}) \\ &= -T \sum_\lambda \ln \left(2\cosh\left(\frac{\beta\epsilon_\lambda}{2} \right) \right). \end{aligned} \tag{3.44}$$

The probabilty for each $\mathbb{Z}_2$ gauge field configuration is

$$p(\{u_{ij}\}) = \frac{1}{\mathcal{Z}} e^{-\beta F(\{u_{ij}\})}, \tag{3.45}$$

which is guaranteed to be positive and real, since $e^{-\beta F}$ is not an operator, but an ordinary number. This indicates the absence of a sign problem.

As the gauge field consists of classical Ising variables ± 1 located on the bonds, the Metropolis algorithm becomes applicable in a very intuitive way. A quantum Monte Carlo step consists of

1. a single flip of a random $\mathbb{Z}_2$ gauge field variable, $u_{ij} \to -u_{ij}$,
2. which is accepted with a probability [1]

$$\alpha = e^{-\beta \Delta F}, \tag{3.46}$$

where $\Delta F = F(\{u'_{ij}\}) - F(\{u_{ij}\})$ is the free energy difference between the initial $\mathbb{Z}_2$ gauge field configuration $\{u_{ij}\}$ and the proposed new configuration $\{u'_{ij}\}$. Note that for the calculation of the free energy, Eq. (3.44), the full set of eigenvalues $\{\epsilon_\lambda\}$ of $\mathcal{H}(\{u_{ij}\})$ is required.

The described update scheme naturally fulfills the conditions for the Markov chain, as the normalization of the transition matrix and detailed balance are inherent to the Metropolis algorithm, and the ergodicity follows from the local Ising update.

To calculate the Metropolis weight, an exact diagonalization of the Majorana Hamiltonian $\mathcal{H}(u_{ij})$ is required in each Monte Carlo step, amounting to diagonalizing an $N \times N$ matrix for a lattice system with N sites. With standard divide-and-conquer techniques [152], such a matrix diagonlization scales with $\mathcal{O}(N^3)$. In Sec. 3.4.3, we present the Green's-function-based Kernel Polynomial method [45, 146, 147], which enables us to perform more efficient Monte Carlo updates with linear scaling in N.

To summarize, the quantum Monte Carlo simulation for Kitaev systems is sign-problem-free if the system is transformed to the Majorana basis. In this basis, we can benefit from two facts. First, the $\mathbb{Z}_2$ gauge field, which emerges in the Majorana basis, is static, and can therefore be treated as a classical variable. Secondly, for a given $\mathbb{Z}_2$ gauge field configuration $\{u_{ij}\}$, the Majorana Hamiltonian $\mathcal{H}(\{u_{ij}\})$ is quadratic in the Majorana operators c_i, such that there is an eigenbasis of $\mathcal{H}(\{u_{ij}\})$, which is also a basis of the partial (fermionic) Hilbert space H_f. These two properties enable us to map the quantum partition function to a classical sum, without the need to introduce an additional (e.g. imaginary time) dimension.

[1] In practice, we used the slightly modified weight $\alpha = \frac{1}{1+e^{\beta \Delta F}}$.

3.4.2 Jordan-Wigner and local transformation

Local Transformation: Hilbert space extension

There remain some non-trivial considerations on the validity of the derivation in the last section, namely the step presented in Eq. (3.42). Concretely, the latter contained an explicit summation over all possible fermionic occupancies $n_\lambda \in \{0, 1\}$ for the single-particle states λ. Some of these fermionic states in the Majorana partion function are, however, unphysical. This is a consequence of Kitaev's local transformation approach. By replacing each spin with 4 Majorana operators, $\sigma_i^\gamma \to i b_i^\gamma c_i$, the Hilbert space is artificially increased by a factor 2 for each spin. In total, the many-body Hilbert space is extended to the dimension 4^N, while the dimension of the physical subspace is only 2^N. The latter is defined by the gauge transformation $D_i = b^x b^y b^z c_i$, and contains only those states $|\xi\rangle$ for which $D_i |\xi\rangle = |\xi\rangle$ [27].

Reprojection

Thus, in order to avoid unphysical contributions to the Majorana partition function $\mathcal{Z}_{\mathrm{Maj}}(\{u_{ij}\})$, which, in the end, might blur the numerical results, it seems that a reprojection to the physical subspace needs to be included in each QMC step. Such a reprojection operator has been introduced by Kitaev as a symmetrization over all gauge transformations D_i [27],

$$\mathcal{P} = \frac{\prod_i (1 + D_i)}{2}, \tag{3.47}$$

with $\mathcal{P}^2 = \mathcal{P}$, $[\mathcal{P}, \mathcal{H}_{\mathrm{Kitaev}}] = 0$, and $D_i \mathcal{P} = \mathcal{P}\ \forall i$, such that any wavefunction $\mathcal{P} |\Psi\rangle$ indeed lies in the physical subspace.

Every many-body wavefunction for the Kitaev model can be written as

$$|\Psi\rangle = |u\rangle \otimes |m\rangle\,, \tag{3.48}$$

with the gauge part $|u\rangle$ and the fermionic (matter) part $|m\rangle$. A detailed analysis of the operator $\mathcal{P}$ shows that the forbidden states are hidden in the matter sector, while there is no particular gauge configuration $\{u_{ij}\}$, that is, in principal, physically excluded [144]. Although the $\{u_{ij}\}$ are not invariant under the gauge transformation D_i, since the latter flips the gauge variable u_{ij} on all bonds connected to the site i, the underlying $\mathbb{Z}_2$ plaquette flux W_p is invariant under D_i. Therefore, it is insightful to rewrite the operator $\mathcal{P}$ as a product of an operator $\mathcal{P}_0$, which contains all terms that only act on the matter sector, and another operator $\mathcal{S}$,

which contains all terms that only act on the gauge sector [144] (Appendix B.1),

$$\mathcal{P} = \mathcal{S} \cdot \underbrace{\left(\frac{1 + \prod_{i=1}^{N} D_i}{2} \right)}_{:=\mathcal{P}_0}. \tag{3.49}$$

In the expression for $\mathcal{P}_0$, we can reexpress the operators D_i with the corresponding Majorana operators b_i^γ, c_i. Afterwards, we follow the transformation procedure used for the solution of the model, regroup the b_i^γ to $\mathbb{Z}_2$ bond operators $\hat{u}_{ij}$, and transform the Majorana operators to spinless fermions. This way, $\mathcal{P}_0$ assumes the form [144] (Appendix B.1)

$$\mathcal{P}_0 = \frac{1}{2} \left(1 + (-1)^\phi \cdot \prod_{\langle i,j \rangle} u_{ij} \cdot \det(Q) \cdot \hat{\pi} \right), \tag{3.50}$$

with some integer phase factor ϕ, which depends on the lattice geometry, the transformation matrix Q, Eq. (2.11), and the fermionic parity operator [144]

$$\hat{\pi} = \prod_{\lambda} (1 - 2\hat{n}_\lambda). \tag{3.51}$$

A closer look at Eq. (3.50) shows that all terms in the parentheses give a ± 1, and all but the parity operator $\hat{\pi}$ depend either on the lattice or the $\mathbb{Z}_2$ gauge field configuration $\{u_{ij}\}$. Thus, for a given lattice and gauge field configuration, the eigenvalue of $\mathcal{P}_0$ only depends on the parity operator $\hat{\pi}$: Only fermionic states with *either* even *or* odd parity lead to an eigenvalue 1, and the other states to an eigenvalue 0. It can be concluded that those many-body wavefunctions which give an eigenvalue 0 are strictly unphysical, while all other wavefunctions have some overlap with physical states, since the operator $\mathcal{S}$ only acts on the gauge part $|u\rangle$ of the wavefunction $|\Psi\rangle$ [144]. This implies that on a given lattice, a gauge configuration $\{u_{ij}\}$ physically allows for either even or odd fermionic parity, and states with the other parity are unphysical.

The dimension of the extended many-body Hilbert space for the fractionalized degrees of freedom is 4^N for the N-site system, corresponding to $2^{3N/2}$ gauge configurations $\{u_{ij}\}$, and $2^{N/2}$ fermionic states. We have now seen that, given the lattice and the gauge configuration $\{u_{ij}\}$, only half of the fermionic states are physical, corresponding to a dimension of $2^{N/2-1}$. The extension of the gauge sector is, with the argument given above, merely a redundant counting of physical plaquette flux sectors, which has no effect on the observables of the system. On the other hand, the summation over arbitrary fermionic states is expected to affect

the results. For instance, the energy of an arbitrary basis state $|n\rangle$ of the matter sector is given by

$$E = \frac{1}{2}\sum_{\lambda=1}^{N/2}(-1)^{1-n_\lambda}\epsilon_\lambda. \tag{3.52}$$

Since the distinctive difference between physical and unphysical states is parity, an unphysical state can be considered as a physical state, where a single fermion $a_\lambda^\dagger$ has been added or removed, giving an energy difference $|E - E'| = |\epsilon_\lambda|$.

To get rid of this effect from unphysical fermionic states, the parity projection has to be included in the Majorana partition function $\mathcal{Z}_{\mathrm{Maj}}(\{u_{ij}\})$. The explicit implementation of this step has been recently presented in Refs. [206, 207]. This, however, means that in each Monte Carlo step, the determinant of the transformation matrix Q has to be calculated, in order to determine the allowed parity. This diagonalization step increases the numerical computation time and puts an additional restriction on the accessible system sizes – which is something we want to avoid, in order to be able to simulate 3D Kitaev systems beyond the realm of strong finite-size effects.

Jordan-Wigner transformation: No unphysical states

It is possible to avoid the reprojection and prevent the numerical artifacts from unphysical fermionic states at the same time. In fact, there are several ways to transform the spin degrees of freedom in the Kitaev system to Majorana fermions and a $\mathbb{Z}_2$ gauge field [89]. One is built on a *non-local* Jordan-Wigner transformation [77–80] (Sec. 2.1.4). This approach is used in earlier quantum Monte Carlo simulations of Kitaev systems [44–47, 90].

The Jordan-Wigner transformation [76] is well known as an exact solution method for one-dimensional spin models like the Heisenberg chain. Here, instead of locally transforming a spin according to Eq. (2.2), they are transformed *chain-wise* to Majorana operators. The Jordan-Wigner chains have to be chosen to consist of two of the three subclasses of γ-bonds, while only the third class of bonds carries the $\mathbb{Z}_2$ gauge degrees of freedom, here usually denoted by $\{\eta\}$. The major advantage of this approach is its faithfulness to the Hilbert space dimensionality of the spin model. In contrast to the local transformation, the Jordan-Wigner ansatz makes no use on an artificial Hilbert space extension. This makes sure we do not integrate over unphysical states when calculating the Majorana partition function, Eq. (3.42), and subsequently, the thermodynamic observables. However, there remains a weak spot in this approach. In order to avoid the introduction of nonlocal parity terms that have to be considered when closing the Jordan-Wigner strings, open boundary conditions have to be imposed in (at least) one spatial direction,

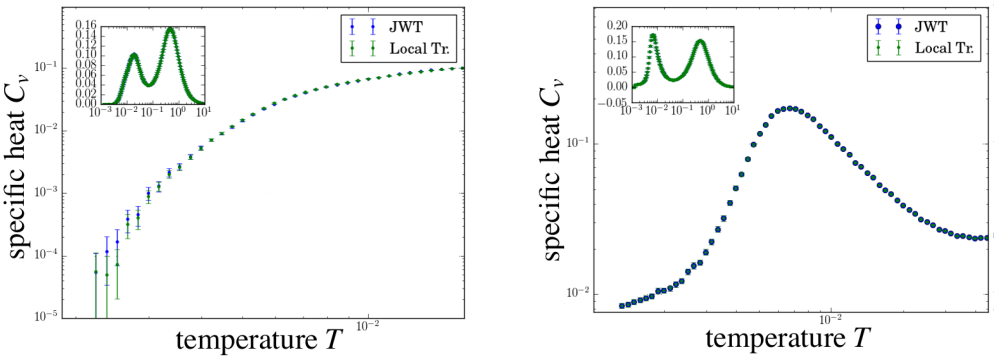

(a) system size $N = 32$ **(b)** system size $N = 108$

Figure 3.1: Comparison of QMC results for the (10,3)a (hyperoctagon) lattice with periodic boundary conditions in the $\mathbf{a_1}$-direction. We have performed QMC simulations with a Jordan-Wigner (JWT) and local transformation for systems with 32 (a) and 108 sites (b). In the first method, $\mathbb{Z}_2$ gauge variables are only sampled on the z-bonds, and in the second method on all bonds. The Jordan-Wigner transformation is exact for this choice of boundary conditions, and both approaches give consistent results.

while, within the local transformation approach, there is, intrinsically, no restriction on boundary conditions.

Comparing the Jordan-Wigner and the local approach, we see that both transformations lead to the same Hamiltonian, if, within the local approach, the $\mathbb{Z}_2$ gauge field on two subclasses of bonds is fixed to a specific configuration [80]. In this case, the remaining $\mathbb{Z}_2$ gauge degrees of freedom u_{ij}^{γ} on the γ-bonds are equivalent to the $\mathbb{Z}_2$ gauge variables η from the Jordan-Wigner transformation. Since we know that the latter leads to an exact analytic expression for the Majorana partition function, it is therefore guaranteed that the QMC results from both methods are exact. This is the case if the corresponding lattice system possesses open boundary conditions in the direction of the Jordan-Wigner strings.

Benchmark calculations have further shown us that even if we move away from this exact equivalence and sample semi-open systems over all $\mathbb{Z}_2$ gauge variables u_{ij}, the results still remain within the error margins of the exact (Jordan-Wigner) results. The effect of sampling over "too many bonds" is therefore interpreted as an overcounting of physical states, which does not affect the measurement results of the physical observables. Results for the (10,3)a (hyperoctagon) lattice with periodic boundary conditions in the $\mathbf{a_1}$-direction are shown in Fig. 3.1.

Boundary conditions

In addition to the stated exactness of both QMC methods for semi-open systems, we can argue that the two can be extended also to systems with periodic boundary

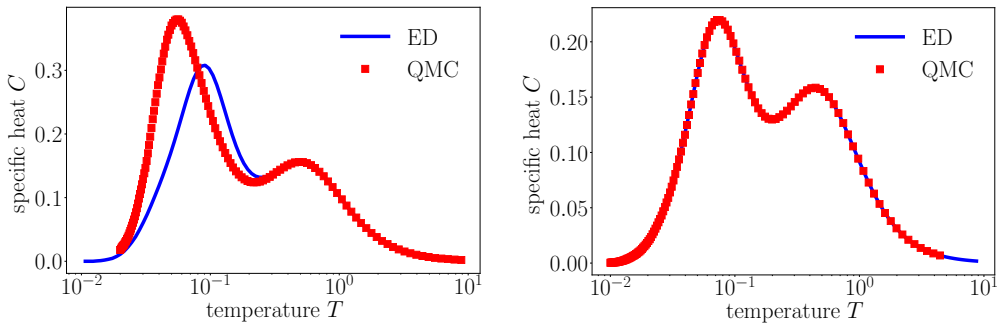

(a) periodic boundary conditions

(b) semi-open boundary conditions

Figure 3.2: Comparison of QMC and ED results. We compare results (i) for an 8-site Honeycomb cluster with periodic boundary conditions in both spatial directions (a), and (ii) for the same cluster with an open boundary condition in the horizontal direction (b). For the cluster with periodic boundary conditions, neglecting the difference between fermionic parities leads to a deviation $\Delta T \sim 0.04$ in the T-location of the low-temperature peak. This effect is expected to scale as $1/N$ with the system size N, and become negligible for large systems. For the cluster with the open boundary, the Majorana Hamiltonian underlying the QMC approach is equivalent to the one obtained from a Jordan-Wigner transformation, which does not make use of an artificial Hilbert space extension. Thus, there is an exact correspondence to the result from the ED of the spin system even for this very small cluster.

conditions in *all* spatial directions, and that the implementation of a reprojection to the physical subspace is not necessary for large systems. This follows from a simple scaling argument for the local transformation approach. Every unphysical fermionic state in the Majorana partition function possesses a physical "partner". With respect to this partner state, it is a single fermion that has been added or removed in the unphysical state, resulting in an energy difference of one single particle energy $|\epsilon_\lambda|$, which enters the summation over the fermionic states in Eq. (3.42). The effect of unphysical states on numerical measurements is therefore expected to be a finite-size effect, which scales as $1/N$ for a system with N sites [145]. The same argument applies if the parity term from the Jordan-Wigner transformation is regarded, which shows up whenever a Jordan-Wigner string is closed along a periodic boundary.

We can see the numerical effect from unphysical states if we compare the results from a QMC simulation with exact diagonalization results for the spin system on a small cluster. We perform these simulations on an 8-site Honeycomb system with periodic boundary conditions and measure the specific heat as a function of temperature (Fig. 3.2 a). The double-peak curve from the exact diagonalization is qualitatively reproduced and quantitatively exact for temperatures $T > 0.3$. Below this region, the low-temperature peak from the QMC simulation deviates to lower temperatures, and its extremal point is shifted by $\Delta T \sim 0.04$. With the

argument given above, this effect is expected to influence the results for finite-sized Kitaev systems, and to vanish for $N \to \infty$. We also observe that for the same system with an open boundary in one spatial direction, where the Jordan-Wigner transformation is exact, there is perfect agreement between the QMC and ED results down to lowest temperatures (Fig. 3.2 b).

Based on these arguments, we perform the QMC simulations on elementary 3D Kitaev systems with the local transformation approach – treating the $\mathbb{Z}_2$ gauge field $\{u_{ij}\}$ on all bonds as free Ising variables. We assure that a Jordan-Wigner transformation is possible on the underlying lattice geometry (Appendix C.7), but use periodic boundary conditions in all spatial dimensions. We see that the finite-size effects arising from this choice of boundary conditions becomes negligible for the considered system sizes $N > 1000$, and especially for the extrapolation of critical temperatures. A detailed discussion of finite-size effects in the numerical results is given in Appendix C. Empirically, we find that the choice of Jordan-Wigner strings has an effect on the scaling behavior of the thermodynamic observables (e.g. the height of specific heat peaks). As a rule of thumb, this behavior becomes more systematic if the lattice geometry of a system allows for a Jordan-Wigner transformation in which all Jordan-Wigner strings have approximately the same length.

Details on the numerical performance of the QMC method are discussed in Appendix B.2.

3.4.3 Green's-function-based Kernel Polynomial method

The bottleneck in the quantum Monte Carlo simulation is the exact diagonalization of the Majorana Hamiltonian, which scales with $\mathcal{O}(N^3)$ for a lattice system with N sites. This performance limitation can be lifted by a numerical technique called *Green's-function-based Kernel Polynomial Method (GF-KPM)* [45, 146, 147]. Here, we obtain the free energy difference ΔF between two gauge configurations *without* calculating the full set $\{\epsilon_\lambda\}$ of the Majorana Hamiltonian.

The key ideas of this method are,

1. to look at the change in the density of states $\rho(E) - \rho'(E)$ in a Monte Carlo update, and

2. express this change in $\rho(E)$ in terms of (a small set of) Green's functions $G(E)$, which can be numerically *approximated* by Chebyshev polynomials.

This method reduces the computational cost of each Monte Carlo update to $\mathcal{O}(N)$, which comes at the expense of introducing an additional systematic error through the Chebyshev approximation. This error is however controlled by the

number of Chebyshev moments which are considered in the approximation. Thus, it is possible to reproduce numerical results from the exact method with a high accuracy down to the lowest temperature scales. In the following, we use the term *QMC-ED* for the Monte Carlo method with exact diagonalization, and the term *QMC-KPM* for the Monte Carlo method with Green's-function-based Kernel Polynomial method.

Theory of the Green's-function-based Kernel Polynomial method

How is the GF-KPM method constructed in detail? Computationally, a local update of the $\mathbb{Z}_2$ gauge variable on a particular bond, $u_{ij} \to -u_{ij}$, means changing the signs of a single pair of entries $\tilde{A}_{ij}$ and $\tilde{A}_{ji}$ of the Hermitian matrix $\tilde{A} := iA$, Eq. (2.9). This update can also be written in the form of a sum [45, 147]

$$\tilde{A} \longrightarrow \tilde{A}' = \tilde{A} + \Delta, \tag{3.53}$$

where Δ is a rank-two matrix, for which only the entries $\Delta_{ij} = -2\tilde{A}_{ij}$ and $\Delta_{ji} = -\Delta_{ij}$ are nonzero. With this knowledge, it is possible to use the information stored in $\tilde{A}$ much more efficiently for the calculation of Metropolis weights than in the QMC-ED approach. To see that, we can define the Green's function [45, 147]

$$G(E) = (\tilde{A} - E \cdot \mathbb{I})^{-1}, \tag{3.54}$$

and use it to reexpress the eigenvalue equation of the updated matrix $\tilde{A}'$ [45, 147],

$$\begin{aligned} \left(\tilde{A} + \Delta\right) |\psi\rangle &= E\,|\psi\rangle\,, \\ \left(\tilde{A} - E + \Delta\right) |\psi\rangle &= 0, \\ G(E)\left(\tilde{A} - E + \Delta\right) |\psi\rangle &= 0, \\ (\mathbb{I} + G(E)\Delta)\,|\psi\rangle &= 0. \end{aligned} \tag{3.55}$$

Thus, the eigenvalues of $\tilde{A}'$ are the given by the roots of the function,

$$d(E) = \det(\mathbb{I} + G(E)\Delta), \tag{3.56}$$

i.e., the values of E for which $d(E) = 0$. The crucial property of the function $d(E)$ is the vanishing of all entries of Δ, except the two given above. Thus, in order to express $d(E)$ explicitly, we only need four Green's functions $G(E)$ [45, 147],

$$d(E) = (1 + \Delta_{ij}G_{ji}(E))(1 - \Delta_{ij}G_{ij}(E)) + \Delta_{ij}\Delta_{ji}G_{ii}(E)G_{jj}(E), \tag{3.57}$$

a fact which is exploited for numerical efficiency. Physically, the function $d(E)$ can be related to the change in the density of states $\Delta\rho(E)$ during the Monte Carlo

update. This becomes apparent if we extend the domain of $d(E)$ to the complex plane by the analytic continuation $E \to z := E + i\epsilon$ and take the derivative of its logarithm [45, 147],

$$\begin{aligned}\frac{1}{\pi}\mathrm{Im}\left(\lim_{\epsilon\to 0}\frac{d\log d(z)}{dz}\right) &= \frac{1}{\pi}\mathrm{Im}\lim_{\epsilon\to 0}\sum_i \frac{1}{\epsilon_i - z} - \frac{1}{\epsilon_i' - z} \\ &= \sum_i \delta(\epsilon_i - E) - \delta(\epsilon_i' - E) \\ &= \rho(E) - \rho'(E). \end{aligned} \tag{3.58}$$

With this relation, it is also possible to express the change in the free energy in terms of $d(z)$ [45],

$$\begin{aligned}\Delta F &= -T\int_0^\infty \log\left(2\cosh\left(\frac{\beta E}{2}\right)\right)(\rho(E) - \rho'(E))\,dE \\ &= -\frac{T}{\pi}\int_0^\infty \log\left(2\cosh\left(\frac{\beta E}{2}\right)\right)\mathrm{Im}\left(\lim_{\epsilon\to 0}\frac{d\log d(z)}{dz}\right) \\ &\overset{*}{=} -\frac{T}{\pi}\int_0^\infty \frac{\beta\sinh\left(\frac{\beta E}{2}\right)}{2\cosh\left(\frac{\beta E}{2}\right)}\mathrm{Im}\left(\lim_{\epsilon\to 0}\log(d(E+i\epsilon))\right)dE \\ &= -\frac{1}{2\pi}\int_0^\infty \tanh\left(\frac{\beta E}{2}\right)\mathrm{Im}\left(\lim_{\epsilon\to 0}\log(d(E+i\epsilon))\right)dE. \end{aligned} \tag{3.59}$$

Here, in step (*), partial integration is used. Thus, we can calculate ΔF by numerically integrating a function that is essentially composed of $d(E)$, which, as he have seen in Eq. (3.57), is given by four Green's functions.

Numerical implementation

The calculation of the Green's functions in Eq. (3.57) is therefore the key step in the improved calculation of acceptance probabilities, and replaces the exact diagonalization of $\tilde{A}'$. Most efficiently, we can write the off-diagonal Green's functions $G_{ij}(E)$ $(i \neq j)$ in terms of diagonal Green's functions $G_{ii}(E)$ via [45]

$$\begin{aligned} G_{ab} &= \frac{1}{2}\left(G_{a+b,a+b} - iG_{a+ib,a+ib} - (1-i)(G_{a,a} + G_{b,b})\right), \\ G_{ba} &= \frac{1}{2}\left(G_{a+b,a+b} + iG_{a+ib,a+ib} - (1+i)(G_{a,a} + G_{b,b})\right), \end{aligned} \tag{3.60}$$

and calculate the diagonal Green's functions $G_{ii}(E)$ with the Chebyshev approximation [45, 146, 147],

$$G_{ii}(E+i\epsilon) = i\frac{\mu_0 + 2\sum_{m=1}^{M-1}\mu_m \exp\left(-im\arccos(E/s)\right)}{\sqrt{s^2 - E^2}}. \tag{3.61}$$

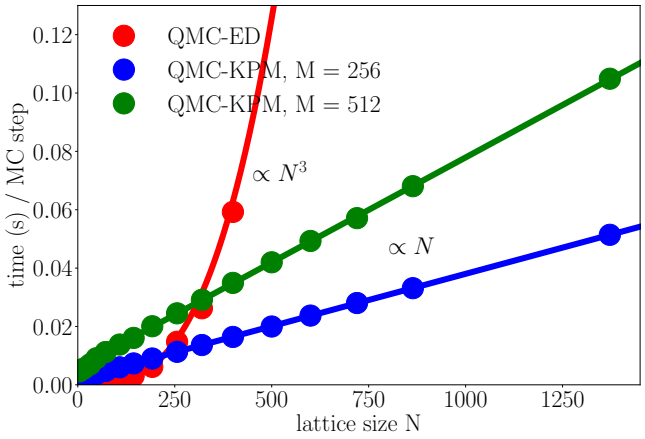

Figure 3.3: Computation time for a single MC step with the QMC-ED and the QMC-KPM method. The QMC-ED method scales cubically with the number of system sites N, which is a consequence of the ED calculation in each Monte Carlo update. With QMC-KPM, the computational cost of the Monte Carlo step can be reduced to linear scaling in N.

Here, M is the number of Chebyshev moments μ_m that are taken into account, and s denotes the bandwidth of the system. It has to be calculated in the beginning of the QMC simulation by a sufficient number of (e.g. 1000) exact diagonalizations of $\tilde{A}$ with random $\mathbb{Z}_2$ gauge field configurations. The Chebyshev moments μ_m are given by [45, 146, 147],

$$\mu_m = g_m \langle i | T_m(H/s) | i \rangle , \tag{3.62}$$

where g_m denotes the Jackson Kernel factor [146]

$$g_m = \frac{(M-m+1)\cdot \cos\left(\frac{\pi m}{M+1}\right) + \sin\left(\frac{\pi m}{M+1}\right)\cot\left(\frac{\pi}{M+1}\right)}{M+1}, \tag{3.63}$$

which has to be included to increase the precision of a Chebyshev iteration which is truncated after a finite amount of M steps. An exact expansion of a function $f(x)$ would require the summation over an infinite series of Chebyshev polynomials, and the truncation usually leads to unwanted oscillations of the expanded series near points where $f(x)$ is not continuously differentiable (so-called Gibbs oscillations). Kernel factors can be used to dampen these oscillations [146]. In the moments $\langle i | T_m(H/s) | i \rangle$ in Eq. (3.62), $|i\rangle$ is the unity vector with all entries zero but the i-th, and iterated by the Chebyshev recursion

$$T_m(x) = 2xT_{m-1}(x) - T_{m-2}(x). \tag{3.64}$$

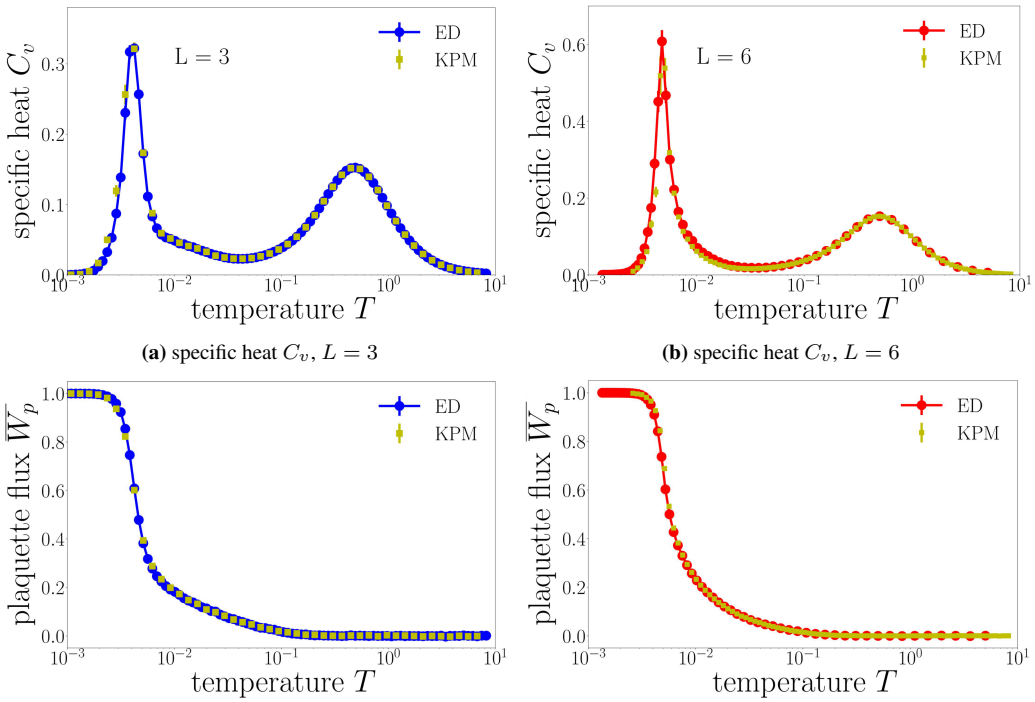

(a) specific heat C_v, $L = 3$

(b) specific heat C_v, $L = 6$

(c) plaquette flux $\overline{W_p}$, $L = 3$

(d) plaquette flux $\overline{W_p}$, $L = 6$

Figure 3.4: Comparison of numerical results for the QMC-KPM / QMC-ED method. Data shown are the specific heat $C_v(T)$ (top) and average plaquette flux $\overline{W}_p$ (bottom) on a (10,3)b Kitaev system (with periodic boundary conditions in the $\mathbf{a_3}$-direction) with 108 (L = 3, a,c) and 864 sites (L = 6, b,d). The number of Chebyshev moments is $M = 512$.

Concretely, the latter is performed by successive multiplications of $|i\rangle$ with the rescaled Hamiltonian H/s [45, 146, 147],

$$\begin{aligned} |u_0\rangle &= \mathbb{I}\,|i\rangle = T_0(H/s)\,|i\rangle\,, \\ |u_1\rangle &= (H/s)\,|u_0\rangle = T_1(H/s)\,|i\rangle\,, \\ |u_m\rangle &= 2(H/s)\,|u_{m-1}\rangle - |u_{m-2}\rangle = T_m(H/s)\,|i\rangle\,, \end{aligned} \tag{3.65}$$

such that

$$\langle i|\,T_m(H/s)\,|i\rangle = \langle i|u_m\rangle\,. \tag{3.66}$$

The necessary calculation steps can be further reduced by a factor of 2, if the relations

$$\begin{aligned} \mu_{2m} &= 2\,\langle u_m|u_m\rangle - \mu_0, \\ \mu_{2m+1} &= 2\,\langle u_{m+1}|u_m\rangle - \mu_1, \end{aligned} \tag{3.67}$$

are used [45, 146, 147].

In summary, a Monte Carlo update of the $\mathbb{Z}_2$ gauge field $u_{jk} \rightarrow -u_{jk}$ now requires the followings steps for the calculation of Metropolis weights:

1. Chebyshev iteration of the Green's functions G_{jj}, G_{kk}, $G_{j+k,j+k}$ and $G_{j+ik,j+ik}$ (note that in the last Green's function, i denotes the imaginary unit!) according to Eqns. (3.61) and (3.67).
2. Calculation of $d(E)$ according to Eq. (3.57).
3. Numerical integration of ΔF, Eq. (3.59).
4. Calculation of the Metropolis weight: $\alpha = \min\left(1, e^{-\beta\Delta F}\right)$.

The subsequent matrix-vector multiplications in Eq. (3.65) are now the most time-consuming part in the Monte Carlo update. If sparse-matrix techniques are applied (Appendix B.3), the scaling of this calculation can be reduced to $\mathcal{O}(N)$, which we have verified with benchmark calculations (Fig. 3.3). The approximative calculation of Green's functions by Chebyshev polynomials introduces a systematic error to the Monte Carlo update. This error is however controlled by the number of Chebyshev moments M which is considered in Eq. (3.61). Benchmark calculations show that for typical system sizes $N \geq 600$, a choice $M = 256 - 512$ leads to a sufficient agreement of the QMC-KPM results with those from QMC-ED calculations (Fig. 3.4). For smaller systems, M has to be increased.

Further technical details on the implementation of the QMC-KPM method are given in Appendix B.3.

3.5 Data Analysis

We close this chapter with a discussion on post-processing and analysis of the numerical data. First, we give a brief review on the statistical basics that are important for any Monte Carlo simulation in statistical physics, most of all the error analysis and the treatment of autocorrelation effects. After that, we review the bootstrap method that can be used to compute the statistical errors for observables that are themselves functions of expectation values, like, for example, the specific heat $C_v(T) = T^{-2}(\langle E^2\rangle - \langle E\rangle^2)$. Finally, we explain the Multiple Histogram Reweighting Method of Ferrenberg and Swendsen [148–150], which we apply for data extrapolation on the (8,3)c Kitaev model (Sec. 4.4).

3.5.1 Statistical Basics

In the general discussion of Monte Carlo simulations, we have seen which condition such a simulation has to fulfill to produce a sequence of system configurations

that obey a certain probability distribution p. Here, we assume that all these conditions are fulfilled. Thus, the Monte Carlo simulation has generated a Markov chain of N configurations $C_1 \to C_2 \to \dots C_N$, on which we measure some observable x, producing a sequence of data

$$\{x_1, x_2, \dots, x_N\}, \tag{3.68}$$

with $x_i = x(C_i)$. In the following, we start by assuming that the x_i are uncorrelated,

$$\chi_{|j-i|} = \langle x_i x_j \rangle - \langle x_i \rangle \langle x_j \rangle = 0. \tag{3.69}$$

From the data sequence, we calculate the *sample mean*

$$\overline{x} = \frac{1}{N} \sum_{i=1}^{N} x_i, \tag{3.70}$$

and the *sample standard deviation*

$$s_x = \sqrt{\frac{1}{(N-1)} \sum_{i=1}^{N} (x_i - \overline{x})^2}, \tag{3.71}$$

from which the *standard error of the mean* follows as

$$\sigma_x = \frac{s_x}{\sqrt{N}}. \tag{3.72}$$

The outcome of $\overline{x}$ depends on the number of measurements N, and for large N, we want $\overline{x}$ to converge against the expectation value $\langle x \rangle = \sum_\Omega x(C_i) p(C_i)$ of the observable x with respect to the probability distribution p. It can be easily checked that the expectation value of $\overline{x}$ is indeed $\langle x \rangle$ [128],

$$\langle \overline{x} \rangle = \frac{1}{N} \sum_{i=1}^{N} \langle x_i \rangle = \frac{1}{N} \sum_{i=1}^{N} \langle x \rangle = \langle x \rangle. \tag{3.73}$$

Explicitly using that $\chi_{|j-i|} = 0$, the variance of $\overline{x}$ is [128]

$$\begin{aligned}
\mathrm{Var}\,(\overline{x}) &= \langle \overline{x}^2 \rangle - \langle \overline{x} \rangle^2 \\
&= \frac{1}{N^2} \left\langle \sum_{i,j} x_i x_j \right\rangle - \langle x \rangle^2 \\
&= \frac{1}{N^2} \left\langle \sum_{i} x_i^2 + \sum_{i \neq j} x_i x_j \right\rangle - \langle x \rangle^2 \\
&= \frac{1}{N} \left\langle \frac{1}{N} \sum_{i=1}^{N} x_i^2 \right\rangle - \frac{1}{N} \langle x \rangle^2 \\
&= \frac{\mathrm{Var}\,(x)}{N}. \qquad (3.74)
\end{aligned}$$

Thus, the variance of $\overline{x}$ is proportional to the variance of the random variable x – an intrinsic property which is per se unknown – and inversely proportional to the number of measurements N. Analogously, it can be shown that [128]

$$\langle \sigma_x^2 \rangle = \frac{\mathrm{Var}(x)}{N}, \qquad (3.75)$$

so σ_x, the standard error of the mean, is an estimate for the deviation of $\overline{x}$ from the expectation value $\langle x \rangle$, which becomes smaller if the number of measurements is increased. The sample standard deviation s_x, on the other hand, is an estimate for the (intrinsic) standard deviation σ of the random variable x. The error bars in the data plots always correspond to the interval $[\overline{x} - \sigma_x, \overline{x} + \sigma_x]$ of a given observable x.

3.5.2 Autocorrelation Effects

In reality, subsequent configurations C_i, C_{i+1} in a Markov chain are always intrinsically correlated, resulting in finite function values $\chi_{|j-i|}$ for observables x. The vanishing of the $\chi_{|j-i|}$ is, however, explicitly assumed upon deriving the relation between the variance of the sample mean $\mathrm{Var}(\overline{x})$ and the variance of the observable $\mathrm{Var}(x)$, Eq. (3.74). Accordingly, while the autocorrelation has no effect on the sample mean $\overline{x}$, it affects the statistical error. Instead of the simplified derivation of $\mathrm{Var}(\overline{x})$, its true relation with the observable variance turns out to be [128]

$$\mathrm{Var}(\overline{x}) = \frac{\mathrm{Var}(x)}{N}(1 + 2\tau_x), \qquad (3.76)$$

with the autocorrelation time

$$\tau_x = \sum_{i=1}^{N-1} \left(1 - \frac{i}{N}\right) \frac{\chi_i}{\chi_0}. \qquad (3.77)$$

Thus, the autocorrelation time τ_x of the observable x reduces the number of statistically independent measurements to $N/(1+2\tau_x)$, which increases the statistical error. The standard error of the mean σ_x does not reflect this, and is therefore too small as an estimate for the statistical error of the data sequence with finite autocorrelation.

There are different possibilities to remedy this problem and obtain a statistical error which considers autocorrelation effects. One way is to calculate the autocorrelation time τ_x explicitly from the time series of results $\{x_1, x_2, \ldots, x_N\}$ with Eq. (3.77).

Another common technique is *binning analysis*. Here, the time series is split up into different *bins* of results, each bin containing an amount of B measurements. In total, there are N_b bins

$$\underbrace{x_1, x_2, \ldots x_B}_{1}, \underbrace{x_{B+1}, x_{B+2}, \ldots x_{2B}}_{2}, \ldots, \underbrace{x_{(N_b-1)B+1}, x_{(N_b-1)B+2}, \ldots x_{N_bB}}_{N_b}, \tag{3.78}$$

and, for each bin, the average of the x_i is calculated separately,

$$\tilde{x}_k = \frac{1}{B} \sum_{i \in \mathrm{k^{th}\ bin}} x_i. \tag{3.79}$$

This, of course, does not affect the sample mean

$$\overline{x} = \frac{1}{N_b} \sum_{j=1}^{N_b} \tilde{x}_j = \frac{1}{N} \sum_{i=1}^{N} x_i, \tag{3.80}$$

but the variance of the bin averages,

$$s^2_{\overline{x}_{\mathrm{bin}}} \approx \frac{1}{(N_b-1)} \sum_{j=1}^{N_b} (\tilde{x}_j - \overline{x})^2, \tag{3.81}$$

which increases with the bin size B.

If B is large enough, all bins become statistically independent. In order to determine for which size B this is the case, we can measure the ratio [128]

$$R_x = \frac{s^2_{\overline{x}_{\mathrm{bin}}}}{s^2_x}, \tag{3.82}$$

as a function of B. This function first increases with B, and converges to some finite value R^f_x, when the bins are large enough and become uncorrelated. The root of this value $\sqrt{R^f_x}$ determines the ratio between the standard deviation of the

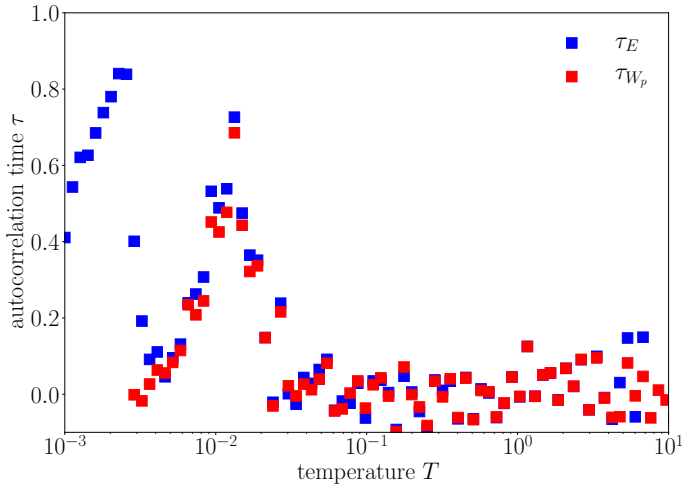

Figure 3.5: Autocorrelation times of the energy E and plaquette flux $\overline{W}_p$ for the Kitaev honeycomb model with linear size $L = 10$. The autocorrelation time has a local maximum at $T \sim J/100$, where the system undergoes a thermal crossover. The autocorrelation times are calculated using the ALEA library [208] of the ALPS project [209, 210].

bin averages $s_{\overline{x}_{\text{bin}}}$ and the sample standard deviation s_x that would be obtained without binning. Thus, the corrected standard error of the mean is

$$\tilde{\sigma}_x = \sqrt{R_x^f} \frac{s_x}{\sqrt{N}}, \tag{3.83}$$

and the autocorrelation time is calculated from R_x^f as

$$\tau_x = \frac{1}{2} \left(R_x^f - 1 \right). \tag{3.84}$$

We perform the binning analysis on our simulation data using the ALEA library [208] of the ALPS project [209, 210].

3.5.3 Bootstrapping

The described binning method is not only suited for determining the autocorrelation time of a given observable, but also for calculating the error of observables which are themselves functions of expectation values, or, more general, the i-th moments of random variables x, $f = f(\langle x \rangle, \langle x^2 \rangle, \ldots \langle x^n \rangle)$. This is the case for the specific heat C_v, which is given by

$$C_v(T) = \frac{1}{T^2} \left(\langle E^2 \rangle - \langle E \rangle^2 \right). \tag{3.85}$$

For E and E^2, we can save time series of measurements $\{E_i\}$, $\{E_i^2\}$ during the Monte Carlo simulation, and use it to calculate the standard error of the mean according to Eq. (3.72). But if we calculate the sample means $\overline{E}$, $\overline{E^2}$ from this entire time series, we only obtain one measurement for C_v. Furthermore, calculating the standard error of the mean with Gaussian error propagation is not trivial here, since E and E^2 are correlated random variables.

The simplest way to solve this issue is to split the time series for E and E^2 again into bins, whose size B exceeds the autocorrelation time τ_x, and calculate C_v separately for each bin. The standard error can then be calculated from the bin variance $\sqrt{s^2_{\overline{x}_{\mathrm{bin}}}}$.

More sophisticated techniques are the *bootstrap* and the *jackknife method* [127, 128]. In the bootstrap method, the time series $\{x_1, \ldots, x_N\}$ is *resampled*, i.e., N measurements x_i from the time series are subsequently picked at random. Here, it is explicitly allowed to pick the same number several times. The result is a new time series of resampled data $\{\tilde{x}_1, \ldots, \tilde{x}_N\}$, from which we can calculate the quantity of interest. The resampling is then repeated several times, until we obtain a large enough time series of data for f, $\{f_1, \ldots, f_M\}$. From this time series, we can calculate the standard error of the mean according to [127]

$$\sigma_f = \sqrt{\overline{f^2} - \overline{f}^2}. \tag{3.86}$$

The jackknife method slightly differs from bootstrapping. Here, there is no resampling of the whole time series. Instead, we start from the set $\{x_1, \ldots, x_N\}$, take away the first value x_1, and calculate $f(\overline{x})$ from the remaining set $\{x_2, \ldots, x_N\}$. Then, we put x_1 back in, take away x_2, and again calculate $f(\overline{x})$. We repeat the procedure for all $i \in \{1, \ldots N\}$, and thereby obtain a time series $\{f_1, \ldots, f_{N-1}\}$. The error of f is then given by [127]

$$\sigma_f = \sqrt{\sum_{i=1}^{N} (f_i - \overline{f})^2}, \tag{3.87}$$

where $\overline{f}$ is calculated from the whole time series $\{x_1, \ldots, x_N\}$.

We use the bootstrap method for calculating the statistical errors for reweighted data sets.

3.5.4 Multiple Histogram Reweighting

The information obtained from simulations at certain temperatures $\{T_i\}$ can be used to extend the data analysis also to other temperatures, which have not been

directly simulated. The numerical techniques for this purpose are called single-histogram [148] and multiple-histogram *reweighting* [149, 150], and allow for an interpolation and extrapolation of data that have a stronger physical foundation than the usual numerical methods, such as least-squares fitting or spline interpolation. This is due to the fact that reweighting is based on the information about the density of states that is extracted from the Monte Carlo simulations.

The idea of the multiple histogram technique is outlined as follows [127]: From a Monte Carlo simulation at some temperature T_i, we obtain an estimate for the density of states $\rho_i(E)$, which is determined by the number of sweeps M_i, the number of times a particular energy E is measured, $N_i(E)$, and the partition function $\mathcal{Z}_i$. Taking a number of Monte Carlo simulations at different (but close) temperature points i yields different estimates

$$\rho_i(E) = \frac{N_i(E)}{M_i} \frac{\mathcal{Z}_i}{e^{-\beta_i E}}. \tag{3.88}$$

In practice, the $\rho_i(E)$ are different histogram curves with some overlap, and it is justified to assume that the histograms for other temperatures, which are in close range to the ones simulated, have some overlap with the $\rho_i(E)$.

Now, the idea is to use the curves $\rho_i(E)$ to generate a best estimate for the "true" density of states $\rho(E)$. This best estimate can be shown to be given by [127]

$$\rho(E) = \frac{\sum_i N_i(E)}{\sum_j M_j \mathcal{Z}_j^{-1} e^{-\beta_j E}}, \tag{3.89}$$

where the partition functions $\mathcal{Z}_j$ are unknown, but can be expressed recursively for each temperature T_k,

$$\begin{aligned} \mathcal{Z}_k &= \sum_E \rho(E) e^{-\beta_k E} \\ &= \sum_E \frac{\sum_i N_i(E)}{\sum_j M_j \mathcal{Z}_j^{-1} e^{(\beta_k - \beta_j)E}} \\ &= \sum_{i,s} \frac{1}{\sum_j M_j \mathcal{Z}_j^{-1} e^{(\beta_k - \beta_j)E_{i,s}}}. \end{aligned} \tag{3.90}$$

Here, in the last expression, the indices i, j again label the simulations at different temperatures T_i, T_j, while the index s labels the summation over different sweeps.

The major part of the reweighting calculation is now focused on the recursion equation (3.90). Starting from an initial estimate, $\mathcal{Z}_k$ is iteratively calculated for each temperature point T_k, until it converges to a fixed point. We now possess estimates of $\mathcal{Z}_k$ for all *simulated* temperatures T_k. But it is also possible to calculate

an estimate for $\mathcal{Z}$ at any other inverse temperature β that has *not* been simulated, provided $\rho(E)$ still possesses some overlap with the $\rho_i(E)$ from the simulations.

Explicitly, the partition function, Eq. (3.90), is generalized for any inverse temperature β as

$$\mathcal{Z}(\beta) = \sum_{i,s} \frac{1}{\sum_j M_j \mathcal{Z}_j^{-1} e^{(\beta-\beta_j)E_{i,s}}}. \tag{3.91}$$

Being able to produce an estimate for the partition function at any β, we can now also calculate estimates for other thermodynamic observables $\mathcal{O}$ as

$$\begin{aligned} \langle \mathcal{O} \rangle &= \frac{1}{\mathcal{Z}(\beta)} \sum_{i,s} \mathcal{O}_{i,s} w_{i,s}, \\ w_{i,s} &= \frac{1}{\sum_j M_j \mathcal{Z}_j^{-1} e^{(\beta-\beta_j)E_{i,s}}}. \end{aligned} \tag{3.92}$$

In the case of the Kitaev model, the Boltzmann weights are expressed in terms of the free energy F, which is a function of the single-particle energies ϵ_λ. Thus, in Eq. (3.92), the logarithmic weights have to be replaced according to

$$-\beta E \longrightarrow -\beta \sum_\lambda \log\left(2\cosh\left(\frac{\beta\epsilon_\lambda}{2}\right)\right). \tag{3.93}$$

Therefore, for every temperature point i and for every sweep s, we need to save the full set of eigenvalues $\{\epsilon_\lambda\}_{i,s}$ from the QMC simulation to be able to perform the reweighting.

In practice, we use the multiple-histogram reweighting to extrapolate low-temperature estimates for the thermodynamic observables of the (8,3)c Kitaev system, in the region where QMC fails to converge even with parallel tempering (Sec. 4.4). For the implementation, we use the open source tool FerrenbergSwendsenReweighting.jl [211] which is designed for the Julia programming language [212].

For the analysis of the statistical errors $\Delta\mathcal{O}$ of the reweighted observables, we use a particular implementation of the bootstrap method. In reweighting, subsequent eigenvalue configurations $\{\epsilon_\lambda\}_{i,s}$ from the QMC simulation at temperature T_i are correlated. But, in addition, there is a finite correlation also between the configurations at neighboring temperature points, which is a consequence of exchanging replicas. We treat these autocorrelation effects by a combination of binning and resampling. For a given temperature point i, we first regroup subsequent sets of eigenvalue configurations $\{\epsilon_\lambda\}_{i,s}$ to bins, where the bin length B is generously chosen to exceed the autocorrelation time τ_E within one QMC process by multiple times. This way, we obtain a set d of, in total, M/B data sequences s_l, i.e.

$$d = \left\{ s_1, \ldots, s_{\frac{M}{B}} \right\}, \tag{3.94}$$

in which the s_l contain the correlated eigenvalue configurations,

$$s_l = \{\{\epsilon_\lambda\}_{l,1}, \ldots \{\epsilon_\lambda\}_{l,B}\}\,. \tag{3.95}$$

Now, for each temperature point T_i, we generate a number of resamples of the sequence d,

$$d_n = \left\{s_{i_1}, \ldots, s_{i_{M/B}}\right\}, \tag{3.96}$$

which we separately feed into the reweighting calculation, and, thereby, generate a time series of reweighted observables $\{\mathcal{O}_i\}$. The statistical error $\Delta\mathcal{O}$ is then calculated by the standard error for resamples, as given in Eq. (3.86).

3.6 Summary

In this chapter, we have presented the technical underpinning of our quantum Monte Carlo simulation approach which we use for the numerical study of Kitaev systems at finite temperatures. We have seen how this approach is rooted in the Majorana basis of the Kitaev model. Here, the partition function can be separated into a sum over classical field configurations, namely the static $\mathbb{Z}_2$ gauge field $\{u_{ij}\}$, and a trace over the Majorana fermions. The latter is exactly diagonalized for each $\mathbb{Z}_2$ gauge field configuration $\{u_{ij}\}$. This way, we map the partition function to a sum over classical probabilities, without having to introduce an additional (imaginary time) dimension as, for example, in world line QMC. The effect from the artificial extension of the Hilbert space, which is used in Kitaev's local transformation from spins to Majorana operators, can be either neglected, if we perform the QMC simulations on large systems, or avoided, by alternatively using a non-local Jordan-Wigner transformation, which preserves the Hilbert space dimension of the spin model. The computational bottleneck in the Monte Carlo update is the exact diagonalization of the Majorana Hamiltonian – a numerical calculation which scales with $\mathcal{O}(N^3)$ for system sizes N. It can be significantly accelerated by using the Green's-function-based Kernel polynomial method. Here, one exploits that a gauge field update $u_{ij} \longrightarrow -u_{ij}$ only leads to a rank-2 update of the Hamiltonian, and the change in the free energy ΔF that determines the Metropolis weights can be efficiently calculated in terms of four Green's functions. The Chebyshev expansion used in this method only relies on repeated matrix-vector multiplications, which, applying sparse-matrix techniques, scale with $\mathcal{O}(N)$. The Chebyshev expansion introduces a systematic error to the calculation of acceptance probabilities, which can be controlled by the number of considered Chebyshev moments. Apart from the QMC method itself, we have presented the most important techniques for the analysis of our numerical data, including multiple histogram reweighting.

Chapter 4

Thermodynamic classification of 3D Kitaev spin liquids

In Sec. 2.2.6, we have given a brief introduction to the thermodynamics of the Kitaev model. In general, Kitaev systems exhibit two characteristic thermal transitions, namely the fractionalization of spins into Majorana fermions and a $\mathbb{Z}_2$ gauge field, and the low-temperature ordering of the gauge field. A manifestation of these transitions is a two-peak structure in the specific heat. In three spatial dimensions, the $\mathbb{Z}_2$ gauge ordering is associated with a thermal phase transition, which is determined by the proliferation of system-spanning vison excitations and belongs to the class of inverted Ising transitions that occur in certain lattice $\mathbb{Z}_2$ gauge theories [50] (Sec. 1.1.2). These phase transitions deviate from the conventional Ginzburg-Landau paradigm, in the sense that they are not described by any local order parameter. The occurrence of the thermal phase transition in 3D Kitaev systems and its underlying mechanism have been shown and explained in earlier quantum Monte Carlo studies on individual systems [44, 45].

The aim of the numerical studies presented in this chapter is to deepen this understanding of the $\mathbb{Z}_2$ gauge physics in three spatial dimensions. For that, we present quantum Monte Carlo results for a set of elementary, tricoordinated 3D Kitaev systems [96] (Tab. 4.1), which have been studied in a series of earlier works on the classification of Majorana ground states [35, 36, 48, 93, 213].

We start with the numerical verification that the ground state flux sectors in all considered 3D Kitaev systems follow the prediction by Lieb's theorem [85–87], although the geometrical conditions for its rigorous applicability are only given for one of the lattice systems. After that, we discuss the signatures of the thermal transitions. In particular, we use the results on the low-temperature specific heat peaks to extrapolate critical temperatures T_c for all systems, and show that T_c is correlated with the size of the vison gap Δ – a result which corroborates the picture of a phase transition that separates different vison loop regimes. Apart

from the focus on the $\mathbb{Z}_2$ gauge field in this chapter, we also present an analysis of the Majorana density of states (DOS).

In the last part of this chapter, we discuss a lattice system which falls out of the "conventional" thermodynamical scheme. In the Kitaev system on the (8,3)c lattice, a peculiar interplay between the loop length and a geometrical constraint on the $\mathbb{Z}_2$ fluxes leads to geometrically frustrated gauge configurations, with a macroscopic number of (energetically) degenerate states. We call this phenomenon *gauge frustration*. We show that the degeneracy of the $\mathbb{Z}_2$ gauge field leads to a suppression of the thermal ordering transition down to a particularly low temperature scale. At this critical temperature, it is a subtle interplay between the $\mathbb{Z}_2$ gauge field and the Majorana fermions which determines the lifting of the degeneracy.

The first three sections in this chapter discuss work which has been reported in Ref. [214]. The work discussed in section 4 has been reported in Ref. [143].

4.1 Ground state flux sectors

The conserved, gauge-invariant physical quantity which underlies the $\mathbb{Z}_2$ gauge field in Kitaev systems is the magnetic $\mathbb{Z}_2$ plaquette flux $W_p = e^{i\Phi}$ (Sec. 2.1.2). In order to obtain the exact ground state solution for a Kitaev system, one first needs to find the $\mathbb{Z}_2$ flux configuration $\{W_p\}$ with minimal energy. A statement about this ground state flux configuration is provided by Lieb's Theorem, which states that it is the (even) length $|p|$ of the elementary plaquette of bipartite lattice systems which determines the energy-minimizing plaquette flux. If $|p| \mod 4 = 2$, all plaquettes have to remain flux-free ($\Phi = 0 \leftrightarrow W_p = 1$), while for $|p| \mod 4 = 0$, it is a flux $\Phi = \pi$ per elementary loop ($W_p = -1$), which gives the ground state. The prediction is valid for any tight-binding Hamiltonian describing a half-filled band system of hopping electrons, and the theorem is therefore also extendable to the hopping Majorana fermions in Kitaev systems (Sec. 2.1.2).

However, Lieb's theorem is rigorously proven only for bipartite lattice geometries which fulfill certain mirror symmetry conditions. All plaquettes and the lattice system itself must be symmetric with respect to mirror planes that do not cut through any of the lattice vertices. Among the elementary tricoordinated lattices considered here, these symmetry conditions are only fulfilled for (8,3)b, and partly (8,3)n.

As a consequence, the energy-minimizing flux sector for most 3D Kitaev systems is, strictly speaking, unknown. This, however, does not necessarily mean that Lieb's theorem is completely useless here. It only means that the flux conjecture cannot be strictly proven on these lattices. Despite that, it can be argued that Lieb's theorem still provides the right guideline for determining the ground

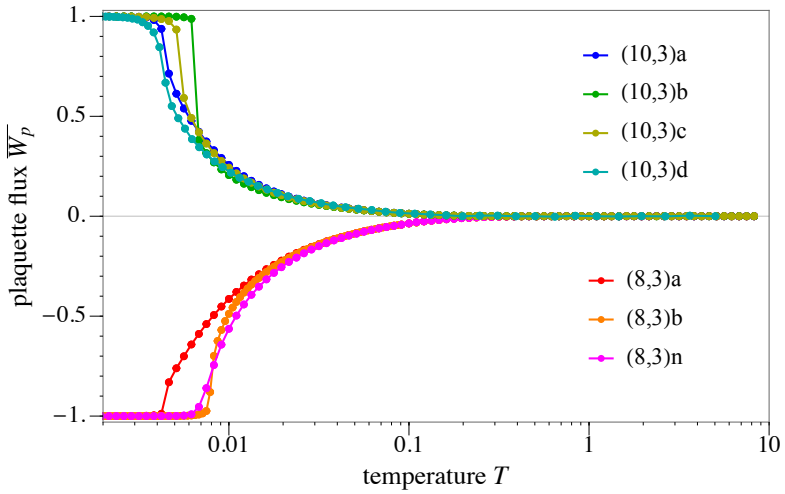

Figure 4.1: Plaquette flux $\overline{W_p}$ [214]. The numerical data shows that the ground state flux configuration $0/\pi$ (corresponding to a W_p-eigenvalue ± 1) is determined by the elementary plaquette length $|p|$ for each lattice. For $|p| \mod 4 = 0$, the ground state has a π-flux per plaquette, while the flux for systems with $|p| \mod 4 = 2$ is 0. This prediction by Lieb's theorem is valid for all considered 3D Kitaev systems, even for those that do not fulfill the mirror symmetry conditions that are required for its strict proof – which are all except (8,3)b. Data shown is for the linear system size $L = 7$, except for (8,3)n and (10,3)d (here, $L = 5$). Error bars are smaller than the symbol sizes.

state flux sector. One might think of at least two different strategies to corroborate the flux conjecture: The first one is routed as well in symmetry considerations. It can be asked if the flux predicted by Lieb's theorem is consistent with the point-group symmetries of the lattice. If this is the case, it would be very unintuitive if the Kitaev system on this lattice geometry assumed another ground state flux configuration. The second strategy is to check the ground state flux configurations numerically. This has been partly done, namely for small periodic clusters, in Ref. [36], which supports the ground state flux configurations according to Lieb (Sec. 2.2.3).

Our QMC results verify this conjecture also for large systems. In the numerical experiments on finite, real-space Kitaev systems, where the $\mathbb{Z}_2$ gauge variables are independent degrees of freedom, we have confirmed that all considered systems assume those ground state flux configurations which follow the prediction by Lieb's theorem. All bipartite systems with a plaquette length $|p|$ dividable by 4 possess a π-flux ground state, while all lattice systems with $|p| \mod 4 = 2$ have a ground state where all plaquettes are flux-free (Fig. 4.1).

Based on this result, the elementary, bipartite 3D Kitaev systems can be systematically categorized into different families, which are characterized by their plaquette length and the corresponding ground state flux sector (Tab. 4.1). The

Lattice	Alternative names	Ground state flux sector	Lieb theorem
(10,3)a	hyperoctagon [35]	0	
(10,3)b	hyperhoneycomb [91]	0	
(10,3)c		0	
(10,3)d		0	
(8,3)a		π	
(8,3)b	hyperhexagon	π	Yes
(8,3)n		π	
(8,3)c*		frustrated	
(9,3)a*	hypernonagon [95]	$\pm\pi/2$	

Table 4.1: Overview of the elementary three-dimensional, tricoordinated lattices [36, 214]. The plaquette length $|p|$ is the quantity which determines the ground state flux configuration for all bipartite lattice systems (see Fig. 4.1), while Lieb's Theorem is only strictly applicable for (8,3)b. The lattices (8,3)c and (9,3)a, indicated by an asterisk, do not possess the conventional ground state flux $0/\pi$. For (8,3)c, additional geometric conditions determine a frustrated flux ground state, while the flux sector of the non-bipartite system (9,3)a is characterized by spontaneous breaking of time-reversal symmetry and plaquette fluxes $\pm\pi/2$ [90, 95].

Schläfli convention (Sec. 2.2) provides an intuitive notation for this classification, since the naming of the lattices is, here, started by the plaquette length. Among the bipartite lattices, we find the family (10,3)x with flux-free ground states, and the family (8,3)x, where the plaquettes generally carry the (maximal) flux π in the ground state. Among the lattices with plaquette length 8, (8,3)c is the only one that has a more exotic ground state flux sector, and is separately discussed in Sec. 4.4.

4.2 Thermal phases

The thermal signatures of fractionalization and gauge ordering have been established in earlier quantum Monte Carlo studies of 3D Kitaev systems, namely on the (10,3)b [44] and (10,3)a lattice [45]. The specific heat of these systems has been shown to exhibit a characteristic two-peak structure, indicating two thermal transitions. At $T' \sim J$ (J being the coupling constant of the Kitaev interaction), a high-temperature peak, which shows no lattice- or system-size-dependent modifications, indicates a thermal crossover. It is here that the spins locally fractionalize, and itinerant Majorana fermions, which are situated on the vertices of the lattices, couple to the static $\mathbb{Z}_2$ gauge field that is located on the lattice bonds. The fractionalization can be further read off at this temperature scale from the characteristic behavior of the spin-spin-correlator $S_{\gamma\gamma} = \langle \sigma_i^\gamma \sigma_j^\gamma \rangle$, a quantity which is equivalent to the kinetic energy $-i\langle c_i c_j \rangle_\gamma$ of the Majorana fermions [43, 46]. It has been shown that, below the crossover temperature T', $S_{\gamma\gamma}$ assumes a finite plateau

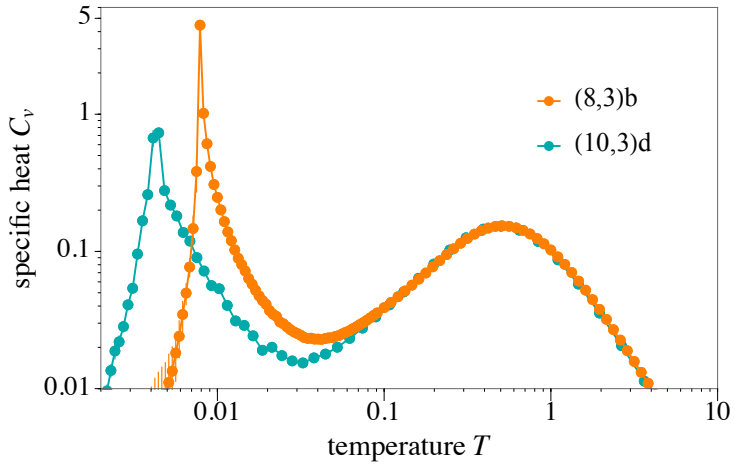

Figure 4.2: Two peaks in the specific heat C_v [214]. The high-temperature peak at $T' = 0.51(5)$ is the signature of the thermal crossover associated with spin fractionalization. The low-temperature peak indicates the thermal phase transition associated with the ordering of the $\mathbb{Z}_2$ gauge field into the ground state flux configuration. Data shown is for lattice systems (10,3)d with linear system size $L = 5$ and (8,3)b with linear system size $L = 7$. Error bars are indicated, but mostly smaller than the symbol sizes.

value, thereby indicating that the Majorana fermions become itinerant here.

At a temperature scale which is two orders of magnitude smaller than T', namely at $T_c \sim J/100$, the 3D Kitaev systems show a second peak in the specific heat. Unlike the crossover peak, this peak is strongly sensitive to the geometry of the underlying lattice system, as well as to the system size. Its generically diverging behaviour with growing system size is the signature of a thermal phase transition. This phase transition is a feature which is only characteristic for the three-dimensional Kitaev systems, and distinct from the low-temperature crossover which is usually encountered in their 2D counterparts [46]. It is at the low-temperature phase transition that the gauge ordering happens, and the Kitaev systems enter their respective ground state flux sector, which is measurable in terms of the average plaquette flux (eigenvalue) $\overline{W_p}$.

Between the two thermal transitions, the system is thus in a peculiar state where the spins are already *fractionalized*, i.e., its properties are already governed by the parton degrees of freedom, but the $\mathbb{Z}_2$ gauge field, to which the Majorana fermions are coupled, remains *disordered*. This intermediate phase has been shown to appear as a flattened region in the entropy curve $S(T)$ [44, 45], underlining its relative thermal stability. The fact that this intermediate regime spans two orders of magnitude in temperature space raises the expectation that it might be a candidate for experimental detection in a real material.

Our quantum Monte Carlo results show that the described thermal signatures

are generic features of the considered systems. The details are discussed in the following. We have simulated all Kitaev systems at the isotropic coupling point, where $J_x = J_y = J_z = 1/3$. The unit of the temperature corresponds to this choice of the coupling, and is omitted in the following (to restore the unit J, all temperatures have to be multiplied by 3). The assignment of Kitaev couplings has been chosen in accordance with Ref. [36]. We have performed the quantum Monte Carlo simulations on systems with linear sizes up to $L = 7$, and, deviantly, $L = 5$ for (8,3)n, which has a particularly large unit cell of 16 sites, and (10,3)d, which has been simulated solely with the QMC-ED method. This choice of L corresponds to largest system sizes with $N = 1000 - 2058$ sites. All lattice systems have been implemented with periodic boundary conditions, with the exception of (10,3)d, where open boundary conditions in the a_2- and a_3-direction have been used to reduce finite-size effects. A detailed overview of the individual numerical results for each lattice and a discussion of finite-size effects is provided in Appendix C.

4.2.1 Thermal crossover and local spin fractionalization

We start the discussion of the numerical results by closely inspecting the specific heat $C_v(T)$. For all 3D Kitaev systems, it shows the aforementioned two-peak structure (Fig. 4.2, appendices C.3, C.4). To achieve a more precise understanding on how the fractionalized degrees of freedom differ with respect to their physical behaviour, it is convenient to examine the specific heat contributions of the (itinerant) Majorana fermions and the $\mathbb{Z}_2$ gauge field separately [215], and to compare them with the added result from both contributions. The Majorana contribution is given by the derivative of the internal energy E_f of the Majorana system (Appendix B.4),

$$C_{v,\mathrm{MF}}(T) = -\frac{1}{T^2}\left\langle \frac{\partial E_f(\{u_{jk}\})}{\partial \beta} \right\rangle_{MC}, \tag{4.1}$$

a term which appears in the full specific heat formula due to the explicit temperature dependence of E_f. Here, the bracket $\langle \dots \rangle_{MC}$ denotes averaging over Monte Carlo samples.

The full specific heat curve $C_v(T)$ and its Majorana part $C_{v,\mathrm{MF}}(T)$ are plotted for the different 3D Kitaev systems in Fig. 4.3. The peak temperature is $T' = 0.51(5)$ for all lattice systems, and we can also see that all specific heat curves lie (almost) exactly on top of each other. In fact, only the curve of (10,3)d appears slightly shifted with respect to the others, which is an effect from the open boundary conditions that this system is implemented with. For the full specific heat, this correspondence holds down to a temperature scale of $T \sim 0.1$, below which the curves of the lattices start to differ and evolve into the respective

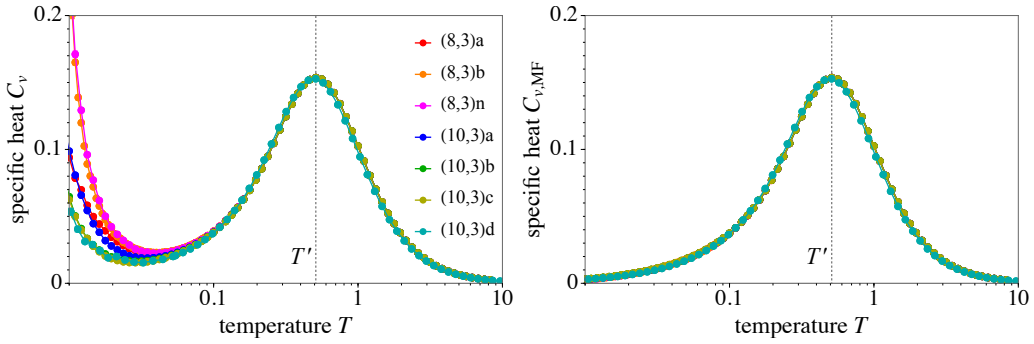

(a) specific heat C_v **(b)** Majorana contribution $C_{v,\mathrm{MF}}$

Figure 4.3: Specific heat C_v in the high-temperature region (a), and its Majorana contribution $C_{v,\mathrm{MF}}$ (b) [214]. The high-temperature peak indicates a thermal crossover, caused by the (local) fractionalization of spins into (itinerant) Majorana fermions and a (static) $\mathbb{Z}_2$ gauge field. The position and shapes of the peaks are (nearly) equal for all lattice systems, which underlines the local character of the thermal transition. Data shown is for the linear system size $L = 7$, except for (8,3)n and (10,3)d (here, $L = 5$). The dotted line indicates the crossover temperature $T' = 0.51(5)$. Error bars are smaller than the symbol sizes.

low-temperature peaks. For the Majorana contribution $C_{v,\mathrm{MF}}(T)$, the correspondence of the lattice curves holds down to lowest temperatures, and for $T \to 0.01$, $C_{v,\mathrm{MF}}(T)$ becomes 0 for all lattice systems.

We can draw a number of conclusions from these observations. The first one is associated with the energy scales on which the fractionalized degrees of freedom in the system become relevant. Clearly, the specific heat contribution from the $\mathbb{Z}_2$ gauge field is measurable only below $T \sim 0.1$, which signifies that the strongest fluctuations of the gauge field lie within this energy scale. In contrast with that, the weakest fluctuations of the itinerant Majoranas have a magnitude which lies above $T \sim 0.01$. Below the temperature scale $T \sim 0.01$, the system is entirely governed by the fluctuations of the $\mathbb{Z}_2$ gauge field, and above $T \sim 0.1$, it is entirely governed by fluctuations of the Majorana fermions. In the intermediate temperature regime $0.01 \leq T \leq 0.1$, fluctuations of both fractionalized degrees of freedom play a role. This corresponds exactly to the regime which is dubbed *disordered $\mathbb{Z}_2$ spin liquid*, where the itinerant Majorana fermions are coupled to a disordered $\mathbb{Z}_2$ gauge field.

Secondly, there are no changes in the high-temperature peak, neither for different lattice geometries (albeit there is a slight shift for systems with open boundary conditions), nor for different system sizes. Thus, it can be stated that for all 3D Kitaev systems, the thermal transition associated with the fractionalization of spins is a local phenomenon, i.e. a thermal crossover. Numerical measurements of the spin-spin correlator S_{zz} (see Fig. 4.4) further show that all systems approach a finite plateau value $S_{zz} \sim 0.52$ below the crossover temperature T' (with the

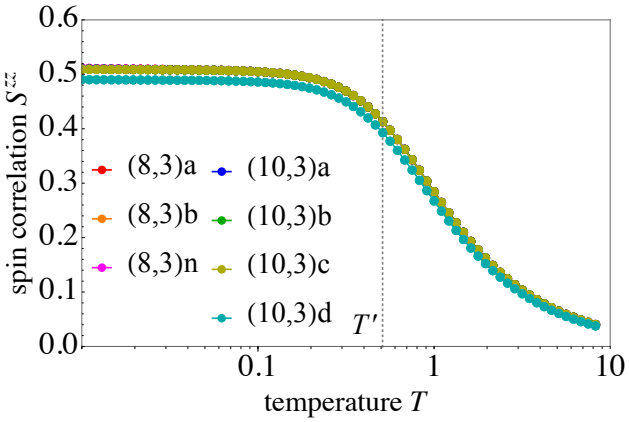

Figure 4.4: Spin correlator $S_{zz} = \langle \sigma_i^z \sigma_j^z \rangle$. This quantity is equivalent to the kinetic energy of the itinerant Majorana fermions, $-i\langle c_i c_j \rangle_\gamma$. Below the thermal crossover at $T' = 0.51(5)$ (indicated by the dotted line), the correlator assumes a finite plateau value for all lattice systems. Hence, the thermal crossover can be interpreted as being caused by the local fractionalization of spins into itinerant Majorana fermions, which are coupled to a static $\mathbb{Z}_2$ gauge field. Data shown is for the linear system size $L = 7$, except for (8,3)n and (10,3)d (here, $L = 5$). Error bars are smaller than the symbol sizes.

exception of (10,3)d, where the plateau value is $S_{zz} \sim 0.48$). This confirms the picture of spins σ_i that locally fractionalize at the crossover, $\sigma_i^\gamma \to i b_i^\gamma c_i$, and of the Majorana fermions c_i becoming itinerant at this temperature.

4.2.2 Thermal phase transition and $\mathbb{Z}_2$ gauge ordering

In contrast to the high temperature region, where the different specific heat curves $C_v(T)$ lie on top of one another, the latter differ at temperatures below a scale of $T \sim 0.1$. Here, the physical behaviour of the system becomes more and more governed by the fluctuations of the $\mathbb{Z}_2$ gauge field $\{u_{jk}\}$, which can be seen from comparing the full specific heat $C_v(T)$ with its Majorana contribution $C_{v,\mathrm{MF}}(T)$ (Fig. 4.3). For $T \to 0.01$, $C_{v,\mathrm{MF}}(T)$ goes to 0. Thus, the specific heat in the low-temperature region $T \leq 0.05$ is effectively given by its gauge contribution, which is captured by the variance of the internal energy E_f,

$$C_{v,\mathrm{GF}}(T) = \frac{1}{T^2} \left(\langle E_f^2(\{u_{jk}\}) \rangle_{MC} - \langle E_f(\{u_{jk}\}) \rangle_{MC}^2 \right). \tag{4.2}$$

The results for $C_{v,\mathrm{GF}}(T)$ on the different lattice systems are shown in Fig. 4.5. We can see that the thermal signature in the gauge-dominated regime, the low-temperature peak of $C_{v,\mathrm{GF}}(T)$, is qualitatively different from the high-temperature peak described above. Here, the 3D Kitaev systems show relatively sharp low temperature peaks, and the sizes, shapes and positions in temperature space of these

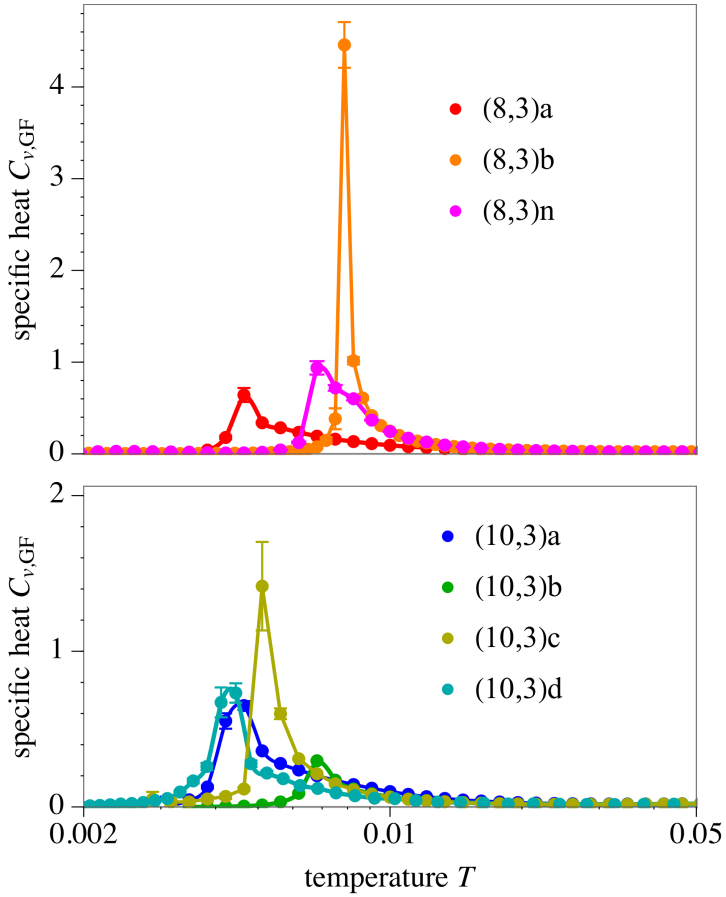

Figure 4.5: Specific heat $C_{v,\mathrm{GF}}$ in the low-temperature region [214]. The low-temperature peak indicates a thermal phase transition, caused by the ordering of the $\mathbb{Z}_2$ gauge field. Its position in temperature space is lattice-specific and correlated with the size of vison gap Δ (see Fig. 4.7). Data shown is for the linear system size $L = 7$, except for (8,3)n and (10,3)d (here, $L = 5$).

peaks strongly differ for distinct lattice geometries. The sharpest low-temperature peak is found for (8,3)b and has the highest position in temperature space. In contrast, (10,3)a has the broadest peak with the lowest position in temperature space. A comparison of $C_{v,\mathrm{GF}}(T)$ with the results for $\overline{W_p}$ (Fig. 4.1, 5.4) shows that the peak positions T'' coincide with the ordering of the $\mathbb{Z}_2$ fluxes. This confirms that the low-temperature peak indicates a gauge ordering transition, which, for different lattice systems, happens at different temperatures. Regarding a specific lattice geometry, the precise location of the peak and the ordering of fluxes is further altered by the choice of boundary conditions (Fig. C.7).

A close inspection of the finite-size behaviour of $C_{v,\mathrm{GF}}(T)$ shows that the low-temperature peak diverges for increased system sizes (Fig. 5.4). For some systems, this diverging behavior is concealed by finite-size effects, which are shown and

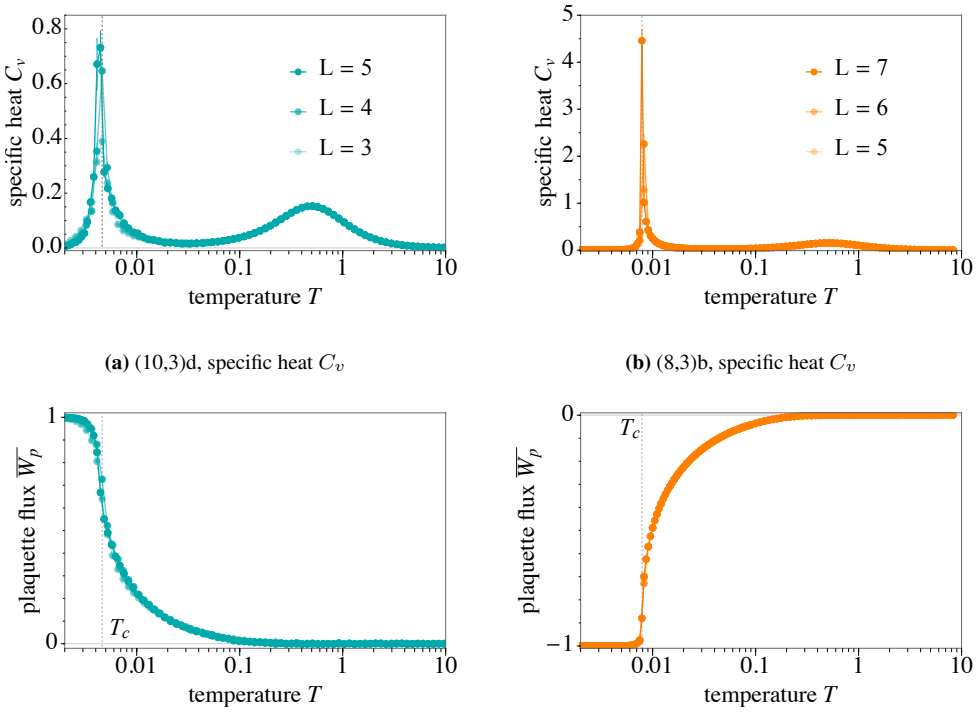

(a) (10,3)d, specific heat C_v

(b) (8,3)b, specific heat C_v

(c) (10,3)d, plaquette flux $\overline{W}_p$

(d) (8,3)b, plaquette flux $\overline{W}_p$

Figure 4.6: Finite-size scaling of the specific heat C_v and the average plaquette flux W_p. While the high-temperature peak of the specfic heat (a,b) is unchanged for increased system sizes, the low-temperature peak diverges in the thermodynamic limit. This is a clear signature of a thermal phase transition, which is associated with the ordering of $\mathbb{Z}_2$ fluxes (c,d).

discussed in Appendix C. The divergence of the low-temperature peak is a clear indicator that the gauge ordering is, for all 3D Kitaev systems, associated with a thermal phase transition. In the following, we examine the physical mechanism within the gauge field that leads to this phase transition.

Phase transition mechanism

For the analysis of the low-temperature transition, we have used the specific heat peak positions T'' at different system sizes N to extrapolate the critical temperatures T_c for each lattice system. Concretely, we have regarded the peak position T'' as a function of the inverse system size $1/N$, and performed a linear fit to obtain T_c as the limit of the fit function for $1/N \to 0$ (Appendix C.6). For (10,3)a, (10,3)b, (8,3)c and (9,3)a, results on T_c have already been published in Refs. [44, 45]. We have used these literature results in the following analysis, and discuss the agreement of our results with the literature values in Appendix C.6.

Lattice	Vison gap Δ	Critical temperature T_c	T_c/Δ
(10,3)a	0.0299(13)	0.00405(9) [45]	0.135(7)
(10,3)b	0.0426(4)	0.00519(9) [44]	0.121(2)
(10,3)c	0.046(2)	0.0049(2)	0.107(6)
(10,3)d	0.030(2)	0.00462(1)	0.154(10)
(8,3)a	0.0197(13)	0.0044(8)	0.22(4)
(8,3)b	0.0532(3)	0.0079(3)	0.148(6)
(8,3)n	0.05397(10)	0.0071(3)	0.132(6)
(8,3)c*	0.0219(6)	0.0020(2) [143]	0.091(9)
(9,3)a*	0.034(1) [90]	0.00244(4) [90]	0.072(2)

Table 4.2: Overview of the vison gaps Δ and critical temperatures T_c for the elementary 3D Kitaev systems. Quantum Monte Carlo simulations show that the temperature at which the Kitaev systems undergo a thermal phase transition from a disordered to an ordered $\mathbb{Z}_2$ spin liquid is determined by the size of the vison gap (Fig. 4.7). For the lattices (8,3)c and (9,3)a, indicated by an asterisk, the physical mechanism underlying the low-temperature phase transition is different from the rest due to special characteristics of the gauge field in these systems. Literature values are indicated by references. For the calculation of the vison gaps Δ, we use the raw data from Ref. [36] (except for (8,3)c and (10,3)d), rescale and refit it. Details on the calculations of Δ and T_c are given in Appendices C.5 and C.6.

We compare the critical temperature estimate T_c with the vison gap Δ for each system. The vison gap is the energy difference between the ground state flux configuration of the Kitaev system and the configuration with the smallest possible flux excitation, which is generated by carefully picking the right $\mathbb{Z}_2$ gauge variable u_{ij} and flipping it. The energy difference is calculated by exact diagonalization of the Majorana Hamiltonian in the respective gauge sectors. Results for the vison gaps have been published in Ref. [36]. Since the ground state flux sectors in these calculations are verified by our QMC results, we have used the raw data for all lattices except (8,3)c and (10,3)d from Ref. [36], rescaled it to the coupling strength $J = 1/3$, and refitted it, in order to improve the estimates on the error of Δ (Appendix C.5).

The results for the critical temperatures T_c and the vison gaps Δ are given in Tab. 4.2, and plotted in Fig. 4.7. We see that the critical temperature T_c lies within the range $T = 0.004 - 0.008$ for all systems except (8,3)c and (9,3)a. Above all, it is clearly correlated with the vison gap Δ. This is suggested by a linear (least-squares) fit of the data, which gives an approximately vanishing y-intersect $T = 0.0000(13)$, i.e., a vanishing critical temperature for $\Delta \to 0$. For all data points except (9,3)a, the error bars at least overlap with the statistical error of the fit.

The linear correlation between T_c and Δ confirms the understanding of the phase transition mechanism that is discussed in Refs. [44, 81, 97]. The phase transition is a continuous, inverted Ising transition which generically occurs in lattice

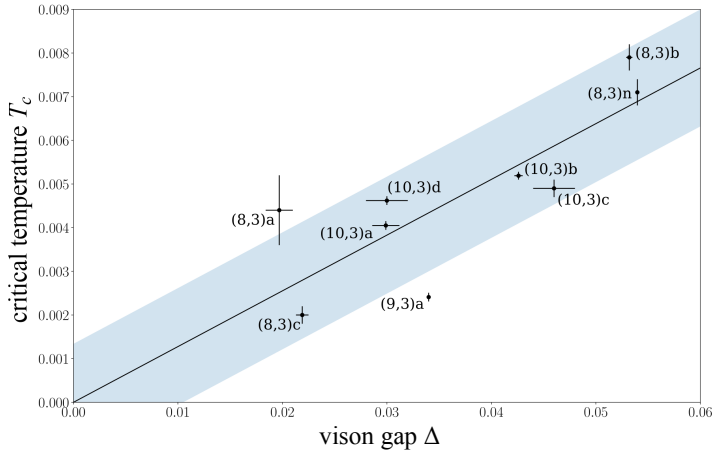

Figure 4.7: Critical temperature T_c and vison gap Δ [214]. Both quantities are clearly correlated, indicated by the black linear fit line. The shaded area indicates the error of the y-intersect of the least-squares fit. The values of T_c are extrapolated from the positions of the low-temperature peaks in the specific heat C_v. At this phase transition temperature, the loop-like vison excitations of the 3D Kitaev systems proliferate and become system-spanning, line-like objects. The values for Δ and T_c are given in Tab. 4.2. Details on the calculations of Δ and T_c are given in Appendices C.5, C.6.

$\mathbb{Z}_2$ gauge theories [50]. It cannot be described by spontaneous symmetry breaking in terms of a local order parameter, and, in this sense, deviates from the conventional Ginzburg-Landau paradigm. The underlying geometric reason for this is the linear dependence of the loop operators W_p. An excitation from the ordered $\mathbb{Z}_2$ ground state flux configuration is, as we have seen, created by flipping the $\mathbb{Z}_2$ gauge degree of freedom u_{jk} on a particular bond $\langle j, k\rangle$. In three dimensions, this generates flux excitations on all the adjacent plaquettes of the bond, which corresponds to the creation of a loop-like quasi-particle, the *vison* (Fig. 2.9). By heating the system up, more and more vison excitations are generated by thermal fluctuations of the $\mathbb{Z}_2$ gauge field, and some neighbouring visons merge with one another to form larger loops. The thermal phase transition separates the low-temperature regime, where the visons are still small objects, from the high-temperature phase that is characterized by the proliferation of system-spanning, *macroscopic* loops, which form a confining potential for the fermions (Fig. 4.8). Thus, it constitutes a *deconfinement-confinement* transition in the sense of lattice $\mathbb{Z}_2$ gauge theory, which separates two topologically distinct regimes (Sec. 1.1.2). If the plaquette fluxes ± 1 are considered as Ising spins on the dual lattice, the low-temperature and high-temperature phase of this system are reversed with respect to the conventional 3D Ising model. In this picture, the visons can also be understood as domain walls.

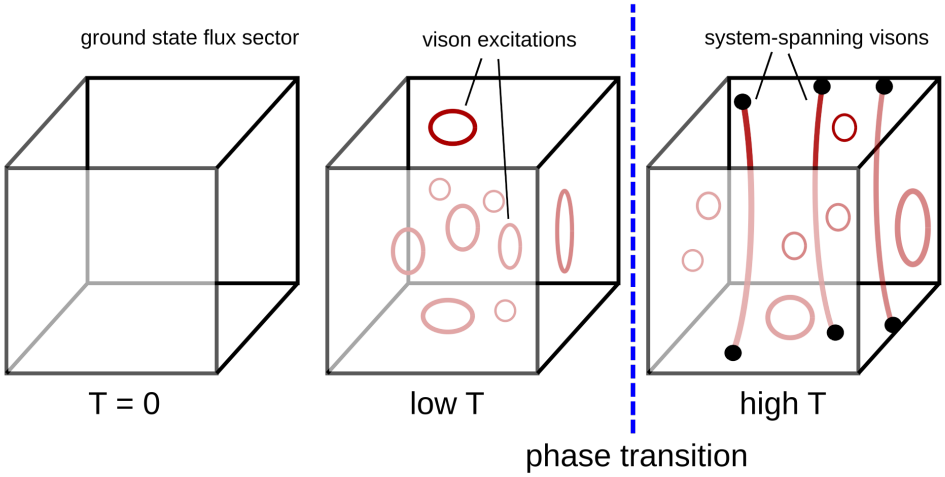

Figure 4.8: Low-temperature phase transition in 3D Kitaev systems [43, 44, 81]. Unlike in 2D systems, here, the loop operators W_p are linearly dependent. Exciting the $\mathbb{Z}_2$ gauge variable on a lattice bond amounts to creating a loop-like vison excitation that perpetrates all adjacent plaquettes. The phase transition is produced by such loop-like vison excitations being converted into system spanning, line-like objects. This constitutes an inverted Ising gauge transition, which separates the deconfined and confined phase in lattice $\mathbb{Z}_2$ gauge theory.

In Ref. [44], the existence of system-spanning visons above T_c is verified by measuring the Wilson loop W_c – the equivalent of W_p along the edge of an open boundary. The thermal average of this quantity is shown to sharply drop from $\overline{W_c} = 1$ to $\overline{W_c} = 0$ at T_c, and therefore, W_c serves as a non-local equivalent to an order parameter. This underlines that the phase transition cannot be understood as being caused by spontaneous breaking of $\mathbb{Z}_2$ symmetry by the variables W_p.

For systems with periodic boundary conditions, we cannot define a Wilson loop $\overline{W_c}$ along some edge of the system. However, we can probe the described mechanism also in an indirect way, namely by understanding how the magnitude of the critical temperature T_c is determined. The energy that is required for the creation of macroscopic vison excitations is expected to be proportional to their length L and a (temperature-dependent) loop tension (energy per length) τ, which is considered to be a function of the vison gap Δ. In the thermodynamic limit $L \to \infty$, the energy of the extended loops diverges, but the free energy of the system is lowered by the large entropy they are accompanied with. This mechanism renormalizes the *effective loop tension* (free energy per length) $\tilde{\tau}$ of macroscopic loops to lower, and finally, negative values at the critical temperature T_c [81], which results in their proliferation. In this picture, T_c is expected to show a dependance on the vison gap Δ through the loop tension. In this sense, the (linear) correlation between T_c and Δ, which we extracted from the numerical results,

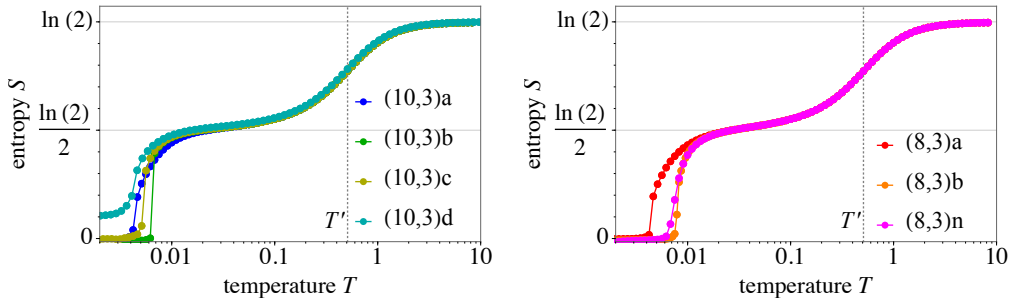

(a) (10,3)x lattices

(b) (8,3)x lattices

Figure 4.9: Entropy S per site [214]. The entropy in the paramagnetic (high-temperature) region is $S = \ln(2)$, indicating two possible states per spin. At the thermal crossover, $T' = 0.51(5)$ (dotted line), the system releases half of its entropy due to the fractionalization of the spins into (itinerant) Majorana fermions and a (static) $\mathbb{Z}_2$ gauge field. The latter remains disordered in this intermediate region. It is at the thermal phase transition at $T_c \sim 0.05$ that the system releases its remaining entropy, and the $\mathbb{Z}_2$ gauge field freezes into an ordered configuration, indicated by a sharp drop. For (10,3)d, open boundary conditions in two spatial directions cause a residual entropy for $T \to 0$, since $\mathbb{Z}_2$ gauge degrees of freedom on the edge bonds may fluctuate without a cost in energy. The residual entropy approaches 0 when the system size is increased. Data shown is for the linear system size $L = 7$, except for (8,3)n and (10,3)d (here, $L = 5$). Error bars are smaller than the symbol sizes.

corroborates the theoretical model. Specifically, the linear fit indicates that for $\Delta \to 0$, also T_c vanishes.

For most systems, the ratio T_c/Δ is $\sim 0.1 - 0.14$ (Tab. 4.1). This ratio is considerably larger for (8,3)a (~ 0.22), where also the error estimate on the critical temperature T_c is particularly large, and possibly, an improved extrapolation of T_c for numerically so far inaccessible system sizes may produce a slightly lower estimate for T_c. For (8,3)c and (9,3)a, on the other hand, T_c/Δ is smaller than 0.1. This can be explained with the different nature of the thermal phase transition in these systems. In (8,3)c, the gauge field is geometrically frustrated, which leads to a suppression of the gauge-ordering transition down to a particularly low temperature scale $T_c = 0.0020(2)$. The phase transition in (9,3)a, on the other hand, has been shown to be first-order, and to comprise several physical effects at once: The described vison proliferation mechanism, along with spontaneous breaking of time-reversal symmetry, and the spontaneous breaking of a number of point-group symmetries of the lattice [90].

A summarized view on the thermal phases in 3D Kitaev systems can be obtained from looking at the entropy per site $S(T)$ of the Kitaev systems (Fig. 4.9). Our results on $S(T)$ confirm those from earlier QMC studies [44, 45]. In the paramagnetic phase of the Kitaev spin model, where the Majorana fermions and the

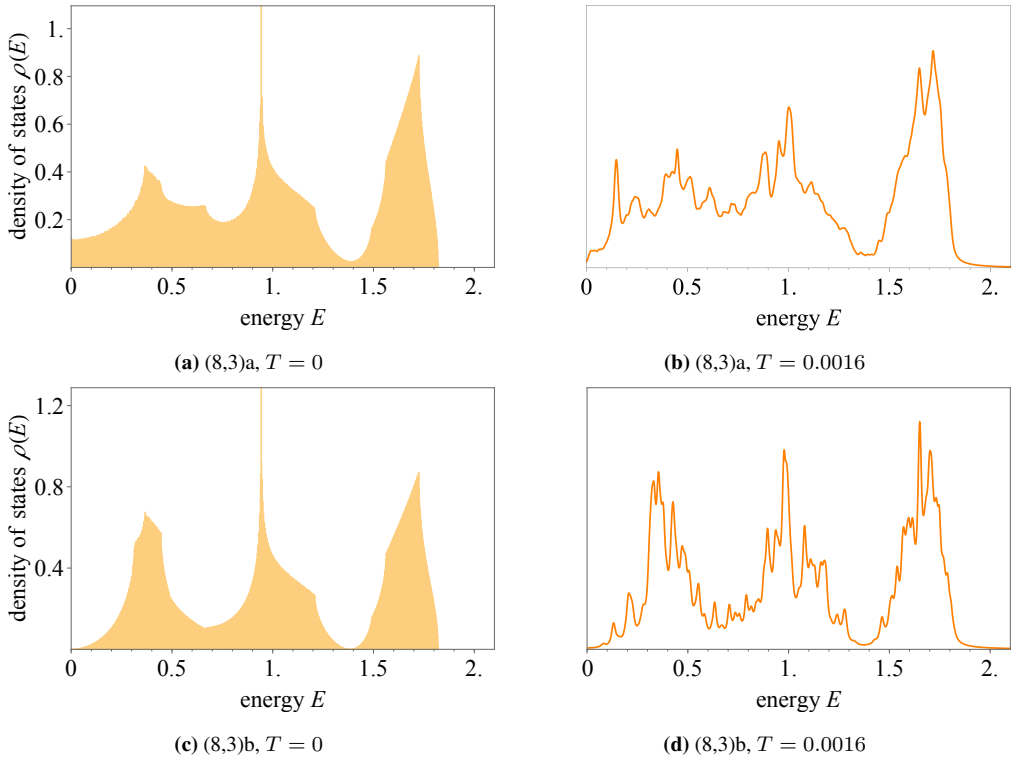

(a) (8,3)a, $T = 0$ **(b)** (8,3)a, $T = 0.0016$

(c) (8,3)b, $T = 0$ **(d)** (8,3)b, $T = 0.0016$

Figure 4.10: Density of states (DOS) for the lattice systems (8,3)a and (8,3)b [214]. The numerical DOS (b,d) is extracted from QMC simulations of systems with the linear size $L = 7$.

$\mathbb{Z}_2$ gauge field are still glued together as spin-$1/2$ degrees of freedom, the entropy is $S = \ln(2)$, which corresponds to two possible states per spin: $\sigma^z \in \{|\uparrow\rangle, |\downarrow\rangle\}$. At the thermal crossover, $T' = 0.51(5)$, the spin system releases half of its entropy due to the fractionalization of spins into parton degrees of freedom. Between this temperature scale and the thermal phase transition at $T_c \sim 0.004 - 0.008$, we encounter a plateau in the entropy with $S \sim \ln(2)/2$. Here, the system is in the relatively stable regime of itinerant Majorana fermions coupled to a disordered $\mathbb{Z}_2$ gauge field, and governed by fluctuations both of the gauge degrees of freedom and the Majorana fermions. At the thermal phase transition, the remaining entropy is released, and within this region, the system is entirely determined by the (small) fluctuations of the $\mathbb{Z}_2$ gauge field. Note that on (10,3)d, the entropy is not fully released for $T \to 0$ due to semi-open boundary conditions. Here, the $\mathbb{Z}_2$ gauge field on the surface remains fluctuating without a cost in energy. This is a finite-size effect that gets systematically smaller if we go over to large systems.

As we have shown in this section, our numerical results reproduce the thermal signatures known from earlier QMC simulations on Kitaev systems [44, 45], and verify that the selection of elementary, bipartite 3D Kitaev systems considered

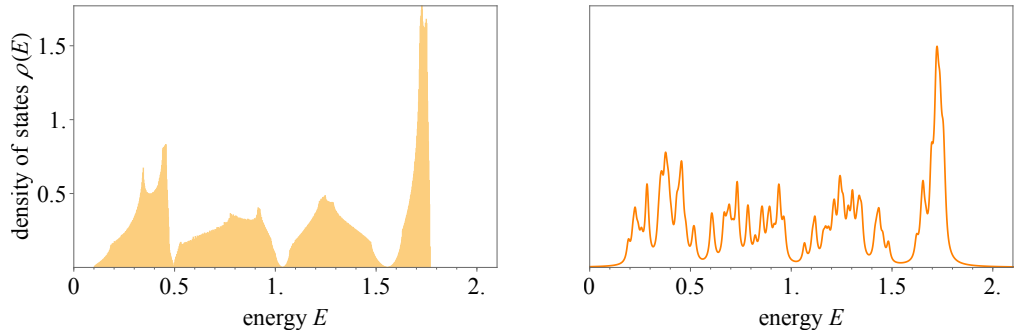

(a) (8,3)n, $T = 0$ **(b)** (8,3)n, $T = 0.0016$

Figure 4.11: Density of states (DOS) for the lattice system (8,3)n [214]. The numerical DOS (b) is extracted from the QMC simulations of a system with the linear size $L = 4$.

here shows the same thermodynamic behavior. The numerical results also confirm the theoretical understanding of the inverted Ising phase transition in these systems, which is a deconfinement-confinement transition characterized by the proliferation of macroscopic vison excitations. This mechanism manifests itself in a (linear) correlation between the critical temperature T_c and the vison gap Δ – quantities which are expected to be related through the loop tension τ.

4.3 Majorana density of states

In addition to the thermodynamic observables discussed so far, we show numerical results for the density of states (DOS) $\rho(E)$ of the Majorana fermions close to the ground state. In the QMC simulation, the DOS corresponds to the distribution of eigenvalues (single-particle energies) ϵ_λ of the Majorana Hamiltonian, which are calculated and saved after each Monte Carlo sweep. In order to get an approximate version of the ground state DOS from the Monte Carlo data, we regard the eigenvalue configurations at a temperature that is well below the thermal phase transition, but high enough for the Monte Carlo simulation not to be "frozen" into a single gauge field configuration. Typically, we show the density of states $\rho(E)$ for the systems at a temperature $T \sim 0.0016$ (Figs. 4.12 - 4.11).

In order to compare the numerical results, we also show analytical results for the DOS $\rho(E)$ at $T = 0$. For that, we have Fourier-transformed the Majorana Hamiltonians $\mathcal{H}(\{u_{jk}\})$, and fixed the $\mathbb{Z}_2$ gauge variables u_{jk}, in order to produce the ground state flux configuration. Then, we have diagonalized $\mathcal{H}(\{u_{jk}\})$ at the L_k^3 k-points of the discretized Brillouin zone. Typically, we have chosen $L_k = 400$ for this calculation.

The analytical and numerical results for the DOS are given in Figs. 4.12 -

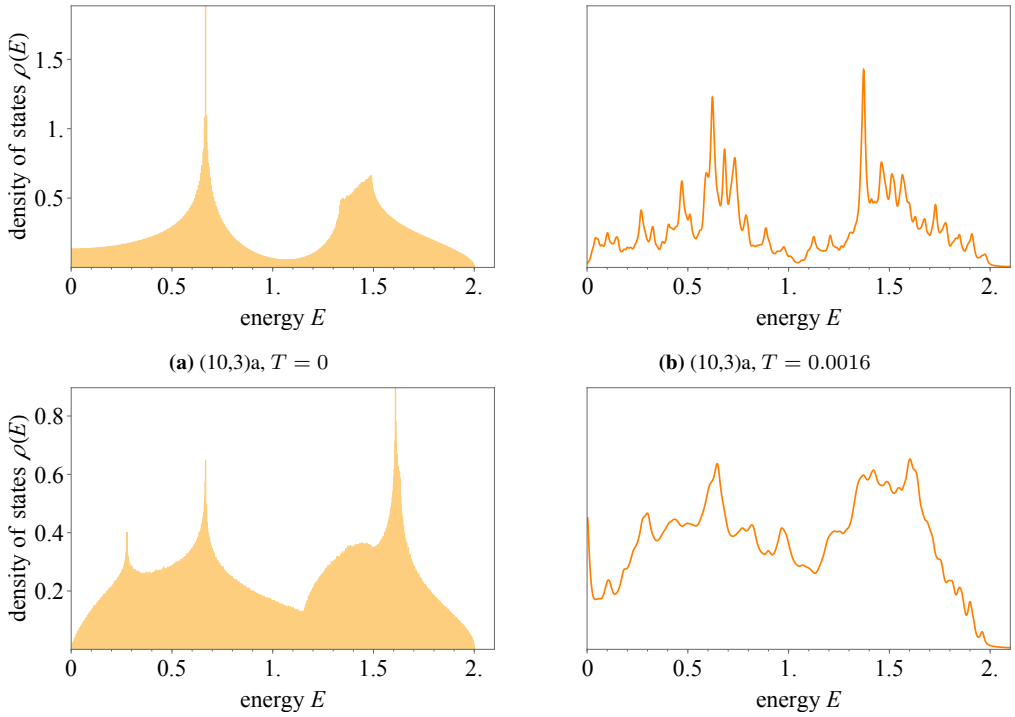

(a) (10,3)a, $T = 0$ **(b)** (10,3)a, $T = 0.0016$

(c) (10,3)d, $T = 0$ **(d)** (10,3)d, $T = 0.0041$

Figure 4.12: Density of states (DOS) for the lattice systems (10,3)a and (10,3)d [214]. The analytic ground state DOS (a,c) is calculated via exact diagonalization of the Majorana Hamiltonian in reciprocal space. The numerical DOS (b,d) is obtained from QMC simulations of finite real-space systems at the stated temperatures. The numerical data shown is for the linear system size $L = 7$ for (10,3)a, and $L = 5$ for (10,3)d.

4.11. We see that the numerical results qualitatively reproduce the features from the exact ground-state DOS. It is only in the region of lowest energies ($E \ll 0.25$) that the numerical results notably deviate from the exact DOS. This is expected due to finite-size and finite-temperature effects in the QMC simulation. For the lowest-lying energy levels, where the DOS is expected to be zero (unless it possesses a Fermi surface), there is a certain occupancy probability if the temperature is low, but finite. To further approach the analytic DOS at this scale would require simulation times that exceed those of our calculations by many times. Hence, at the current state of the QMC method, it is not possible to extract low-energy signatures coming from the Majoranas, as the numerically reachable temperature scale does not allow for an effective distinction between the different nodal structures.

The behaviour of the analytic DOS in the region around $E \sim 0$ is an indicator for the topological band structure of the corresponding Majorana (semi-)metal. (8,3)a and (10,3)a possess a Fermi surface, which manifests itself in a finite DOS also for the lowest-lying energy levels (Figs. 4.12 and 4.10). The majority of

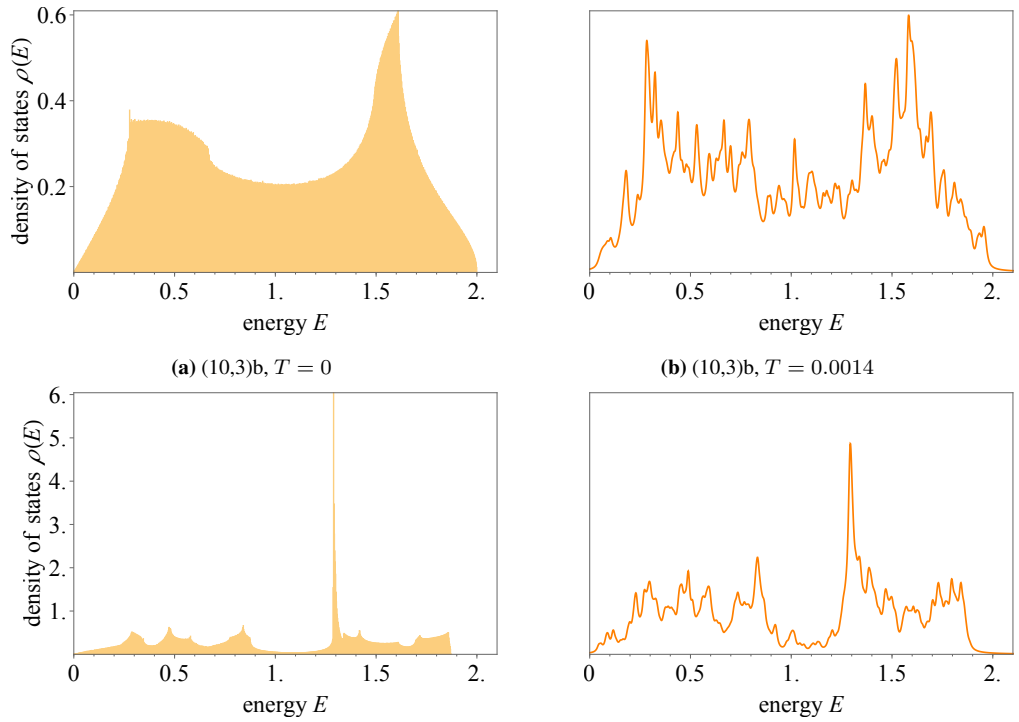

(a) (10,3)b, $T = 0$

(b) (10,3)b, $T = 0.0014$

(c) (10,3)c, $T = 0$

(d) (10,3)c, $T = 0.0016$

Figure 4.13: Density of states (DOS) for the lattice systems (10,3)b and (10,3)c [214]. The numerical DOS (b,d) is extracted from QMC simulations of systems with the linear size $L = 7$.

the other lattice systems host Majorana (semi-)metals with Weyl nodes or nodal lines as topological features. Here, the DOS always approaches zero for $E \to 0$, but the topological features reveal themselves in a characteristic shape of the low-energy DOS. Those systems that possess a nodal line in the ground state – (10,3)b and (10,3)c – show a linear increase of the DOS close to $E = 0$ (Fig. 4.13 a,c). This is reminiscent of the 2D Kitaev honeycomb model, where the band structure possesses Dirac cones in the ground state, and also an E-linear DOS for low energies [46]. For (8,3)b, a system that exhibits Weyl nodes, the increase of the low-E DOS is instead quadratic (Fig. 4.10 c). Finally, as a deviating example from the rest of the systems, the Kitaev system on (8,3)n possesses a finite gap also for the isotropic point (Fig. 4.11 a). The gap here is also visible in the numerical result.

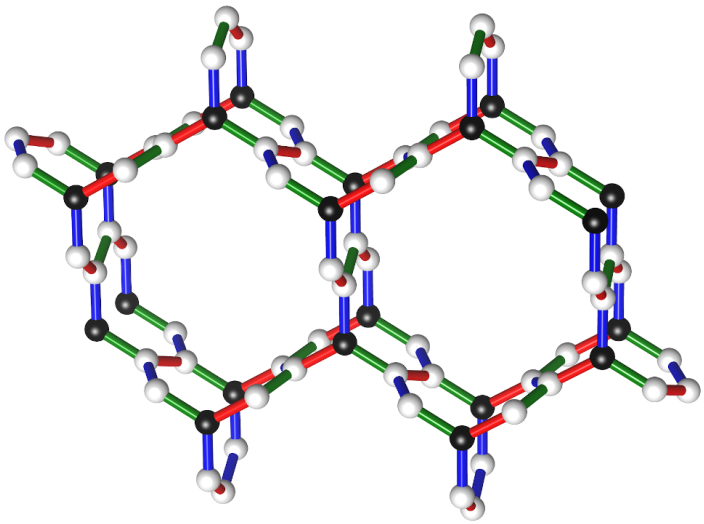

Figure 4.14: The (8,3)c lattice [143]. The elementary 8-plaquettes form a hexagonal lattice of plaquette triplets (indicated by the black sites). Their plaquette length lets expect a uniform ground state flux configuration of π-fluxes. However, each plaquette triplet forms the boundary of a closed volume. Therefore, the product of fluxes W_p is, for each triplet, constrained to $\prod_p W_p = 1$. In consequence, one plaquette in every triplet has to carry a 0-flux (see also Fig. 4.15).

4.4 Gauge frustration

So far, we have closely examined the prototypical thermodynamic behavior of bipartite 3D Kitaev systems, which is, in the low-temperature regime, characterized by a thermal phase transition associated with the ordering of the $\mathbb{Z}_2$ gauge field. With the gauge ordering, the Kitaev systems assume their $\mathbb{Z}_2$ ground state flux configurations, which, for all systems considered so far, is a unique, uniform configuration of either 0- or π plaquette fluxes, the choice for which entirely depends on the length of the elementary plaquettes. However, this rule comes with an exception: On the (8,3)c lattice, we encounter a remarkable deviation from this conventional thermal behavior of 3D Kitaev systems. Here, the emergence of a uniform ground state flux configuration is prevented – or *frustrated* – by an interplay between the elementary plaquette length $|p| = 8$, which favors a π-flux, and a volume constraint which explicitly forbids the π-flux to be assumed on all lattice plaquettes. The result is the emergence of a highly degenerate *constrained gauge manifold*. In this scenario, which we call *gauge frustration*, the gauge ordering transition is suppressed down to a temperature scale that is (almost) one order of magnitude lower than in the other Kitaev spin liquids. Finally, it is the interaction between the itinerant Majorana fermions and the $\mathbb{Z}_2$ gauge field which leads to a partial lift of the gauge degeneracy, and the selection of a non-trivial ground state flux order.

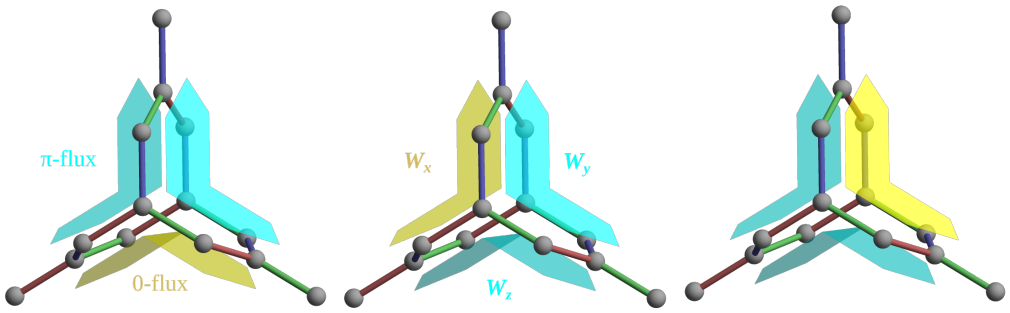

Figure 4.15: Gauge frustration on the (8,3)c Kitaev system [143]. The elementary plaquette length $|p| = 8$ asks for a π-flux ground state. However, three plaquettes form the boundary of a closed volume, which constrains the product of their loop operator eigenvalues to $\prod W_p = 1$. Hence, per plaquette triplet, there are three allowed flux states that minimize the energy. Two plaquettes carry a π-flux (cyan), while the third plaquette is forced to be flux-free (yellow).

In the following, we introduce the (8,3)c lattice and explain the geometric foundation of gauge frustration. Afterwards, we present how the occurrence of gauge frustration manifests itself in the physical observables. In particular, we introduce a *pseudospin*, a classical auxiliary variable that describes triplets of plaquette fluxes in the lattice, and whose correlator serves to display the degree of frustration in different (an)isotropy and temperature regimes of the (8,3)c Kitaev system. A close look is given to the ground state of the system, and how it emerges as a consequence of the interplay between the $\mathbb{Z}_2$ gauge field and the itinerant Majorana fermions. In the end, we discuss the phase diagram of the gauge-frustrated Kitaev spin liquid in its different (an)isotropy limits.

4.4.1 Volume constraint and gauge frustration

Plaquette triplets

In the (8,3)c lattice, each unit cell possesses 8 sites and four linearly independent loop operators of length 8 (Fig. 4.14). Therefore, according to Lieb's theorem, one would expect the Kitaev system on this lattice to ask for a ground state flux sector with a uniform configuration of π-fluxes. In particular, such a uniform π-flux configuration on all the 8-plaquettes would preserve the point-group symmetries of the lattice – threefold rotation and inversion symmetry – as has been laid out in Ref. [36]. However, it is exactly this uniform π-flux configuration that turns out to be geometrically forbidden. The reason for this is the volume constraint on plaquette fluxes that is in force for lattice systems in three spatial dimensions. The operators W_p on lattice plaquettes which form the boundary of a closed volume V are linearly dependent. The product of their eigenvalues $\prod_{p\in V} W_p$ is constrained

to be 1. In a physical sense, this constraint corresponds to a divergence-free condition on the vison excitations that are formed by the fluxes. In three spatial dimensions, the visons are not point-like, but loop-like, and whenever a vison loop enters a volume through one plaquette, it has to leave through another. In other words. Magnetic monopoles are forbidden in the system.

How does the volume constraint in the (8,3)c lattice now affect the formation of the ground state flux sector? As Fig. 4.14 shows, the elementary 8-plaquettes in the (8,3)c lattice are arranged as a hexagonal lattice of independent triplets t (which is indicated by the lattice sites marked in black). Here, three plaquettes form the boundary of a closed volume. In consequence, it is impossible that all three plaquettes carry a π-flux, since this would lead to a product $\prod_{p\in t} W_p = -1$. Hence, at least one plaquette per triplet must be flux-free, which is dictated by the volume constraint. The three corresponding flux triplet states are visualized in Fig. 4.15. Of course, these are not the only states which are, in principal, allowed by the volume constraint. In addition, there is the triplet with all plaquettes carrying a 0-flux. Here however, we treat the question which configuration gives minimal energy, and for that, it is expected that the triplet assumes the maximum number of π-fluxes which is allowed by the constraint. This maximum is two. Hence, instead of a single ground state flux configuration, the $\mathbb{Z}_2$ gauge field of the system is expected to enter a highly degenerate *constrained gauge manifold* at low temperatures, where each plaquette triplet independently assumes one of the three states with two π-fluxes and one 0-flux. The spin liquid state of the (8,3)c Kitaev model is therefore "doubly frustrated". Apart from the exchange frustration of spins, there is an additional geometric frustration of the $\mathbb{Z}_2$ gauge field. We call this phenomenon *gauge frustration*.

Degeneracy levels in different coupling regimes

A closer inspection of the plaquettes within a triplet further shows that the energy of the triplet states depends on the (an)isotropy of the bond couplings. This can be seen if the number of z-bonds per plaquette is considered. While in each triplet, the two plaquettes with vertical orientation possess three (blue) z-bonds, the plaquette with horizontal orientation always possesses two. Keeping J_x and J_y fixed, a tuning of J_z therefore determines the level of degeneracy, with a strong J_z-coupling "attracting" and a weak J_z-coupling "repulsing" the π-fluxes. We consider the degeneracy as a function of N_t, the number plaquette triplets in the lattice. N_t is related to the number of lattice sites N by $N_t = N/4$ [1]. We encounter the following degeneracy regimes:

[1] There are $\frac{3}{2}$ bonds per site in a Kitaev system, hence, in total, $\frac{3N}{4}$ plaquettes in the (8,3)c lattice. Since 3 plaquettes form a triplet, $N_t = \frac{N}{4}$

- For isotropic coupling parameters $J_z = J_x = J_y$, all three plaquette triplet states are degenerate, and there are 3^{N_t} possible flux states in the system.
- For $J_z < J_x, J_y$, one of the two vertical plaquettes picks the 0-flux state (Fig. 4.15 b,c). Hence, there is a reduced degeneracy, with 2^{N_t} possible flux states in total.
- For $J_z > J_x, J_y$, the 0-flux in the triplet is only assumed by the horizontal plaquettes, which possess fewer z-bonds (Fig. 4.15a). With that, the degeneracy of the gauge field is lifted, and a unique ground state flux configuration is restored.

In our QMC simulations, we have used the convention that the J_γ-couplings add up to 1, and $J_x = J_y$. Therefore, we always indicate the coupling (an)isotropy by the J_z-value, and the other couplings follow as $J_x = J_y = (1 - J_z)/2$. In the following, we see how the gauge frustration for different (an)isotropy limits of the Kitaev system can be measured in terms of physical observables, and how it affects the thermodynamic behavior of the system. We have performed the simulations with the QMC-KPM method. To reduce finite-size effects, we have chosen the smallest size of our systems as $4 \cdot 4 \cdot 6$ unit cells (768 sites), and the largest size as 6^3 unit cells (1728 sites). For the exploration of the lowest-temperature regime, below the region where the QMC simulations converge in a reasonable computation time, we have extrapolated our results with the multiple histogram reweighting method [149, 150].

4.4.2 Signatures of gauge frustration

Average plaquette flux

The easiest way to probe the existence of the gauge-frustrated low-temperature regime in the (8,3)c Kitaev system is by measuring the plaquette flux. Obviously, if the system does not assume a uniform flux configuration, the average plaquette flux does not converge to its usual ground state values $\overline{W_p} = \pm 1$ at low temperatures. Instead, if two plaquettes in each triplet acquire a π-flux ($W_p = -1$), and one plaquette remains flux-free ($W_p = 1$), the expected average plaquette flux for $T \to 0$ is $\overline{W_p} = (-2 + 1)/3 = -1/3$. This is confirmed by the QMC results (Fig. 4.16 a).

Interestingly, this result means that Lieb's theorem still plays its role also in this more exotic lattice geometry, although neither of the plaquettes fulfills the mirror symmetry condition for the theorem. The 8-plaquettes tend to adopt the π-flux that corresponds to their length $|p|$, but, due to the volume constraint, only two out of three may do so. This implies that the plaquette length is a stronger

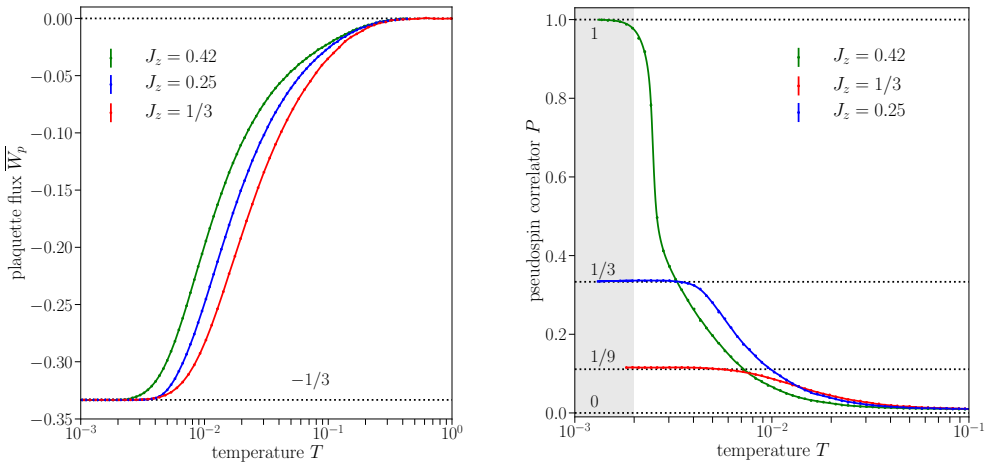

(a) plaquette flux $\overline{W_p}$ **(b)** pseudospin correlator P

Figure 4.16: Average plaquette flux $\overline{W_p}$ and pseudospin correlator P as functions of temperature [143]. In Fig. (a), we see that the average plaquette flux converges to a ground state value $\overline{W_p} = (-2+1)/3 = -1/3$ for all (an)isotropy limits, which corresponds to one plaquette in each triplet assuming a 0-flux. With the pseudospin correlator P in Fig. (b), it is possible to resolve the different levels of degeneracy for each (an)isotropy parameter J_z (see the text). Data shown is for the system size $4 \times 4 \times 6$ ($N = 768$). The shaded region in Fig. (b) indicates the temperature range where we obtain the numerical results from multiple histogram reweighting.

criterium for the choice of the energy-minimizing flux than symmetry considerations. Here, the system energetically prefers to adopt a plaquette flux configuration that breaks the lattice symmetries (threefold rotation and inversion symmetry). Each plaquette triplet assigns the 0-flux independently to one of its constituents. The only allowed flux configuration that preserves all symmetries would be a uniform configuration of 0-fluxes, as has been discussed in Ref. [36]. This configuration, however, has a higher energy.

Pseudospin correlator

In Fig. 4.16 a, we see that the fluxes average to a ground state value $W_p = -1/3$, regardless of the (an)isotropy parameter J_z. The degree of degeneracy is, however, dependent on the ratio between the J_γ-couplings. All plaquette triplets find themselves in a two-π-one-0 flux state, but it is the relative strength of the J_z-coupling that decides which one of the three states of this kind is chosen. This selection between the triplet states is something we cannot see from looking at $\overline{W_p}$, and it is desirable to have another observable at hand which enables us to resolve the selection.

Such an observable is introduced by regarding the plaquette triplets as classical, three-dimensional *pseudospins* $\mathbf{W}$, whose components are given by the flux

operator eigenvalues W_α of the plaquettes in a triplet (for the assignment of the labels $\alpha \in \{x, y, z\}$, see Fig. 4.15),

$$\mathbf{W} = \begin{pmatrix} W_x \\ W_y \\ W_z \end{pmatrix} \overset{\text{(a)}}{=} \begin{pmatrix} -1 \\ -1 \\ 1 \end{pmatrix} \overset{\text{(b)}}{=} \begin{pmatrix} 1 \\ -1 \\ -1 \end{pmatrix} \overset{\text{(c)}}{=} \begin{pmatrix} -1 \\ 1 \\ -1 \end{pmatrix}. \tag{4.3}$$

We can measure the two-point correlator of the pseudospins,

$$P = \frac{4}{3N} \sum_j \langle \mathbf{W_0} \mathbf{W_j} \rangle, \tag{4.4}$$

where the normalization constant $4/3N$ corresponds to the number of plaquette triples $N/4$ and the magnitude of the pseudospin $||W||^2 = 3$. The pseudospin correlator serves to determine the degeneracy of the flux manifolds, which correspond to a certain value of J_z (Appendix C.8.1):

- For isotropic coupling constants $J_z = J_x = J_y$ and "full" gauge degeneracy, all pseudospin states $\mathbf{W}$ given in Eq. (4.3) are expected to be equally distributed in the system. Therefore, the correlator P assumes the characteristic value $P = 1/9$.
- For $J_z < J_x, J_y$, the gauge degeneracy is partially lifted. Here, only the states (b) and (c) in Eq. (4.3) appear in the system, and the correlator is expected to be $P = 1/3$.
- For $J_z > J_x, J_y$, the state (a) in Eq. (4.3) is expected for all plaquette triplets (pseudospins), and the resulting pseudospin correlator is $P = 1$.
- At high temperatures, the system finds itself outside the constrained gauge manifold, and, in addition to the three pseudospin states (a), (b), (c) in Eq. (4.3), the state $\mathbf{W} = (1, 1, 1)^T$ can be adopted, which also fulfills the volume constraint. With the four pseudospin states expected to be equally distributed in the system, the pseudospin correlator goes down to $P = 0$.

The Monte Carlo results for the pseudospin correlator P confirm these expectation values (Fig. 4.16 b).

4.4.3 Thermodynamics

With the set of observables adapted to the physical specifics of the (8,3)c Kitaev system, we have studied its signatures for all temperature scales. The numerical results are presented for the system with isotropic coupling $J_z = 1/3$ (Fig. 4.17).

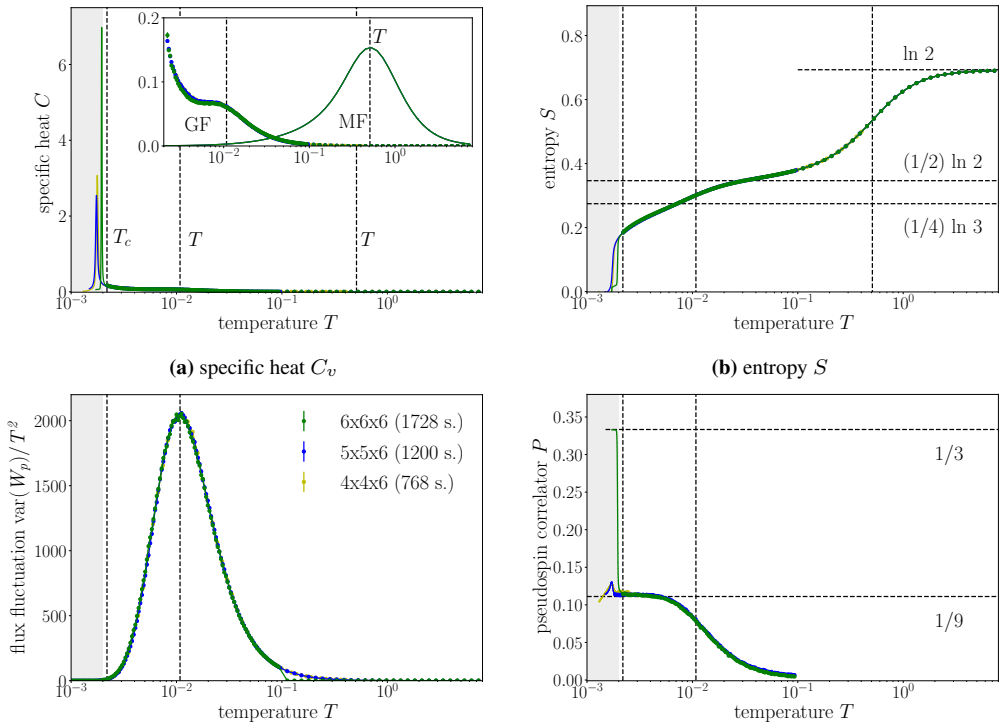

(a) specific heat C_v

(b) entropy S

(c) flux fluctuation $\mathrm{var}(W_p)/T^2$

(d) pseudospin correlator P

Figure 4.17: Thermodynamics of the (8,3)c Kitaev system [143]. Instead of a peak at $T'' \sim 10^{-2}$, the specific heat C_v (a) shows a broad shoulder, indicating a thermal crossover, while the phase transition occurs at a lower temperature T_c. At T'', the entropy (b) assumes the characteristic value $S = \ln(4)/3$, corresponding to 3 possible flux configurations per plaquette triplet. The transition into the degenerate flux manifold is further supported by the peak in the flux fluctuation $\mathrm{var}(W_p)/T^2$ (c), and the pseudospin correlator P (d) assuming its ground state value $P = 1/9$. The shaded region indicates the temperature range where we obtained the numerical results from multiple histogram reweighting.

Here, the grey shaded region indicates the low-temperature scale which has been extrapolated with multiple histogram reweighting.

In Fig. 4.17, the dashed lines mark three relevant temperature scales. The temperature $T' = 0.51(5)$ is again associated with the fractionalization of spins. At $T'' \sim 0.01$, the system enters the constrained gauge manifold, and $T_c = 0.0020(2)$ is the critical temperature (which is extrapolated from the positions of the low-T specific heat peaks). Interestingly, T'' corresponds to the temperature scale, where, in other 3D Kitaev systems, we usually encounter the critical temperature T_c, which is associated with the gauge-ordering transition. Here, the ordering transition is suppressed by the gauge frustration. The characteristic signature for this suppression is a shoulder-like structure of the specific heat $C_v(T)$ at T'' (a), which does not change its shape nor position for increasing system sizes. This in-

dicates that the process of the system entering the constrained gauge manifold is associated with a thermal crossover, not a phase transition. The plaquette triplets assume the two-π-one-0 flux state locally and independently of each other. Again, we have regarded the $\mathbb{Z}_2$ gauge field and itinerant Majorana contributions to the specific heat separately, which is shown in the inset of Fig. 4.17 a. Here, we can see that the thermal crossover at $T'' \sim 10^{-2}$ is a feature which is entirely determined by the fluctuations of the $\mathbb{Z}_2$ gauge field, which is expected and corroborates the picture of the system entering the gauge-frustrated manifold. In consequence, the quantifier of the flux fluctuations, $(\overline{W_p^2} - \overline{W_p}^2)/T^2$ (Fig. 4.17 c) has its peak at T''.

Above T'', the entropy per site S (Fig. 4.17 b) shows the typical behavior known from other Kitaev spin liquids. Starting from the paramagnetic phase, the entropy is $S = \ln(2)$, which corresponds to the two possible states of (unfractionalized) spins. Decreasing the temperature, the system releases half its entropy at the fractionalization crossover at $T' = 0.51(5)$. In the temperature region below the gauge crossover at T'', the entropy assumes a value $S = \ln(3)/4$, which is expected for the constrained gauge manifold, where all plaquette triplet states are energetically degenerate, and, hence, the number of possible flux configurations is $3^{N_t} = 3^{N/4}$. Moreover, the pseudospin correlator P (d) assumes its characteristic ground state value $P = 1/9$ right below T''.

Hence, all numerical results consistently confirm the existence of the constrained gauge manifold. However, the degeneracy of flux configurations is not preserved down to $T \to 0$. This follows most clearly from the fact that, below the crossover temperature T'', the entropy S does not reach a plateau, but keeps going down, and, at T_c, suddenly drops to zero. The specific heat C_v, on the other hand, is not zero below T'', but continues rising for decreasing temperatures, until it shows a very sharp peak at T_c. This peak, which is only visible in the reweighted temperature region, has different shapes and positions for different system sizes, a fact which suggests that it indicates the thermal phase transition that is suppressed at the "usual" temperature scale $T \sim 10^{-2}$. The occurrence of this phase transition can be explained by an additional selection mechanism between the flux configurations within the constrained gauge manifold. In this picture, the plaquette triplet states keep the two-π-one-0 flux states that are dictated by the interplay of their plaquette length and the volume constraint, but a certain order arises among these states.

4.4.4 Ground state selection

Since the extrapolated low-temperature results for the pseudospin correlator P at $T \leq 0.002$ do not give a clear picture on the selection mechanism within the

constrained gauge manifold, we have resorted to analyzing snapshots of the flux configurations in the QMC simulations to clarify the nature of the ground state flux sector. Here, we see that those configurations are selected where the 0-fluxes in the plaquette triplets form a zig-zag order along the columns of hexagonal sites (Appendix C.8.2). This zigzag order is depicted for the limits of weak and strong J_z-coupling in Fig. 4.18 (d-f).

For the geometric reasons outlined above, the orientation of the columnar zigzag order is dependent on the anisotropy parameter J_z:

- For the isotropic coupling limit $J_z = 1/3$, there are three possible orientations of the zigzag order per column, since, here, it does not matter which plaquette in a triplet takes the 0-flux.
- For $J_z < J_x, J_y$, the 0-fluxes are only located on the vertical plaquettes (Fig. 4.18 d). Hence, there are two possible zigzag order states per column (which are simply shifted with respect to each other by one plaquette).
- In the strong-J_z-limit, the 0-flux is bound to the horizontal plaquettes (Fig. 4.18 f). In consequence, for $J_z \gg J_x, J_y$, the unique gauge configuration with all 0-fluxes located on the horizontal plaquettes prevails due to geometric selection. However, there is an intermediate regime (which we find to be in the region $1/3 \leq J_z \leq 0.4$), where each column of hexagonal sites chooses a state where the 0-fluxes on the horizontal plaquettes alternate with 0-fluxes on either of the two vertical plaquettes (Fig. 4.18 e).

What is the nature of columnar order and how does it emerge in the (8,3)c Kitaev spin liquid? On a general level, we can explain the selection of the zigzag gauge order by an interplay between the itinerant Majorana fermions and the $\mathbb{Z}_2$ gauge field. From the perspective of the Majorana fermions, the $\mathbb{Z}_2$ gauge field forms a complex scattering potential, which constitutes the background for the system of hopping Majoranas. Intuitively, it is plausible that the emergence of some ordered configuration in this potential is energetically favorable for the Majorana system. This understanding on the formation of the gauge field ground state can be further deepened by taking a look at the Majorana band structure. As we can see in Fig. 4.18 (a-c), the selection of the columnar zigzag order by the gauge field is accompanied by the Majorana fermions forming a semi-metal, where the band structure shows nodal lines as topological features for all (an)isotropy limits. For the different coupling parameters J_z, we see that the nodal lines only change with respect to their shape and their position in the Brillouin zone of the system. The bandstructures for all zigzag-ordered states and their respective J_z-couplings are documented in Appendix C.8.3. Both effects, the formation of the collective semi-metal state by the Majorana fermions, and the emergence of columnar zigzag

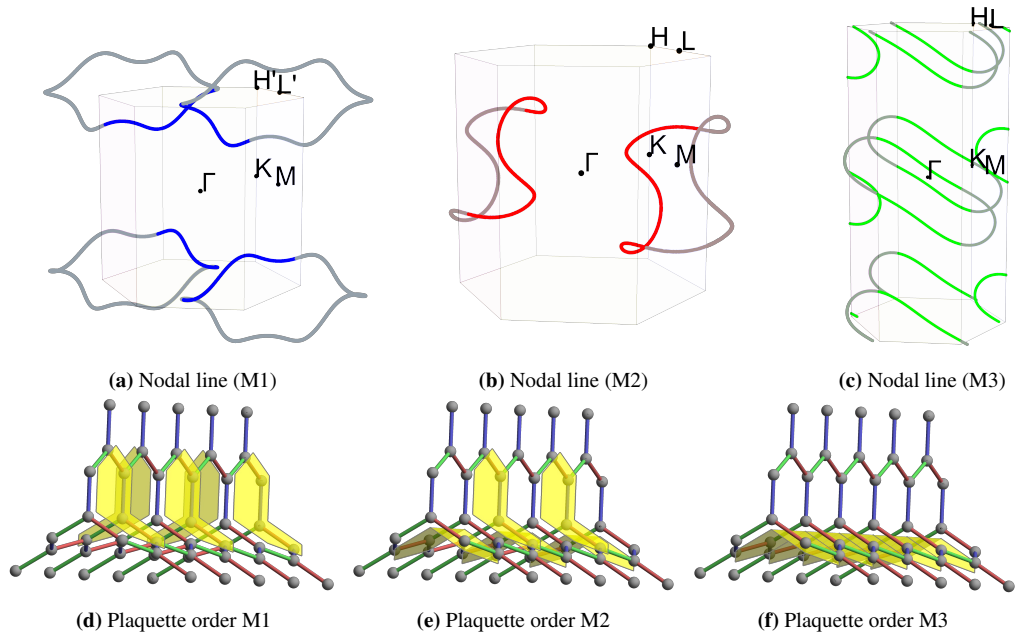

(a) Nodal line (M1) **(b)** Nodal line (M2) **(c)** Nodal line (M3)

(d) Plaquette order M1 **(e)** Plaquette order M2 **(f)** Plaquette order M3

Figure 4.18: Majorana semimetals and columnar gauge ordering [143]. In the top line (a,b,c), the nodal lines in the Majorana band structure are shown for varying coupling J_z. For each parameter, there is a corresponding ground state of the $\mathbb{Z}_2$ gauge field (d,e,f), which is characterized by a columnar zigzag order arising as the result of an interplay between the Majorana fermions and the gauge field (d,e), which is a quantum effect. Only for strong J_z, this effect is overpowered by the classical geometric selection of the horizontal plaquettes as carriers of the 0-fluxes (f).

order within the $\mathbb{Z}_2$ gauge field, can be understood as being two aspects of what is one quantum effect. The collective state of the Majorana fermions in the gauge-frustrated regime is similar to a thermal metal [216–218] (cf. Sec. 5.2.3). Here, the gauge degeneracy in the (8,3)c Kitaev system assumes the role which is usually played by thermal disorder. At lowest temperatures, the Majorana fermions pursue to form an energetically more favorable semimetallic state, which is free of disorder. But, in order to do so, they have to enforce a (partial) lifting of the macroscopic degeneracy in the $\mathbb{Z}_2$ gauge field, which is achieved by inducing the columnar zigzag gauge order.

Hence, the phenomenon of gauge frustration can be understood not only as a geometric curiosity in an exotic 3D lattice system, but, on a conceptual level, as an intermediate phenomenon between two paradigmatic kinds of spin liquids. $\mathbb{Z}_2$ spin liquids are characterized by gapped excitations in the gauge field and spinon degrees of freedom that, in the gapped gauge background, remain non-interacting. This renders the QSL state stable. In the Kitaev model, where the low-energy region is generically described by a $\mathbb{Z}_2$ spin liquid, this property is seen by fractionalized degrees of freedom that fully decouple, meaning that the

Majorana system can be independently regarded for each different configuration of the *static* $\mathbb{Z}_2$ gauge field.

The other paradigm is constituted by the $U(1)$ spin liquids. In the deconfined regime, the $U(1)$ gauge field possesses gapless (photon) excitations, which remain fluctuating at all temperature scales, and, therefore, mediate interactions between the spinons down to $T \to 0$. Therefore, $U(1)$ spin liquids are generically unstable. The stability of the spin liquid phase is further undermined by the instanton effect.

The gauge-frustrated $\mathbb{Z}_2$ spin liquid, on the other hand, exhibits interactions between the Majorana fermions and the $\mathbb{Z}_2$ gauge field which remain relevant in the quantum regime and determine the ground state order.

4.4.5 Phase Diagram

A thermal phase diagram for the (8,3)c Kitaev system in the J_z-T-plane summarizes the results that have been discussed in the last sections (Fig. 4.19). Here, the contour plot in the background shows the pseudospin correlator P. The green and white data points indicate different signatures for the transitions in the system. Starting at high temperatures, the green squares mark the temperatures at which the plaquette fluxes $\overline{W_p}$ are half-ordered, meaning their average value is $\overline{W_p} = -1/6$. Here, the system is still in the disordered $\mathbb{Z}_2$ spin liquid phase for all coupling parameters. The thermal crossover at which the systems enter the constrained gauge manifold is marked by two different observables: 1. The green circles, which indicate the position of the flux fluctuation peak $(\overline{W_p^2} - \overline{W_p}^2)/T^2$, and 2., the white circles, which show the temperature positions at which the pseudospin correlator assumes the value $P = 1/9$. As discussed earlier, the thermal phase transition that usually occurs at this temperature scale, is suppressed in the (8,3)c Kitaev system down to $T_c = 0.0020(2)$. Thus, it occurs within the constrained gauge manifold. Here, it is associated with the selection of the columnar zigzag gauge order by the interplay between the Majorana fermions and the $\mathbb{Z}_2$ gauge field in the parameter regime $0.15 \leq J_z \leq 0.4$. In the phase diagram, this is indicated by the solid white squares, which mark the positions of the low-temperature peaks in the specific heat C_v. As we have discussed in the last section, for $J_z \geq 0.4$, the mechanism of the thermal phase transition is different, which is indicated by the empty white squares. Here, it is not the interplay of Majoranas and gauge field, but classical geometric selection which determines the gauge ordering. In this parameter region, it is only the horizontal plaquettes in the plaquette triplets, which, due to the strong J_z-coupling, carry the 0-fluxes (Fig. 4.18 f). In the contour plot, this is indicated by the yellow region, where the pseudospin correlator is $P = 1$. Accordingly, we distinguish this *unique gauge configuration* regime from the *columnar gauge ordering* regime at lower J_z, where the quantum

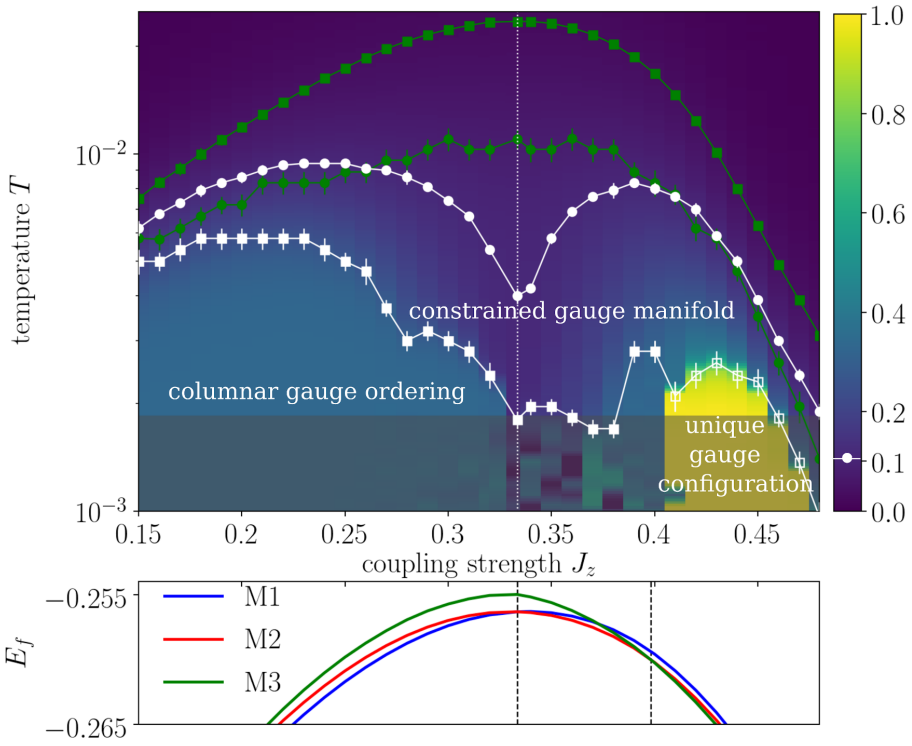

Figure 4.19: Finite-temperature phase diagram of the (8,3)c Kitaev spin liquid [143]. The contour plot shows the pseudospin correlator P, Eq. (4.4). The green squares mark the temperatures for which $\overline{W_p} = -1/6$. The green circles indicate the position of the flux fluctuation peak $\mathrm{var}(W_p)/T^2$, while the white circles mark where the pseudospin correlator is $P = 1/9$. The solid white squares indicate the low-T peaks in the specific heat C_v, which are signatures for the thermal phase transition that happens due to the quantum effect of columnar gauge ordering. The empty white squares indicate the phase transition caused by classical geometric selection at $J_z > 0.4$. Data shown is for the system size $4{\cdot}4{\cdot}6$ ($N = 768$). In the lower panel, we have shown the ground state energies of the different columnar states M1, M2, M3 (see the definition in Fig. 4.18).

effect prevails in the ground state selection. The columnar gauge ordering phase is further separated by the described, different selections of columnar states. At $J_z = 1/3$, each column can, individually, assume three different orientations (with our without horizontal plaquettes carrying 0-fluxes), while for $J_z < 1/3$, only configurations without horizontal plaquettes carrying 0-fluxes are selected. The latter fact is reflected by the value of the pseudospin correlator in this regime, which is, uniformly, $P = 1/3$ below the phase transition temperature T_c.

For further clarification of the selection mechanism within the constrained gauge manifold, we show the ground state energies of the different columnar states in the lower panel of Fig. 4.19). For $J_z < 1/3$, the columnar state M2 (red), which includes horizontal plaquettes, has a higher energy than M1 (blue).

Both columnar states are degenerate at $J_z = 1/3$, and for $1/3 \leq J_z \leq 0.4$, M2 gives the lowest energy. Here, the quantum effect still prevails, which favors the zigzag ordering of 0-fluxes. Finally, it is at $J_z > 0.4$ that the unique flux state M3 becomes the ground state of the (8,3)c Kitaev system by classical selection.

We conclude this section by briefly going back to the discussion of the correlation between critical temperatures T_c and the vison gap Δ (Fig. 4.7). There, we have seen that the (8,3)c Kitaev system has the lowest critical temperature of $T_c = 0.0020(2)$. This corresponds to a small vison gap $\Delta = 0.0219(6)$. These results reflect the singular nature of the phase transition in the (8,3)c system. On the one hand, the phase transition is still associated with gauge ordering. The critical temperature T_c indicates the selection of the columnar gauge-ordered states, and it is natural to think that the amount of energy needed to create visons has to reflect that. On the other hand, both the nature of the ground state gauge configuration and the way it is selected, are different from the conventional phase transition mechanism in other 3D spin liquids. First, there is the intermediate step of the system entering the constrained gauge manifold, whereas in the other systems, the ground state gauge sector is directly entered from the disordered spin liquid state. Secondly, the selection of the ground state gauge configuration is primarily based on the interplay between the Majorana fermions and the $\mathbb{Z}_2$ gauge field.

Hence, it is a remarkable result that the correlation between T_c and Δ is maintained for (8,3)c, although the phase transition mechanism here is more complex than in the other 3D Kitaev systems.

4.5 Summary

In this chapter, we have presented a thermodynamic classification of elementary bipartite 3D Kitaev systems. Based on numerical results from large-scale QMC simulations, we have corroborated the understanding of the finite-temperature physics of these systems, which is mainly characterized by two thermal transitions. A high-temperature crossover at $T' = 0.51(5)$ indicates the local fractionalization of spins into (itinerant) Majorana fermions and a (static) $\mathbb{Z}_2$ gauge field. Its characteristic signatures are a peak in the specific heat $C_v(T)$, whose position and shape is insensitive to the underlying lattice geometry and system size, and the spin-spin correlator $S_{\gamma\gamma}$ assuming a finite low-temperature value. Here, the system enters a disordered $\mathbb{Z}_2$ spin liquid phase, where its physics is determined by the energy fluctuations in both fractionalized degrees of freedom.

A second thermal transition occurs at the lower temperature scale $T_c \sim J/100$. Here, the Kitaev systems undergo a phase transition. This is indicated by C_v-peaks which are highly sensitive to the lattice geometry and diverge in the thermodynamic limit. The thermal phase transition is, for all three-dimensional sys-

tems, determined by the ordering of the $\mathbb{Z}_2$ gauge field, and constitutes an inverted Ising transition. It is here that the elementary plaquettes in the lattice assume the energy-minimizing $\mathbb{Z}_2$ plaquette flux configuration, which is determined by the plaquette length $|p|$. Our numerical results confirm that, for all considered 3D Kitaev systems, this ground state plaquette flux configuration follows the prediction by Lieb's theorem, although the geometric requirements to prove the statement of this theorem are only fulfilled by one of the systems. The correlation between the critical temperature T_c and the vison gap Δ supports the understanding of the physical mechanism which underlies the phase transition, namely the proliferation of extended vison loops.

We have also presented and discussed a particular 3D Kitaev system whose thermodynamic behavior falls out of the scheme outlined above. In the (8,3)c lattice, a peculiar interplay between the elementary plaquette length and a volume constraint leads to a geometric frustration of the $\mathbb{Z}_2$ gauge field, for which we introduced the term *gauge frustration*. Instead of undergoing the inverted Ising phase transition and directly ordering into a unique flux configuration at $T \sim J/100$, the system is first subject to an additional thermal crossover and enters a *constrained gauge manifold*, which consists of a macroscopic number of energetically degenerate $\mathbb{Z}_2$ plaquette flux states. For a wide range of (an)isotropies in the bond couplings, we have shown that the suppressed thermal phase transition is finally caught up at $T_c = 0.0020(2)$, where the Majorana fermions form a semimetallic collective state and, thereby, force the $\mathbb{Z}_2$ gauge field to assume a columnar zigzag order. This phenomenon is a quantum effect and makes this Kitaev system, in some sense, a hybrid between a spin liquid with full decoupling of the parton degrees of freedom (such as it is the usual case in $\mathbb{Z}_2$ spin liquids), and one where the fractionalized degrees of freedom maintain a strong interaction down to lowest temperatures (as in typical $U(1)$ spin liquids).

Chapter 5

Topological phases in a generalized Kitaev model

In Sec. 2.3, we name two classes of spin liquids which are stabilized by the structure of the underlying lattice gauge theory. One class is formed by $\mathbb{Z}_2$ spin liquids, where the gauge bosons are gapped, and which may possess gapless or gapped spinon excitations. The 3D Kitaev systems we have focused on in the last chapter belong to this class. Here, the QSL state is not only stable to quantum fluctuations, but also to thermal fluctuations up to a critical temperature T_c, where it is destroyed by an inverted Ising phase transition. In two spatial dimensions, on the other hand, the destruction of the QSL state is a purely local phenomenon and manifests itself in a smooth thermal crossover to the high-temperature phase.

A second class is given by spin liquids with broken time-reversal (TR) symmetry, which, depending on the spatial dimensionality of the system, leads to an excitation gap also for the spinons. Here, the QSL ground state is stabilized up to a finite-temperature phase transition even in 2D, and possesses a *chiral spin liquid* phase, which is characterized by a finite *Chern number* of the corresponding Majorana band structure. The manifestation of this topologically non-trivial phase is the simultaneous occurrence of a gapped bulk and gapless boundary modes, which cannot be destroyed unless the bulk gap is closed.

In Kitaev models with broken TR symmetry, we find both aforementioned scenarios realized: A $\mathbb{Z}_2$ spin liquid, which, belonging to symmetry class D, may possess a topological ground state in two spatial dimensions [103, 106]. A general way to break TR symmetry in a Kitaev model is to apply a magnetic field, while for non-bipartite Kitaev systems, the ground state breaks TR symmetry even spontaneously, and no magnetic field is required [27, 30]. This is a consequence of the odd plaquette length in such lattices, which causes the plaquette flux operators to have imaginary eigenvalues $W_p = \pm i$. As a consequence, TR symmetry breaking is a byproduct of flux ordering in such systems. Notable examples have been

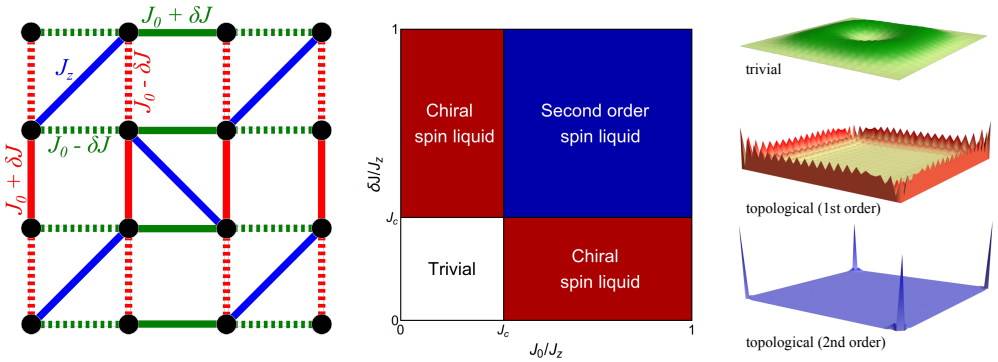

(a) Kitaev Shastry-Sutherland model **(b)** Ground state phase diagram **(c)** Majorana wavefunctions[1]

Figure 5.1: Kitaev Shastry-Sutherland model with staggered bond couplings and its ground state phase diagram as explained in Sec. 2.3.3. There, we discuss the occurrence of zero-temperature phases with a trivial, a first-order and a second-order topology.

analytically and numerically studied in 2D for the Yao-Kivelson model [30, 47], which indeed possesses a topological ground state phase, and in 3D for the Kitaev hypernonagon model [36, 90, 95]. QMC studies on these systems have shown that the breaking of TR symmetry is accompanied by a thermodynamic behavior that deviates from other Kitaev systems. In 2D, a thermal phase transition – instead of a crossover – is measured for all (an)isotropy limits, which includes both the chiral spin liquid and the topologically trivial ground state regime. In 3D, where no topological ground state is present, the loop proliferation mechanism and the spontaneous breaking of TR, along with a number of point group symmetries, occurs at the same time, as a first-order phase transition [90].

Here, we report our numerical results on a generalized 2D Kitaev system on the five-coordinated Shastry-Sutherland lattice (*Kitaev Shastry-Sutherland model*, Fig. 5.1 a), which has been introduced in Sec. 2.3.3. The ground state phase diagram of this model (Fig. 5.1 b) shows a notable variety of topological phases [83]. Apart from a chiral spin liquid and a topologically trivial phase, there is a particular choice of bond coupling parameters for which a *second-order topological insulator* is realized, which has a trivial Chern number, but is characterized by the occurrence of zero-dimensional *corner modes*. We call this phase a *second-order Kitaev spin liquid (SOSL)*. We have performed quantum Monte-Carlo simulations for all these regimes of the model and investigated its finite-temperature behavior. We verify the existence of a thermal phase transition for all (an)isotropy limits. Most strikingly, above the chiral spin liquid phase, this phase transition possesses a critical temperature T_c which is one order of magnitude larger than in other

[1]The Majorana wavefunctions for the Kitaev Shastry-Sutherland model have been calculated and plotted by Dr. Vatsal Dwivedi.

Kitaev systems. Moreover, the system is shown also to exhibit a *thermal metal* phase, which is the third possible regime for symmetry class D beside the trivial and non-trivial insulator.

In the following, we start with a brief recap of the model, a couple of technical remarks on the implementation of the QMC simulation and the measurement of some new observables. After that, we discuss our numerical results one by one for the different regions of the ground state phase diagram, namely (i) the chiral spin liquid regime (Sec. 5.2) and (ii) the second-order spin liquid regime (Sec. 5.3).

This chapter discusses work which has been reported in Refs. [219] and [83].

5.1 Model and method

5.1.1 Kitaev Shastry-Sutherland model

The Kitaev Shastry-Sutherland model (Fig. 5.1 a) is a generalized version of the Kitaev model, which is formulated in terms on Γ-matrices representing spin-$3/2$ degrees of freedom on the vertices of the five-coordinated Shastry-Sutherland lattice,

$$\mathcal{H}_{\text{Kitaev}} = -\sum_{\langle j,k\rangle_\gamma} J^\gamma \Gamma_j^\gamma \Gamma_k^\gamma. \tag{5.1}$$

In Sec. 2.3.3, we show that this higher-order version of the Kitaev model possesses a solution which is analogous to Kitaev's original solution approach for the honeycomb model [82]. With the introduction of staggered bond couplings $J_0 \pm \delta J$ on the horizontal and vertical bonds, and a coupling J_z on the diagonal bonds, the model has been shown to exhibit the ground state phase diagram shown in Fig. 5.1 b, with a topologically trivial phase, a chiral spin liquid phase with a non-trivial first-order topology, and a second-order spin liquid phase with gapless corner modes [83], Fig. 5.1 c.

5.1.2 QMC simulations

We have implemented the quantum Monte Carlo simulation in the Majorana basis of the generalized Kitaev model, as it is described in detail in Sec. 3.4. Here, the local transformation of Γ-matrices to Majorana operators is used, $\Gamma_i^\gamma = ib_i^\gamma c_i$, which, in the same way as for the standard Kitaev model, leads to an analytic expression of the Majorana partition function $\mathcal{Z}_{\text{Maj}}(\{u_{ij}\})$ in a fixed $\mathbb{Z}_2$ gauge configuration $\{u_{ij}\}$, Eq. (3.42). Thus, we can sample the $\mathbb{Z}_2$ gauge field like a classical Ising model on the lattice bonds, and calculate the Metropolis weights in terms of the free energy $F(\{u_{ij}\})$. We remark that the local transformation introduces an artificial extension of the Hilbert space, and the physical subspace

can be restored by using a gauge transformation of the general form that is defined in Eq. (2.51). However, in the derivation of the Majorana partition function, we do not distinguish between physical and unphysical states in the fermionic Fock space. This procedure is justified, since, for a given lattice system and gauge configuration, those states differ with respect to their parity, which amounts to adding or subtracting a single fermion. For a lattice system with N sites, the contribution from unphysical states therefore only contributes deviations of the order $1/N$ to the partition function, and, correspondingly, the physical observables that are extracted from it [145]. Unlike the 3D lattice systems discussed in Chapter 4, there is no way to define a Jordan-Wigner transformation for the Shastry-Sutherland lattice with the bond assignments defined as in Fig. 2.13, for which Jordan-Wigner strings are located along all but one subset of bonds γ. Despite that, we have been able to measure numerical results with a very systematic scaling behavior in the SOSL phase (Fig. 5.20). In other regimes, we see similar finite-size effects as in the 3D Kitaev systems (Fig. 5.4).

We perform QMC simulations for lattice systems with periodic boundary conditions and linear size $L = 10$, which corresponds to $N = 400$ lattice sites. For all simulations, we use the QMC-ED method. Every MC sweep is followed by an attempted replica exchange. The simulations have been performed with 96 parallel processes (95 replicas + 1 master process), which are logarithmically distributed in the temperature interval $[10^{-4}, 10]$, and later supplemented with results from simulations at larger temperatures.

Our calculations comprise two series of such parallel QMC simulations, each of which includes a set of parameter points corresponding to a cut in the ground state phase diagram (using the staggered bond coupling parameters J_z, $J_0 \pm \delta J$ as defined in Fig. 2.13), namely:

1. Choosing the fixed bond coupling parameters $J_0 = 1$, $\delta J = 0$, and varying J_z from 0.1 to 4.0 in steps of 0.1. This corresponds to an *inverted* cut through the horizontal axis of the ground state phase diagram, going from the chiral spin liquid to the topologically trivial phase (Fig. 5.2). The results for this series of simulations are discussed in Sec. 5.2.

2. Choosing the fixed bond coupling parameters $J_z = 1$, $\delta J = 0.7$, and varying J_0 from 0.1 to 0.65 in steps of 0.05. This corresponds to another horizontal cut through the phase diagram, going from the chiral spin liquid to the second-order spin liquid (Fig. 5.16). The results from this series of simulations are discussed in Sec. 5.3. In addition, we have performed QMC simulations within the SOSL regime, at constant $J_0 = 0.9$ and for $\delta J \to J_0$, which corresponds to a tetragonal chain limit [220] of the Kitaev Shastry-Sutherland model.

5.1.3 Plaquette flux and chirality

In the definition of the plaquette flux operator $W_p = \prod(-iu_{ij})$, Eq. (2.18), we use a convention where we take the product of bond terms u_{ij} with *clockwise* orientation along the plaquettes. While this choice of convention has no importance for plaquettes with *even* length, the sign for odd loops $W_l = \pm i$ is changed if the direction of measurement is reversed. Therefore, the average plaquette flux of the triangular plaquettes in the Shastry-Sutherland lattice defines a *chirality* of the system,

$$\kappa = \frac{1}{N_t} \sum_t W_t, \tag{5.2}$$

where $W_t = \pm i$ is the flux for a single triangle, and N_t the number of triangles in the lattice. The chirality changes sign under the time-reversal operation

$$T\kappa T^{-1} = -\kappa, \tag{5.3}$$

and the ground state of the higher-order Kitaev system breaks time-reversal symmetry spontaneously by selecting either of the two chiralities $\kappa = \pm i$, which corresponds to uniform configurations of W_t. In the paramagnetic regime, the average chirality is $\kappa = 0$, in analogy to the average flux $\overline{W_p}$ for plaquettes with even length. Accordingly, as a measure for the ordering of the system, we consider the modulus of the imaginary part of κ,

$$|\mathrm{Im}(\kappa)| \in [0, 1], \tag{5.4}$$

which is 0 for complete disorder, and 1 for any of the two ordered triangular flux states. As it may be noted, this quantity bears strong resemblance to the magnetization in the Ising model.

5.1.4 Chern number

As we briefly mention in Sec. 1.1.3, a manifestation of the chiral spin liquid phase is the occurrence of gapless boundary modes that are topologically protected by the bulk gap of the system, and the existence of these gapless boundary modes can be tracked by a topological $\mathbb{Z}$ invariant, which is the *Chern number*. The Chern number of the n-th energy band of an insulator is the integral of the Berry curvature over the first Brillouin zone,

$$\nu_n = \frac{1}{2\pi} \int_{\mathrm{BZ}} \Omega_n(\mathbf{k}) d\mathbf{k}, \tag{5.5}$$

with the Berry curvature $\Omega_n(\mathbf{k})$ and Berry connection $\mathcal{A}_n(\mathbf{k})$ being defined by [221]

$$\begin{aligned}\mathcal{A}_n(\mathbf{k}) &= i \langle u_n(\mathbf{k})| \nabla_{\mathbf{k}} |u_n(\mathbf{k})\rangle ,\\ \Omega_{n,\mu\nu}(\mathbf{k}) &= \frac{\partial}{\partial k^\mu}\mathcal{A}_{n,\nu}(\mathbf{k}) - \frac{\partial}{\partial k^\nu}\mathcal{A}_{n,\mu}(\mathbf{k})\\ &= \sum_{m\neq n} \mathrm{Im}\frac{\langle u_{nk}| \frac{\partial \mathcal{H}(\mathbf{k})}{\partial k^\mu} |u_{mk}\rangle \langle u_{mk}| \frac{\partial \mathcal{H}(\mathbf{k})}{\partial k^\nu} |u_{nk}\rangle}{(\epsilon_{n\mathbf{k}} - \epsilon_{m\mathbf{k}})^2}.\end{aligned} \tag{5.6}$$

Here, $|u_n(\mathbf{k})\rangle$ is the periodic part of the Bloch wavefunction of the n-th band, $|\psi_{nk}\rangle = e^{i\mathbf{kr}}u_{nk}(\mathbf{r})$. The curvature integral (5.5) is confined to integer values if the 2D surface it is taken over is a closed manifold, which is fulfilled for the Brillouin zone [222]. The Berry connection $\mathcal{A}_n(\mathbf{k})$ is a local gauge potential and can be thought of as a generalization of the real-space vector potential known from electrodynamics to arbitrary parameter spaces (here, momentum space). The Berry curvature $\Omega_n(\mathbf{k})$, on the other hand, is a gauge-invariant quantity and can be interpreted as the (magnetic) field strength in momentum space, which corresponds to the local gauge potential $\mathcal{A}_n(\mathbf{k})$[2]. If the Hamiltonian $\mathcal{H}(\mathbf{k})$ is adiabatically moved along a closed path $\mathcal{C}$ in momentum space, the Berry curvature determines the phase factor $e^{i\gamma_n}$ that the eigenstates $|u_n(\mathbf{k})\rangle$ of $\mathcal{H}(\mathbf{k})$ pick up along this path, due to the influence of other states $|u_m(\mathbf{k})\rangle$ [98]. The (gauge-invariant) Berry phase γ that determines the phase factor,

$$\gamma_n = \int_{\mathcal{C}} \mathcal{A}_n(\mathbf{k}) d\mathbf{k} = \int_{\mathcal{S}} \Omega_n(\mathbf{k}) d\mathbf{k}, \tag{5.7}$$

is then the momentum-space analogon to a magnetic flux. Here, $\mathcal{S}$ is the surface enclosed by the path $\mathcal{C}$, and the relation between the line and the surface integral is given by Stokes' theorem.

Thus, the Chern number ν distinguishes phases with a different band structure topology. If the Hamiltonian is continuously changed with respect to some parameter other than $\mathbf{k}$, for instance a coupling strength J, the Chern number stays unchanged as long as the band gap remains open under this continuous change. Concretely, a nonzero Chern number indicates that the Berry connection $\mathcal{A}_n(\mathbf{k})$ of the band structure cannot be defined as a global function over the entire Brillouin zone [223].

Numerical calculation of the Chern number

In practice, we simulate real-space systems and sample $\mathbb{Z}_2$ gauge field configurations $\{u_{ij}\}$. It is possible to consider these real-space systems as large unit cells

[2]Note that this gauge freedom has nothing to do with the $\mathbb{Z}_2$ gauge field of the Kitaev model!

(supercells), and convert the real-space Hamiltonian $\mathcal{H}(\{u_{ij}\})$ into a momentum-space Hamiltonian $\mathcal{H}_{\mathbf{k}}(\{u_{ij}\})$. Then, we can feed the configurations $\{u_{ij}\}$ from the QMC simulations into $\mathcal{H}_{\mathbf{k}}(\{u_{ij}\})$, and calculate momentum-space quantities as the Chern number ν. In our case, $\mathcal{H}_{\mathbf{k}}(\{u_{ij}\})$ is a 400×400 matrix representing a supercell of the system with $L = 10$. Of course, we are still numerically restricted to finite momentum-space systems. Therefore, it is necessary for the Chern number calculation to consider the underlying gauge quantities – the Berry connection and curvature – not as continuous quantities, but on a discrete grid. A widely used method for this is introduced in Ref. [223] and described in the following.

The band structure of our system is always gapped in the ground state, meaning that the eigenvalues $\epsilon_{n\mathbf{k}}$ of $\mathcal{H}_{\mathbf{k}}(\{u_{ij}\})$ are nonzero for all n and $\mathbf{k}$. However, the band structure in general contains level crossings ($\epsilon_{n\mathbf{k}} = \epsilon_{m\mathbf{k}}$ for some n,m and $\mathbf{k}$), such that a band-wise calculation of Chern numbers ν_n is not possible. Instead, we have to consider the above-defined quantities for the *non-Abelian* case, where the Berry connection translates to a one-form $\mathcal{A}$ [224],

$$\begin{aligned} \mathcal{A}_{\alpha\beta} &= -i \langle u_\alpha | du_\beta \rangle , \\ \Omega &= d\mathcal{A} - i\mathcal{A} \wedge \mathcal{A}, \\ \nu &= \int_{\mathrm{BZ}} \mathrm{tr} \left(\frac{\Omega}{2\pi i} \right). \end{aligned} \tag{5.8}$$

We can write $\mathcal{A}$ in the matrix-valued form $\mathcal{A} = \psi^\dagger d\psi$ [223–226], where ψ is the $M \times M$-matrix that is composed of the multiplet $(|u_1(\mathbf{k})\rangle \dots |u_M(\mathbf{k})\rangle)$ of eigenstates of $\mathcal{H}_{\mathbf{k}}$. In our case, we always use the $M = N/2$ eigenstates corresponding to the lower half of eigenvalues, $\epsilon_1, \dots, \epsilon_{N/2}$, for which the relaxed gap opening condition $\epsilon_{n\mathbf{k}} \neq \epsilon_{m\mathbf{k}}$ for $n \leq N/2$ and $m > N/2$ is fulfilled.

We consider a discretized Brillouin zone, which is a square lattice of $n_i \times n_j$ k-points $\mathbf{k}_l$. Usually, we choose $n_i = n_j = 20$. Links are described by their k-points $\mathbf{k}_l$, $\mathbf{k}_l + \tilde{\mathbf{q}}_i$, with $\tilde{\mathbf{q}}_i = \mathbf{q}_1/n_i$, $\tilde{\mathbf{q}}_2 = \mathbf{q}_2/n_j$. For each link, a $U(N)$ gauge variable is defined by

$$U_{\tilde{q}_i}(\mathbf{k}_l) = \frac{\det\left(\psi^\dagger(\mathbf{k}_l)\psi(\mathbf{k}_l + \tilde{\mathbf{q}}_i)\right)}{|\det\left(\psi^\dagger(\mathbf{k}_l)\psi(\mathbf{k}_l + \tilde{\mathbf{q}}_i)\right)|}, \tag{5.9}$$

and serves to calculate the (gauge-invariant) plaquette field strength

$$F_{12}(\mathbf{k}_l) = \log\left(\frac{U_{\tilde{q}_1}(\mathbf{k}_l) U_{\tilde{q}_2}(\mathbf{k}_l + \tilde{\mathbf{q}}_1)}{U_{\tilde{q}_1}(\mathbf{k}_l + \tilde{\mathbf{q}}_2) U_{\tilde{q}_2}(\mathbf{k}_l)} \right), \tag{5.10}$$

for which

$$-\pi < \frac{1}{i} F_{12}(\mathbf{k}_l) \leq \pi. \tag{5.11}$$

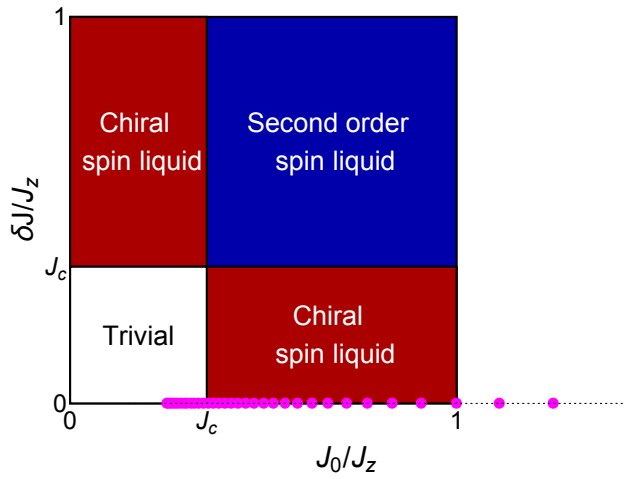

Figure 5.2: Coupling parameters in the QMC simulations (1). We simulate an (inverse) cut through the ground state phase diagram of the Kitaev Shastry-Sutherland model [83] by keeping $J_0 = 1$ and $\delta J = 0$ fixed, and varying J_z from 0.1 to 4.0. This corresponds to moving from the chiral spin liquid regime to the trivial phase (while all parameter points with $J_z < 1$, i.e. $J_0/J_z > 1$, lie outside the phase diagram.

The (numerical) Chern number of the band structure is now given by the sum over all plaquette field strengths in the lattice,

$$\tilde{\nu} = \frac{1}{2\pi i} \sum_l F_{12}(\mathbf{k}_l). \tag{5.12}$$

It is shown in Ref. [223] that $\tilde{\nu} \in \mathbb{Z}$ and $\tilde{\nu} \to \nu$ for a sufficiently fine discretization of the Brillouin zone. The calculation can be performed for any gapped band structure of the Majorana fermions.

5.2 Chiral spin liquid

We start the discussion of our numerical results with the first series of QMC simulations. Here, the choice of bond coupling parameters corresponds to an inverse cut through the horizontal axis of the ground state phase diagram of the spin-$\frac{3}{2}$ Kitaev Shastry-Sutherland model, as is depicted in Fig. 5.2. We fix the coupling parameters on the horizontal and vertical bonds to $J_0 = 1$, $\delta J = 0$, and vary the parameter J_z on the diagonal bonds in steps of $\Delta J_z = 0.1$ from 0.1 to 4.0 (cf. Fig. 2.13 for the assignment of bond couplings). For $J_z < 1$, the parameter points lie outside the ground state phase diagram that is given in Fig. 5.2. Thermal phase diagrams for this series of parameter points are presented in Figs. 5.8 and 5.10, which, apart from the positions of specific heat signatures, show the evolution

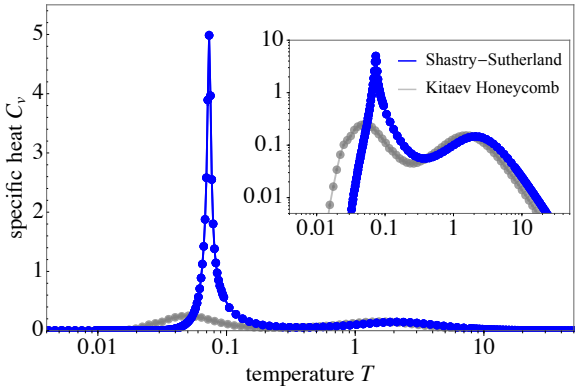

Figure 5.3: Specific heat $C_v(T)$ of the spin-$\frac{3}{2}$ Kitaev Shastry-Sutherland model. The system shows the characteristic double-peak structure known from other Kitaev models (here shown in comparison: the Kitaev honeycomb model): A high temperature peak at $T' \sim 2J_z$ indicates spin fractionalization, and a low-temperature peak, here at $T_c \sim 0.1J_z$, is the signature of a thermal phase transition. Data shown is for the coupling parameter $J_z/J_0 = 1.2$ and linear system size $L = 10$ ($L = 16$ for the Kitaev honeycomb model).

of the chirality $|\mathrm{Im}(\kappa)|$ and the 4-plaquette flux $\overline{W_p}$ as functions of the coupling J_z/J_0 and the temperature T (Fig. 5.8), as well as the Chern number $|\nu|$ for the different ground state regimes (Fig. 5.10). The most important observations are discussed in the following.

5.2.1 Thermal phase transition

In the stated parameter regime, the specific heat $C_v(T)$ of the Kitaev Shastry-Sutherland model shows the characteristic double-peak structure, which is generically encountered in Kitaev systems (Fig. 5.3). For each coupling parameter J_z, there is a high-temperature peak with a maximum at $T' \sim 2J_z$, which has the same position and shape for all system sizes. Just as in the formerly discussed models, this peak indicates a smooth thermal crossover, associated with the (local) fractionalization of spins into Majorana fermions and a $\mathbb{Z}_2$ gauge field.

The low-temperature peak, on the other hand, is strongly sensitive to both the coupling ratio J_z/J_0 and the (linear) system size L, with respect to its position and shape (cf. Fig. 5.4, where the $\mathbb{Z}_2$ gauge field contribution to the specific heat $C_{v,\mathrm{GF}}(T)$ is shown for different linear system sizes L). Its position in temperature space varies from $T \sim 10^{-2}J_z$ deep in the topologically trivial phase, $J_z/J_0 \gg 2\sqrt{2}$, to the considerably large temperature $T \sim 10^{-1}J_z$ in the chiral spin liquid regime, with a maximal value at $J_z/J_0 \sim 1$. Both for the chiral spin liquid and the topologically trivial phase, we find that the low-temperature peak shows a diverging behavior for increased linear system sizes L, a feature which indicates a thermal phase transition. The position of the low-temperature peak

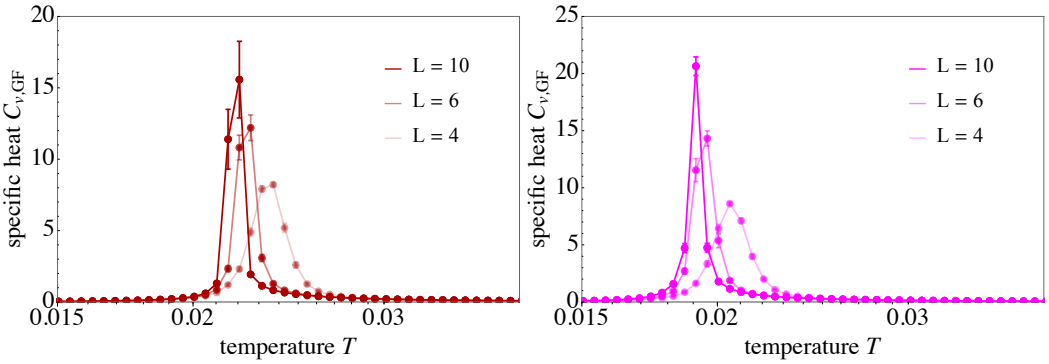

(a) $J_z/J_0 = 2.8$ (chiral spin liquid) **(b)** $J_z/J_0 = 2.9$ (trivial phase)

Figure 5.4: Specific heat $C_{v,\mathrm{GF}}(T)$ for different system sizes. A diverging low-temperature peak is encountered for all parameter regimes, here: The chiral spin liquid phase (a) and the topologically trivial phase (b). This indicates that the spin-$\frac{3}{2}$ Kitaev Shastry-Sutherland model undergoes a thermal phase transition which is associated with the ordering of the $\mathbb{Z}_2$ gauge field and the spontaneous breaking of time-reversal symmetry. This is a major difference to Kitaev models on bipartite 2D lattices.

can serve as an estimate for the critical temperature T_c of the thermal phase transition, and is shown as a function of J_z/J_0 by the filled (open) circles for the chiral (topologically trivial) phase in the phase diagrams presented in Figs. 5.8 and 5.10.

For $J_z/J_0 < 1$, we find that the low-temperature peak splits up into two different peaks, which further separate from each other when the coupling ratio is lowered to $J_z/J_0 \to 0$ (Fig. 5.9). Here, it is the lower peak (again at $T \sim 10^{-1}J_z$) that is associated with a thermal phase transition, while the upper peak is the signature of another thermal crossover. This peak separation is explained by distinct ordering temperatures for the $\mathbb{Z}_2$ flux on the square and triangle plaquettes, a phenomenon which is further discussed in the next section.

There are two significant thermodynamic observations for this model which have to be emphasized here. The first is the fact itself that the spin-$\frac{3}{2}$ Kitaev Shastry-Sutherland model undergoes a thermal phase transition, a property which distinguishes it from other two-dimensional Kitaev systems. The second is the critical temperature $T_c \sim 10^{-1}J_z$ in the chiral spin liquid regime, which is one order of magnitude higher than in other Kitaev systems.

Spontaneous breaking of time-reversal symmetry

Concerning the occurrence of a thermal phase transition, we discuss in Sec. 2.2.6 that, in two spatial dimensions, the point-like nature of the vison excitations inherently destabilizes the quantum spin liquid state of the Kitaev model. Whenever such a vison excitation is created and encircled by Majorana fermions, the lat-

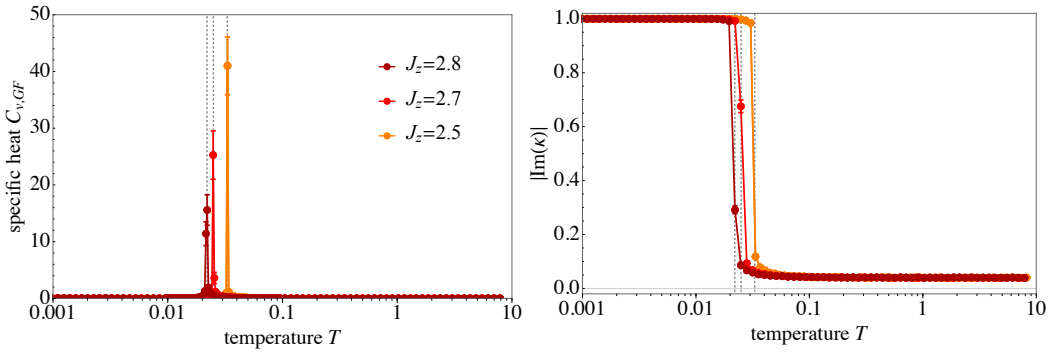

(a) Specific heat $C_{v,\mathrm{GF}}$ (gauge contribution)

(b) absolute chirality $|\mathrm{Im}(\kappa)|$

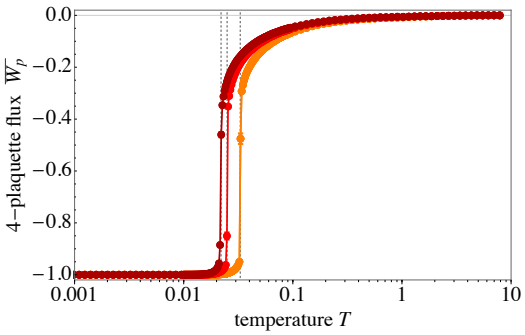

(c) square-plaquette flux $\overline{W_p}$

Figure 5.5: Specific heat $C_{v,\mathrm{GF}}(T)$ ($\mathbb{Z}_2$ gauge field contribution) (a), absolute chirality $|\mathrm{Im}(\kappa)|$ (b) and 4-plaquette flux $\overline{W_p}$ (c) for different parameter values in the topological chiral spin liquid regime. The low-temperature peak indicates a thermal phase transition (dashed lines), which is associated with the ordering of the (imaginary) fluxes $W_t = \pm i$ on the triangular plaquettes of the Shastry-Sutherland lattice. The chirality $\kappa = 1/N_t \sum_t W_t$ is defined as the average 3-plaquette flux of the system, and assumes one of the two ground state values $\kappa = \pm i$, which are connected by time-reversal symmetry. As long as $J_z \geq J_0$, the ordering of the triangle plaquettes also causes the ordering of the average flux $\overline{W_p}$ on the square plaquettes at the same temperature scale.

ter picks up a phase π, which leads to their destructive interference. In 3D, this only happens when the (loop-like) visons become system-spanning, which comes with an energy cost that is comparable to the system size, and, hence, diverges in the thermodynamic limit. This energy cost E is only counterbalanced in the free energy $F = E - TS$ of the system by a diverging configurational entropy S provided by the system-spanning visons, which, however, requires a large enough temperature T to become effective and allow for their proliferation. In 2D, in contrast, the energetic cost for the proliferation of visons does not diverge in the thermodynamic limit. Therefore, the thermal transition from the QSL state to the confined regime is a smooth crossover here.

For Kitaev systems on non-bipartite lattice geometries, the situation is entirely

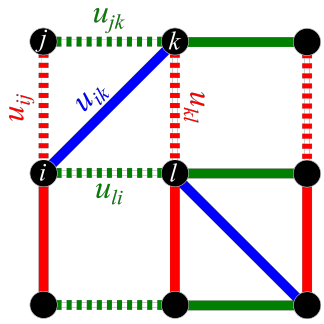

Figure 5.6: Elemtary plaquettes in the Shastry-Sutherland lattice. The flux on the square plaquettes $W_p = u_{ij}u_{jk}u_{kl}u_{li}$ is given by the product of the triangle fluxes $W_{t1} = -iu_{ij}u_{jk}u_{ki}$ and $W_{t2} = -iu_{ik}u_{kl}u_{li}$, which is because $u_{ik} \cdot u_{ki} = -1$. The ordering of the triangle plaquettes for strong diagonal coupling $J_z > J_0$ therefore causes the ordering of half the square plaquettes. The other half of squares order at the same temperature to minimize the energy.

different. Here, the gauge-invariant $\mathbb{Z}_2$ plaquette flux assumes imaginary eigenvalues $W_t = \pm i$ on the elementary loops of the system, and these eigenvalues change their sign under application of the time-reversal operator T. Therefore, the ordering transition of the $\mathbb{Z}_2$ gauge field into a homogeneous flux configuration, $W_t = i$ or $W_t = -i$ for all t, is necessarily accompanied by spontaneous breaking of time-reversal symmetry. This suggests the occurrence of a (continuous) thermal phase transition also in two spatial dimensions, which, for the present model, is verified by our numerical results. Hence, the ordering mechanism is different both from bipartite Kitaev models in 2D, for which there is no phase transition at all, and from those in 3D, where the inverted Ising transition is not accompanied by spontaneous symmetry breaking.

Associated with the spontaneous breaking of time-reversal symmetry, there exists a local *order parameter* for the Kitaev Shastry-Sutherland model, which is given by the chirality $\kappa = 1/N_t \sum_t W_t$, an analogue to the magnetization $\mu = 1/N \sum_i \sigma_i^z$ in the classical Ising model. Numerical results for $|\mathrm{Im}(\kappa)|$ and the average flux on the 4-(square)-plaquettes $\overline{W_p}$ (with $W_p = \pm 1$) are shown in Fig. 5.5 for different coupling parameter values J_z belonging to the chiral spin liquid phase. Here, we see that the position of the specific heat peak $C_{v,\mathrm{GF}}(T)$ corresponds to the temperature where $|\mathrm{Im}(\kappa)|$ sharply drops from the ground state value $|\mathrm{Im}(\kappa)| = 1$ to the large-temperature limit $|\mathrm{Im}(\kappa)| = 0$. At the same transition temperature, we encounter the ordering of the square-plaquette fluxes.

The simultaneous ordering of triangle and square plaquettes is explained as follows: In the Shastry-Sutherland lattice, every second square plaquette is composed of two triangles, and the flux operator eigenvalue on a square plaquette is the product of two triangular flux operator eigenvalues, $W_p = W_{t_1} \cdot W_{t_2}$. Therefore, whenever such a pair of triangles orders into one of the two ground state con-

figurations $(+i, +i)$ or $(-i, -i)$, the corresponding square-plaquette flux eigenvalue becomes $W_p = -1$, which is the expected π-flux ground state for squares. The other half of the square plaquettes, which do not possess diagonal bonds, assume π-fluxes independently at the same temperature, which minimizes the energy. Hence, it is the ordering of triangle plaquettes which determines the ordering of half the square plaquettes, and triggers the ordering of the other half (Fig. 5.6). This mechanism works as long as the coupling on the diagonal bonds J_z is larger or equal the coupling J_0 on the horizontal / vertical bonds. For the other limit, $J_z < J_0$, we encounter that the square plaquettes already order at higher temperatures than the triangles (see Sec. 5.2.2).

In the topologically trivial phase $J_z \geq 2\sqrt{2} = J_c^{-1}$, we find the same qualitative behavior for the specific heat $C_{v,\mathrm{GF}}(T)$, the chirality $|\mathrm{Im}(\kappa)|$ and the square-plaquette flux $\overline{W_p}$ as for the chiral spin liquid regime (Fig. 5.7). Unlike in the Yao-Kivelson model, we have found no indication that the phase transition changes from second-order to first-order when J_z is tuned from the trivial to the CSL phase [47]. Instead, we assume that the phase transitions in both regimes are continuous. In the region below the quantum critical point $J_c^{-1} = 2\sqrt{2}$, we find that the low-temperature specific heat peak gets considerably sharp, reaching an extremal values $C_v > 40$ for $J_z = 2.5$. A summary of the results for the specific heat C_v, the chirality $\mathrm{Im}(\kappa)$ and the square-plaquette flux $\overline{W_p}$ is shown in the two thermal phase diagrams in Fig. 5.8.

Critical temperature T_c

We have seen that the occurrence of a thermal phase transition in two spatial dimensions is a particular property of non-bipartite Kitaev systems with ground states that spontaneously break time-reversal symmetry. In the Yao-Kivelson model, however, the temperature scale of this phase transition has been shown to be of the same (considerably small) order $T_c \sim 10^{-2} J$ as the $\mathbb{Z}_2$ gauge transition in 3D Kitaev systems [47]. Also in bipartite 2D Kitaev systems, such as the Kitaev honeycomb model, where the transition is a local crossover, the temperature scale is of the same order of magnitude.

In this sense, the Kitaev Shastry-Sutherland model distinguishes itself from all so far known Kitaev models by possessing a phase transition that already happens at a temperature $T_c \sim 10^{-1} J_z$, which is an entire order of magnitude larger. We find this large critical temperature T_c in the entire chiral spin liquid regime, with a maximum at $J_z/J_0 \sim 1.2$, as can be seen from the position of the low temperature peaks, indicated as filled circles in the thermal phase diagrams in Fig. 5.8. The transition temperature significantly starts to fall for $J_z > 2$, and reaches the order of magnitude $T_c \sim 10^{-2} J_z$ deep in the topologically trivial phase.

It can be concluded that the gauge ordering transition in Kitaev systems may

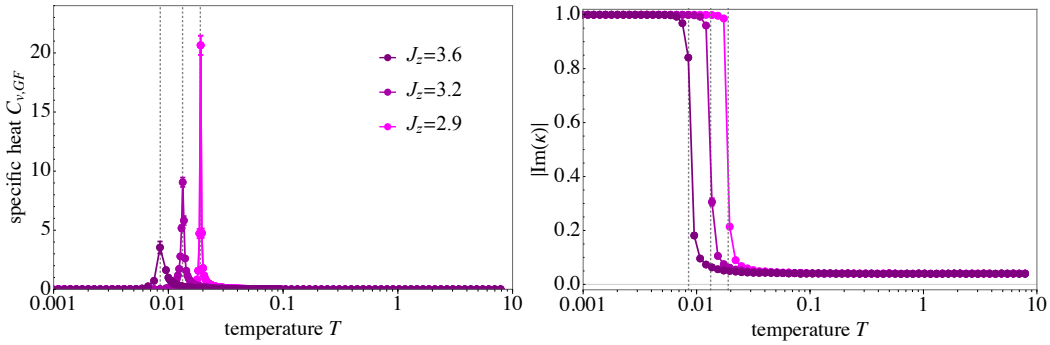

(a) Specific heat $C_{v,\mathrm{GF}}$ (gauge contribution) **(b)** absolute chirality $|\mathrm{Im}(\kappa)|$

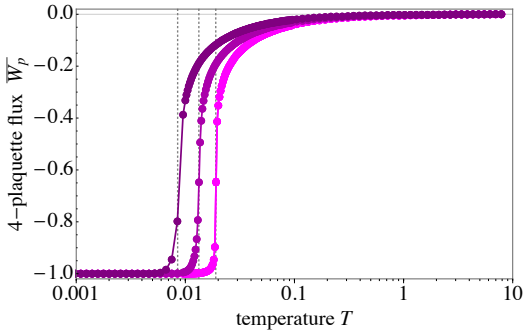

(c) square-plaquette flux $\overline{W_p}$

Figure 5.7: Specific heat $C_{v,\mathrm{GF}}(T)$ ($\mathbb{Z}_2$ gauge field contribution) (a), absolute chirality $|\mathrm{Im}(\kappa)|$ (b) and square-plaquette flux $\overline{W_p}$ (c) for different parameter values in the topologically trivial regime. Here, the thermodynamic signatures are qualitatively the same as for the CSL phase. As the quantum critical point $J_c^{-1} = 2\sqrt{2}$ is approached from either side of the ground state phase diagram, the phase transition peak gets considerably sharper. The dashed lines indicate the positions of the specific-heat peaks.

also happen at larger temperatures than $T_c \sim 10^{-2}J$. This raises the expectation that the detection of the QSL phase in experiment might be facilitated in systems with this property. Therefore, we have to ask what determines the high transition temperature in the Kitaev Shastry-Sutherland model. The most obvious difference to other Kitaev systems is the large coordination number $c = 5$ of the underlying lattice. However, an attempt by us to introduce two additional diagonal bonds on the empty square plaquettes of the Shastry-Sutherland lattice, and thereby construct a toy model with increased coordination number $c = 7$, did not lead to a further increase of the transition temperature. Therefore, we assume that the reason for an increase in the transition temperature is more intricate than merely considering the coordination number. Nonetheless, the search for other (generalized) Kitaev systems, which possess large transition temperatures, recommends itself as an interesting theoretical endeavor for the future.

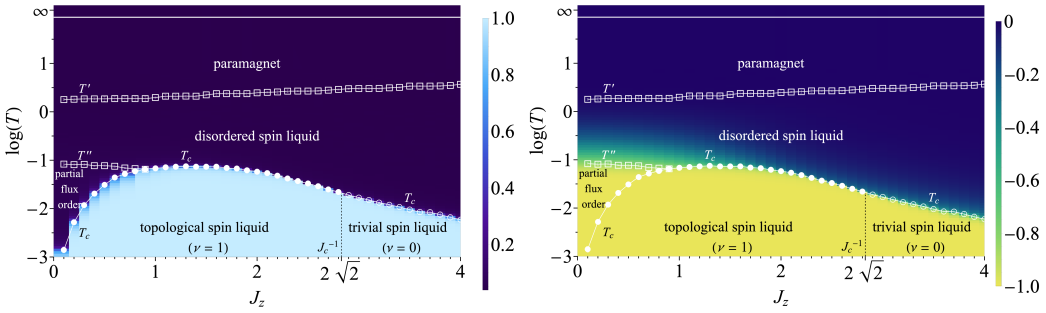

(a) absolute chirality $|\mathrm{Im}(\kappa)|$ **(b)** square-plaquette flux $\overline{W_p}$

Figure 5.8: Thermal phase diagram (1) for fixed coupling parameters $J_0 = 1, \delta J = 0$. The transition temperatures of the system are given as a function of the coupling ratio J_z/J_0 (white / black data points). The density plots show the chirality $|\mathrm{Im}(\kappa)|$ (a), and the average square-plaquette flux operator eigenvalue $\overline{W_p}$ (b). The filled (open) circles indicate the position T_c of the low-temperature peak in the chiral spin liquid (trivial) parameter regime. For both regimes, the low-T peak is the signature of a thermal phase transition. For $J_z < J_0$, we encounter an additional partial flux-order phase above T_c, where the square plaquettes are already ordered, while the triangle plaquettes remain disordered. A thermal crossover at T'' separates this phase from the regime with full flux disorder (disordered $\mathbb{Z}_2$ spin liquid).

5.2.2 Partial flux ordering

We now discuss the phenomenon of partial flux ordering, which is encountered in the regime $J_z/J_0 < 1$. In the thermal phase diagrams in Fig. 5.8, the ordering of the two different plaquette fluxes is shown as two contour plots. Fig. 5.8 a shows the ordering of triangle plaquettes, which is measured in terms of the chirality $|\mathrm{Im}(\kappa)|$. The contour plot in Fig. 5.8 b shows the average flux operator eigenvalue $\overline{W_p}$ on the square plaquettes. Both phase diagrams show homogeneously ordered flux regions below the phase transition temperature T_c (the location of the low-T peak), which is marked by the filled (open) circles for the chiral spin liquid (trivial) phase. In the region below J_z/J_0, the low-T specific heat peak splits up into two peaks, which separate for $J_z/J_0 \to 0$. While the peak at lower temperatures, which marks the phase transition, drops by one order of magnitude (thereby keeping the ratio $T_c \sim 0.1 J_z$ intact), the upper peak, which indicates a crossover and is marked by open squares, remains almost constant at $T \sim 0.1 J_0$. In the region which is enclosed by the two peak functions, the values of the fluxes strongly differ. While the square plaquettes assume an ordered configuration $\overline{W_p} = -1$ below the upper peak (indicated as an additional yellow region in the lower left corner of the phase diagram), the chirality remains $|\mathrm{Im}(\kappa)| = 0$ (indicated as a blue region in the same corner). Hence, in this region in the (J_z/J_0)-T plane, the flux ordering on the two sets of elementary plaquettes is decoupled.

Further details for this decoupling are presented in Fig. 5.9, where the gauge

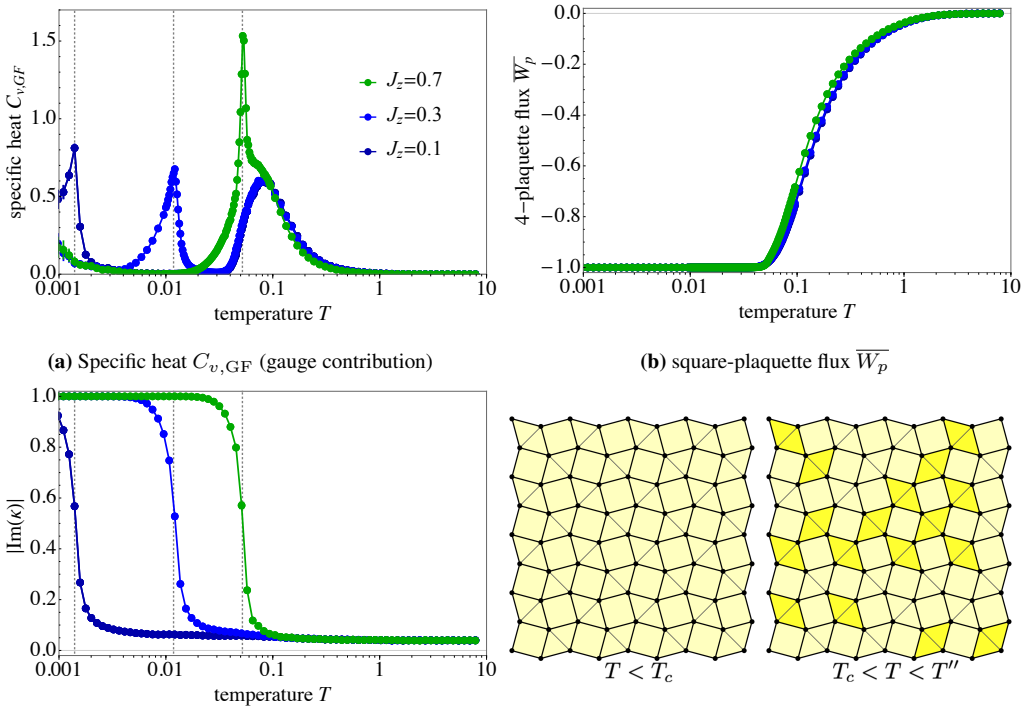

(a) Specific heat $C_{v,\mathrm{GF}}$ (gauge contribution)

(b) square-plaquette flux $\overline{W_p}$

(c) absolute chirality $|\mathrm{Im}(\kappa)|$

(d) Visualization of partial flux ordering.

Figure 5.9: Partial flux ordering. For $J_z < J_0$, the low-T specific heat peak $C_{v,\mathrm{GF}}(T)$ splits up into two peaks, which is caused by the separation of temperature scales for the ordering of triangle and square plaquettes. At $T'' \sim 0.1J_0$, the ordering of square plaquettes is associated with a thermal crossover, while the thermal phase transition caused by the ordering of triangle fluxes happens at $T_c \sim 0.1J_z$ (dashed lines).

contribution to the specific heat $C_{v,\mathrm{GF}}(T)$ (a), the square-plaquette flux $\overline{W_p}$ (b) and the chirality $|\mathrm{Im}(\kappa)|$ (c) are shown for the coupling parameters $J_z \in \{0.1, 0.3, 0.7\}$, along with a visualization of the regions of disordered and ordered triangle plaquettes (d). We can see that the upper peak of the specific heat is associated with the ordering of the square-plaquettes. The temperature of this ordering transition does not change much if J_z is lowered. The lower-T peak corresponds to the ordering of the chirality $|\mathrm{Im}(\kappa)|$, which moves to lower temperatures for decreasing J_z. Since the spontaneous breaking of time-reversal symmetry is only associated with the ordering of triangle plaquettes, we can conclude that the lower-T specific heat peak indeed indicates a phase transition, while the upper peak is the signature of a particular realization of the thermal crossover known from other 2D Kitaev systems. Here, the square plaquettes locally freeze into their ground state configuration. The temperature scale for the ordering of plaquette fluxes is always set by the bond coupling parameters. We have seen above that, as long as the diagonal bond coupling J_z is larger than the coupling on the other bonds

J_0, the ordering of the triangles also determines the ordering of half the squares. But this relation is not mutual. If $J_z < J_0$, the square plaquettes order at a temperature scale set by the value of J_0, which here is $T'' \sim 0.1J_0$. This, however, does not affect the flux values on the triangles, as a π-flux on a square plaquette ($W_p = -1$) allows for the two triangle configurations $(W_{t_1}, W_{t_2}) = (+i, +i)$ and $(-i, -i)$. Hence, above $T_c \sim 0.1J_z$, the J_z-bonds on the triangles continue to individually flip between these two configurations. At T_c, a homogeneous triangle configuration $W_t = +i$ or $-i$ is spontaneously selected for the entire lattice.

As a final remark, we note that the ordering of square-plaquette fluxes happens faster for strong values of J_z, which is seen by comparing the sharp drop of $\overline{W_p}$ in the Figs. 5.5 and 5.7 with the smaller slope of the $\overline{W_p}$-curve in Fig. 5.9. The T-region of flux ordering in Fig. 5.8 b is the yellow region above T_c / T'', which evolves from relatively broad to very narrow as we go from small to large values of J_z/J_0. This observation is explained by the same argument as the decoupling of the flux ordering for the two plaquette types. For $J_z > J_0$, the coupling strength J_z sets the temperature scale for the ordering of both triangle and square plaquettes. For very strong J_z, this ordering happens as a sharp transition, explaining the narrow yellow band at $J_z \gg J_0$. In the other limit $J_z < J_0$, the temperature scale for the ordering of square plaquettes is determined by the constant coupling parameter $J_0 = 1$, making the transition less sharp.

5.2.3 Gapless-gapped transition at intermediate temperatures

Chern number results

How does the separation of the ground state phase diagram into a (topologically non-trivial) chiral spin liquid and a trivial phase evolve at finite temperatures? We have already seen that, at least along the phase diagram cut considered here, the existence of the two phases does not manifest itself in qualitative differences in the thermodynamic signatures. Both phases possess a low-temperature thermal phase transition and a high-temperature crossover. The position of the transition temperatures is a smooth function of the coupling ratio J_z/J_0. And there is apparently no such distinction as second-order versus first-order phase transition with respect to the two ground state regimes. Aside from the discovery of the partially flux-ordered phase, there are also no insights on the medium and high-temperature regime which could be drawn from looking at the plaquette fluxes. Both the chirality $|\mathrm{Im}(\kappa)|$ and the square plaquette flux $\overline{W_p}$ suggest that the thermal regime above the phase transition is the usual disordered $\mathbb{Z}_2$ spin liquid phase, which is characterized by itinerant Majorana fermions coupled to a disordered $\mathbb{Z}_2$ gauge field, and that there is no further structure in this phase.

A more complex picture emerges when we look at the Chern number $|\nu|$ of

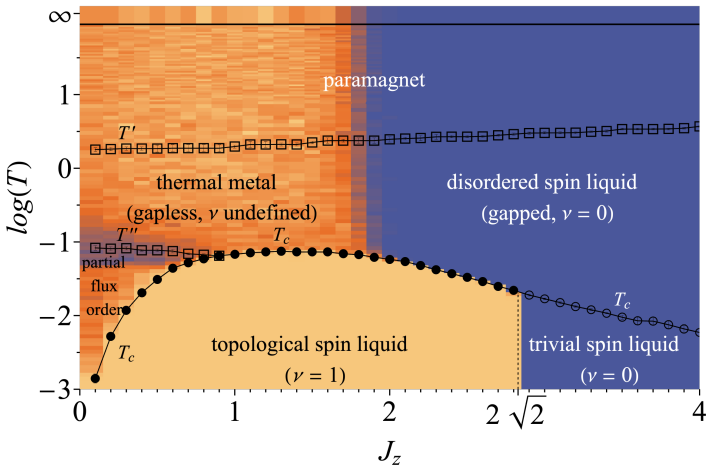

Figure 5.10: Thermal phase diagram (2) for fixed coupling parameters $J_0 = 1, \delta J = 0$. The transition temperatures of the system are given as a function of the coupling ratio J_z/J_0 (black data points). The density plot shows the Chern number $|\nu|$, which distinguishes the chiral spin liquid ground state ($|\nu| = 1$) from the trivial phase ($|\nu| = 0$). Above the thermal phase transition, the Chern number is only well-defined in gapped regions of the system. Such a band gap is verified for $J_z/J_0 > 2$ at high temperatures (Fig. 5.12), and for the partially flux-ordered phase (Fig. 5.14). The gapless intermediate-temperature phase at $J_z/J_0 < 2$ can be interpreted as an effective thermal metal, where signatures of symmetry class D survive in the Majorana band structure (see Fig. 5.13). In Appendix D, we show Chern number results along different cuts of this phase diagram.

the Majorana band structure as a function of the coupling ratio J_z/J_0 and the temperature T. Using the method which is explained in Sec. 5.1.4, we calculate ν from the $\mathbb{Z}_2$ gauge field samples $\{u_{ij}\}$, which we have obtained in the QMC simulation, and by considering the k-space Hamiltonian $\mathcal{H}_{\mathbf{k}}(\{u_{ij}\})$ for the $L = 10$ supercell. The results are shown as a contour plot in the thermal phase diagram in Fig. 5.10n (more details are shown in Appendix D). Below the thermal phase transition, the system is always gapped and the Chern number ν therefore well-defined also for finite temperatures. Here, we find that $|\nu| = 1$ in the chiral spin liquid regime, $0 < J_z < J_c^{-1}$, and $|\nu| = 0$ in the trivial phase (with $J_z > J_c^{-1}$). By comparing the result for ν with the chirality κ for different $\mathbb{Z}_2$ gauge field configurations in the CSL phase, we learn that both quantities always carry the same sign if we use the clockwise definition of the triangle plaquette flux W_t. A $\mathbb{Z}_2$ gauge field configuration $\{u_{ij}\}$, for which the Majorana band structure has a non-trivial Chern number $\nu = 1$, corresponds to a system with only clockwise fluxes, $\kappa = i$. Likewise, $\nu = -1$ corresponds to a system with only counterclockwise fluxes, $\kappa = -i$. Hence, we can interpret the chirality of the $\mathbb{Z}_2$ gauge configuration in the chiral spin liquid regime as an indicator for a right-moving ($\kappa = +i$) or left-

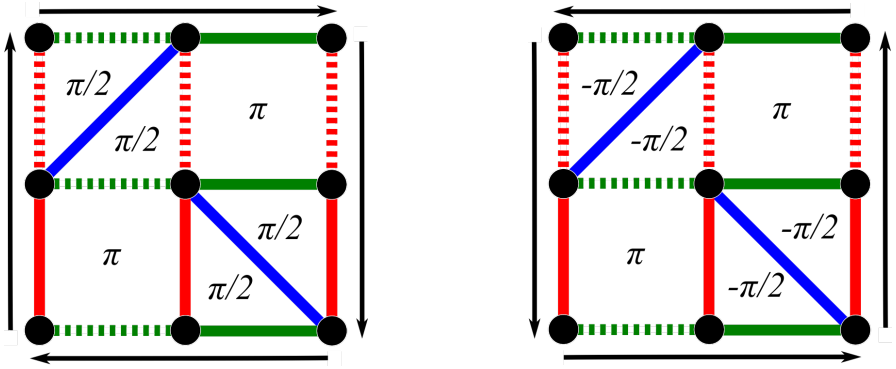

(a) positive chirality $\kappa = +i$ **(b)** negative chirality $\kappa = -i$

Figure 5.11: Chirality and edge modes in the chiral spin liquid phase. For $J_z < J_c$, the ground state of the Kitaev Shastry-Sutherland system has a finite Chern number $\nu = \pm 1$. Here, the sign of ν corresponds to the sign of the chirality $\kappa = \pm i$, and indicates a right-moving ($\nu = +1$) or left-moving ($\nu = -1$) gapless edge mode (if the periodic system is cut along the two spatial axes). In the topologically trivial phase, the chirality κ is not associated with an edge mode.

moving ($\kappa = -i$) gapless boundary mode, which would occur if the (periodic) system was cut along the two spatial axes (Fig. 5.11). This boundary mode cannot be destroyed by any continuous deformation of the Hamiltonian $\mathcal{H}_{\mathbf{k}}$ which leaves the bulk gap intact. At zero temperature, it is only destroyed at $J_z = J_c^{-1}$, the quantum critical point at which the bulk system itself becomes gapless. Beyond the quantum critical point, for $J_z > J_c^{-1}$, the chirality $\kappa = \pm i$ of the $\mathbb{Z}_2$ gauge field is not associated with a gapless edge mode any more, and the Chern number is $\nu = 0$.

Above the thermal phase transition, the Chern number calculation is physically meaningful only if the band structure of the Majorana fermions is gapped. This is fulfilled for the blue regions in the phase diagram in Fig. 5.10: (i) for $T > T_c$ and $J_z \gtrapprox 2$, and (ii) and in a small region around the square-ordering transition temperature T'' for $J_z < J_0$. Here, the numerical results indicate a constant, trivial Chern number $|\nu| = 0$ (note the top segment of the phase diagram, which gives the Chern number results for $T = \infty$).

Beyond these regions, where the contour plot of $|\nu|$ is orange, the situation is less clear. Above the temperature limit which is set by critical temperature T_c for $J_z/J_0 > 1$, and the square-ordering crossover temperature T'' for $J_z/J_0 \leq 1$, the system is gapless and the Chern number ν is ill-defined. Here, the relaxed gap opening condition $\epsilon_{n\mathbf{k}} \neq \epsilon_{m\mathbf{k}}$ for $n \leq N/2$ and $m > N/2$ is violated, on which the numerical calculation is based. The fact that the code produces results here is only a consequence of numerical accuracy: $\epsilon_{n\mathbf{k}} - \epsilon_{m\mathbf{k}}$ is not strictly zero in the calculation, but some small, finite number. We have verified that the Chern number results really reflect a gapless-gapped transition by calculating the band

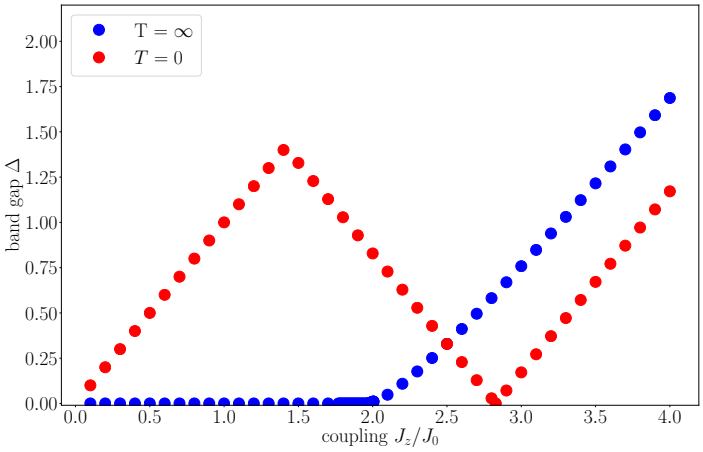

Figure 5.12: Band gap versus bond coupling parameter J_z/J_0 for $T = \infty$ (blue) and $T = 0$ (red) [219]. The red curve shows the gapless point at $J_c^{-1} = 2\sqrt{2}$, while in the infinite-temperature limit, we find a gapless-gapped transition for the Majorana fermions at $J_c^{\infty} \sim 2$, which separates a *thermal metal* phase of the Majoranas from a trivial insulator. This limit describes the physical behavior of the Kitaev Shastry-Sutherland model below the spin fractionalization crossover.

gaps for numerous coupling parameters J_z/J_0 in the infinite-temperature limit. The results are given in Fig. 5.12, where we can see that at $T = \infty$, the gap of the system opens for $J_z/J_0 \gtrapprox 2$ (the band gaps for $T = 0$ are given in the same plot, where we can see the gapless point at $J_z = J_c^{-1}$).

Remarkably, we find that the disordered $\mathbb{Z}_2$ spin liquid regime of the Kitaev Shastry-Sutherland model in the specified parameter range is not a homogeneous phase, but further subdivided into a gapless and gapped region in terms of the Majorana band structures. In our calculations, this subdivision even extends to the high-temperature paramagnetic phase at $T = \infty$. However, we consider that the description of the Kitaev spin system in terms of fractionalized quasiparticles does not reflect the true physical behavior of the system above the fractionalization crossover. Here, it is in the paramagnetic phase, and described by disordered spins. Therefore, the gapless-gapped transition in the Chern number results at $T = \infty$ in Fig. 5.10 can be regarded as an artifact of the Majorana description.

Thermal metal

Below the fractionalization crossover, in contrast, the system is well described by the fractionalized quasiparticles. Thus, the gapless-gapped transition seen in Fig. 5.13 is a feature which truly belongs to the intermediate-temperature region. Concretely, the gapless phase here can be interpreted as a *thermal metal* of Majorana fermions in the presence of a disordered background [216–218, 228–230].

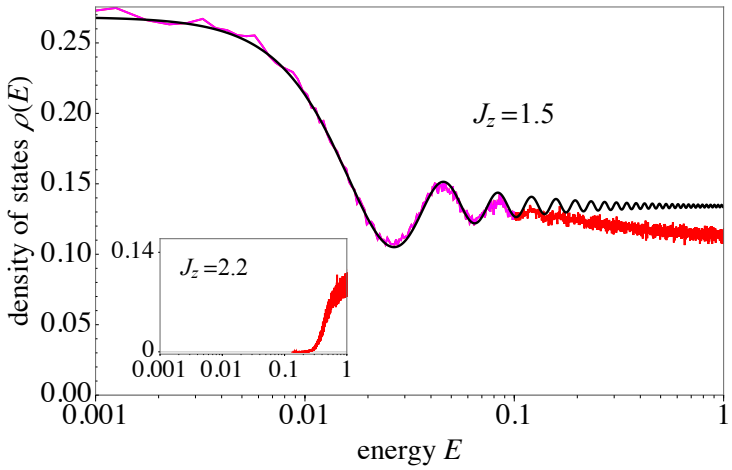

Figure 5.13: Low-energy density of states $\rho(E)$ for the Kitaev Shastry-Sutherland model at $T = 1.86$ and $J_z = 1.5$ (inset: $J_z = 2.2$). The oscillations of $\rho(E)$ follow the sinusoidal function $\rho(E) = \alpha + \sin(2\pi EL^2)/(2\pi EL^2)$ predicted by random matrix theory for the metallic state in symmetry class D [218, 227]. This supports that the disordered $\mathbb{Z}_2$ spin liquid phase of the system in the gapless limit can already be effectively described as a thermal metal, although time-reversal symmetry is only broken at lower temperatures. For $J_z > 2$, the system becomes gapped (inset).

This phase is one of three possible regimes that may occur in free fermion systems with symmetry class D, namely beside the topological and trivial insulator phase. In the intermediate-temperature regime of the Kitaev Shastry-Sutherland model, the disordered background is obviously provided by the $\mathbb{Z}_2$ gauge field. However, since the intermediate phase is situated at temperatures higher than T_c, the system is, in the strict sense, not in symmetry class D anymore, because class D requires broken time-reversal symmetry. Nonetheless, we find a clear signature of the thermal metal phase when we look at the low-energy density of states $\rho(E)$ of the Majorana fermions in the intermediate temperature regime. For $E \to 0$, the DOS shows oscillations which are typical for class D, and correspond to a characteristic sinusoidal function $\rho(E) = \alpha + \sin(2\pi EL^2)/(2\pi EL^2)$ (with a fit parameter α) that has been predicted by random matrix theory [218, 227] (see Fig. 5.13 for the DOS at $J_z = 1.5$ and $T = 1.86$). This supports the idea that signatures of symmetry class D survive in the gapless intermediate-temperature regime of the Kitaev Shastry-Sutherland model, which allows for an effective description of this phase as a thermal metal. Notably, the gapless-gapped transition is not an extension of the chiral to trivial transition at $T = 0$, which occurs at the gapless quantum critical point $J_z = J_c^{-1}$. Instead, the transition jumps from J_c^{-1} to $J_c^{\infty} \sim 2$. For $J_z \to \infty$, the Kitaev Shastry-Sutherland system transforms into a dimer model.

Apart from the gapped intermediate-temperature phase at $J_z > J_c^{\infty}$, the Chern

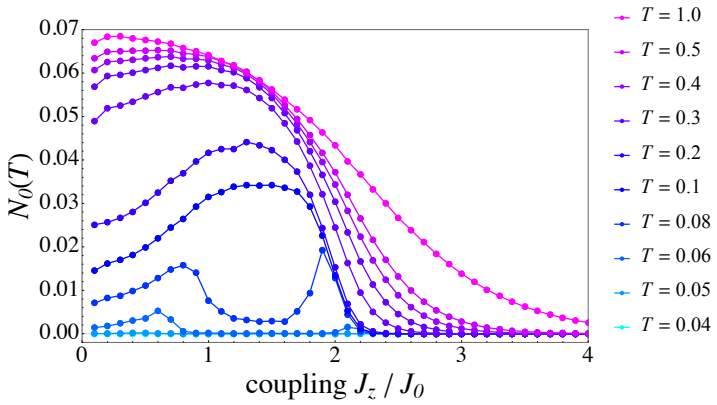

Figure 5.14: Integral $N_0(T) = -\int_{E=0}^{\infty} \frac{\partial n_F(E,T)}{\partial E} \rho(E) dE$ as function of the coupling ratio J_z/J_0. For finite temperatures, $N_0(T)$ gives an estimate for the density of states close to the Fermi level $E = 0$. The value $N_0(T) = 0$ therefore suggests a finite band gap. This is the case for the data points with $J_z/J_0 < 0.3$ and temperatures $T = 0.02 - 0.04$, which correspond to the partially flux-ordered phase. We therefore assume that the partially flux-ordered phase is gapped, and that the gap vanishes at the square-ordering crossover temperature T''.

number results suggest another gapped region for $J_z < 1$. Here, a narrow blue stripe above the partially flux-ordered phase encloses the thermal crossover points associated with the ordering of square plaquettes. For this stripe, the Chern number is apparently $|\nu| \sim 0$, while the contour plot for the partially flux-ordered region itself shows a similar orange shade as the gapless intermediate-temperature phase, indicating an average $0 < |\nu| < 1$. To determine if the partially flux-ordered phase is gapless or gapped, we consider the integral

$$N_0(T) = -\int_{E=0}^{\infty} \frac{\partial n_F(E,T)}{\partial E} \rho(E) dE, \tag{5.13}$$

where $\rho(E)$ is the Majorana density of states, and $n_F(E,T)$ the Fermi function at temperature T, whose derivative $\frac{\partial n_F(E,T)}{\partial E}$ has a peak in the vicinity of $E = 0$. For $T \to 0$, this peak becomes a negative Delta-function

$$\frac{\partial n_F(E,T)}{\partial E} \xrightarrow{T\to 0} -\delta(E), \tag{5.14}$$

and the integral $N_0(T)$ just gives the density of states at the Fermi level $E = 0$,

$$N_0(T) \xrightarrow{T\to 0} \rho(E = 0). \tag{5.15}$$

For finite temperatures, the Delta-function becomes a finite peak with a width $\Delta\epsilon \sim T$ (for small T), and the integral $N_0(T)$ provides an estimate for the density of states in the vicinity of the Fermi level.

We evaluate $N_0(T)$ as a function of the coupling ratio J_z/J_0 for different temperatures T (Fig. 5.14). Since $N_0(T)$ estimates the density of states at low E, it is zero whenever the system is gapped. We can see in the plot that this is the case for the temperatures $T = 0.02 - 0.04J_0$, which lie well above the phase transition temperature $T_c < 0.01J_0$ for $J_z/J_0 < 0.3$, but below the square-ordering crossover at $T'' \sim 0.1J_0$ (Fig. 5.10), and therefore right within the partially flux-ordered phase. Thus, the results for $N_0(T)$ suggest that the partially flux-ordered phase is gapped. For increased temperatures, on the other hand, the values of $N_0(T)$ become finite for all coupling ratios J_z/J_0, which includes the range of the partially flux-ordered phase, and converge to zero only for very large values of J_z/J_0. This agrees qualitatively with results for the infinite-temperature band gaps that are shown in Fig. 5.12.

For $J_z/J_0 < 1$, we can conclude that the Kitaev Shastry-Sutherland system starts in the gapped chiral spin liquid ground state at $T = 0$. For increasing temperatures, it undergoes a thermal phase transition at T_c and enters the partially flux-ordered phase, which is still gapped, but where the gap is shrinking when T is raised. For $T \to T''$, the gap vanishes, and the system enters the thermal metal phase, which inherits some class-D-signatures of the CSL ground state. The paramagnetic phase is finally reached at the spin fractionalization crossover at T'.

5.2.4 Vison gaps

We close the discussion of the first phase diagram cut by examining the relation between the transition temperatures and the vison gaps[3] of the system (Fig. 5.15). Corresponding to the two sets of elementary plaquettes in the Shastry-Sutherland lattice, we can distinguish two kinds of vison excitations. A pair of visons on the *triangle plaquettes* is created by flipping a diagonal J_z bond, whereas flipping a horizontal or vertical bond generates a pair of visons on the *square plaquettes*. Fig. 5.15 a shows the values of the critical temperature T_c as a function of the triangle-plaquette vison gap Δ_t. Fig. 5.15 b shows the values of the square-ordering transition temperature, which is T'' for $J_z/J_0 \leq 0.9$ and T_c for $J_z/J_0 \geq 0.9$, as a function of the square-plaquette vison gap Δ_s.

We can determine a pronounced linear correlation between T_c and Δ_s for a wide range of values $\Delta_s \leq 0.5$, which corresponds to coupling parameter values $J_z/J_0 > 1.5$ (orange and blue data points). For the partial-flux order limit $J_z/J_0 < 1$, there is apparently also a linear correlation between the square-ordering temperature T'' and Δ_s with a different (negative) slope (red data points). This implies that a larger vison gap corresponds to a lower transition temperature

[3]The vison gaps have first been calculated by Dr. Vatsal Dwivedi.

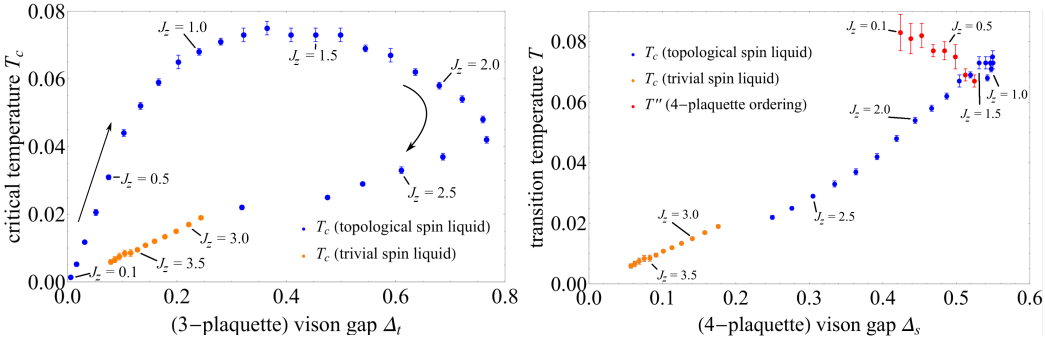

(a) 3-plaquette vison gaps

(b) 4-plaquette vison gaps

Figure 5.15: Transition temperature of the triangle- / square plaquettes as a function of the vison gap Δ_t / Δ_s. Both curves suggest correlations between the quantities, which supports results from 3D Kitaev systems (Fig. 4.7). The arrows indicate increasing values of J_z/J_0.

T'' in this limit. For $1 \leq J_z/J_0 \leq 1.5$, where Δ_s is the largest, the data points are too close to each other to determine a functional relation. It is here that the T-Δ_s curve "U-turns" after the gap Δ_s reaches its largest value.

For the 3-plaquettes, we see a linear correlation between T_c and Δ_t for the trivial phase $J_z/J_0 > 2.8$ and parts of the chiral phase $J_z/J_0 \geq 2.3$, where Δ_t has its maximum value. The pronounced "U-turn" of the T_c-Δ_t-curve thereafter corresponds to moving J_z to lower values. For $J_z/J_0 \leq 1$, there is again a linear correlation between both quantities.

These results are consistent with the correlation between the flux-ordering temperature T_c and the vison gap Δ for 3D Kitaev systems (Fig. 4.7). However, the "U-turn"-behavior that is witnessed for both the T-Δ_s- and the T_c-Δ_t-curve suggests that the relation between transition temperature and gap is not a simple, global linear function $T(\Delta) = m\Delta$. Instead, the slope m is changed in different parameter regions, whereas in the region of extremal Δ-values, there is no linear correlation at all. Nonetheless, it can be stated that a general correlation between both quantities is verified by these results.

5.3 Second-order spin liquid

In the second part of our results discussion, we look at the horizontal cut trough the phase diagram which is depicted as a set of magenta points in Fig. 5.16. Here, we choose a fixed diagonal bond coupling $J_z = 1$ and staggering parameter $\delta J = 0.7$, and modify the parameter for the horizontal and vertical coupling J_0 in steps of $\Delta J_0 = 0.05$ from 0.1 to 0.65. This cut through the phase diagram starts in the chiral spin liquid phase for low values $J_0 < J_c = \frac{1}{2\sqrt{2}}$, and enters the second-order topological insulator phase beyond the quantum critical point, for $J_0 > J_c$.

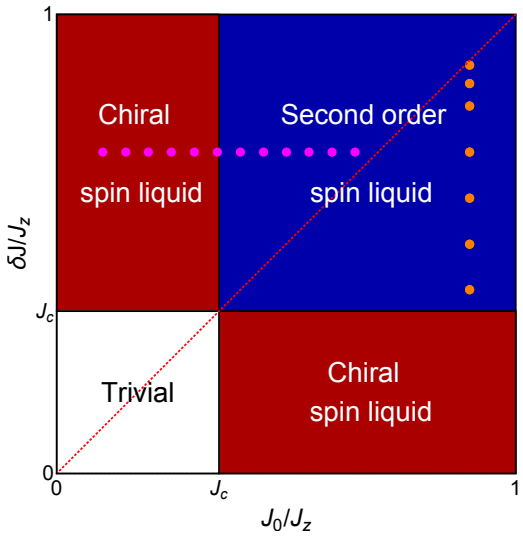

Figure 5.16: Coupling parameters in the QMC simulations (2). Another horizontal cut through the ground state phase diagram of the spin-$3/2$ Kitaev model [83] is realized by keeping $J_z = 1$ and $\delta J = 0.7$ fixed, and varying J_0 from 0.1 to 0.65 (magenta points). This corresponds to moving from the chiral spin liquid to the second-order spin liquid phase. In addition, we examine the evolution of thermal signatures in SOSL phase for the tetragonal chain approximation $\delta J \to J_0$ at constant $J_0 = 0.9$ (orange points). At $J_0 = \delta J$ (red dottted line), the model is transformed into decoupled chains of square plaquettes (Fig. 5.21).

Thermal phase diagrams analogous to the ones presented in the last section are shown for this cut in Figs. 5.17 and 5.18, with the specific heat signatures, the chirality $|\mathrm{Im}(\kappa)|$, the square-plaquette flux $\overline{W_p}$ and the Chern number $|\nu|$ given as functions of the coupling ratio J_z/J_0 and the temperature T.

In the following, we discuss the occurrence of thermal transitions along this horizontal cut through the phase diagram, and observe what is another kind of partially flux ordered phase, which the Kitaev Shastry-Sutherland model exhibits above the second-order spin liquid regime. The occurrence of this phase manifests itself in an additional thermal crossover, which is presented in detail at the example of another parameter point in the ground state phase diagram (the results for which have formerly been presented in Ref. [83]). In addition, we discuss results for the tetragonal chain limit of the system, which is constructed by increasing the staggering parameters as $\delta J \to J_0$.

5.3.1 Thermal transitions

Our numerical results confirm the existence of the low-temperature phase transition also for the second-order spin liquid regime of the Kitaev Shastry-Sutherland model. In Figs. 5.17 and 5.18, the position of the corresponding low-temperature

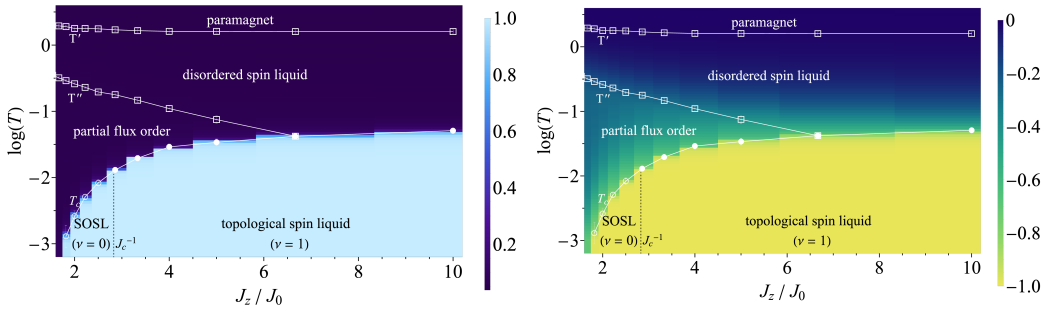

(a) absolute chirality $|\mathrm{Im}(\kappa)|$ **(b)** square-plaquette flux $\overline{W_p}$

Figure 5.17: Thermal phase diagram (1) for fixed coupling parameters $J_z = 1$, $\delta J = 0.7$, and $J_0 \in [0.1, 0.65]$. The transition temperatures of the system are given as a function of the coupling ratio J_z/J_0 (white / black data points). The density plots show the chirality $|\mathrm{Im}(\kappa)|$ (a), and the average 4-plaquette flux $\overline{W_p}$ (b). Filled (open) circles indicate phase transition temperatures T_c in the CSL (SOSL) regime. Open squares indicate thermal crossovers associated with partial flux ordering (T'') and spin fractionalization (T').

peak in the specific heat C_v is indicated by the filled circles for the chiral spin liquid, and by open circles for the second-order spin liquid (SOSL) regime. The occurrence of the thermal phase transition is expected due to the fact that the ground state of the SOSL phase also breaks time-reversal symmetry by ordering of the triangle plaquettes. This ordering is shown by the results for chirality $|\mathrm{Im}(\kappa)|$ in Fig. 5.17a, which is $|\mathrm{Im}(\kappa)| = 1$ below the low-temperature transition, and $|\mathrm{Im}(\kappa)| = 0$ above. A finite-size scaling analysis of the low-temperature peak in the SOSL phase is presented in Fig. 5.20 for the parameter point $J_z = 1$, $J_0 = 0.9$, $\delta J = 0.4$, and shows that this peak diverges with the system size.

In Fig. 5.17, we see that the position of the low-T transition in temperature space monotonously decreases if J_z/J_0 is decreased. In the chiral spin liquid phase, it shows the particularly high value $T_c \sim 0.1 J_z$ for large values of J_z/J_0, a phenomenon which is discussed above. For $J_z/J_0 \to J_c^{-1} = 2\sqrt{2}$, the transition temperature reaches the order of magnitude $T_c \sim 10^{-2} J_z$, and, in the SOSL phase, it is further lowered to $T_c \to 10^{-3} J_z$. We note that for $J_z/J_0 < 1.8$, the transition temperature T_c moves below the temperature range of our QMC simulations. In this limit, where the coupling $J_0 - \delta J$ on half of the lattice bonds approaches 0, it is expected that the transition temperature rapidly decreases to lower temperature scales. At $J_0 = \delta J$, the Kitaev Shastry-Sutherland model becomes a set of decoupled chains, where one half of the square plaquettes, namely the one that is composed of two triangles, is connected by the diagonal J_z-bonds (see Fig. 5.21). We closely examine the evolution of physical observables in this limit, which is discussed in Sec. 5.3.3.

Above the thermal phase transition, we observe two additional peaks in the

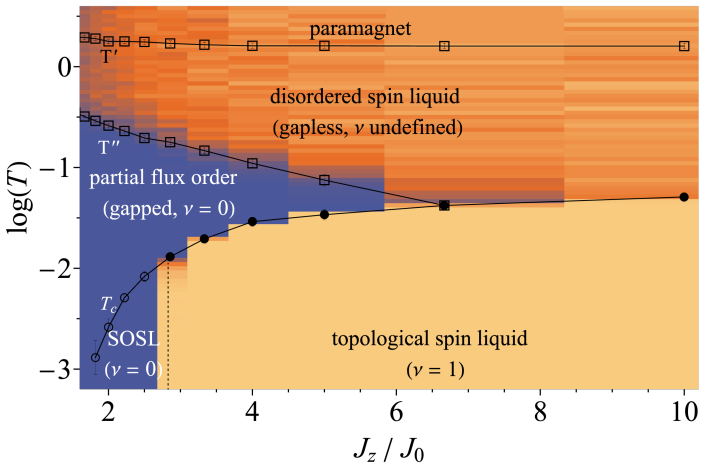

Figure 5.18: Thermal phase diagram (2) for fixed parameters $J_z = 1$, $\delta J = 0.7$. The transition temperatures of the system are given as a function of the coupling ratio J_z/J_0 (white / black data points). The density plot shows the Chern number $|\nu|$, which is trivial $|\nu| = 0$ in the SOSL and partially flux-ordered phase, and finite, $|\nu| = 1$, in the CSL phase.

specific heat at coupling parameters $J_z/J_0 \lesssim 6.7$, which are marked by the open squares in the phase diagrams in Fig. 5.17. Apart from the expected high-temperature peak, which lies constantly at $T' \sim 2J_z$, there is an additional peak at $T'' \sim 10^{-1}J_z$. Both peaks show no divergence in the finite-size scaling analysis and therefore suggest the occurrence of thermal crossovers at the corresponding temperature scales (Fig. 5.20). While the high-temperature crossover at T' is again associated with spin fractionalization, and separates the high-temperature paramagnetic phase from the intermediate disordered $\mathbb{Z}_2$ spin liquid regime, the intermediate-temperature crossover at T'' signals the transition of the system into a particular phase with partially ordered square-plaquette fluxes. This version of partial flux ordering in the SOSL phase is discussed in detail in the next section.

The numerical results for the Chern number $|\nu|$ are presented in the contour plot in Fig. 5.18. As expected for the low-temperature limit, the chiral spin liquid phase has a finite Chern number $|\nu| = 1$ below T_c, whereas for $J_z/J_0 = J_c^{-1}$, we encounter a sharp cut, and $|\nu| = 0$ in the second-order spin liquid (SOSL) regime. We have discussed in Sec. 2.3.3 that the SOSL regime corresponds to a second-order topological insulator in terms of the Majorana fermions, which is characterized by a trivial Chern number and the absence of topologically protected edge modes, but possesses corner modes. These corner modes are invariant under deformations of the Hamiltonian which leave its anticommutation relation with the mirror symmetry operators $\mathcal{M}_{11}$, $\mathcal{M}_{1\bar{1}}$ and the bulk gap intact, Eq. (2.54).

The occurrence of these topologically protected corner modes cannot be mea-

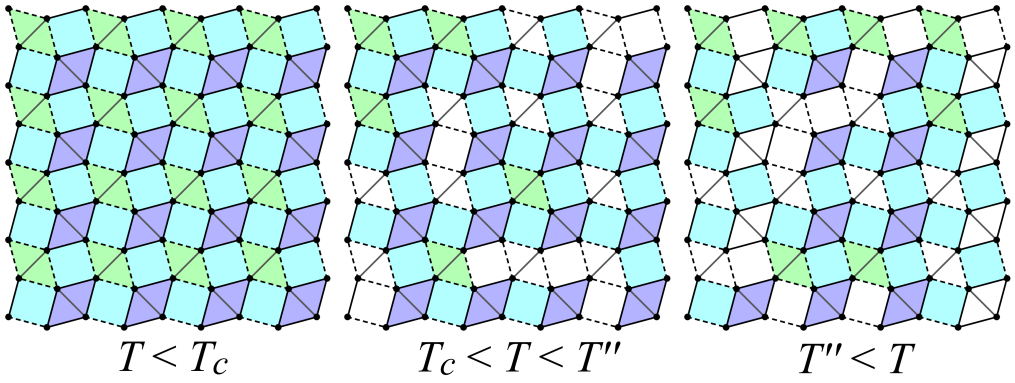

Figure 5.19: Partial flux order II. In the SOSL phase, the partial flux ordering is determined by the staggering of bond couplings (dashed / solid lines). At $T < T_c$, all square plaquettes have a π-flux (green). At T_c, the plaquettes with only weak edge couplings $J_0 - \delta J$ are the first to become disordered, with π- and 0-fluxes (green / red). Within this partially flux-ordered phase at $T_c < T < T''$, the squares with two weak and two strong bond couplings become disordered. Finally, at T'', also the square plaquettes with strong couplings disorder.

sured in terms of the finite Chern number, but has been shown by analyzing the Wannier band structure of the system in this phase in Ref. [83]. With the QMC simulations presented here, we cannot directly access the topological features of the SOSL phase, but investigate how this phase develops at finite temperatures. Here, we find that the gapped nature of the ground state phases survives above the finite-temperature phase transition for $J_z/J_0 \lesssim 6.7$, where the partial flux ordered phase inherits the vanishing Chern number $|\nu| = 0$ from the SOSL phase (see the blue region in Fig. 5.18). Above T'' (which is identical to T_c above $J_z/J_0 \sim 6.7$, where no partial flux ordering occurs), the system enters the disordered $\mathbb{Z}_2$ spin liquid regime, which is gapless for all parameters, although a gap is expected to open in the tetragonal chain limit $\delta J \to J_0$ [220]. The latter is suggested by the Chern number results, and has been confirmed by calculations of the band gaps at $T = \infty$.

5.3.2 Partial flux order II

The phase diagrams in Fig. 5.17 reveal a particular kind of partially flux ordered regime, which exists in the parameter range $J_z/J_0 \lesssim 6.7$ and sets in above the thermal phase transition at T_c. Here, things are slightly different from the situation seen before, for the chiral-trivial transition corresponding to the first phase diagram cut. While there, we observe a small region where the square plaquettes are *fully* ordered, while the triangle plaquettes remain disordered, the partial flux order regime here is characterized by *partial* order of the square plaquettes, while the triangle plaquettes remain fully disordered.

This can be most clearly seen when comparing the two contour plots in Fig. 5.17, which show the chirality $|\mathrm{Im}(\kappa)|$ (Fig. 5.17 a) and the square-plaquette flux operator eigenvalue $\overline{W_p}$ (Fig. 5.17 b) as function of J_z/J_0 and T. We see that the chirality is always ordered for $T < T_c$ (indicated by the light blue region) and ordered for $T > T_c$ (blue region). The square plaquette fluxes are also fully ordered at $T < T_c$, which is shown by the yellow region indicating a flux operator eigenvalue $\overline{W_p} = -1$. Full disorder of the square plaquettes is, however, only reached above the intermediate-T crossover indicated by the open squares. Here, the region with fully disordered fluxes, $\overline{W_p} = 0$, is shown in blue. The intermediate-temperature regime between the crossover and the thermal phase transition on the other hand appears as a green region in Fig. 5.17 b, which corresponds to average flux operator eigenvalues $-0.75 \lessapprox \overline{W_p} \lessapprox -0.25$. A visualization of this partial flux order is shown in Fig. 5.19.

The occurrence of an intermediate partially flux-ordered regime is a generic phenomenon of the Kitaev Shastry-Sutherland model in the SOSL phase. A more detailed understanding of this regime can be gained from looking at the data curves for $\overline{W_p}$. In Fig. 5.20, we show numerical results for a parameter point belonging to the second (vertical) cut through the SOSL phase, which is depicted as a set of orange points in Fig. 5.16. Here, we can see the specific heat C_v showing a three-peak structure, with a low-temperature peak that strongly scales with the system size, and two high-temperature peaks showing no such scaling behavior. The critical temperature T_c, which is extrapolated from the positions of the low-T peak, and the two crossover temperatures T' and T'' are indicated by the dashed grey lines in all figures. This makes it easy to see that, at the high-temperature peak at T', which corresponds to spin fractionalization, the square-plaquette flux, measured by the operator eigenvalue $\overline{W_p}$, slowly starts to order, and assumes the value $\overline{W_p} = -0.25$ just at the temperature of the intermediate crossover T''. In the entropy S, the region below T'' exhibits a plateau. Lowering the temperature, the square plaquette flux $\overline{W_p}$ further decreases until reaching the value $\overline{W_p} = -0.75$ at the position of the low-temperature specific heat peak. Here, at the thermal phase transition, we find a sudden drop of $\overline{W_p}$ to the ground state value $\overline{W_p} = -1$.

What is the explanation for the two characteristic transition values $\overline{W_p} = -0.25/-0.75$, which signal the ordering of three quarters / one quarter of all N_p square plaquettes? When looking at the Shastry-Sutherland lattice with the staggered coupling parameters $J_0 \pm \delta J$, we see that the latter is composed of three different kinds of plaquettes: Every fourth plaquette contains diagonal J_z-bonds *and* four (horizontal and vertical) bonds with strong coupling $J_0 + \delta J$. It is expected that these $N_p/4$ plaquettes with strong coupling are the last to become disordered if δJ is finite and the temperature is increased. Analogously, there is another set of $N_p/4$ plaquettes which possesses diagonal bonds and only weakly coupling edges $J_0 - \delta J$. We can expect that only a small temperature is required

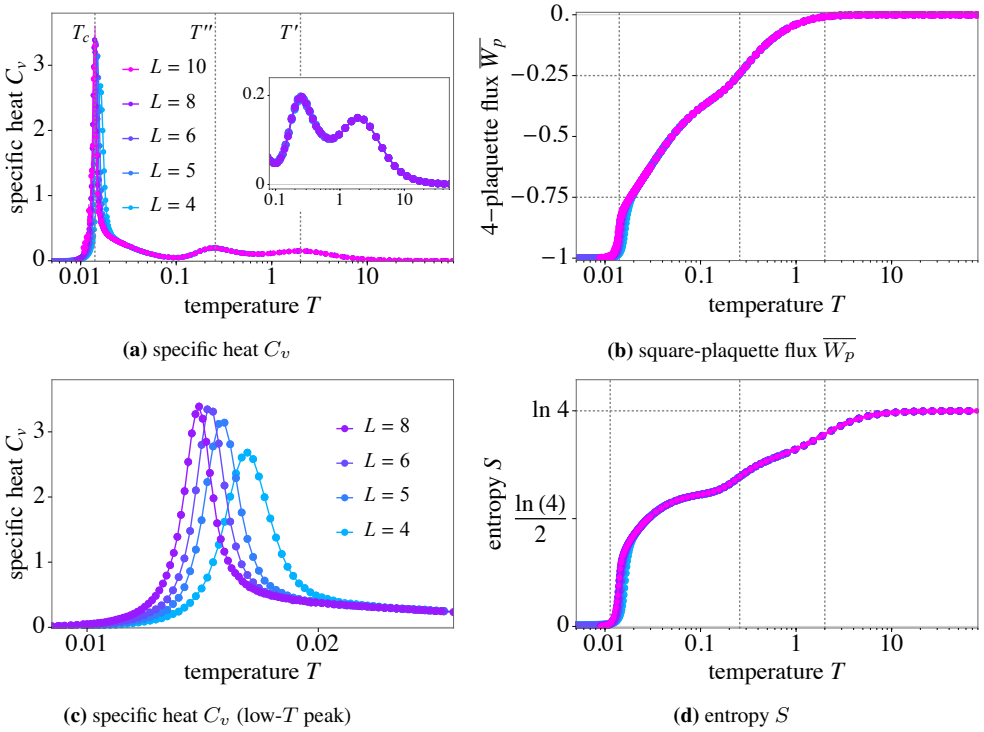

(a) specific heat C_v

(b) square-plaquette flux $\overline{W_p}$

(c) specific heat C_v (low-T peak)

(d) entropy S

Figure 5.20: Partial flux ordering in the SOSL phase (here, $J_0 = 0.9$ and $\delta J = 0.4$) [83]. The specific heat C_v (a,c) shows at three-peak structure, indicating a thermal phase transition at $T \sim 0.01 J_z$ and two thermal crossovers at $T'' \sim 0.25 J_z$ and $T' \sim 2 J_z$. While the high-temperature crossover is associated with spin fractionalization and the low-T phase transition with spontaneous breaking of time-reversal symmetry, due to the ordering of triangles, the intermediate crossover indicates a partial flux-ordering of square plaquettes (b), which is a consequence of staggered bond couplings $J_0 \pm \delta J$. This choice of coupling generates a hierarchy between the square plaquettes of the lattice, which results in different ordering temperature scales. In the entropy S (d), the partial flux order manifests itself as a plateau at intermediate temperatures.

to disorder these $N_p/4$ plaquettes. The remaining $N_p/2$ plaquettes has two edges with strong coupling $J_0 + \delta J$ and two edges with weak coupling $J_0 - \delta J$, which suggests an intermediate temperature scale for their disordering.

Thus, the emergence of the partially flux-ordered phase at intermediate temperatures can be explained as follows: At $T = 0$, all square plaquettes are in the ordered π-flux phase. If the temperature is increased to the scale of the critical temperature T_c, the triangle plaquettes become disordered. We saw in the last section that the ordering of triangles implies the ordering of squares, but, on the other hand, the squares may assume an ordered configuration even if the triangles remain disordered. Since the temperature scale for the ordering of triangles is set by the diagonal bond coupling parameter J_z, the squares may order at higher temperatures if their bonds are equipped with a stronger coupling than J_z. In the last sec-

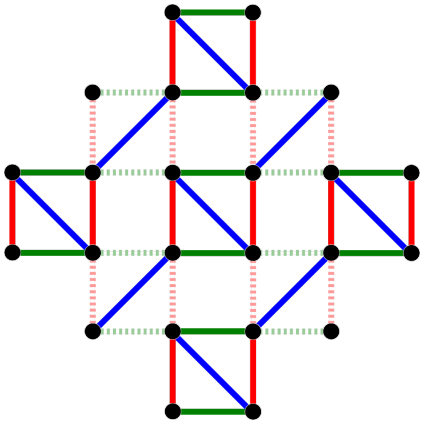

Figure 5.21: Chain limit of the Kitaev Shastry-Sutherland model. For $\delta J \to J_0$, the couplings on one half of the lattice bonds vanish, and the system becomes a decoupled set of tetragonal chains [220].

tion, δJ is chosen as zero, and all horizontal and vertical bonds have a coupling J_0. Here, on the other hand, the finite staggering parameter δJ leads to the described hierarchy of plaquettes with respect to their bond couplings. For all choices of parameters in the SOSL phase, we find that $J_0 - \delta J < J_z$, so the ordering of triangles implies the ordering of square plaquettes with only weak bond coupling $J_0 - \delta J$ on the edges. Since these plaquettes form $1/4$ of all square plaquettes, their disordering explains the average flux operator eigenvalue $\overline{W_p} = -0.75$ at the critical temperature T_c. In the intermediate-temperature phase, the plaquettes with two strong and two weak edge couplings become disordered due to thermal fluctuations, which form $1/2$ of all square plaquettes. Thus, the value of $\overline{W_p}$ slowly rises from $\overline{W_p} = -0.75$ to $\overline{W_p} = -0.25$. The squares with only strong bond couplings $J_0 + \delta J$ become the last to disorder under thermal fluctuations. This partial flux ordering / disordering is a purely local phenomenon, which is analogous to the low-temperature flux ordering in the Kitaev honeycomb model. Therefore, it only produces a smooth thermal crossover at the temperature $T'' = 0.25 J_z$.

5.3.3 Tetragonal chain limit

In a final step, we examine the tetragonal chain limit [220] of the Kitaev Shastry-Sutherland model by increasing the staggering parameter $\delta J \to J_0$ (see the orange points in the ground state phase diagram, Fig. 5.16). A visualization of this limit is presented in Fig. 5.21. As δJ approaches J_0, the coupling on the dashed bonds, $J_0 - \delta J$, vanishes, and the model effectively becomes a set of decoupled tetragonal chains. These consist of the $N_p/4$ plaquettes with diagonal J_z-bonds and only strong edge couplings $J_0 + \delta J$, which are connected by the other half of J_z-bonds.

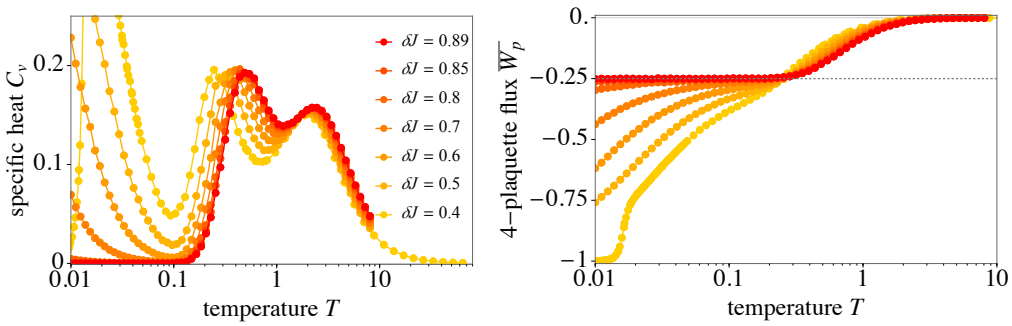

(a) specific heat C_v

(b) square-plaquette flux $\overline{W_p}$

Figure 5.22: Observables in the tetragonal chain limit [83]. As we increase $\delta J \to J_0$, the ordering on three quarters of the square plaquettes (those which possess weak edge couplings), is effectively suppressed along with the thermal phase transition. At the same time, the coupling $J_0 + \delta J$ is increased, which leads to a higher crossover temperature T''.

Numerical results for fixed coupling parameters $J_z = 1$, $J_0 = 0.9$ and different choices for δJ are presented in Fig. 5.22. Again, we consider the specific heat C_v and the average square-plaquette flux $\overline{W_p}$, and focus on the intermediate-temperature regime, where the thermal crossover associated with partial square-plaquette flux ordering is situated. In the specific heat C_v (Fig. 5.22 a), we can see that the increasing of δJ leads the thermal crossover peak at T'' to approach the spin fractionalization peak at T', until both peaks form a joined double-peak structure, while at the same time, the low-temperature peak at T_c, which is associated with the thermal phase transition, rapidly moves towards lower temperature scales. This merging tendency of the two high-temperature specific heat peaks is accompanied by the square-plaquette flux, measured in terms of the operator eigenvalue $\overline{W_p}$, showing a lower and lower slope below T'', until the (red) curve for $\delta J = 0.89$ saturates at $\overline{W_p} = -0.25$ (Fig. 5.22 b).

We can understand this behavior with the arguments presented in the last section, in the context of partial flux ordering. Lowering $J_0 - \delta J$ reduces the temperature scale at which the dashed square plaquettes in Fig. 5.21 assume the ordered π-flux configuration, and, at the same time, reduces the scale for the ordering of triangle plaquettes. Therefore, as we increase δJ, the low-temperature phase transition peak moves towards $T \to 0$, below the temperature range we performed the QMC simulations in. Likewise, the ordering of half the square plaquettes with two weak and two strong edge couplings is shifted to lower temperatures, which manifests itself in the decreasing slope of $\overline{W_p}$ below T''. The partially flux ordered phase, where only the square plaquettes with strong edge coupling carry a π-flux, thereby becomes a more and more stable phase in temperature space, especially as increasing δJ makes the edge coupling on these ordered plaquettes even stronger and raises the crossover temperature T''. In the extremal case $\delta J \to J_0$,

the ordering of all plaquettes except the ones with strong edge couplings is fully suppressed, and we observe the ordering at $\overline{W_p} = -0.25$ down to lowest temperatures.

5.4 Summary

This chapter has presented quantum Monte Carlo results for the spin-$\frac{3}{2}$ Kitaev Shastry-Sutherland model in different (topological) parameter regimes. With the assignment of staggered bond coupling parameters, the ground state phase diagram of the model separates into two chiral spin liquid phases with finite Chern number $\nu = \pm 1$, along with a topologically trivial and a second-order topological insulator phase (which we dubbed second-order Kitaev spin liquid), the latter two with $\nu = 0$. All these ground state phases are characterized by spontaneous breaking of time-reversal symmetry, which is a consequence of the odd elementary plaquette length in non-bipartite lattice systems. Therefore, all ground state phases of this system are separated from the intermediate-temperature (disordered spin liquid) phase by a thermal phase transition. This distinguishes the system from bipartite Kitaev models, where the gauge-ordering transition at low temperatures is a smooth crossover. The occurrence of spontaneous symmetry breaking also distinguishes the phase transition here from the inverted Ising transition in 3D Kitaev systems. A local order parameter is defined by the chirality κ. The critical temperature in the chiral spin liquid regime, $T_c \sim 0.1 J_z$, is found to be one order of magnitude larger than in other Kitaev systems.

Our QMC studies reveal that the existence of odd (triangle) and even (square) plaquettes in this lattice manifests itself in the occurrence of different phases of the generalized Kitaev model where the $\mathbb{Z}_2$ plaquette fluxes are only *partially* ordered. In these partially flux-ordered phases, the triangle plaquettes always remain disordered, while the square plaquettes either fully order at higher temperatures (which happens in the coupling limit $J_z < J_0$ above the chiral spin liquid phase), or partially order according to the differing coupling scales of their edge bonds (which has been shown to happen above the second-order spin liquid phase). The numerical results confirm a correlation between the transition temperature and the size of vison gaps on the triangle / square plaquettes for different coupling parameters.

Apart from the occurrence of partially flux-ordered phases, we have shown that the intermediate-temperature phase above the chiral spin liquid separates into a gapless and gapped part. The gapless phase can be described as an effective thermal metal, in which signatures of symmetry class D in the Majorana band structure survive the thermal phase transition at lower temperatures.

For the second-order spin liquid phase of the model, we have carefully examined the tetragonal chain limit $\delta J \to J_0$, which is characterized by the sup-

pression of the low-temperature phase transition along with an increase of the square-ordering crossover temperature T''.

Chapter 6

Summary and Outlook

In this thesis, we have presented numerical results from large-scale, sign-problem-free quantum Monte Carlo simulations of 2D and 3D Kitaev systems. The low-temperature behavior of these quantum spin liquid models is described by (itinerant) Majorana fermions, which are coupled to an emergent (static) $\mathbb{Z}_2$ gauge field [27]. Kitaev systems therefore belong to the class of $\mathbb{Z}_2$ spin liquids, for which the physical behavior can be captured in terms of lattice $\mathbb{Z}_2$ gauge theories [50]. In particular, the elementary vison excitations of the $\mathbb{Z}_2$ gauge field are known to be always gapped, while the Majorana fermions may form gapless *or* gapped collective states.

Kitaev systems exhibit a high-temperature thermal crossover, which is associated with the fractionalization of spins, and has been verified for all models presented in this thesis. The primary focus of this work has been on the low-temperature ordering of the $\mathbb{Z}_2$ gauge field into different flux configurations, which are generally characterized by the presence or absence of $\mathbb{Z}_2$ plaquette fluxes. This ordering is associated with a thermal transition, which, depending on the dimensionality of the underlying lattice geometry, and on the presence or absence of sublattice symmetry, may constitute a phase transition *or* a smooth crossover.

Our first study has been focused on Kitaev systems on a family of elementary, tricoordinated 3D lattices. We have verified that the ground state $\mathbb{Z}_2$ flux configurations in these models follow the prediction of Lieb's theorem, which relates the energy-minimizing flux to the plaquette length. The validity of this theorem for the considered lattice systems had been unclear, since all but one of them lack the geometric requirements for the theorem's proof and rigorous application. We have also shown that all considered 3D Kitaev systems undergo a low-temperature thermal phase transition, which is a particular realization of an *inverted Ising transition*. With respect to the $\mathbb{Z}_2$ gauge field, it constitutes a deconfinement-confinement transition that separates different topological regimes of the (loop-like) vison excitations in 3D, namely the high-temperature regime

of proliferating system-spanning visons, versus a low-temperature phase characterized by the absence of such macroscopic visons. We have corroborated this understanding of the thermal phase transition by showing a clear (linear) correlation between the critical temperature and the size of the vison gap.

Apart from supporting this general understanding of the gauge thermodynamics in 3D, we have introduced the concept of "gauge frustration", a phenomenon which is shown to occur in the Kitaev model on a particular 3D lattice. Here, a peculiar competition between the elementary plaquette length and a volume constraint on the plaquette fluxes prohibits a unique $\mathbb{Z}_2$ flux order for a wide range of coupling (an)isotropies, and leads to the emergence of a highly-degenerate, geometrically frustrated gauge manifold at low temperatures. Thereby, the thermal phase transition is suppressed to a lower temperature scale, and realized as an interplay between the Majorana fermions and the $\mathbb{Z}_2$ gauge field, which finally forces the latter into a non-trivial columnar zigzag order. We understand the phenomenon of gauge frustration as an intermediate scenario between the conventional $\mathbb{Z}_2$ spin liquid, which is characterized by a full decoupling of Majorana fermions and gauge field, and a $U(1)$ spin liquid, where the parton degrees of freedom typically remain strongly interacting down to lowest temperatures.

In a second study, we have investigated a generalized 2D version of the Kitaev model on the five-coordinated Shastry-Sutherland lattice. Here, the ordering of the $\mathbb{Z}_2$ gauge field at low-temperatures is accompanied by the spontaneous breaking of time-reversal symmetry, a consequence of the odd plaquette length in this non-bipartite lattice system. Because of the symmetry breaking, the ordering transition is here, unlike in bipartite 2D Kitaev systems, also associated with a thermal phase transition. In addition, the dimensionality of the lattice allows for the occurrence of topological ground states, namely a chiral spin liquid and a second-order spin liquid regime. We show that the critical temperature of the thermal phase transition is particularly large in the chiral spin liquid phase. Moreover, the model possesses a number of (intermediate-temperature) regimes which are characterized by a *partial* ordering of $\mathbb{Z}_2$ fluxes, a result which we show by presenting two thermal phase diagrams for different parameter regimes of the model.

With respect to the method, we have shown in this thesis that the quantum Monte Carlo approach for Kitaev systems introduced by Nasu and Motome [44] can be extended to a Majorana representation based on Kitaev's original, local transformation approach. This modification is possible without the implementation of an explicit reprojection of the Majorana system to the physical subspace, which is supported by scaling arguments and benchmark calculations [145].

This work has treated a number of fields in condensed matter physics which are currently dynamically evolving. On the experimental side, there are various recent approaches for the observation of gauge fields in condensed matter systems, such as optical lattices [231–234]. We have outlined in the introductory chapter of

this thesis that also the hunt for spin liquids is an ongoing mission which includes a broad range of activities [3–8]. In particular, a better understanding of the Kitaev spin liquid and the search for its possible material realizations remain a very active field [38, 43, 73]. From the numerical side, there are numerous lines of research which are suited to support these endeavors. We finish this concluding chapter by naming a few selected paths which have a close physical and methodological relation to the work presented here.

One important line of numerical research is focused on Kitaev systems in magnetic fields. In his original work [27], Kitaev has shown that a small magnetic field perturbation leads to the emergence of a gapped spin liquid with non-Abelian topological order, which is eventually destroyed by an enforced ferromagnetic ordering at a certain critical field strength. The understanding of this well-established scenario for ferromagnetic Kitaev systems has recently been supplemented by an exact diagonalization study of their antiferromagnetic counterparts, which turn out to exhibit a more complex behavior. Here, at intermediate field strengths, the gapped $\mathbb{Z}_2$ spin liquid has been shown to undergo a Higgs transition to a $U(1)$ spin liquid, where the elementary gauge excitations are gapless (massless) [235]. From the perspective of quantum Monte Carlo simulations, it has to be noted that the introduction of a magnetic field term leads to a non-vanishing commutation relation between the Kitaev Hamiltonian and the plaquette flux variable W_p, and therefore lies beyond the scope of the method presented in this thesis. However, such systems have been investigated with a continuous-time quantum Monte Carlo method, which works in the spin basis of the model [236]. These theoretical studies are complemented by numerous experimental activities on Kitaev systems in magnetic fields [118–125].

A modification of the quantum Monte Carlo method used in this thesis is based on the explicit reprojection of the Majorana system into the physical subspace. This approach has also introduced a way to measure dynamical spin correlation functions and structure factors for configurations of $\mathbb{Z}_2$ fluxes, which may lead to the establishment of new physical signatures for fractionalization in Kitaev systems [206, 207].

Finally, an older line of research has opened an interesting perspective by combining Monte Carlo simulations with machine learning techniques [237], and has been explicitly introduced for double-exchange models [238, 239]. The extension of such machine-learning-based Monte Carlo techniques to Kitaev systems remains an open task in computational physics.

Appendix A

Kitaev model

A.1 Lieb's Theorem

[1] The problem of finding the flux ground state for a half-filled band of hopping electrons has been intensely studied in mathematical physics in the early 1990's. The interest for this problem roots in the attention on an intriguing phenomenon that arises in the context of correlated electron systems and superconductivity. It had been noticed that under certain conditions, i.e. in systems with a high electron density, the effect of diamagnetism can be reversed. In these systems, the application of a magnetic field does in fact not raise, but *lower* the energy.

This discovery has led to the formulation of the *flux phase conjecture*, which states that on a planar square lattice with free hopping electrons, the energy minimizing magnetic flux is π per square, if the electron filling factor is $\frac{1}{2}$. More general, it has been stated that on planar lattices, the optimum flux choice per plaquette (circuit) is π for plaquettes containing 0 (mod 4) sites, and 0 for plaquettes with 2 (mod 4) sites. This conjecture has been proven by Lieb and coworkers for several lattice graphs, such as rings, trees of rings, ladders and necklaces [85], which has laid the foundation for the later formulation of *Lieb's theorem* [86].

The set up for Lieb's theorem is a finite graph Λ, consisting of $|\Lambda|$ sites, which are indexed by x, y, and hopping amplitudes $t_{xy} = |t_{xy}|e^{i\phi(x,y)}$ (with $\phi(x,y) = -\phi(y,x)$ and $t_{xx} = 0$ for all x). The quest is for the numbers $\phi(x,y)$ which minimize the electronic ground state energy of the tight-binding Hamiltonian $K = -\sum_{x,y} t_{xy} c_x^\dagger c_y$ (in fact, different fluxes for up- and down-spins are also allowed, as well as further terms in the Hamiltonian, which introduce longer range density-density or spin-spin interactions). It had been formerly proven [85] that the spectrum of the Hermitian matrix $T = \{t_{xy}\}$ only depends on the numbers ϕ trough the *fluxes*. The latter are defined on closed loops (circuits), i.e. sequences

[1] This appendix has been published in Ref. [214].

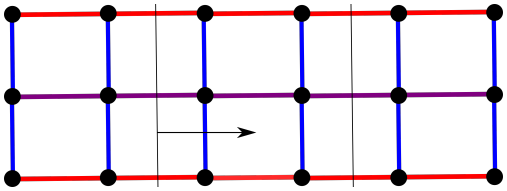

Figure A.1: Reflection symmetry in Lieb's theorem [86]. Square lattice with periodic boundary conditions in the horizontal direction (the sites on the left hand side and on the right hand side are the same). The thin black lines are mirror lines. All the bond couplings (indicated in red, purple and blue) are mirror-symmetric. Lieb's theorem states that a flux π per square minimizes the energy for the plaquettes that are cut in half by the mirror lines. Since the mirror symmetry condition is also fulfilled if the mirror lines are moved by integer multiples of the horizontal lattice vector (indicated in black), it is proven that the π flux is the optimal choice for any square plaquette. The theorem includes the statement that a 0-flux optimizes the mirror-symmetric hexagonal plaquette. It can be generalized to a D-dimensional lattice with (D-1)-dimensional hyperplanes that do not intersect any vertices.

of connected lattice points $x_1, x_2, ..., x_n, x_1$ (with $t_{x_i,x_{i=1}} \neq 0$ for all i) by

$$\Phi = \sum_{i}^{n} \phi(x_i, x_{i+1}) \mod 2\pi. \tag{A.1}$$

Note that in the Kitaev model, the $\mathbb{Z}_2$ gauge field u_{ij} corresponds to the hopping phase factor $e^{i\phi(x,y}$ in the general setup, and the loop operator eigenvalue W_p to the exponentiated flux term $e^{i\Phi}$. The ground state energy of K is given by the sum over the negative eigenvalues of T

$$E_0 = \sum_{\lambda=1}^{N/2} \epsilon_\lambda(T). \tag{A.2}$$

The flux conjecture is proven for systems with a certain periodicity requirement. The lattice Λ has to be (at least) half-periodic in the horizontal direction. Then, it can be cut into two half-cylinders, with the cutting lines intersecting only bonds, such that the two half-cylinders are mirror images of each other in terms of the bond couplings $|t_{xy}|$ (Fig. A.1). The proof of Lieb's theorem, which we do not reproduce in detail here, now shows that the energy-minimizing flux is π for the squares containing the cutting lines. If in addition to the aforementioned geometric requirement, reflection symmetry of the bond couplings is fulfilled for *any* choice of cutting lines, it follows from Lieb's theorem that π is the optimal flux choice for every square of Λ.

The theorem includes the prediction of the respective ground state fluxes of hexagonal, octagonal and further plaquettes with the same argument. It can be further generalized to D-dimensional hypercubes instead of squares, if reflection

symmetry is realized with respect to (D-1)-dimensional hyperplanes. Then, Lieb's theorem states that π is the optimal flux choice for each two-dimensional square plaquette that is cut by the hyperplane. Also here, it follows that the flux is optimal for every plaquette if periodicity in (D-1) dimensions is fulfilled. Among the 3D Kitaev systems, the reflection symmetry condition is completely fulfilled only for (8,3)b, while in (8,3)n, seven out of eight elementary plaquettes per unit cell are mirror-symmetric in the described way.

An alternative proof of Lieb's theorem has later been presented by Macris et al. [87], which makes use of the same symmetry requirements as the proof by Lieb. To summarize, we see that the applicability of the mirror symmetry argument is a *sufficient*, but not a *necessary* condition for the validity of the flux phase conjecture.

Appendix B

Quantum Monte Carlo simulations on Kitaev systems

B.1 The projection operator

The projection operator for the Kitaev model in the Majorana basis is defined as the symmetrization over all $\mathbb{Z}_2$ gauge transformations D_i,

$$\mathcal{P} = \prod_i \left(\frac{1 + D_i}{2} \right). \tag{B.1}$$

$\mathcal{P}$ commutes with $\mathcal{H}_{\text{Kitaev}}$ and defines a projection, as $\mathcal{P}^2 = \mathcal{P}$. Its eigenvalues are $\{0, 1\}$. It can be rewritten as [144]

$$\begin{aligned}
\mathcal{P} &= \prod_{i=1}^{N} \left(\frac{1 + D_i}{2} \right) \\
&= \frac{1}{2^N}(1 + D_1)(1 + D_2)...(1 + D_N) \\
&= \frac{1}{2^N} \left(1 + \sum_i D_i + \sum_{i<j} D_i D_j + ... + \prod_{i=1}^{N} D_i \right) \\
&= \frac{1}{2^N} \sum_{\{i\} \subset \Lambda} \prod_{i \in \{i\}} D_i.
\end{aligned} \tag{B.2}$$

In the last step, $\Lambda = \{1, 2, ..., N\}$ denotes the set of site indices, and the sum is over all subsets $\{i\} \subset \Lambda$. If a term $D_{i_1}...D_{i_k}$ corresponding to a subset $\{i\}$ is multiplied by the whole product $\prod_{i=1}^{N} D_i$, the result is another term which corre-

sponds to the complementary subset $\Lambda\backslash\{i\}$ [144],

$$(D_{i_1}...D_{i_k})\cdot\prod_{i=1}^{N}D_i = D_1D_2...\underbrace{D_{i_1}D_{i_1}}_{=1}...\underbrace{D_{i_k}D_{i_k}}_{=1}...D_N, \tag{B.3}$$

which follows from $D_i^2 = 1$. Therefore, $\mathcal{P}$ can be rewritten as the product [144]

$$\mathcal{P} = \underbrace{\left(\frac{1}{2^{N-1}}\tilde{\sum_{\{i\}}}\prod_{i\in\{i\}}D_i\right)}_{:=\mathcal{S}}\cdot\underbrace{\left(\frac{1+\prod_{i=1}^{N}D_i}{2}\right)}_{:=\mathcal{P}_0}. \tag{B.4}$$

In the operator $\mathcal{S}$, the tilded sum $\tilde{\sum}$ indicates the restriction of the summation to half of the subsets: $\Lambda\backslash\{i\}$ is not included if $\{i\}$ is.

The product of all single-vertex gauge transformation operators D_i in $\mathcal{P}_0$ can be evaluated by [144]

$$\begin{aligned}\prod_{i=1}^{N}D_i &= b_1^xb_1^yb_1^zc_1...b_N^xb_N^yb_N^zc_N\\ &= \prod_i b_i^x\prod_j b_j^y\prod_k b_k^z\prod_l c_l.\end{aligned} \tag{B.5}$$

Now, the operators b_i^γ are commuted with each other, such that the bond operators $\hat{u}_{ij}^\gamma$ can be rebuilt by replacing $b_i^\gamma b_j^\gamma = -i\hat{u}_{ij}^\gamma$. This reordering leads to a prefactor $(-1)^\phi$, where the exponent ϕ depends on the connections of sites in the lattice [144],

$$\prod_{i=1}^{N}D_i = (-1)^\phi\cdot\prod_{\langle i,j\rangle}u_{ij}\cdot(-i)^N\underbrace{\prod_{l=1}^{N}c_l}_{=:\hat{\pi}_c}. \tag{B.6}$$

Based on the transformation of the Majorana fermions c_i to normal modes (using $b_i' = b_{2i}, b_i'' = b_{2i+1}$) [144],

$$c_i = \sum_j^N Q_{ij}b_j, \tag{B.7}$$

the Majorana parity operator $\hat{\pi}_c$ can be replaced by a fermionic parity operator $\hat{\pi}$

via [144]

$$\hat{\pi}_c = \det(Q) \prod_{i=1}^{N} b_i \tag{B.8}$$

$$= \det(Q) \underbrace{\prod_{\lambda=1}^{N/2} (1 - 2n_\lambda)}_{=:\hat{\pi}} . \tag{B.9}$$

The final expression for $\mathcal{P}_0$ results as [144]

$$2\mathcal{P}_0 = 1 + (-1)^{\phi} \cdot \prod_{\langle i,j \rangle} u_{ij} \cdot \det(Q) \cdot \hat{\pi}. \tag{B.10}$$

The phase factor ϕ has arisen due to the reordering of the operators b_i^γ, and therefore depends on the connections in the lattice. It leads to a sign ± 1. For a fixed $\mathbb{Z}_2$ gauge field configuration $\{u_{ij}\}$, both the product $\prod u_{ij}$ and the determinant of the transformation matrix Q are fixed and give signs ± 1. Thus, for a certain lattice and a certain gauge field configuration, the eigenvalue of $\mathcal{P}_0$ solely depends on the parity operator $\hat{\pi} = \prod(1 - 2n_\lambda)$. Explicitly, if $2\mathcal{P}_0$ is applied to a given fermionic Fock state $|n\rangle$,

$$2\mathcal{P}_0 |n\rangle \in \{0, 1\}. \tag{B.11}$$

If the eigenvalue is 0, the state $|n\rangle$ is clearly projected out by $\mathcal{P}$, implying it cannot be a physical state [144].

B.2 Numerical performance

Having presented the analytical background of the quantum Monte Carlo approach in Sec. 3.4, we here discuss a number of technical details of its implementation. First of all, our simulation program is written in the C++ programming language [240]. For matrix operations, we use the linear algebra library Armadillo [241, 242]. Simulations have been performed on the JUWELS high-performance cluster at Forschungszentrum Juelich and the CHEOPS cluster at the University of Cologne.

Apart from this general information, we explain the concrete implementation of the parallel tempering method [179–183] that is used to improve the numerical convergence in the low-temperature limit. Afterwards, we discuss the equilibration and convergence behavior of the simulations. Finally, after looking at the computational efficiency of the program, we present a simple way to address its bottleneck, namely the exact diagonalization required in each Monte Carlo update.

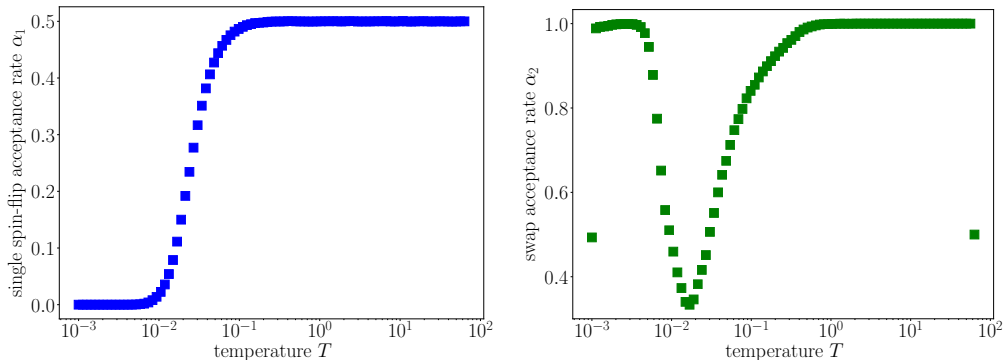

(a) Single spin-flip acceptance rate

(b) Replica exchange (swap) acceptance rate

Figure B.1: Single spin-flip and swap acceptance rate in the QMC simulation on the Kitaev honeycomb model (L = 16). In the region between $T \sim 10^{-2}$ and $T \sim 10^{-1}$, the single-flip acceptance rate (a) drops nearly to zero, while the swap acceptance rate (b) shows a sharp valley here. The T-region corresponds to the thermal crossover of the system (cf. Fig. 3.2).

B.2.1 Parallel Tempering

A large part of the physically interesting behaviour of the Kitaev model happens at very low temperatures. This is particularly true for the physics of the emergent $\mathbb{Z}_2$ gauge field, which is the focus of this work. The ordering of the $\mathbb{Z}_2$ gauge field takes place at a very small temperature scale of $T \sim J/100$. While in two-spatial dimensions, this ordering is accompanied by a thermal crossover, where the $\mathbb{Z}_2$ plaquette flux degrees of freedom locally freeze into their respective ground state configuration, the situation in three dimensions is different. Here, the gauge-ordering comes with a thermal phase transition.

Both low temperatures and phase transitions have a notorious slowing-down effect on Monte Carlo simulations. For low temperatures, the single spin flip Monte Carlo weights $\alpha = e^{-\beta\Delta F}$ get exponentially small, such that the single spin-flip acceptance rate typically drops to zero here (Fig. B.1 a). In the thermal region around a phase transition, on the other hand, the autocorrelation function, Eq. (3.15), for consecutive configuration samples diverges. Thus, subjecting the $\mathbb{Z}_2$ gauge field $\{u_{ij}\}$ only to the presented single spin-flip update is not sufficient to reach an appropriate convergence of the simulation down to the interesting temperature region $T \leq 0.01$.

Therefore, we additionally implement the parallel tempering method [179–183] to the QMC simulation, which is also known by the name *replica exchange*. Here, a Monte Carlo run consists of a set of parallel simulations (processes), which run at different temperatures T_i. Each process has its own system configuration C_i (here, a $\mathbb{Z}_2$ gauge field configuration $\{u_{jk}\}$), and consists of the usual single spin-flip updates of the gauge field, followed by ED calculations. With parallel

tempering, after a number of Monte Carlo sweeps, the processes additionally perform *swaps* with their neighboring processes. The processes i and j attempt an exchange of their configurations, which is, analogously to the single spin-flip step, accepted according to the Metropolis criterium [44],

$$\begin{aligned} \alpha &= \min\left(1, p(C_i, C_j)\right), \\ p(C_i, C_j) &= \frac{e^{-\beta_i F(\beta_i, C_j) - \beta_j F(\beta_j, C_i)}}{e^{-\beta_i F(\beta_i, C_i) - \beta_j F(\beta_j, C_j)}}, \end{aligned} \tag{B.12}$$

with inverse temperature β and free energy F. Note that the free energy has to be calculated four times. Apart from the actual free energy of process i (j), calculated in the gauge field configuration C_i (C_j) at inverse temperature β_i (β_j), which appear in the denominator and have been, ideally, saved within each Monte Carlo process, there are, in addition, the "mixed" free energies (gauge field C_i with temperature β_j and vice versa) in the numerator.

One swap consists of one replica exchange proposal per pair of neighbouring processes $(i, i+1)$, with $i \in \{1, \ldots, N_p\}$ and N_p being the number of parallel processes. We always start with the processes at lowest temperatures T_1, T_2 (Fig. B.2). This way, it is possible that the configuration C_1 wanders through the whole temperature space to process N_p within one swap. In our QMC simulations, we typically perform simulations with $N_p = 64 - 96$ parallel processes. We perform one swap after every Monte Carlo sweep.

The accessible temperature range of the Monte Carlo simulation with parallel tempering depends on the lattice system and the choice of coupling parameters. Typically, this limit is set by the critical temperature, which decreases for anisotropic coupling parameters J^γ. In the best cases, we can reach convergence of our numerical results down to temperatures $T \sim 10^{-4}$, using logarithmically distributed sets of temperature points on intervals $[T_{\min}, T_{\max}]$, that span all physically relevant temperature scales. Typically, we choose $T_{\min} = 10^{-4} - 10^{-3}$ and $T_{\max} = 10 - 100$. In fact, including processes with high temperatures into the swap has turned out to be important to improve the numerical convergence.

Further improvements on the convergence of Monte Carlo with parallel tempering can be reached if, instead of using a generic linear or logarithmic distribution of temperature points, the temperature set is adjusted to the performance of the replica exchanges via advanced *ensemble optimization techniques* [243, 244]. Generally, the distribution of temperature points has to be chosen such that the densities of states $\rho(E)$ at neighbouring temperature points have a finite overlap, i.e. for each pair of neighbouring temperature points, there have to be energy states that are occupied at both temperatures. For the replicas, which can be thought of as performing a random walk in temperature space, the "amount of overlap" determines the local diffusivity between temperatures T_i, T_{i+1}. If this diffusivity is

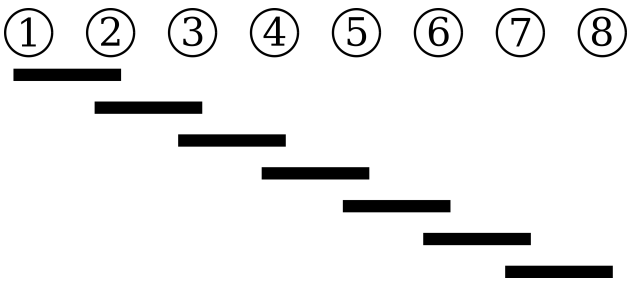

Figure B.2: Replica exchange scheme for one parallel tempering step (swap). One swap consists of one exchange proposal for replicas at neighbouring processes $(i, i+1)$. We always start with the processes at lowest temperatures T_1, T_2, and move forward to higher temperatures.

low in some T-region, for example the region surrounding a thermal crossover or a phase transition, the rate of accepted swaps goes down (Fig. B.1 b). In this case, it is possible to enhance the mobility of the replicas by inserting more temperature points into the respective region. A measure for the replica mobility in the full simulation interval $[T_{\min}, T_{\max}]$ is given by the round-trip current [243, 244]

$$j = D(T)H(T)\frac{df}{dT}. \tag{B.13}$$

A "round trip" refers to a replica moving from $T_{\min}$ to $T_{\max}$ and backwards. In Eq. (B.13), $D(T)$ is the local diffusivity, $H(T)$ the probability distribution of the temperatures ($H(T) \propto 1/\Delta T$), and the function f,

$$f(T) = \frac{n_+(T)}{n_+(T) + n_-(T)}, \tag{B.14}$$

is a ratio of histograms $n_+(T)$ and $n_-(T)$, which count the replicas moving "right" in T-space ("+"), i.e. coming from $T_{\min}$ and moving towards $T_{\max}$, and those moving "left" (coming from $T_{\max}$ and moving towards $T_{\min}$). These histograms are recorded during the QMC simulation. An example plot for the function $f(T)$ is given in Fig. B.3. Having the values of $f(T)$ for a given distribution of temperature points at hand, an improved distribution $H(T)$, which maximizes the round trip current j, can be easily generated. In Ref. [243, 244], it is shown that the optimized set is given by

$$H_{\text{opt}}(T) \propto \frac{1}{\sqrt{D(T)}}, \tag{B.15}$$

and the n-th temperature point of the optimized set can be obtained by numerical integration

$$\int_{T_0'}^{T_n'} H_{\text{opt}}(T)dT = \frac{n}{N}, \tag{B.16}$$

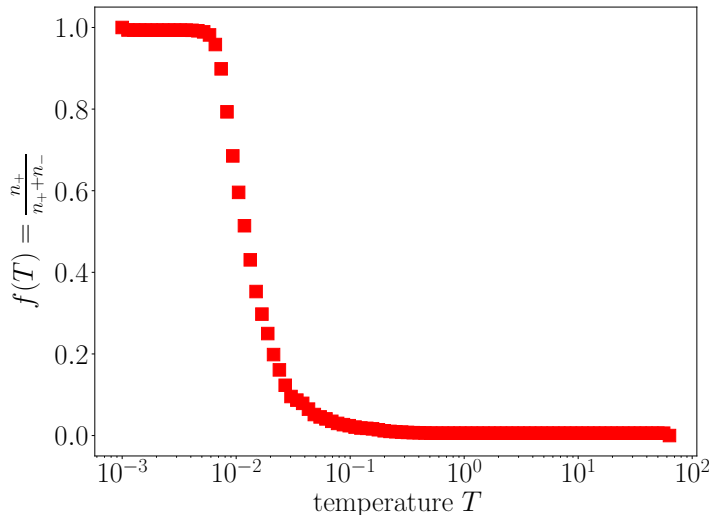

Figure B.3: Histogram ratio function $f(T)$ for the QMC simulation on the Kitaev honeycomb model (L = 16). $f(T)$ gives a ratio for the histograms n_+ and n_-, which, during the Monte Carlo simulation with parallel tempering, measure the replicas coming from $T_{\min}$ and $T_{\max}$. The number of "right-moving" replicas n_+ decreases in the region of the thermal crossover of the Honeycomb Kitaev system (Fig. 3.2). The function $f(T)$ is used to generate an optimized ensemble of temperature points.

where N is the total number of temperature points.

We have carefully analyzed the function $f(T)$ for our QMC simulations. For the study of most Kitaev systems, it is not necessary to further optimize the distribution of temperature points, so we keep the initial, logarithmic distribution. For the (9,3)a Kitaev system, which is the only 3D Kitaev system that possesses a first-order phase transition at low temperatures, ensemble optimization techniques have been proven useful to increase the numerical convergence in the region around the critical temperature [90].

B.2.2 Equilibration and convergence

The time series for the energy E_f as a function of Monte Carlo sweeps N_{sw} shows the significant speedup in convergence which is reached if parallel tempering is implemented in the QMC simulation (Fig. B.4). Typically, physical observables reach their equilibrium value after < 10000 Monte Carlo sweeps for low temperatures $T \leq 0.01$, and much faster for higher temperatures. In order to achieve converged results for all data points, we experience that, usually, a simulation time of the order of 10.000 sweeps is required.

Thus, we perform a typical QMC simulation with 10.000 Monte Carlo sweeps for the thermalization, followed by 10.000 - 50.000 sweeps for the measurements.

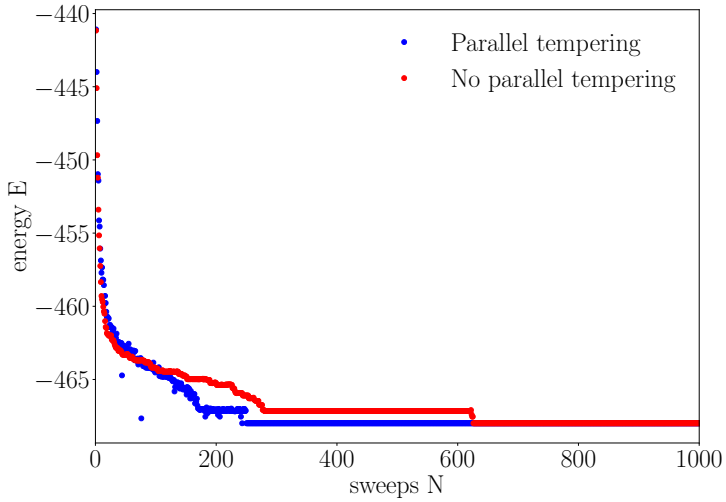

Figure B.4: Time series for the internal energy E_f of the Kitaev Shastry-Sutherland model (L = 10) with (blue) and without replica exchange (red). The simulations are started from different random seeds at $T = 0.019$.

B.2.3 Computational cost

The computationally most expensive step in the simulation is the exact diagonalization of the fermionic sector, which is required in every Monte Carlo update. For the calculation of the free energy F in the Metropolis weights $e^{-\beta\Delta F}$ the full set of eigenvalues $\{\epsilon_\lambda\}$ of the matrix iA, Eq.2.9, is needed.

The usual matrix diagonalization techniques used by standard linear algebra libraries are based on the tridiagonalization of the matrix and scale cubically with the matrix size, i.e. involve a computational cost of $\mathcal{O}(N^3)$ for an $N \times N$ matrix. We have verified this cubic scaling for our simulations (Fig. B.5).

For a whole Monte Carlo sweep, which consists of N attempted single spin-flip updates, the computational scale is therefore $\mathcal{O}(N^4)$. In practice, this restricts the accessible system sizes with this QMC method on state-of-the-art high-performance clusters in reasonable amounts of time to $\sim$ 1000 (see Fig. B.5). Therefore, an exhaustive study of 3D Kitaev models asks for a significant speed-up of the Monte Carlo update.

The Majorana matrix iA is either saved or constructed on the fly during the simulation. Although it is sparse (every spin has three interaction partners, so each row in the matrix contains only three nonzero elements), we cannot resort to faster eigensolver techniques like the Lanczos algorithm [155], since we need the full spectrum $\{\epsilon_\lambda\}$.

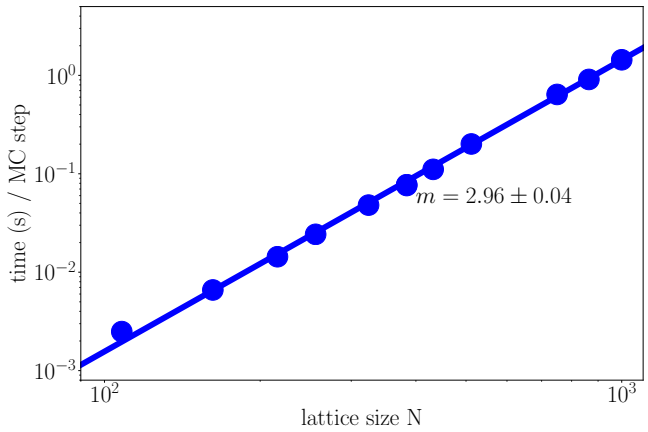

Figure B.5: Computation time for one Monte Carlo step (single spin-flip update with exact diagonalization) as a function of system size. Due to the exact diagonalization needed to calculate Metropolis weights, the computation time scales cubically with the system size. Hence, in double-logarithmic scale, the time per MC step is straight line with a slope $m = 2.96(4) \approx 3$.

B.2.4 Numerical Improvements

Since the exact diagonalization of the fermions is the computational bottleneck step in our QMC method, numerical improvements of the simulation mainly have to address this issue.

The standard ansatz to make ED calculations faster is to search for suitable symmetries of the underlying system, which might enable to rewrite the matrix in a block-diagonal form. This is also an option for Kitaev systems, most of which are defined on bipartite lattices. In this case, we can use the sublattice symmetry and reorder the numbering of the sites according to the sublattices A and B. Sites in sublattice A are numbered by $1, \ldots, N/2$, and those in sublattice B by $N/2+1, \ldots, N$ With this transformation, the Majorana Hamiltonian, Eq. (2.9), assumes the form [145]

$$\mathcal{H}\left(\{u_{ij}\}\right) = \left(\underline{c}_A^T \;\; \underline{c}_B^T\right) \underbrace{\begin{pmatrix} 0 & M \\ -M^T & 0 \end{pmatrix}}_{=iA} \begin{pmatrix} \underline{c}_A \\ \underline{c}_B \end{pmatrix}, \tag{B.17}$$

where the vectors $\underline{c}_{A/B}$ denote the Majorana fermions which live on the lattice sites in sublattice A/B.

Now, instead of diagonalizing the whole matrix iA, it is sufficient to perform a singular value decomposition (SVD) of the block matrix M. The singular values of M are the eigenvalues $\{\epsilon_\lambda\}$ of iA (since iA is Hermitian, its eigenvalues come in pairs $\pm\epsilon_\lambda$, such that the calculation of the negative or positive half is suf-

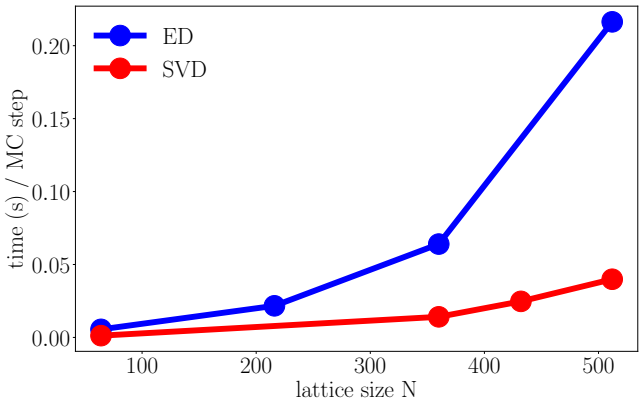

Figure B.6: Computation time for one Monte Carlo step with exact diagonalization / singular value decomposition. On bipartite lattice systems, the Majorana Hamiltonian can be brought into a block-diagonal form, Eq. (B.17). Instead of exactly diagonalizing the full Hamiltonian, it is computationally more efficient to perform a singular value decomposition of its off-diagonal subblock with size $N/2 \times N/2$, in order to obtain the eigenvalues $\{\epsilon_\lambda\}$.

ficient). The numerical cost of SVD also scales cubically with the matrix size, but, since M has only a size $N/2 \times N/2$, the calculation time for an N-site system is significantly reduced, and larger systems become accessible. We confirm this improvement of the computational scaling with benchmark calculations up to $N = 512$ (Fig. B.6).

The block transformation with subsequent SVD is a faster approach for bipartite Kitaev systems and best-suited if obtaining the full set of eigenvalues $\{\epsilon_\lambda\}$ is really necessary in each Monte Carlo update.

B.3 GF-KPM

We give a number of technical remarks on the concrete implementation of the QMC-KPM method.

- The number M of Chebyshev moments that have to be taken into account depends on the lattice, and, in particular, its size. For small systems, a gauge field update comes with a larger relative change in the free energy $\Delta F/F$. Thus, a higher precision in the calculation of ΔF is required, and therefore, M needs to be chosen larger. For medium-sized and large systems ($N \geq 600$), choosing $M = 256 - 512$ turned out to be sufficient to achieve good accordance with results from QMC-ED simulations (see Fig. 3.4, where an example for a benchmark plot is given). In addition, a closer analysis of

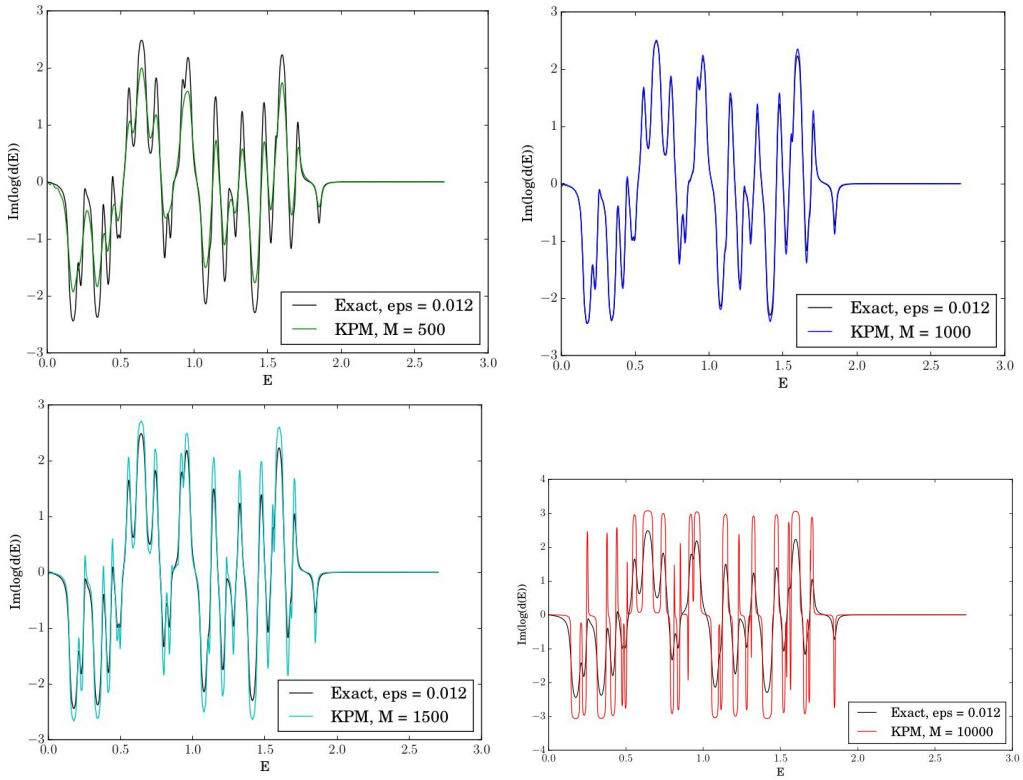

Figure B.7: Benchmark calculations for $\mathrm{Im}\log(d(E+i\epsilon))$. The black line shows the exact function, which is calculated from the eigenvalues ϵ_λ, ϵ'_λ [147], and the colored lines the Chebyshev-approximated function with expansion order $M = 500, 1000, 1500, 10000$. It can be seen that the best approximation is achieved for $M = 1000$.

the Chebyshev expansion of the function $\mathrm{Im}\log(d(E+i\epsilon))$ shows that the approximation does not further improve for expansion orders $M \gg 1000$ (Fig. B.7).

- In practice, the numerical integration of ΔF has to be restricted to the half-open interval $[0, s)$ (s being the bandwidth of $\mathcal{H}$) to achieve good precision. We used the extended trapezoidal rule for semi-open intervals [245]

$$\int_{x_1=0}^{x_M=s} f(x)dx \approx h\left(\frac{1}{2}f_1 + f_2 + \cdots + f_{M-2} + \frac{3}{2}f_{M-1}\right) + \mathcal{O}\left(\frac{1}{M^2}\right), \tag{B.18}$$

  where $f_i := f(x_i)$. For optimized results, the number M of equally-spaced abscissa points x_i on the interval $[0, s)$ should correspond to the number of Chebyshev moments.

- Since the recursive calculation of the moments $\langle i|\, T_m(H/s)\, |i\rangle$ is done by

subsequent matrix-vector multiplications, this step is the most expensive part in each Monte Carlo update. In order to reach maximal efficiency, the sparse matrices and vectors should be stored in the compressed row-storage format (CRS) [246]. In this format, the numerical effort for the multiplication of N-sized matrices and vectors scales with $\mathcal{O}(N)$. This, in the end, also determines the linear scaling of the whole algorithm (see Fig. 3.3). With the GF-KPM method, lattice system sizes up to $N \sim 2800$ become computationally accessible.

In addition, it has to be remarked that the GF-KPM method gives sufficiently exact results only for the free energy change during the MC update and cannot be used for the calculation of thermodynamic observables. Hence, an exact diagonalization of the Hamiltonian remains necessary after each sweep, in order to calculate observables from the eigenvalues $\{\epsilon_\lambda\}$. The latter are also needed to compute the Boltzmann weights for the replica exchange, Eq. (B.12), since here, swapped configurations differ in general by more than two matrix entries. This implies that the matrix Δ in Eq. (3.53) does not necessarily have a low rank, such that more than four Green's functions are needed for expressing the function $d(E)$, and the decisive advantage of the GF-KPM method is lost.

Finally, the GF-KPM method is not applicable to all lattice systems. Our simulations have shown that it fails with systems whose density of states (DOS) shows exotic features like δ-functions. In our studies, we faced this problem with the lattices (10,3)d and (8,3)c, the latter in case of strong anisotropy in the J_γ-couplings.

B.4 Thermodynamic observables

The partition function of the Kitaev system can be written as a double trace, where the outer trace is effectively a sum over classical $\mathbb{Z}_2$ gauge field configurations $\{u_{ij}\}$ (Sec. 3.4.1). For each gauge field configuration, the partition function of the Majorana fermions $\mathcal{Z}_{\mathrm{Maj}}(\{u_{ij}\})$ can be regarded separately, and it has the analytical form [44]

$$\mathcal{Z} = \sum_{\{u_{ij}\}} \underbrace{\prod_{\lambda=1}^{N/2} \left(2\cosh\left(\frac{\beta\epsilon_\lambda}{2}\right)\right)}_{=:\mathcal{Z}_{\mathrm{Maj}}(\{u_{ij}\})} . \tag{B.19}$$

Accordingly, the thermodynamic observables can be numerically measured for each $\mathbb{Z}_2$ gauge field configuration $\{u_{ij}\}$ that is sampled in the QMC simulation.

Most of them are direct derivations of $\mathcal{Z}_{\mathrm{Maj}}(\{u_{ij}\})$, such as the **free energy** [44],

$$\begin{aligned} F(\{u_{ij}\}) &= -T \ln \mathcal{Z}_{\mathrm{Maj}}(\{u_{ij}\}) \\ &= -T \sum_{\lambda=1}^{N/2} \ln\left(2\cosh\left(\frac{\beta\epsilon_\lambda}{2}\right)\right). \end{aligned} \tag{B.20}$$

Analogously, we obtain the **internal energy** $E_f\left(\{u_{ij}\}, T\right) = \langle E \rangle_F$ of the Majorana system [44],

$$\begin{aligned} E_f\left(\{u_{ij}\}, T\right) &= \mathrm{tr}_{\{c_i\}}\, \mathcal{H}\left(\{u_{ij}\}\right) e^{-\beta\mathcal{H}(\{u_{ij}\})} \\ &= -\frac{1}{\mathcal{Z}_{\mathrm{Maj}}(\{u_{ij}\})} \frac{\partial}{\partial\beta} \mathcal{Z}_{\mathrm{Maj}}(\{u_{ij}\}) \\ &= -\frac{\partial \ln \mathcal{Z}_{\mathrm{Maj}}(\{u_{ij}\})}{\partial\beta} \\ &= -\frac{\partial}{\partial\beta}\left(\sum_{\lambda=1}^{N/2} \ln\left(2\cosh\left(\frac{\beta\epsilon_\lambda}{2}\right)\right)\right) \\ &= -\sum_{\lambda=1}^{N/2} \frac{2\sinh\left(\frac{\beta\epsilon_\lambda}{2}\right)}{2\cosh\left(\frac{\beta\epsilon_\lambda}{2}\right)} \cdot \frac{\epsilon_\lambda}{2} \\ &= -\sum_{\lambda=1}^{N/2} \frac{\epsilon_\lambda}{2} \tanh\left(\frac{\beta\epsilon_\lambda}{2}\right), \end{aligned} \tag{B.21}$$

which, for low temperatures, $\beta \to \infty$, converges against the ground state energy $E = -\sum_\lambda \epsilon_\lambda/2$, Eq. (2.15).

For the calculation of the **specific heat** $C_v(T)$, the fluctuations in the $\mathbb{Z}_2$ gauge field and the itinerant Majorana fermions can be regarded separately, as has been formerly shown at the example of a double-exchange spin ice model, where the partition function has an analogous structure [215]. The full specific heat C_v is the sum

$$C_v T = C_{v,\mathrm{GF}}(T) + C_{v,\mathrm{MF}}(T). \tag{B.22}$$

$C_{v,\mathrm{GF}}(T)$ denotes the contribution from the gauge fluctuations,

$$C_{v,\mathrm{MF}}(T) = \frac{1}{T^2}\left(\left\langle E_f^2(\{u_{jk}\})\right\rangle_{MC} - \left\langle E_f(\{u_{jk}\})\right\rangle_{MC}^2\right), \tag{B.23}$$

where the bracket $\langle ... \rangle_{MC}$ indicates averaging over Monte Carlo samples. $C_{v,\mathrm{MF}}(T)$ is given by the Monte Carlo average of the fermionic fluctuations,

$$C_{v,\mathrm{MF}}(T) = \frac{1}{T^2}\langle \langle E^2 \rangle_F - \langle E \rangle_F^2 \rangle_{MC}. \tag{B.24}$$

Here, we use the notation $\langle E\rangle_F = E_f\left(\{u_{ij}\}, T\right)$. For the evaluation of Eq. (B.24), the only term which is left to calculate is $\langle E^2\rangle_F$,

$$\begin{aligned}
\langle E^2\rangle_F &= \mathrm{tr}_{\{c_i\}}\, \mathcal{H}^2\left(\{u_{ij}\}\right) e^{-\beta\mathcal{H}(\{u_{ij}\})} \\
&= \frac{1}{\mathcal{Z}_{\mathrm{Maj}}(\{u_{ij}\})}\frac{\partial^2}{\partial\beta^2}\mathcal{Z}_{\mathrm{Maj}}(\{u_{ij}\}) \\
&= \frac{1}{\mathcal{Z}_{\mathrm{Maj}}(\{u_{ij}\})}\frac{\partial}{\partial\beta}\left(\sum_{\mu=1}^{N/2}\epsilon_\mu \sinh\left(\frac{\beta\epsilon_\mu}{2}\right)\cdot\prod_{\lambda\neq\mu}2\cosh\left(\frac{\beta\epsilon_\lambda}{2}\right)\right) \\
&= \frac{1}{\mathcal{Z}_{\mathrm{Maj}}(\{u_{ij}\})}\sum_{\mu=1}^{N/2}\left(\frac{\epsilon_\mu^2}{2}\cosh\left(\frac{\beta\epsilon_\mu}{2}\right)\cdot\prod_{\lambda\neq\mu}2\cosh\left(\frac{\beta\epsilon_\lambda}{2}\right)\right. \\
&\qquad \left. + \epsilon_\mu \sinh\left(\frac{\beta\epsilon_\mu}{2}\right)\cdot\sum_{\nu\neq\mu}\epsilon_\nu\sinh\left(\frac{\beta\epsilon_\nu}{2}\right)\prod_{\lambda\neq\nu}2\cosh\left(\frac{\beta\epsilon_\lambda}{2}\right)\right) \\
&= \sum_{\lambda=1}^{N/2}\frac{\epsilon_\lambda^2}{4} + \sum_{\mu\neq\lambda}\epsilon_\lambda\epsilon_\mu\tanh\left(\frac{\beta\epsilon_\lambda}{2}\right)\tanh\left(\frac{\beta\epsilon_\mu}{2}\right).
\end{aligned} \tag{B.25}$$

We can check that

$$\begin{aligned}
\langle E^2\rangle_F - \langle E\rangle_F^2 &= \sum_{\lambda=1}^{N/2}\frac{\epsilon_\lambda^2}{4}\left(1-\tanh^2\left(\frac{\beta\epsilon_\lambda}{2}\right)\right) \\
&= -\frac{\partial\langle E\rangle_F}{\partial\beta}.
\end{aligned} \tag{B.26}$$

Hence, the Majorana contribution to the specific heat is [44]

$$C_{v,\mathrm{MF}}(T) = -\frac{1}{T^2}\left\langle\frac{\partial E_f(\{u_{jk}\})}{\partial\beta}\right\rangle_{MC}. \tag{B.27}$$

The **entropy** $S(T)$ can be calculated by numerical integration over the specific heat,

$$S/N = \log(2) - \int_T^{T=\infty}\frac{C_v(T)}{NT}dT. \tag{B.28}$$

There also exists a numerically improved version based on the integration over the internal energy, for which the statistical errors are typically far smaller than for the specific heat $C_v(T)$) [45],

$$S/N = \log(2) + \beta\langle\frac{E_f}{N}\rangle_{MC} - \int_0^\beta\langle\frac{E_f}{N}\rangle_{MC}d\beta. \tag{B.29}$$

Finally, we can calculate the **spin-spin correlator** $S_{\gamma\gamma}(T)$ as [46]

$$\begin{aligned} S_{\gamma\gamma}(T) &= \frac{2}{N}\left\langle \sum_{\langle i,j\rangle_\gamma} \left\langle \sigma_i^\gamma \sigma_j^\gamma \right\rangle \right\rangle_{MC} \\ &= \frac{2}{N}\left\langle \sum_{\langle i,j\rangle_\gamma} \left\langle -iu_{ij}^\gamma c_i c_j \right\rangle \right\rangle_{MC} \\ &= \frac{2}{N}\left\langle \sum_{\langle i,j\rangle_\gamma} \left(-\sum_{\lambda=1}^{N/2} \langle\lambda| - iu_{ij}^\gamma |\lambda\rangle \tanh\left(\frac{\beta\epsilon_\lambda}{2}\right)\right) \right\rangle_{MC}, \end{aligned} \tag{B.30}$$

where $|\lambda\rangle$ is the eigenvector of $\mathcal{H}$ corresponding to the eigenvalue ϵ_λ.

Appendix C

Thermodynamic classification of 3D Kitaev spin liquids

C.1 Lattice definitions

In the following, we document the geometric definitions (unit cells and lattice vectors) of the elementary, tricoordinated 3D Kitaev systems. The lattice definitions and the assignments of the Kitaev couplings J_γ correspond to those in Ref. [36].

C.1.1 (10,3)x lattice family

The (10,3)x family contains the tricoordinated lattices with elementary loop length $|p| = 10$, which comprise the lattices (10,3)a (hyperoctagon), (10,3)b (hyperhoneycomb), (10,3)c and (10,3)d. The definitions of unit cells and lattice vectors are given in the table C.1 and pictured in Figs. C.1, C.2.

Generally, the elementary tricoordinated 3D lattices and their fundamental symmetries can be easily and systematically understood by looking how they are mutually related and connected with a couple of known tricoordinated 2D lattices [36]. For instance, the lattices (10,3)a (hyperoctagon lattice) and (10,3)d can be regarded as two different three-dimensional versions of the square-octagon lattice. As the name of the latter already tells, it consists of two different kinds of elementary plaquettes. Square plaquettes with length $|p| = 4$ are arranged to a square lattice, and connected by diagonal bonds, such that additional, octagonal plaquettes ($|p| = 8$) are formed. Starting from this 2D lattice, one arrives at the (10,3)a system by replacing the square plaquettes with co-rotating spirals, which expand in the third dimension. The arising geometry does not possess any more closed loops of length 4 nor 8 - instead, the elementary plaquette now has a length $|p| = 10$. Likewise, the (10,3)d lattice is constructed from the square-

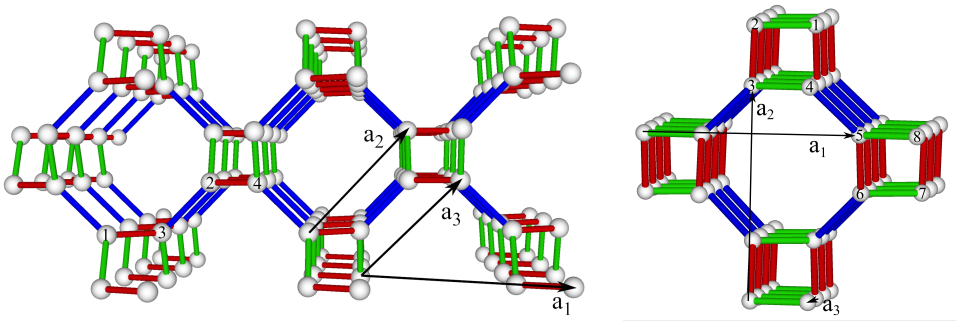

(a) (10,3)a **(b)** (10,3)d

Figure C.1: Unitcells of (10,3)a and (10,3)d [36, 93].

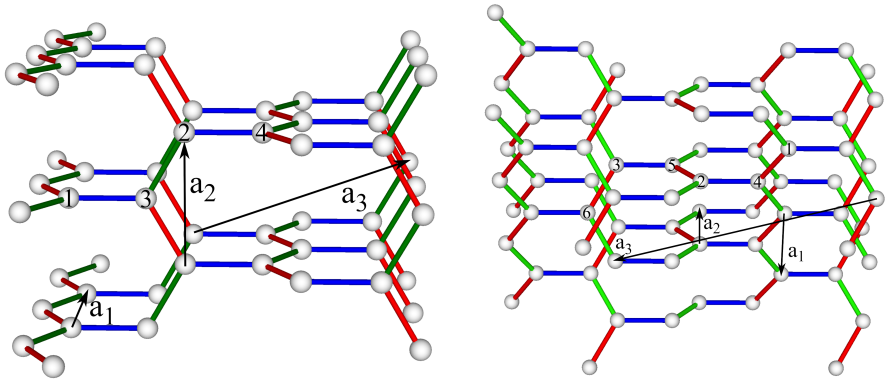

(a) (10,3)b **(b)** (10,3)c

Figure C.2: Unitcells of (10,3)b and (10,3)c [36].

octagon lattice by replacing the square plaquettes with counter-rotating spirals, i.e., here, neighbouring spirals have an opposite winding direction. (10,3)a and (10,3)d can therefore be regarded as geometric "partner" lattices. Their elementary symmetries differ on the grounds of the different rotating behavior of the bond spirals. While the (10,3)a lattice breaks inversion symmetry, (10,3)d is inversion-symmetric [36]. In both cases, the canonical assignment of Kitaev couplings is realized by choosing the diagonal bonds as z-bonds, and place the x- and y-bonds along the square-shaped spirals. With this choice, a Jordan-Wigner transformation can be most easily performed along the xy-spirals (Fig. C.16), which leads to a $\mathbb{Z}_2$ gauge field $\{\eta\}$ that is located solely on the diagonal bonds.

Similarly, the lattices (10,3)b and (10,3)c can be constructed from the honeycomb lattice (which, in Schläfli notation, is denoted by (6,3)a). (10,3)b (hyper-honeycomb lattice) can be visualized in terms of parallel xy-zigzag chains along two perpendicular directions, which are connected by z-bonds. The honeycomb

lattice is regained as the 2D projection of this system, which can be seen if the lattice is regarded from a 60 degree angle. In (10,3)c, on the other hand, the xy-zigzag chains form along three different directions that are 120-degree rotated against each other. In close analogy to the formerly discussed pair of lattice systems, (10,3)b is inversion symmetric, while (10,3)c breaks inversion symmetry [36]. Again, there is a natural implementation of the Jordan-Wigner transformation along the xy-spirals in both lattices (Fig. C.17).

(10,3) a			
Lattice vectors:	$\mathbf{a_1} = (1,0,0)$	$\mathbf{a_2} = \left(\frac{1}{2},\frac{1}{2},-\frac{1}{2}\right)$	$\mathbf{a_3} = \left(\frac{1}{2},\frac{1}{2},\frac{1}{2}\right)$
Unit cell:	$\mathbf{r_1} = \left(\frac{1}{8},\frac{1}{8},\frac{1}{8}\right)$ $\mathbf{r_4} = \left(\frac{7}{8},\frac{3}{8},\frac{1}{8}\right)$	$\mathbf{r_2} = \left(\frac{5}{8},\frac{3}{8},-\frac{1}{8}\right)$	$\mathbf{r_3} = \left(\frac{3}{8},\frac{1}{8},-\frac{1}{8}\right)$
(10,3) b			
Lattice vectors:	$\mathbf{a_1} = (-1,1,-2)$	$\mathbf{a_2} = (-1,1,2)$	$\mathbf{a_3} = (2,4,0)$
Unit cell:	$\mathbf{r_1} = (0,0,0)$ $\mathbf{r_4} = (2,3,1)$	$\mathbf{r_2} = (1,2,1)$	$\mathbf{r_3} = (1,1,0)$
(10,3) c			
Lattice vectors:	$\mathbf{a_1} = (1,0,0)$	$\mathbf{a_2} = \left(-\frac{1}{2},\frac{\sqrt{3}}{2},0\right)$	$\mathbf{a_3} = \left(0,0,\frac{3\sqrt{3}}{2}\right)$
Unit cell:	$\mathbf{r_1} = \left(\frac{1}{4},\frac{1}{4\sqrt{3}},\frac{1}{2\sqrt{3}}\right)$ $\mathbf{r_4} = \left(\frac{3}{4},\frac{1}{4\sqrt{3}},\frac{1}{\sqrt{3}}\right)$	$\mathbf{r_2} = \left(\frac{3}{4},\frac{1}{4\sqrt{3}},\frac{2}{\sqrt{3}}\right)$ $\mathbf{r_5} = \left(\frac{1}{2},\frac{1}{\sqrt{3}},\frac{5}{2\sqrt{3}}\right)$	$\mathbf{r_3} = \left(\frac{1}{2},\frac{1}{\sqrt{3}},\frac{7}{2\sqrt{3}}\right)$ $\mathbf{r_6} = \left(\frac{1}{4},\frac{1}{4\sqrt{3}},\frac{4}{\sqrt{3}}\right)$
(10,3) d			
Lattice vectors:	$\mathbf{a_1} = \left(\frac{1}{2},-\frac{1}{2},0\right)$	$\mathbf{a_2} = \left(\frac{1}{2},\frac{1}{2},0\right)$	$\mathbf{a_3} = \left(0,0,\frac{1}{2}\right)$
Unit cell:	$a = \frac{1}{4}\cdot\left(2-\sqrt{2}\right)$ $\mathbf{r_1} = \left(0,-a,\frac{3}{4}c\right)$ $\mathbf{r_4} = (a,0,0)$ $\mathbf{r_7} = \left(a,-\frac{1}{2},\frac{3}{4}c\right)$	$c = \frac{1}{2}$ $\mathbf{r_2} = \left(-a,0,\frac{1}{2}c\right)$ $\mathbf{r_5} = \left(-a,-\frac{1}{2},\frac{1}{4}c\right)$ $\mathbf{r_8} = \left(0,-a-\frac{1}{2},0\right)$	$\mathbf{r_3} = \left(0,a,\frac{1}{4}c\right)$ $\mathbf{r_6} = \left(0,a-\frac{1}{2},\frac{1}{2}c\right)$

Table C.1: Lattice definitions of the (10,3)x family [36, 93].

C.1.2 (8,3)x lattice family

The (8,3)x family contains the tricoordinated lattices with elementary loop length $|p| = 8$, which comprise the lattices (8,3)a, (8,3)b (hyperhexagon), (8,3)c and

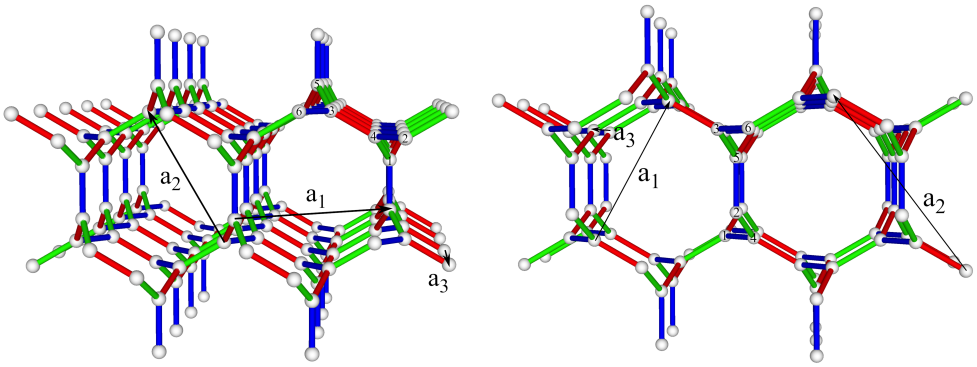

(a) (8,3)a **(b)** (8,3)b

Figure C.3: Unitcells of (8,3)a and (8,3)b [36].

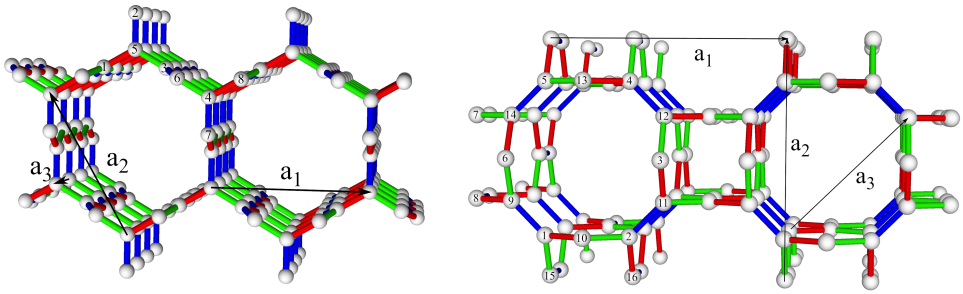

(a) (8,3)c **(b)** ((8,3)n

Figure C.4: Unitcells of (8,3)c and (8,3)n [36].

(8,3)n. The definitions of unit cells and lattice vectors are given in the tables C.2, C.3 and are pictured in Figs. C.3, C.4.

For two of the systems in this family, we find a similar geometric relation as amongst the (10,3)x systems. (8,3)a and (8,3)b can be regarded as three-dimensional versions of a 2D lattice, which is the “decorated honeycomb" lattice [30, 47]. Similarly to the (10,3)a / d pair, the lattices (8,3)a and (8,3)b differ with respect to the mutual rotation orientation of their bond spirals. In (8,3)a, the triangular plaquettes of the decorated honeycomb lattice are replaced by co-rotating “triangular” spirals in the third dimension, while (8,3)b possesses counter-rotating spirals. Likewise, (8,3)a is the chiral partner in this pair, which breaks inversion symmetry, while (8,3)b preserves inversion-symmetry. The latter is also the only 3D lattice system which possesses all the required mirror symmetries to allow for the application of Lieb’s theorem.

Unlike the pair (8,3)a / b, the other two lattices have a unique geometric structure and cannot be geometrically related in a similar manner to another of the 3D

systems which are considered here. (8,3)n can be regarded as a system of layers of a generalized version of the square-octagon lattice, where each square plaquette possesses an additional vertex per bond. Here, seven out of the eight elementary plaquettes are mirror-symmetric, with a mirror plane that does not cut through any of the lattice sites. (8,3)c is special due to the occurrence of gauge-frustration as a consequence of a particular volume constraint.

In addition, there is an important geometric property that distinguishes all (8,3)x lattices from their counterparts with loop length 10. Unfortunately the lattice geometries of the (8,3)x systems do not allow for an assignment of Kitaev couplings that works as orderly as, for example, in the (10,3)a / d pair, where the xx- and yy-interactions could be located entirely on the bond spirals. Instead, for the (8,3)a and (8,3)b lattice, there are unique bond assignments (up to permutation of the three bond types), which preserve most of the lattices' point-group symmetries, and where the x-, y- and z-bonds are related by a threefold rotation symmetry [36]. With these assignments, the bond spirals on both systems carry all sorts of interactions. For (8,3)c and (8,3)n, the situation is similar.

This fact has an important consequence for the analytic foundation of our quantum Monte Carlo simulations. While for the lattice systems (10,3)a and (10,3)d, there are easy implementations for the Jordan-Wigner transformation along spirals or (parallel) zigzag chains, there is no such simple realization here. Instead, the Jordan-Wigner strings have to be winded through the lattices in a more complicated way, and always end up with different lengths for finite systems (Figs. C.18 and C.19). For this reason, there is no elegant choice of boundary conditions to reduce the finite-size effects. However, finite-size effects are less pronounced in the (8,3)x systems than in the (10,3)x family.

C.2 Remarks on finite-size effects

For some systems, for example (10,3)a, (10,3)b, (8,3)n, the divergence of the specific heat peak is somewhat concealed by an unsystematic scaling behavior of the peaks, which is a finite-size effect. On most lattice systems, we experience this effect up to linear system sizes $L = 4-5$, and the scaling behavior gets systematic beyond these sizes. For (10,3)a and (10,3)b, on the other hand, the finite-size effect remains present up to $L = 7$, and for (8,3)n, where the unit cell is particularly large, up to $L = 5$, which has been the largest accessible system size in the QMC simulation. Typically, the occurrence of finite-size effects depends on the choice of boundary conditions, and is stronger on systems which are implemented with periodic boundary conditions. Here, it is reinforced by the summation over unphysical states in the Monte Carlo simulation, respectively the ignoring of parity terms upon the closing of Jordan-Wigner strings.

(8,3) a			
Lattice vectors:	$\mathbf{a_1} = (1,0,0)$	$\mathbf{a_2} = \left(-\frac{1}{2}, \frac{\sqrt{3}}{2}, 0\right)$	$\mathbf{a_3} = \left(0,0, \frac{3\sqrt{2}}{5}\right)$
Unit cell:	$\mathbf{r_1} = \left(\frac{1}{2}, \frac{\sqrt{3}}{10}, 0\right)$	$\mathbf{r_2} = \left(-\frac{3}{5}, \frac{\sqrt{3}}{5}, \frac{2\sqrt{2}}{5}\right)$	$\mathbf{r_3} = \left(\frac{1}{10}, \frac{3\sqrt{3}}{10}, \frac{\sqrt{2}}{5}\right)$
	$\mathbf{r_4} = \left(\frac{4}{10}, \frac{\sqrt{3}}{5}, \frac{\sqrt{2}}{5}\right)$	$\mathbf{r_5} = \left(0, \frac{2\sqrt{3}}{5}, 0\right)$	$\mathbf{r_6} = \left(-\frac{1}{10}, \frac{3\sqrt{3}}{10}, \frac{2\sqrt{2}}{5}\right)$
(8,3) b			
Lattice vectors:	$\mathbf{a_1} = \left(\frac{1}{2}, \frac{1}{2\sqrt{3}}, \frac{\sqrt{2}}{5\sqrt{3}}\right)$	$\mathbf{a_2} = \left(0, \frac{1}{\sqrt{3}}, \frac{2\sqrt{2}}{5\sqrt{3}}\right)$	$\mathbf{a_3} = \left(0,0, \frac{\sqrt{6}}{5}\right)$
Unit cell:	$\mathbf{r_1} = \left(\frac{1}{10}, \frac{1}{2\sqrt{3}}, \frac{\sqrt{2}}{5\sqrt{3}}\right)$	$\mathbf{r_2} = \left(\frac{1}{5}, \frac{\sqrt{3}}{5}, \frac{\sqrt{6}}{5}\right)$	$\mathbf{r_3} = \left(\frac{3}{10}, \frac{11}{10\sqrt{3}}, \frac{4\sqrt{2}}{5\sqrt{3}}\right)$
	$\mathbf{r_4} = \left(\frac{1}{5}, \frac{2}{5\sqrt{3}}, \frac{2\sqrt{2}}{5\sqrt{3}}\right)$	$\mathbf{r_5} = \left(\frac{3}{10}, \frac{3\sqrt{3}}{10}, \frac{\sqrt{6}}{5}\right)$	$\mathbf{r_6} = \left(\frac{2}{5}, \frac{1}{\sqrt{3}}, \frac{\sqrt{2}}{\sqrt{3}}\right)$
(8,3) c			
Lattice vectors:	$\mathbf{a_1} = (1,0,0)$	$\mathbf{a_2} = \left(-\frac{1}{2}, \frac{\sqrt{3}}{2}, 0\right)$	$\mathbf{a_3} = \left(0,0, \frac{\sqrt{2}}{5}\right)$
Unit cell:	$\mathbf{r_1} = \left(-\frac{1}{5}, \frac{4}{5\sqrt{3}}, \frac{1}{10}\right)$	$\mathbf{r_2} = \left(0, \frac{7}{5\sqrt{3}}, \frac{1}{10}\right)$	$\mathbf{r_3} = \left(\frac{1}{5}, \frac{4}{5\sqrt{3}}, \frac{1}{10}\right)$
	$\mathbf{r_4} = \left(\frac{1}{2}, \frac{1}{2\sqrt{3}}, \frac{3}{10}\right)$	$\mathbf{r_5} = \left(0, \frac{1}{\sqrt{3}}, \frac{1}{10}\right)$	$\mathbf{r_6} = \left(\frac{3}{10}, \frac{7}{10\sqrt{3}}, \frac{3}{10}\right)$
	$\mathbf{r_7} = \left(\frac{1}{2}, \frac{1}{10\sqrt{3}}, \frac{3}{10}\right)$	$\mathbf{r_8} = \left(\frac{7}{10}, \frac{7}{10\sqrt{3}}, \frac{3}{10}\right)$	

Table C.2: Definitions of the lattices (8,3)a - (8,3)c [36].

(8,3) n			
Lattice vectors:	$\mathbf{a} = (1, 0, 0)$	$\mathbf{b} = (0, 1, 0)$	$\mathbf{c} = \left(0, 0, \frac{4}{2\sqrt{3}+\sqrt{2}}, \right)$
	$\mathbf{a_1} = \mathbf{a}$	$\mathbf{a_2} = \mathbf{b}$	$\mathbf{a_3} = \frac{1}{2}(\mathbf{a} + \mathbf{b} + \mathbf{c})$
Unit cell:	$x = \frac{\sqrt{3}+\sqrt{2}}{2\left(2\sqrt{3}+\sqrt{2}\right)}$		
	$z = \frac{1}{8}$		
	$\mathbf{r_1} = x \cdot \mathbf{a} + \left(\frac{1}{2} - x\right) \cdot \mathbf{b} + \frac{\mathbf{c}}{4}$		
	$\mathbf{r_2} = (1 - x) \cdot \mathbf{a} + \left(\frac{1}{2} - x\right) \cdot \mathbf{b} + \frac{\mathbf{c}}{4}$		
	$\mathbf{r_3} = \left(\frac{1}{2} + x\right) \cdot \mathbf{a} + \frac{\mathbf{b}}{2} + \left(\frac{1}{2} - z\right) \cdot \mathbf{c}$		
	$\mathbf{r_4} = (1 - x) \cdot \mathbf{a} + \left(\frac{1}{2} + x\right) \cdot \mathbf{b} + \frac{\mathbf{c}}{4}$		
	$\mathbf{r_5} = x \cdot \mathbf{a} + \left(\frac{1}{2} + x\right) \cdot \mathbf{b} + \frac{\mathbf{c}}{4}$		
	$\mathbf{r_6} = \left(\frac{1}{2} - x\right) \cdot \mathbf{a} + \frac{\mathbf{b}}{2} + \left(\frac{1}{2} - z\right) \cdot \mathbf{c}$		
	$\mathbf{r_7} = (1 - x) \cdot \mathbf{b} + z \cdot \mathbf{c}$		
	$\mathbf{r_8} = x \cdot \mathbf{b} + z \cdot \mathbf{c}$		
	$\mathbf{r_9} = \left(\frac{1}{2} - x\right) \cdot \mathbf{a} + x \cdot \mathbf{b} + \frac{\mathbf{c}}{4}$		
	$\mathbf{r_{10}} = \frac{\mathbf{a}}{2} + \left(\frac{1}{2} - x\right) \cdot \mathbf{b} + \left(\frac{1}{2} - z\right) \cdot \mathbf{c}$		
	$\mathbf{r_{11}} = \left(\frac{1}{2} + x\right) \cdot \mathbf{a} + x \cdot \mathbf{b} + \frac{\mathbf{c}}{4}$		
	$\mathbf{r_{12}} = \left(\frac{1}{2} + x\right) \cdot \mathbf{a} + (1 - x) \cdot \mathbf{b} + \frac{\mathbf{c}}{4}$		
	$\mathbf{r_{13}} = \frac{\mathbf{a}}{2} + \left(\frac{1}{2} + x\right) \cdot \mathbf{b} + \left(\frac{1}{2} - z\right) \cdot \mathbf{c}$		
	$\mathbf{r_{14}} = \left(\frac{1}{2} - x\right) \cdot \mathbf{a} + (1 - x) \cdot \mathbf{b} + \frac{\mathbf{c}}{4}$		
	$\mathbf{r_{15}} = x \cdot \mathbf{a} + z \cdot \mathbf{c}$		
	$\mathbf{r_{16}} = (1 - x) \cdot \mathbf{a} + z \cdot \mathbf{c}$		

Table C.3: Lattice definition of (8,3)n [36].

On lattices where the geometry allows for Jordan-Wigner strings that have approximately the same length, we find that the introduction of boundaries apparently remedies the finite-size effect and leads to a more systematic scaling behavior already for smaller systems. This is the case for (10,3)b and (10,3)d. It is not the case for the lattices of the (8,3)x-family, where the Jordan-Wigner strings have very different lengths in finite systems. Based on the argument that finite-size effects are overcome for most lattice systems by just going over to larger systems, we have preferred to keep the boundary conditions, in principal, periodic. Only for (10,3)d, where the resulting improvement is the largest, we have applied all QMC simulations with open boundary conditions in the a_2- and a_3-direction.

Apart from the described finite-size effects, for some systems (e.g. (8,3)a, (10,3)c), we also note the appearance of a numerical even-odd effect on the peak height with respect to the linear system size L. Due to this effect, the statistical error of the extrapolated critical temperature estimate T_c is increased for these systems. Even-odd effects also appear in the average plaquette flux $\overline{W_p}$ and result in a ground state value $|\overline{W_p}| < 1$. This effect arises from additional volume constraints on the plaquette fluxes that may appear in small, finite systems.

C.3 Numerical results for the 10-loop lattices

The described geometric relations between the lattice systems manifest themselves in the physical properties of the Kitaev systems. It is remarkable that both portrayed geometric pairs in the (10,3)x family also appear as pairs of neighbouring points in the plot of the critical temperature T_c versus the vison gap Δ (Fig. 4.7). Thus, (10,3)a and (10,3)d, as well as (10,3)b and (10,3)c, possess both similar vison gaps and critical temperatures. This property distinguishes the (10,3)x lattice systems from those in the (8,3)x-family.

In the following, we discuss the numerical results for the different lattice systems individually.

C.3.1 (10,3)a

The hyperoctagon lattice possesses 4 vertices and 2 linearly independent loop operators per unit cell (see Fig. C.1). From Ref. [36], it is known that the exact solution of the Kitaev model at the isotropic coupling point possesses topological Fermi surfaces, i.e. Fermi surfaces that encapsule Weyl nodes situated at finite energy. With projective symmetry arguments, it is shown in Ref. [36] that the latter property is related to the fundamental symmetries of the lattice geometry. (10,3)a has a non-trivial sublattice symmetry, i.e. a sublattice symmetry which is not invariant under the translation vectors of the entire lattice, and thus requires

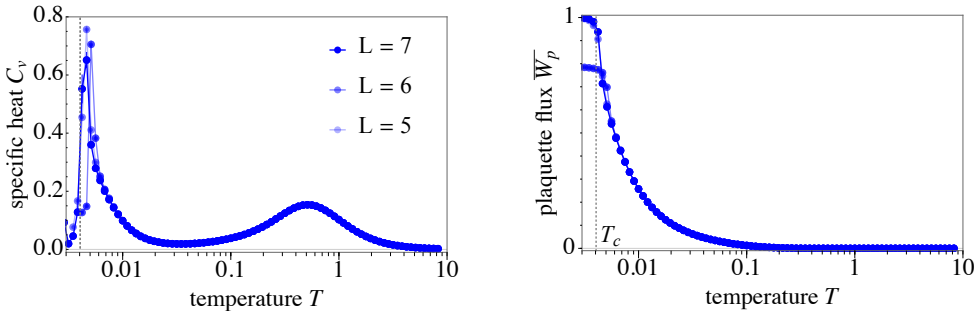

(a) specific heat C_v

(b) plaquette flux $\overline{W_p}$

Figure C.5: Specific heat $C_v(T)$ and plaquette flux $\overline{W_p}$ for (10,3)a. The systems are implemented with periodic boundary conditions in all spatial directions. For this choice of boundary conditions, the low-temperature peak of $C_v(T)$ shows finite-size effects up to the linear scale $L = 7$, which manifest themselves in an unsystematic scaling behavior of the peak height. The extrapolation of the T_c-value from this data is documented in Fig. C.14 and gives a result $\tilde{T}_c = 0.0044$, which is close to the literature value $T_c = 0.00405(9)$ (dotted line) [45]. The convergence of $\overline{W}_p$ to $W_p \sim 0.8$ instead of 1 for $L = 6$ is also a finite-size effect, which is sometimes seen for systems with (semi-)periodic boundary conditions due to additional volume constraints.

an enlargement of the unit cell for the implementation of a sublattice gauge transformation. At the same time, the lattice breaks inversion symmetry. Otherwise, the Weyl nodes would be constrained to lie exactly at the Fermi energy [36, 93].

Our analytical calculation of the zero-temperature density of states $\rho(E)$ verifies the occurrence of the Fermi surface, which manifests itself in a finite DOS at $E \to 0$ (Fig. 4.12 a). In the numerical result, the DOS at $E \to 0$ is also finite, but the quality of the results in this region does, in principle, not allow for a distinction between true low-E features and effects that just arise from the finite temperature.

The elementary plaquettes of this lattice do not fulfill the mirror symmetry requirements for Lieb's theorem to be applicable here. At the same time, it is explained in Ref. [36] that a uniform configuration of 0-fluxes ($W_p = +1$) for all plaquettes, which would be the prediction by this theorem for length-10-plaquettes, is consistent with all point-group symmetries of the lattice. A uniform configuration of π-fluxes, on the other hand, is forbidden by a volume constraint. It is therefore expected by symmetry that the ground state assumes the uniform 0-flux configuration. The QMC results confirm this (Figs. 4.1, C.5).

The low-temperature peaks of the specific heat $C_v(T)$ are in close vicinity to each other for the different linear system sizes $L = 5, 6, 7$. At the same time, the scaling behaviour of the peak height remains unsystematic up to these sizes. This is a mixture of a finite-size and an even-odd-effect (appendix C.2). Ref. [45] has presented QMC results with a more systematic scaling behavior of the low-

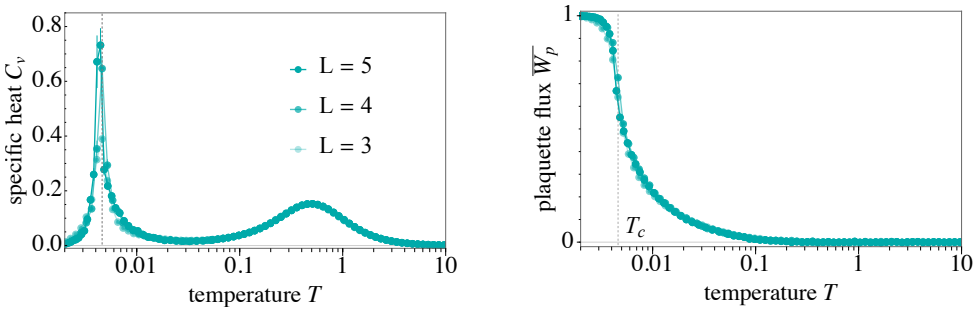

(a) specific heat C_v

(b) plaquette flux $\overline{W_p}$

Figure C.6: Specific heat $C_v(T)$ and plaquette flux $\overline{W_p}$ for (10,3)d [214]. Data shown is for systems with periodic boundary condition in the a_1- and open boundary conditions in the a_2- and a_3-direction. This choice of boundary conditions allows for an exact solution in terms of equal-length Jordan-Wigner strings, which manifests itself in a systematic scaling behavior of the low-temperature peak. The extrapolated value for the critical temperature is $T_c = 0.00462(1)$, which is marked by the dotted line (see Fig. C.14 for the details of the analysis).

temperature peak for systems with semi-open boundary conditions. Our extrapolated estimate for the critical temperature, $\tilde{T}_c = 0.0044$ (fitted only from the peak data for the system sizes $L = 5, 7$) is close to the literature value $T_c = 0.00405(9)$. Note that it is usual that small deviations between the T_c-estimates arise if those are extrapolated from systems with different boundary conditions.

In this system, the plaquette flux $\overline{W}_p$ also shows a finite-size effect. For L = 6, the flux does not order at $W_p = 1$ for $T \to 0$, but at a finite value $W_p \sim 0.8$. This effect is also seen in other systems with periodic or semi-periodic boundary conditions. On small systems, these boundary conditions may lead to unusual constraints on plaquettes that are partially spanned by periodic bonds. In all cases, this effect vanishes if the simulation is performed on larger systems.

C.3.2 (10,3)d

The inversion-symmetric partner system of the hyperoctagon lattice has a rather large unit cell, with 8 sites and 8 elementary loop operators (Fig. C.1). In addition to the inversion symmetry, it possesses a glide mirror symmetry. The latter makes this lattice the only non-symmorphic system in the present classification of 3D Kitaev models, a fact which has been outlined in an earlier study on the ground state of this system in Ref. [93]. In this paper, it is shown that the additional symmetry is responsible for a very specific feature of the (10,3)d Kitaev system. Its ground state possesses nodal lines that are, in contrast to the generic case, not gapped out to an even number of Weyl nodes upon applying time-reversal (TR)

symmetry breaking. Instead, the nodal lines remain stable under breaking of TR symmetry.

In the Majorana DOS, the signature of the nodal line ground state is the linearity of the DOS in E for small E, which, again, can be seen in our analytical DOS-results (Fig. 4.12). In the numerical DOS at small T, this linear behavior cannot be seen, which, in this particular case, is not an issue of numerical precision, but due to the open boundary of the system. The semi-open system possesses a drumhead surface state [93], and this surface state appears as a peak in $\rho(E)$ at $E = 0$.

(10,3)d is the only lattice system where the GF-KPM method fails. Usually, such a failure is related to exotic features in the DOS, such as singularities. Although the DOS of (10,3)d has a peculiar shape when compared to the other lattice systems, we cannot identify a specific feature here that inhibits the approximation of the density of states in terms of Green's functions. However, as a consequence of the failure of GF-KPM, all simulations that are presented here have been performed with the QMC-ED method. This technical restriction limits the accessible linear system size to $L = 5$ ($N = 1000$ sites). In order to counterbalance the finite-size effects which are expected to show up in this range of L, we have performed the QMC simulations on systems with open boundary conditions in the a_2- and a_3-direction. The Hamiltonian of this system is equivalent to the one obtained by a Jordan-Wigner transformation, where the Jordan-Wigner strings are composed of the x- and y-bonds along the counterrotating spirals. In particular, they have equal length. This generally leads to a more systematic scaling behaviour of the low-temperature peak, which is also the case here (Fig. C.6). The low-temperature peaks lie almost exactly at the same temperature T'' for all system sizes. From these peaks, we have extrapolated the critical temperature $T_c = 0.00462(1)$ (Fig. C.14). The peak positions nicely coincide with the inflection point of the average plaquette flux $\overline{W_p}$. Unlike in (10,3)a, the plaquette fluxes order at $W_p = 1$ for all system sizes.

C.3.3 (10,3)b

The hyperhoneycomb lattice is the inversion-symmetric 3D version of the honeycomb lattice, and the most prominent lattice in this classification. In fact, it is realized in nature as the Iridium sublattice in the material β-Li_2IrO_3 [91]. (10,3)b has 4 sites and 2 linearly independent loop operators per unit cell (Fig. C.2). It has a trivial sublattice symmetry and a ground state band structure that possesses a nodal line [36].

Accordingly, the Majorana DOS is E-linear for smallest energies, as we can see from the analytic calculation (Fig. 4.13 a).

Although Lieb's Theorem is not applicable for this lattice, the uniform 0-flux

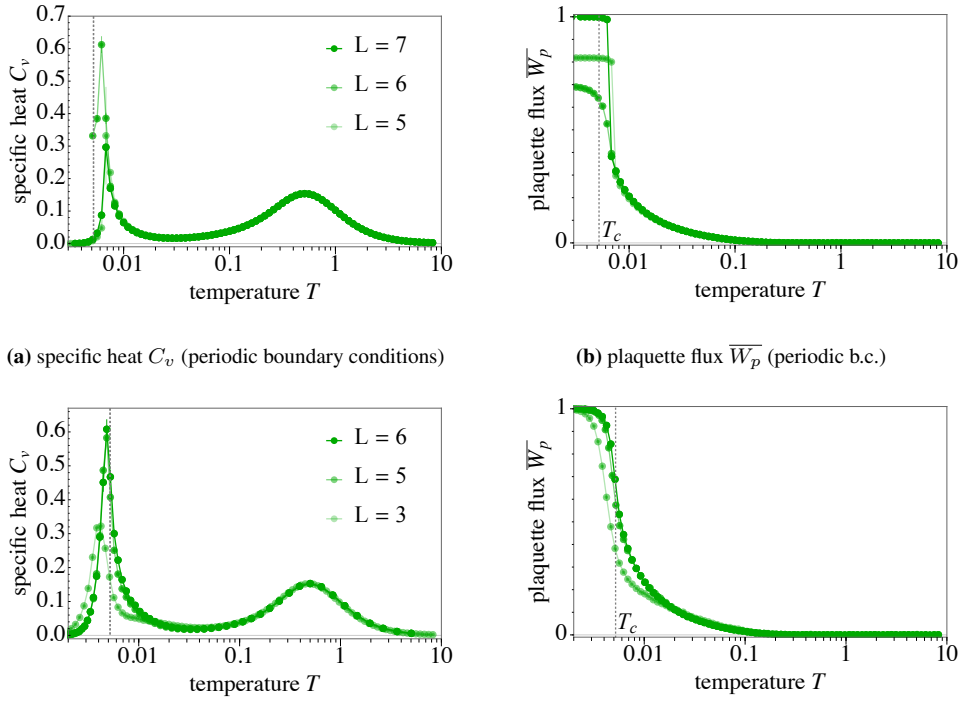

(a) specific heat C_v (periodic boundary conditions)

(b) plaquette flux $\overline{W_p}$ (periodic b.c.)

(c) specific heat C_v (semi-open b.c.)

(d) plaquette flux $\overline{W_p}$ (semi-open b.c.)

Figure C.7: Specific heat $C_v(T)$ and plaquette flux $\overline{W_p}$ for (10,3)b, with periodic boundary conditions (a,b) and open boundary conditions in the a_1- and a_2-direction (c,d). While the periodic system shows strong finite-size and even-odd effects in the low-temperature peak, the scaling behavior of the semi-open system is very systematic, which is due to the underlying exact solution with equal-length Jordan-Wigner strings. The literature value for the critical temperature $T_c = 0.00519(9)$ is, in all plots, indicated by the dotted vertical line [44]. As we can see, the low-temperature peaks of the periodic systems are shifted with respect to T_c, which is not unexpected for differing boundary conditions. The finite-size effect in $\overline{W_p}$ for the periodic systems with $L = 5, 6$ is the same as for the (10,3)a system.

configuration predicted to appear on plaquettes with length 10 is adopted by the ground state. Again, this flux configuration preserves all point group symmetries of the lattice [36]. The smallest vison loop has length 6 and is generated by flipping an x- or y-bond [36].

Numerical results for the specific heat C_v and the average plaquette flux $\overline{W_p}$ are given in Fig. C.7. Here, we can compare the results for systems with periodic boundary conditions in all spatial directions (a,b), and for systems with open boundary conditions in the a_1- and a_2-direction (c,d). Again, on the system with semi-open boundary conditions, we can perform a Jordan-Wigner transformation without closing the JW strings. Therefore, we don't have to neglect non-trivial parity terms when calculating thermodynamic observables. This is precisely what

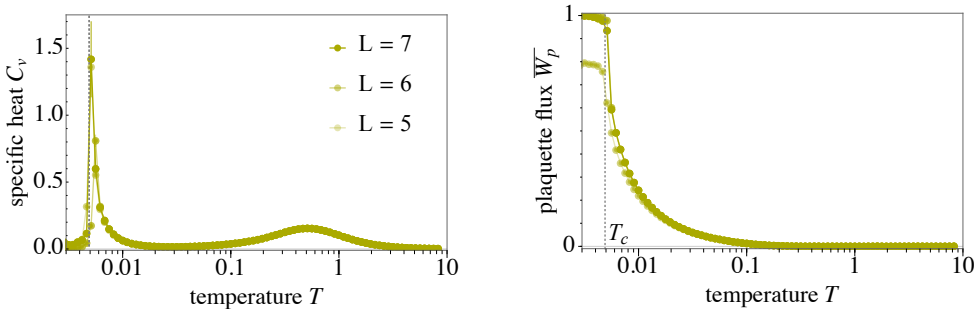

(a) specific heat C_v

(b) plaquette flux $\overline{W_p}$

Figure C.8: Specific heat $C_v(T)$ and plaquette flux $\overline{W_p}$ for (10,3)c [214]. Data shown is for systems with periodic boundary conditions in all directions. Here, the low-temperature peak of C_v shows a more systematic behavior for the periodic system than (10,3)b, although an even-odd effect on the peak height is noticeable. The extrapolated critical temperature is $T_c = 0.0049(2)$. The average plaquette flux $\overline{W_p}$ for $L = 5$ converges to a finite value $W_p \sim 0.8$, which is a finite-size effect.

has been done in an earlier QMC study on hyperhoneycomb systems with semi-open conditions, which has yielded the literature value for the critical temperature, $T_c = 0.00519(9)$ [44]. Here, the JW strings, which are given by the xy-zigzag chains in the lattice, have the same length, which usually leads to a more systematic scaling behavior of the thermal signatures. This is also the case here, where the low-temperature peak is getting sharper with increased system sizes in the semi-open system, whereas, in the periodic system, it still shows a noticeable finite-size and a drastic even-odd effect (with the low-temperature peak for $L = 6$ being far taller than the ones for $L = 5, 7$). The extrapolated critical temperature $\tilde{T}_{c,1} = 0.0048(1)$ is close to the literature value for the semi-open systems. For periodic systems, the estimate $\tilde{T}_{c,2} = 0.0063(4)$ is shifted, which is not unexpected for systems with different boundary conditions.

A finite-size effect is also visible in the plaquette flux results for the periodic systems. For L = 5, the flux converges to a finite value $W_p \sim 0.8$ (instead of $W_p = 1$ for $T \to 0$, which is similar to the behavior of the (10,3)a system.

C.3.4 (10,3)c

The (10,3)c lattice is the chiral counterpart of (10,3)b, as it breaks inversion symmetry. (10,3)c also has a larger unit cell, which contains six sites (Fig. C.2). There are three length-10 and three length-12 loop operators per unit cell, which form three closed volumes, thus leaving 3 linear independent loop operators per unit cell. The ground state of the Kitaev system has two nodal lines [36].

The nodal line band structure manifests itself in the E-linear behavior of the Majorana DOS (Fig. 4.13 c). Apart from that, the analytical Majorana DOS shows a very dominant van-Hove singularity at $E \sim 1.3$, which also appears in the numerical DOS results.

Also in this case, all point group symmetries of the lattice are preserved by the uniform 0-flux configuration [36], and the latter is confirmed by the QMC results. As discussed in the introductory part of this section on the geometric relations between the lattices, the geometric "partnership" with (10,3)b manifests itself in very similar vison gaps Δ and critical temperatures T_c.

Here, the low-temperature peak in the specific heat C_v shows a more systematic behavior for systems with periodic boundary conditions than in the case of (10,3)b (Fig. C.8), yielding a critical temperature estimate $T_c = 0.0049(2)$. An even-odd effect is, however, visible, since the peak for $L = 6$ is smaller than the peaks for $L = 5, 7$.

The average plaquette flux $\overline{W_p}$ for $L = 5$ converges to a finite value $W_p \sim 0.8$, which is a finite-size effect known also from the lattices (10,3)a and (10,3)b.

C.4 Numerical results for the 8-loop lattices

Despite the close relation of (8,3)a and (8,3)b, both lattices possess very different vison gaps Δ and critical temperatures T_c, which is unlike their counterparts in the (10,3)x family.

We continue with a brief, individual discussion of the geometric specifics and numerical results for each lattice.

C.4.1 (8,3)a

(8,3)a has a relatively large unit cell, containing 6 sites (Fig. C.3). There are three loop operators of length 8 (plus three of length 14) per unit cell. The Kitaev system on the (8,3)a lattice has a Majorana metal ground state whose band structure possesses topological Fermi surfaces. The emergence of this topological band structure is determined by the same symmetry arguments as in the case of (10,3)a, namely the occurrence of both a non-trivial sublattice symmetry and a broken inversion symmetry [36].

We see the signature of the Fermi surface as a finite Majorana DOS at lowest E in the analytical DOS (Fig. 4.10 a). Actually, the shape of the DOS is very similar for (8,3)a and (8,3)b, with the exception of the low-E region. Interestingly, both lattices have a dominant van-Hove singularity at $E \sim 1$, which is also visible in the numerical DOS results.

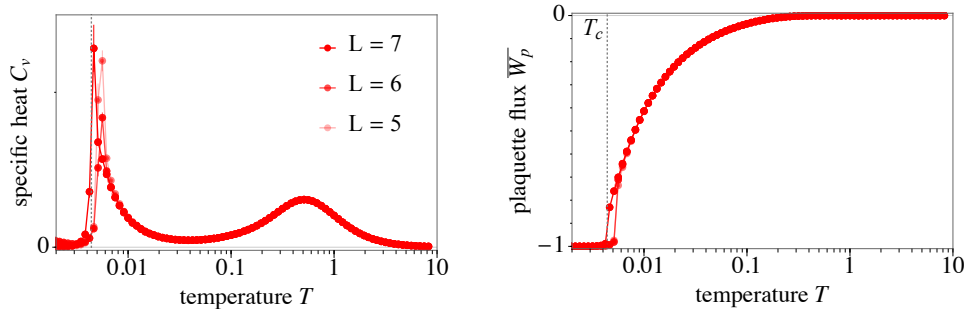

(a) specific heat C_v

(b) plaquette flux $\overline{W_p}$

Figure C.9: Specific heat $C_v(T)$ and plaquette flux $\overline{W_p}$ for (8,3)a [214]. The specific heat C_v shows a similar even-odd effect as (10,3)c. The critical temperature estimate $T_c = 0.0044(8)$ is indicated by the dotted vertical line. There are no finite-size effects appearing in the average plaquette flux $\overline{W_p}$.

On the (8,3)a Kitaev system, Lieb's theorem is not applicable. However, taking Lieb's theorem as a guideline, we expect all length-8 plaquettes to order with a π-flux ($W_p = -1$), and all length-14 plaquettes to order with a 0-flux. This configuration again preserves all point-group symmetries of the lattice [36] and is therefore expected to be assumed by the ground state. The QMC results confirm this (Fig. C.9).

(8,3)a has the lowest vison gap and one of the lowest critical temperatures among all 3D Kitaev systems. The specific heat C_v shows a similar even-odd effect as the one that is observed for (10,3)c, with the low-temperature peak for $L = 6$ being smaller than for $L = 5, 7$. For $L = 7$, however, the peak is the sharpest. The critical temperature estimate is $T_c = 0.0044(8)$.

There are no finite-size effects visible in the average plaquette flux $\overline{W_p}$.

C.4.2 (8,3)b

With a similar geometry as (8,3)a, the (8,3)b lattice possesses six sites per unit cell (Fig. C.3). Here, inversion symmetry is preserved, which, in combination with a non-trivial sublattice symmetry, determines the existence of gapless Weyl points instead of Fermi surfaces[36].

In the Majorana DOS, the Weyl point band structure manifests itself in an E-quadratic behavior for $E \to 0$. Except for the low-E region, the DOS has a similar shape as the one of (8,3)a.

(8,3)b is the only lattice among the elementary tricoordinated 3D systems which, globally and for each plaquette, has a mirror symmetry with mirror planes that do nut cut through any of its vertices, which is the geometric requirement for

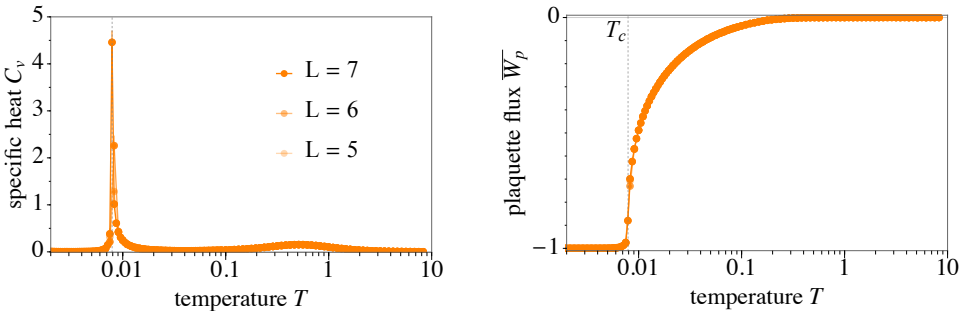

(a) specific heat C_v

(b) plaquette flux $\overline{W_p}$

Figure C.10: Specific heat $C_v(T)$ and average flux $\overline{W}_p$ for (8,3)b [214]. Here, the low-temperature peak of the specific heat is the sharpest, showing a systematic increase for growing system sizes. (8,3)b is the only system where Lieb's theorem applies, and also has the largest critical temperature of all 3D Kitaev systems, $T_c = 0.0079(3)$.

Lieb's theorem. The theorem is therefore applicable here and predicts a π-flux per length-8 plaquette. This ground state flux configuration preserves the point-group symmetries of the lattice [36], and is confirmed by the QMC results (Fig. C.10).

In drastic contrast to its geometric counterpart (8,3)a, (8,3)b has the largest critical temperature $T_c = 0.0079(3)$ of all the lattices regarded in this article, and the second-largest vison gap $\Delta = 0.0532(3)$.We see no finite-size effects in the specific heat for linear system sizes $L = 5, 6, 7$. Instead, the low-temperature peak, which is particularly sharp, diverges for increased system sizes, without wandering in temperature-space. This allows for the extrapolation of the critical temperature T_c with a relatively small error estimate. Also, no finite-size effects appear in the plaquette flux curves $\overline{W_p}$.

C.4.3 (8,3)n

The unit cell of (8,3)n is the largest of the lattices considered here, having 16 sites and 8 linearly independent loop operators of lengths 8 and 10 (Fig. C.4). In Ref. [36], it is shown to be the only 3D Kitaev system which does not possess a gapless Majorana phase. Analytic results for the Majorana DOS $\rho(E)$ confirm the occurrence of a band gap at the isotropic coupling point (Fig. 4.11).

Interestingly, the symmetries of the elementary plaquettes of the (8,3)n lattice allow for the application of Lieb's theorem for all but one plaquette. It has been laid out in Ref. [36] that a uniform configuration of π-fluxes also preserves all the point-group symmetries of the lattice. The QMC results confirm this.

The vison gap $\Delta = 0.005397(10)$ of the (8,3)n Kitaev system is the largest of all systems considered here, and correlates with a large critical temperature

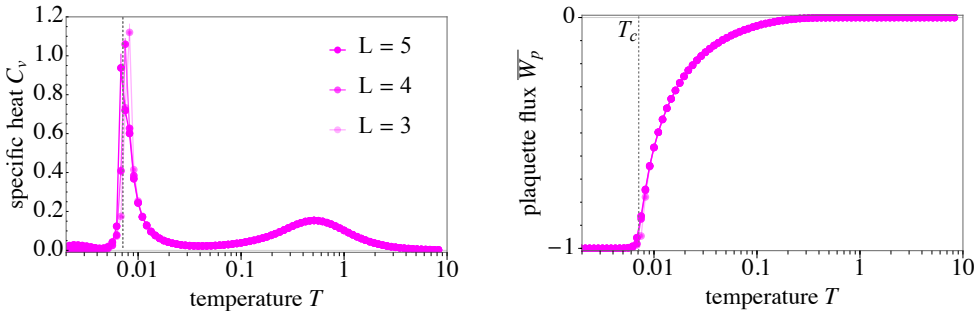

(a) specific heat C_v

(b) plaquette flux $\overline{W_p}$

Figure C.11: Specific heat $C_v(T)$ and average flux $\overline{W_p}$ for (8,3)n. The vison gap $\Delta = 0.005397(10)$ of the (8,3)n Kitaev system is the largest of all systems considered here, which correlates with a large critical temperature $T_c = 0.0071(3)$. The data for C_v shows finite-size effects for the considered system sizes, resulting in a non-systematic scaling behavior of the low-temperature peak. The results for the average plaquette flux $\overline{W_p}$ show no finite-size effects.

$T_c = 0.0071(3)$. Not unexpectedly for a system with such a large unit cell, the computational restriction on the accessible system sizes with quantum Monte Carlo prevents us from overcoming the realm of noticeable finite-size effects. As we can see in the plot of the specific heat C_v (Fig. C.11), there is no systematic divergence of the low-temperature peak for $L = 3, 4, 5$. However, for larger systems, the peak appears to move slightly towards lower temperatures, which facilitates the extrapolation of a T_c-estimate. The QMC results for the average plaquette flux $\overline{W_p}$ show no finite-size effects.

C.5 Vison gaps

The vison gap Δ is the energy difference between the ground state flux configuration of the Kitaev system and the configuration with the smallest possible flux excitation, which is generated by carefully picking the right $\mathbb{Z}_2$ gauge variable u_{ij} and flipping it. It is calculated by exact diagonalization of the Majorana Hamiltonian in the respective gauge sectors. For most systems, we use the vison gap data from Ref. [36]. We have rescaled this data to Kitaev couplings $J_\gamma = 1/3$, and refitted it to obtain improved estimates on the standard deviation. For the lattice systems (8,3)c and (10,3)d, we have performed all the vison gap calculations. The results for all systems are presented in the Figs. C.12 and C.13.

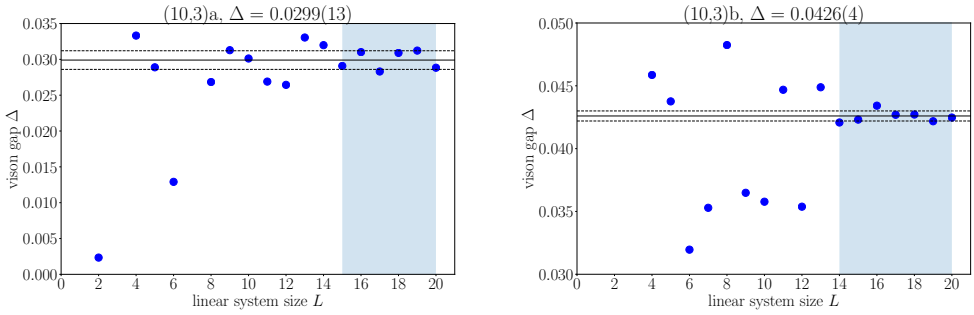

(a) (10,3)a **(b)** (10,3)b

(c) (10,3)c **(d)** (10,3)d

Figure C.12: Vison gaps for the lattices of the (10,3)x family [36]. The blue-shaded regions indicate the intervals for the least-squares fit.

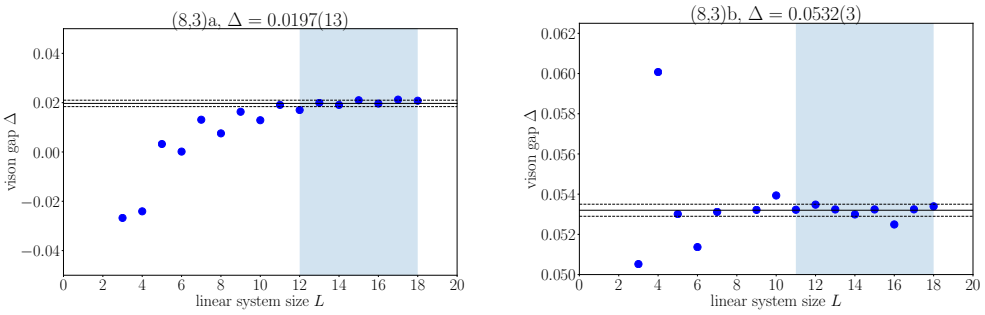

(a) (8,3)a **(b)** (8,3)b

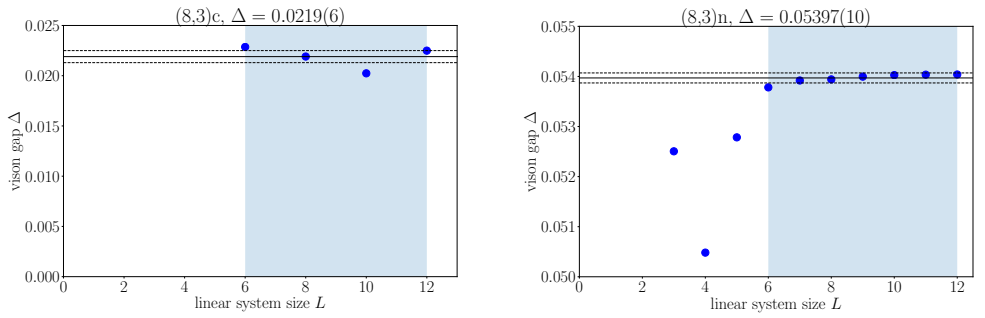

(c) (8,3)c **(d)** (8,3)n

Figure C.13: Vison gaps for the lattices of the (8,3)x family [36]. The blue-shaded regions indicate the intervals for the least-squares fit.

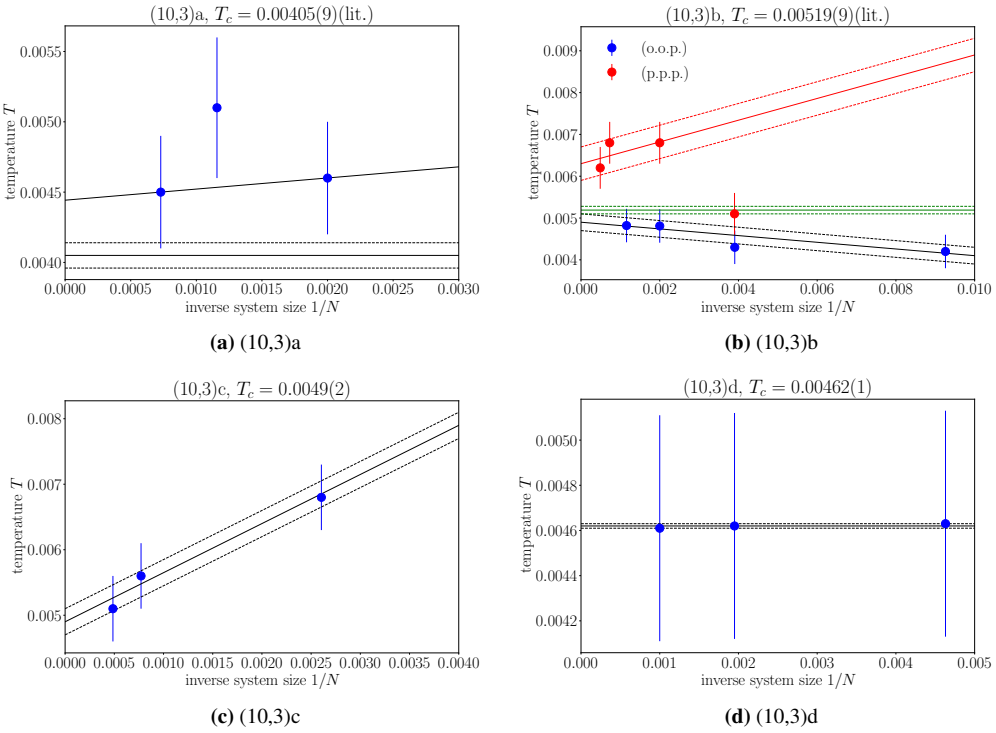

(a) (10,3)a **(b)** (10,3)b

(c) (10,3)c **(d)** (10,3)d

Figure C.14: Critical temperature estimates for the (10,3)x lattice family. The literature values for (10,3)a (a) and (10,3)b (b) are indicated, along with their error estimates, by the horizontal black (green) line [44, 45]. For (10,3)a, we have also extrapolated T_c for a different system with periodic boundary conditions. For (10,3)b, we have extrapolated a T_c-estimate for systems with open-open-periodic (blue) and periodic boundary conditions (red). The specific heat plots corresponding to the peak positions presented here are shown in Figs. C.5 - C.8.

C.6 Critical temperatures

We obtain the estimates for T_c from the positions T'' of the low-temperature specific-heat peaks as a function of the inverse system size $1/N$, and extrapolating them for the thermodynamic limit $N \to \infty$. The extrapolation plots are documented in the Figs. C.14 and C.15.

For the lattice systems (10,3)a and (10,3)b, values for T_c have formerly been presented in Refs. [44] and [45]. We have used these values for the verification of the correlation between T_c and the vison gap Δ, and compared them with own simulation results (Fig. C.14 a, b). The results for the (10,3)b (hyperhoneycomb) system with semi-periodic boundary conditions reproduce the value of T_c from Ref. [44]. The results for the system with periodic boundary conditions lead to a deviating T_c estimate, which is a typical effect for changed boundary conditions. We see the same effect for (10,3)a. A T_c-estimate for the (9,3)a Kitaev system has

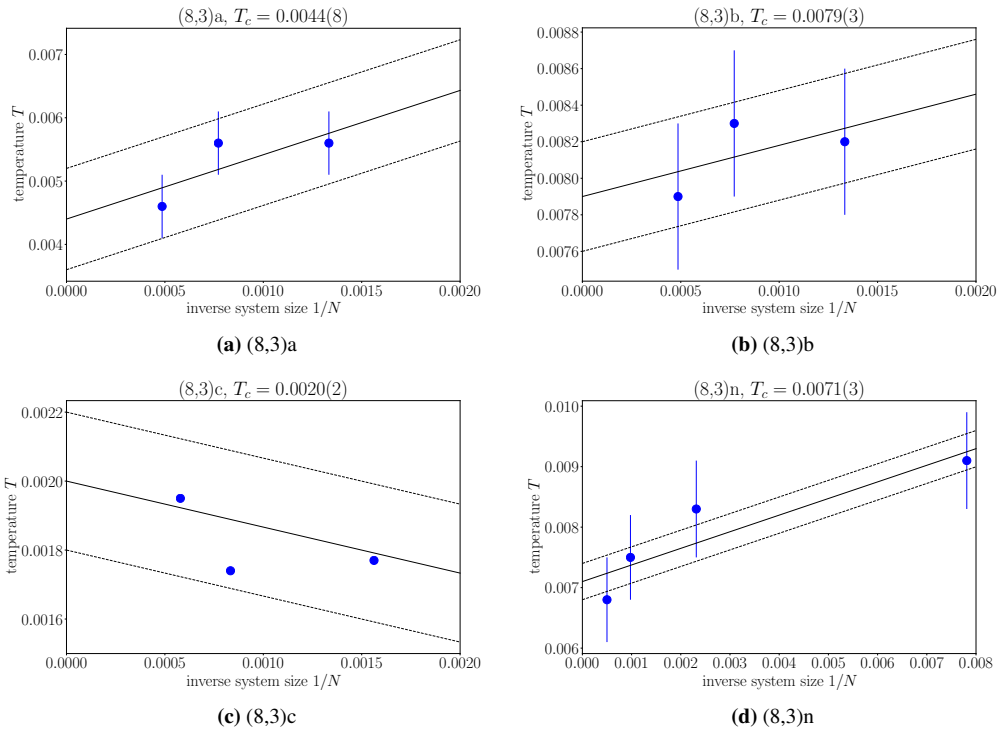

(a) (8,3)a **(b)** (8,3)b

(c) (8,3)c **(d)** (8,3)n

Figure C.15: Critical temperature estimates for the (8,3)x lattice family. The specific heat plots corresponding to the peak positions presented here are shown in Figs. C.9 - C.11.

been published in Ref. [90].

C.7 Jordan-Wigner transformation

On the Hamiltonian-level, the difference between the local transformation and the Jordan Wigner ansatz is the number of $\mathbb{Z}_2$ gauge variables in the system. The local transformation generates $\mathbb{Z}_2$ gauge variables u_{ij} on *all* bonds, while the $\mathbb{Z}_2$ gauge variables η in the JW-transformed Hamiltonian only live on *one* subclass of bonds (here, the z-bonds). For a system with open boundary conditions, both Hamiltonians are equivalent if the gauge field in the local version is fixed on the x- and y-bonds. However, benchmark calculations on small Kitaev clusters have shown that the QMC simulation based on the local transformation gives results that are within the error bars of the data points obtained from a QMC simulation with JW strings (Fig. 3.1), even for very small systems, where the deviations are expected to be the largest. We can therefore conclude that the error arising from the local transformation ansatz, where the Hilbert space is artificially enlarged for each spin, is negligible in the large-scale QMC simulations. The interpretation

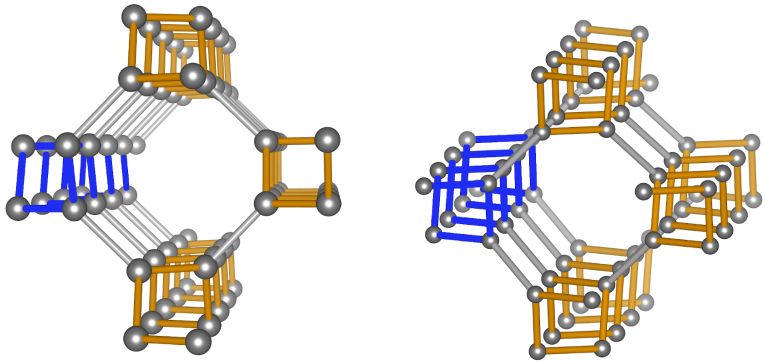

(a) (10,3)a **(b)** (10,3)d

Figure C.16: Jordan-Wigner strings for (10,3)a and (10,3)d. Jordan-Wigner strings can be defined along the x- and y-bonds, while the z-bonds host the $\mathbb{Z}_2$ gauge variable η. For (10,3) a (d), the JW strings extend along the co-rotating (counter-rotating) spirals.

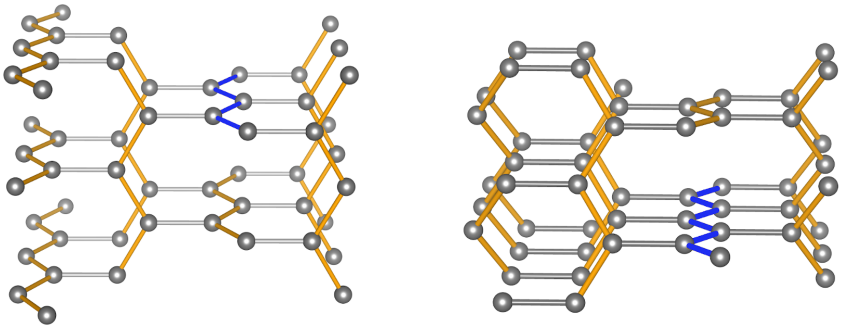

(a) (10,3)b **(b)** (10,3)c

Figure C.17: Jordan-Wigner strings for (10,3)b and (10,3)c. The JW strings are defined along x- and y-bonds (yellow). For both lattices, they extend along the zigzag chains. Individual JW strings are highlighted in blue.

is that on systems with a well-defined JW-transformed Hamiltonian of the form in Eq. 2.34, the additional gauge variables u_{ij} of the local transformation only lead to an overcounting of physical states. Thus, the existence of a Jordan-Wigner solution on a given Kitaev system ensures us that the results are correct, even if the QMC simulation is based on the local transformation ansatz. Therefore, we have checked that for all elementary, tricoordinated three-dimensional lattices considered in this thesis, there is a well-defined Jordan-Wigner transformation if appropriate bond subsets are chosen for the one-dimensional strings (see Figs. C.16 - C.19).

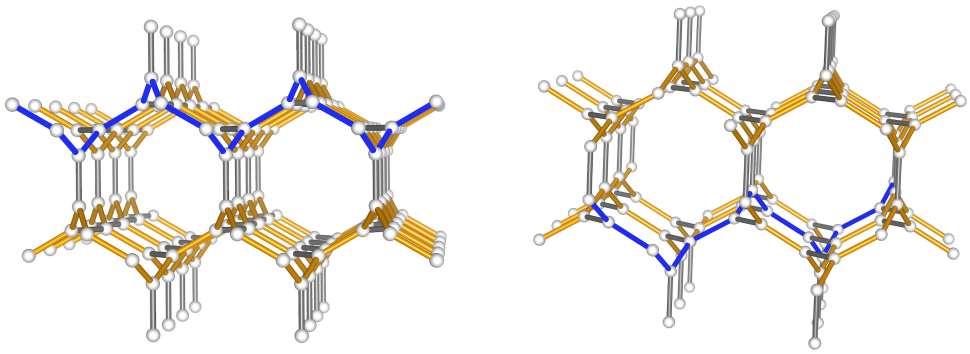

(a) (8,3)a **(b)** (8,3)b

Figure C.18: Jordan-Wigner strings for (8,3)a and (8,3)b. For both lattices, the JW transformation is defined along x- and y-bonds (yellow). Individual JW strings are highlighted in blue.

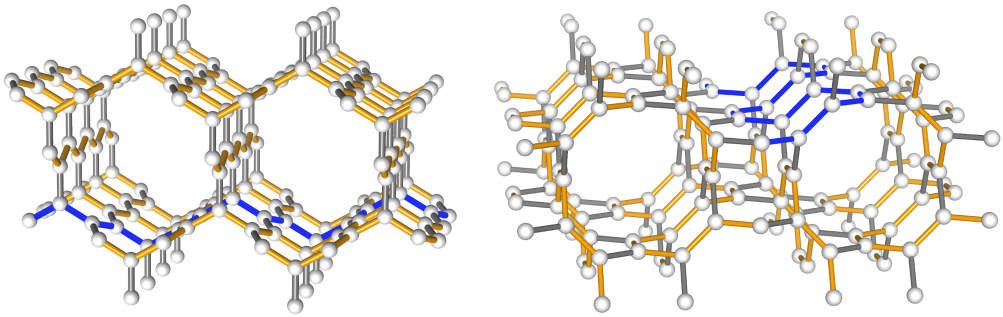

(a) (8,3)c **(b)** (8,3)n

Figure C.19: Jordan-Wigner strings for (8,3)c and (8,3)n (yellow). On (8,3)c, the JW transformation can be defined along x- and y-bonds, while on (8,3)n, it is of more advantage to use y- and z-bonds for the JW-strings, in order to avoid closed JW strings. Individual JW strings are highlighted in blue.

C.8 Gauge frustration in the (8,3)c Kitaev model

C.8.1 Pseudospin Correlator

The pseudospin correlator defined in Eq. (4.4) can be used to identify the ground state manifolds of the different (an)isotropic regimes of the (8,3)c Kitaev system. It can be easily seen that $\|\mathbf{W}_m\| = \sqrt{3}$ for all $m \in \{a, b, c\}$ and

$$\frac{\mathbf{W}_m \cdot \mathbf{W}_n}{\|\mathbf{W}_m\|\|\mathbf{W}_n\|} = \begin{cases} -\frac{1}{3}, & m \neq n \\ 1, & m = n \end{cases} \tag{C.1}$$

For large temperatures T, all (four) possible 3-flux states are allowed, so we expect P to average to 0. For the low temperature regime of the isotropic system ($J_x = J_y = J_z$), the pseudospins $\mathbf{W}_a$, $\mathbf{W}_b$, $\mathbf{W}_c$ from Eq. (4.3) are equally distributed in the system, giving the correlator expectation value

$$P_{abc} = \frac{1}{9}\left(1 + 1 + 1 - 6 \cdot \frac{1}{3}\right) = \frac{1}{9}, \tag{C.2}$$

For the weak-J_z limit, only the pseudospins $\mathbf{W}_b$, $\mathbf{W}_c$ are selected, resulting in

$$P_{bc} = \frac{1}{4}\left(1 + 1 - 2 \cdot \frac{1}{3}\right) = \frac{1}{3}\,, \tag{C.3}$$

while for the strong-J_z limit, all plaquette triplets select the state $\mathbf{W}_a$, leading to

$$P_a = 1\,. \tag{C.4}$$

C.8.2 Flux snapshots

We see the emergence of a columnar zigzag plaquette flux order in the (8,3)c Kitaev model in low-temperature snapshots of the flux configurations, which are taken during the QMC simulation. We document the relevant snapshots for the isotropic system ($J_z = 1/3$) and the system where the gauge degeneracy is partially lifted ($J_z = 0.25$). For $J_z \gg 1/3$, the nature of the ground state is determined by the geometric selection of the plaquette flux order, which has been verified with measurements of the pseudospin correlator P and shown in the finite-temperature phase diagram (Fig. 4.19).

C.8.3 Band structures

In Fig. 4.18, we define the ground state plaquette flux orders for the different (an)isotropic limits of the (8,3)c Kitaev system, and show the nodal line structures of the corresponding Majorana semimetal ground state. The plaquette flux

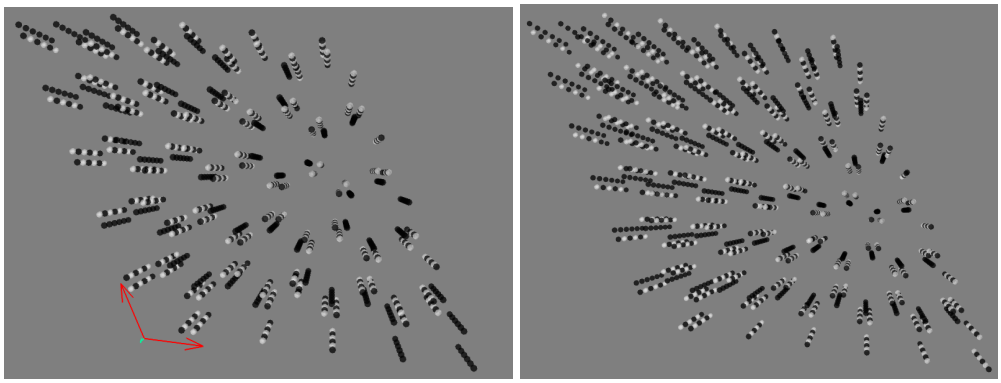

(a) $J_z = 1/3$, system size $5 \cdot 5 \cdot 6$, $T = 0.0015$ **(b)** $J_z = 0.25$, system size $6 \cdot 6 \cdot 6$, $T = 0.0021$

Figure C.20: Snapshots of flux configurations for $J_z = 1/3$ (a) and $J_z = 0.25$ (b). Black spheres indicate π-fluxes, white spheres 0-fluxes. We can distinguish the M1-plaquette-flux order (Fig. 4.18) in (b) from the M2-order in (a), which also allows for 0-fluxes on the horizontal plaquettes.

orders comprise the columnar zigzag orders M1 and M2, which emerge due to the interplay of the Majorana fermions with the frustrated $\mathbb{Z}_2$ gauge field, which is a quantum effect. The third plaquette order M3 is the result of the classical geometric selection of the horizontal lattice plaquettes to carry the 0-fluxes, which happens in the limit $J_z \geq 0.4$.

In the following, we document the band structures for the different ground state gauge orders M1 - M3 (Figs. C.21 - C.25).

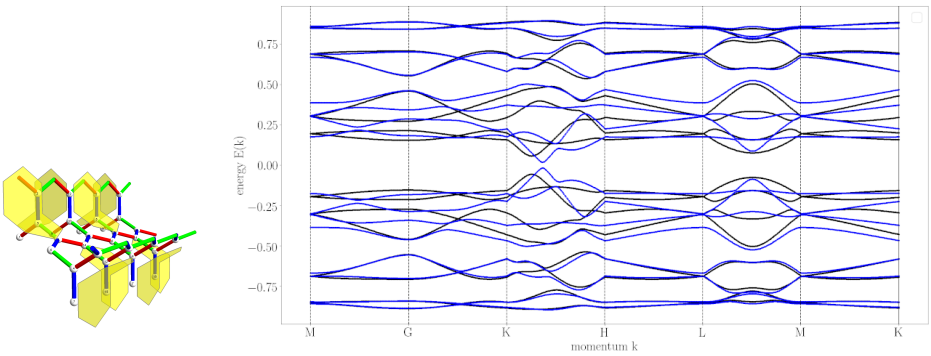

Figure C.21: Columnar zigzag gauge order M1 and corresponding band structure. Black: $J_z = 1/3$, blue: $J_z = 0.25$.

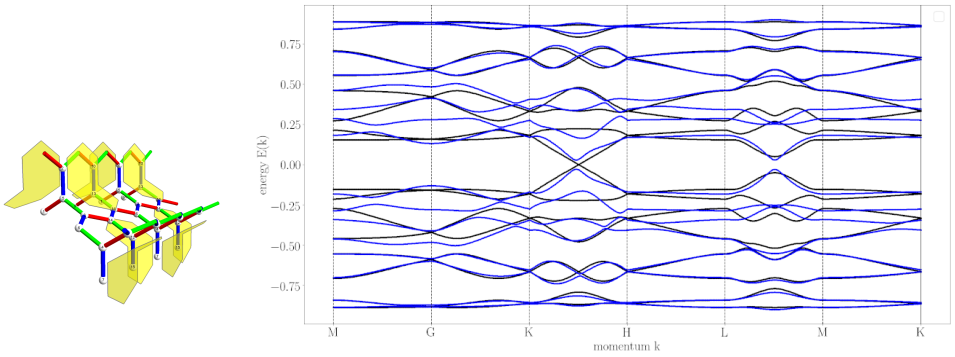

Figure C.22: Columnar zigzag gauge order M1 and corresponding band structure. Black: $J_z = 1/3$, blue: $J_z = 0.25$.

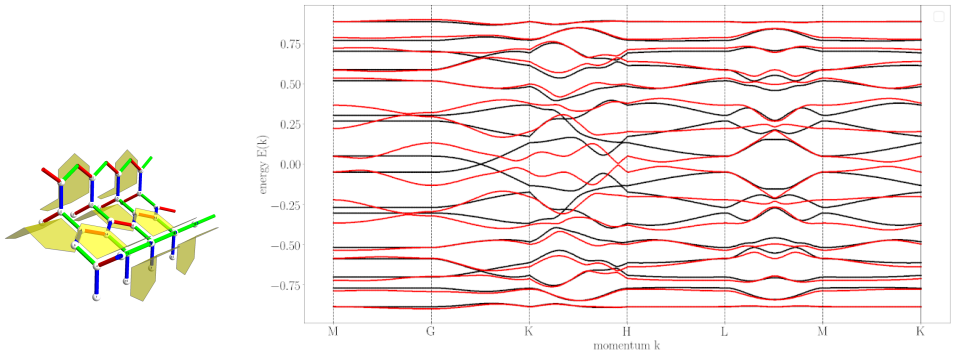

Figure C.23: Columnar zigzag gauge order M2 and corresponding band structure. Black: $J_z = 1/3$, red: $J_z = 0.42$.

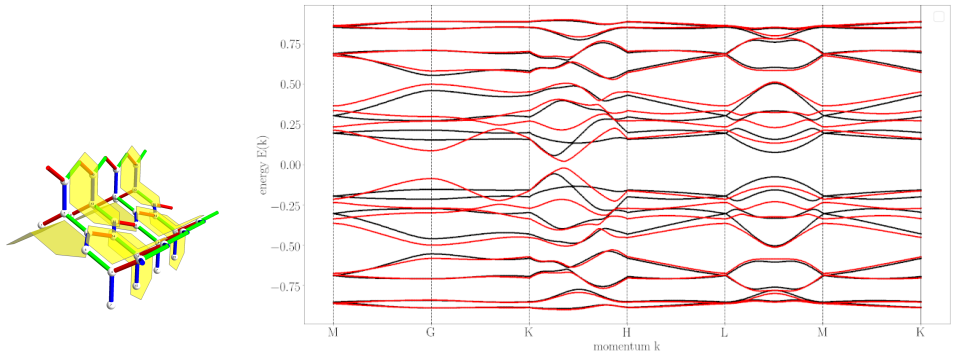

Figure C.24: Columnar zigzag gauge order M2 and corresponding band structure. Black: $J_z = 1/3$, red: $J_z = 0.42$.

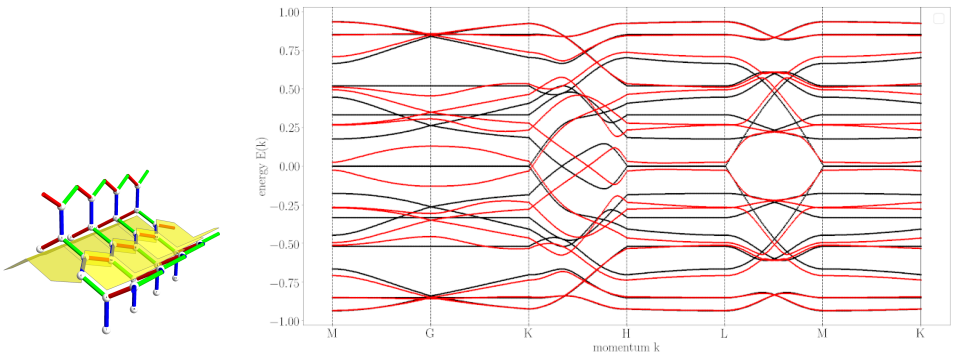

Figure C.25: Unique gauge order M3 and corresponding band structure. Black: $J_z = 1/3$, red: $J_z = 0.42$.

Appendix D

Topological phases in a generalized Kitaev model

D.1 Average Chern number

In Sec. 5.2.3, we show numerical results for the average Chern number $|\nu|$ of the Majorana band structure in fixed $\mathbb{Z}_2$ gauge field configurations. The calculation method is described in Sec. 5.1.4. In the following Figs. D.1 - D.4, we present ν-histograms, band structures and detailed Chern number results for different parameter points (cuts) in phase diagram 5.10.

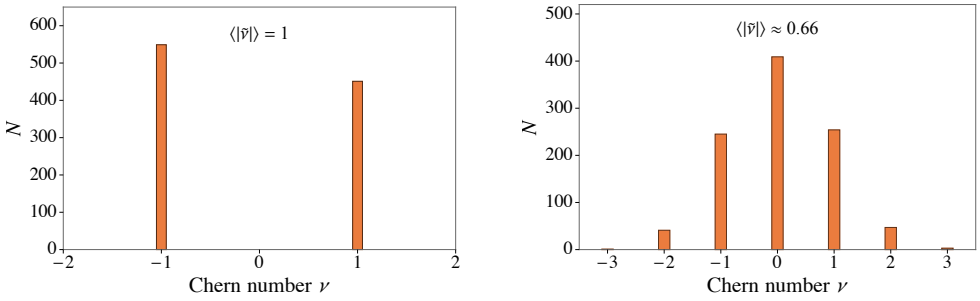

(a) $J_z = 1.5, T = 0.0075$ **(b)** $J_z = 1.5, T = 0.105$

Figure D.1: Chern number histograms for two different temperatures at the parameter point $J_z = 1.5$ (in phase diagram 5.10). In the intermediate-temperature regime, the occurrence of integer Chern number results is an artifact, since here, the system is in a gapless phase.

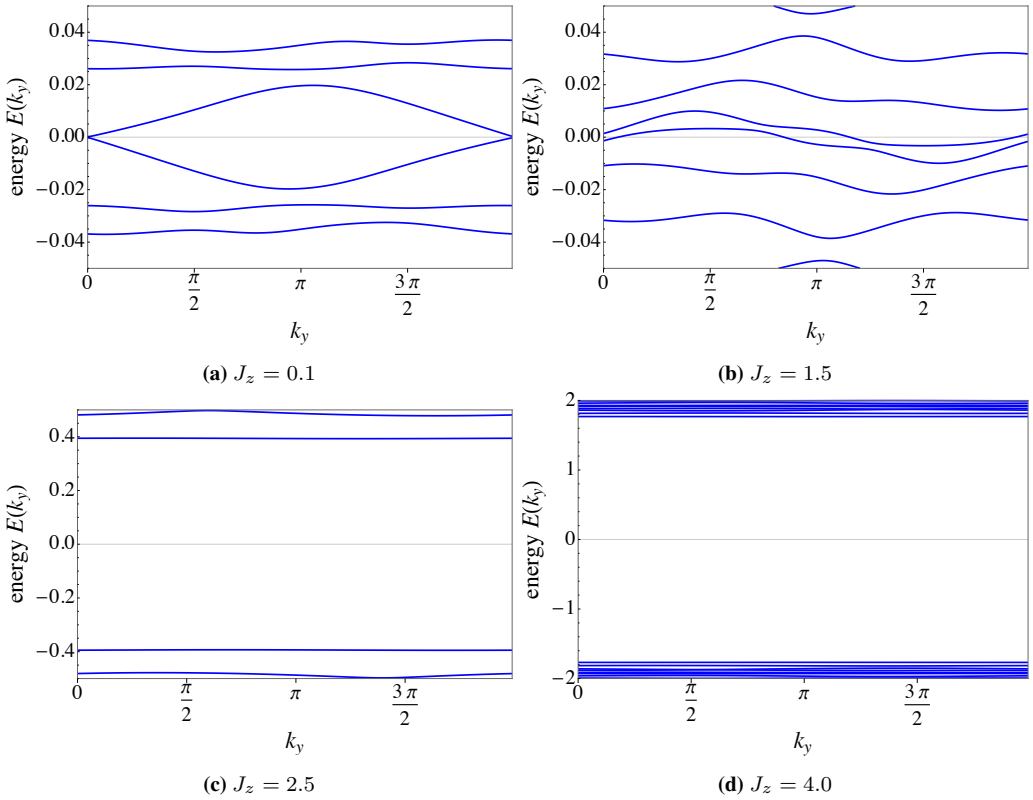

(a) $J_z = 0.1$ **(b)** $J_z = 1.5$

(c) $J_z = 2.5$ **(d)** $J_z = 4.0$

Figure D.2: Band structures near $E = 0$ for different parameters values J_z at $T = \infty$ (in phase diagram 5.10), showing the transition from the gapless to the gapped high-temperature phase.

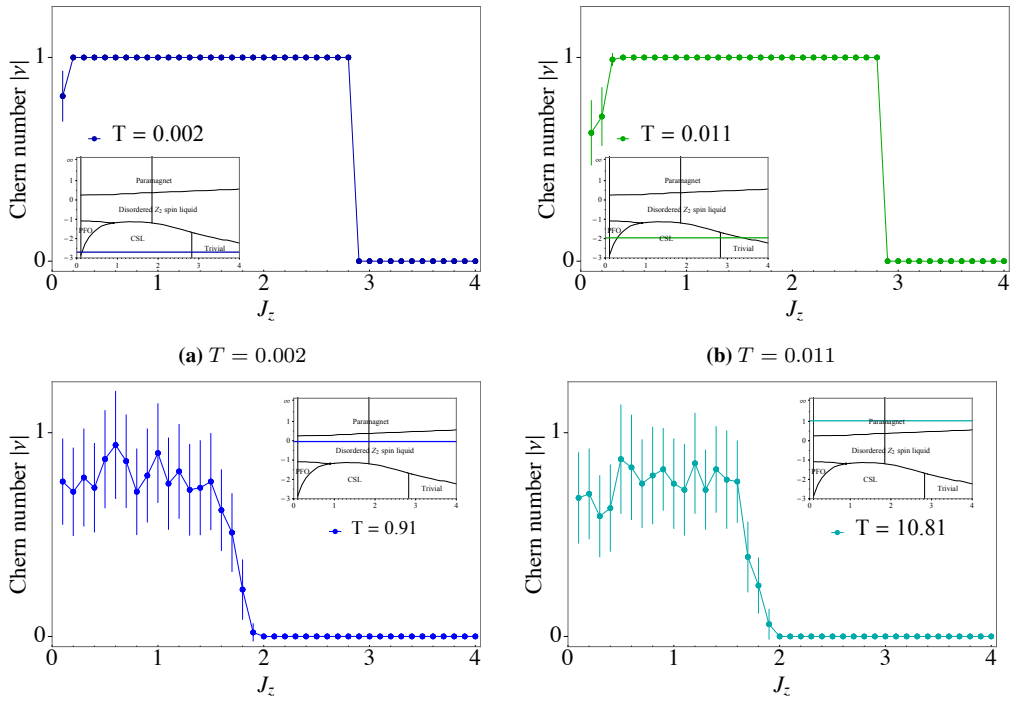

(a) $T = 0.002$ **(b)** $T = 0.011$

(c) $T = 0.91$ **(d)** $T = 10.81$

Figure D.3: Average chern number $\langle|\nu|\rangle$ for different horizontal (constant temperature) cuts in phase diagram 5.10.

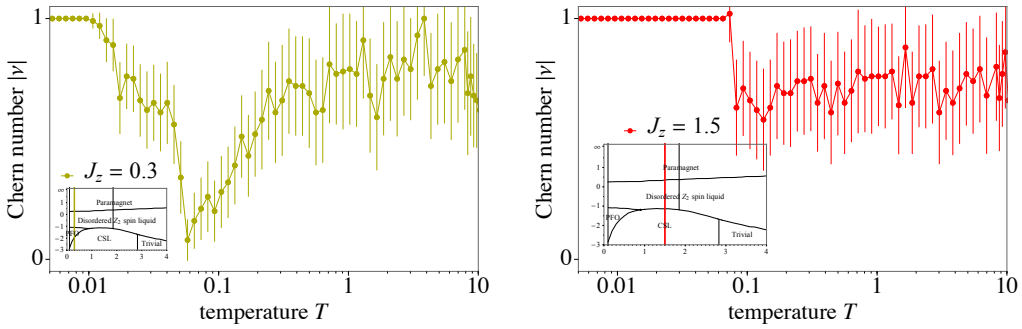

(a) $J_z = 0.3$ **(b)** $J_z = 1.5$

(c) $J_z = 2.5$ **(d)** $J_z = 3.5$

Figure D.4: Average chern number $\langle|\nu|\rangle$ for different vertical (constant J_z) cuts in phase diagram 5.10.

Bibliography

[1] P. W. Anderson, Resonating valence bonds: A new kind of insulator? Mater. Res. Bull. **8**, 153 (1973).

[2] P. Fazekas and P. W. Anderson, On the ground state properties of the anisotropic triangular antiferromagnet, Phil. Mag. **30**, 423 (1974).

[3] L. Balents, Spin liquids in frustrated magnets, Nature **464**, 199 (2010).

[4] C. Lacroix, P. Mendels, and F. Mila, eds., Introduction to Frustrated Magnetism (Springer, 2011).

[5] H. T. Diep, Frustrated Spin Systems, 2nd ed. (World Scientific, 2013).

[6] Y. Zhou, K. Kanoda, and T.-K. Ng, Quantum spin liquid states, Rev. Mod. Phys. **89**, 025003 (2017).

[7] L. Savary and L. Balents, Quantum spin liquids: a review, Rep. Prog. Phys. **80**, 016502 (2017).

[8] J. Knolle and R. Moessner, A Field Guide to Spin Liquids, Annual Review of Condensed Matter Physics **10**, 451 (2019).

[9] P. W. Anderson, The Resonating Valence Bond State in La_2CuO_4 and Superconductivity, Science **235**, 1196 (1987).

[10] X.-G. Wen, F. Wilczek, and A. Zee, Chiral spin states and superconductivity, Phys. Rev. B **39**, 11413 (1989).

[11] A. Kitaev, Fault-tolerant quantum computation by anyons, Ann. Phys. **303**, 2–30 (2003).

[12] A. Kitaev and C. Laumann, Topological phases and quantum computation, arXiv:0904.2771 .

[13] L. Landau, The Theory of Phase Transitions, Nature **138**, 840 (1936).

[14] L. D. Landau, On the theory of phase transitions, Zh. Eksp. Teor. Fiz. **7**, 19 (1937).

[15] V. Ginzburg and L. Landau, On the Theory of superconductivity, Zh. Eksp. Teor. Fiz. **20**, 1064 (1950).

[16] X.-G. Wen, Quantum orders and symmetric spin liquids, Phys. Rev. B **65**, 165113 (2002).

[17] X.-G. Wen, Quantum order: a quantum entanglement of many particles, Physics Letters A **300**, 175–181 (2002).

[18] X.-G. Wen, Topological Order: From Long-Range Entangled Quantum Matter to a Unified Origin of Light and Electrons, ISRN Condensed Matter Physics **2013**, 1–20 (2013).

[19] X. G. Wen, Vacuum degeneracy of chiral spin states in compactified space, Phys. Rev. B **40**, 7387 (1989).

[20] X. G. Wen, Mean-field theory of spin-liquid states with finite energy gap and topological orders, Phys. Rev. B **44**, 2664 (1991).

[21] V. Kalmeyer and R. B. Laughlin, Equivalence of the resonating-valence-bond and fractional quantum Hall states, Phys. Rev. Lett. **59**, 2095 (1987).

[22] J. B. Kogut, An introduction to lattice gauge theory and spin systems, Rev. Mod. Phys. **51**, 659 (1979).

[23] T. Banks, R. Myerson, and J. Kogut, Phase transitions in Abelian lattice gauge theories, Nuclear Physics B **129**, 493 (1977).

[24] E. Fradkin and S. H. Shenker, Phase diagrams of lattice gauge theories with Higgs fields, Phys. Rev. D **19**, 3682 (1979).

[25] N. Read and B. Chakraborty, Statistics of the excitations of the resonating-valence-bond state, Phys. Rev. B **40**, 7133 (1989).

[26] T. Senthil and M. P. A. Fisher, Z_2 gauge theory of electron fractionalization in strongly correlated systems, Phys. Rev. B **62**, 7850 (2000).

[27] A. Kitaev, Anyons in an exactly solved model and beyond, Ann. Phys. **321**, 2 (2006).

[28] G. Kells, J. Kailasvuori, J. K. Slingerland, and J. Vala, Kaleidoscope of topological phases with multiple Majorana species, New Journal of Physics **13**, 095014 (2011).

[29] S. Yang, D. L. Zhou, and C. P. Sun, Mosaic spin models with topological order, Phys. Rev. B **76**, 180404 (2007).

[30] H. Yao and S. A. Kivelson, Exact Chiral Spin Liquid with Non-Abelian Anyons, Phys. Rev. Lett. **99**, 247203 (2007).

[31] S. Ryu, Three-dimensional topological phase on the diamond lattice, Phys. Rev. B **79**, 075124 (2009).

[32] T. Si and Y. Yu, Exactly soluble spin-1/2 models on three-dimensional lattices and non-abelian statistics of closed string excitations, arXiv:0709.1302 .

[33] T. Si and Y. Yu, Anyonic loops in three-dimensional spin liquid and chiral spin liquid, Nuclear Physics B **803**, 428 (2008).

[34] S. Mandal and N. Surendran, Exactly solvable Kitaev model in three dimensions, Phys. Rev. B **79**, 024426 (2009).

[35] M. Hermanns and S. Trebst, Quantum spin liquid with a Majorana Fermi surface on the three-dimensional hyperoctagon lattice, Phys. Rev. B **89**, 235102 (2014).

[36] K. O'Brien, M. Hermanns, and S. Trebst, Classification of gapless $\mathbb{Z}_2$ spin liquids in three-dimensional Kitaev models, Phys. Rev. B **93**, 085101 (2016).

[37] G. Jackeli and G. Khaliullin, Mott Insulators in the Strong Spin-Orbit Coupling Limit: From Heisenberg to a Quantum Compass and Kitaev Models, Phys. Rev. Lett. **102**, 017205 (2009).

[38] S. Trebst, Kitaev Materials, arXiv:1701.07056 .

[39] S. M. Winter, A. A. Tsirlin, M. Daghofer, J. van den Brink, Y. Singh, P. Gegenwart, and R. Valentí, Models and materials for generalized Kitaev magnetism, Journal of Physics: Condensed Matter **29**, 493002 (2017).

[40] M. Hermanns, I. Kimchi, and J. Knolle, Physics of the Kitaev Model: Fractionalization, Dynamic Correlations, and Material Connections, Annu. Rev. Condens. Matter Phys. **9**, 17 (2018).

[41] H. Takagi, T. Takayama, G. Jackeli, G. Khaliullin, and S. E. Nagler, Concept and realization of Kitaev quantum spin liquids, Nature Reviews Physics **1**, 264 (2019).

[42] L. Janssen and M. Vojta, Heisenberg–Kitaev physics in magnetic fields, Journal of Physics: Condensed Matter **31**, 423002 (2019).

[43] Y. Motome and J. Nasu, Hunting Majorana Fermions in Kitaev Magnets, Journal of the Physical Society of Japan **89**, 012002 (2020).

[44] J. Nasu, M. Udagawa, and Y. Motome, Vaporization of Kitaev Spin Liquids, Phys. Rev. Lett. **113**, 197205 (2014).

[45] P. A. Mishchenko, Y. Kato, and Y. Motome, Finite-temperature phase transition to a Kitaev spin liquid phase on a hyperoctagon lattice: A large-scale quantum Monte Carlo study, Phys. Rev. B **96**, 125124 (2017).

[46] J. Nasu, M. Udagawa, and Y. Motome, Thermal fractionalization of quantum spins in a Kitaev model: Temperature-linear specific heat and coherent transport of Majorana fermions, Phys. Rev. B **92**, 115122 (2015).

[47] J. Nasu and Y. Motome, Thermodynamics of Chiral Spin Liquids with Abelian and Non-Abelian Anyons, Phys. Rev. Lett. **115**, 087203 (2015).

[48] M. Hermanns, K. O'Brien, and S. Trebst, Weyl Spin Liquids, Phys. Rev. Lett. **114**, 157202 (2015).

[49] X.-G. Wen, Quantum Field Theory of Many-Body Systems, Oxford Graduate Texts (OUP Oxford, 2004).

[50] F. J. Wegner, Duality in Generalized Ising Models and Phase Transitions without Local Order Parameters, Journal of Mathematical Physics **12**, 2259 (1971).

[51] S. Sachdev, Topological order, emergent gauge fields, and Fermi surface reconstruction, Reports on Progress in Physics **82**, 014001 (2018).

[52] K. G. Wilson, Confinement of quarks, Phys. Rev. D **10**, 2445 (1974).

[53] K. M. O'Brien, Three-Dimensional Kitaev Spin Liquids, Ph.D. thesis, Universität zu Köln (2019).

[54] A. Polyakov, Quark confinement and topology of gauge theories, Nuclear Physics B **120**, 429 (1977).

[55] R. Peierls, On Ising's model of ferromagnetism, Mathematical Proceedings of the Cambridge Philosophical Society **32**, 477–481 (1936).

[56] K. G. Wilson and M. E. Fisher, Critical Exponents in 3.99 Dimensions, Phys. Rev. Lett. **28**, 240 (1972).

[57] M. Schuler, S. Whitsitt, L.-P. Henry, S. Sachdev, and A. M. Läuchli, Universal Signatures of Quantum Critical Points from Finite-Size Torus Spectra: A Window into the Operator Content of Higher-Dimensional Conformal Field Theories, Phys. Rev. Lett. **117**, 210401 (2016).

[58] S. Whitsitt and S. Sachdev, Transition from the $\mathbb{Z}_2$ spin liquid to antiferromagnetic order: Spectrum on the torus, Phys. Rev. B **94**, 085134 (2016).

[59] G. Baskaran, Z. Zou, and P. Anderson, The resonating valence bond state and high-Tc superconductivity — A mean field theory, Solid State Communications **63**, 973 (1987).

[60] I. Affleck, Z. Zou, T. Hsu, and P. W. Anderson, SU(2) gauge symmetry of the large-U limit of the Hubbard model, Phys. Rev. B **38**, 745 (1988).

[61] E. Dagotto, E. Fradkin, and A. Moreo, SU(2) gauge invariance and order parameters in strongly coupled electronic systems, Phys. Rev. B **38**, 2926 (1988).

[62] D. P. Arovas and A. Auerbach, Functional integral theories of low-dimensional quantum Heisenberg models, Phys. Rev. B **38**, 316 (1988).

[63] N. Read and S. Sachdev, Large-N expansion for frustrated quantum antiferromagnets, Phys. Rev. Lett. **66**, 1773 (1991).

[64] C. L. Kane and E. J. Mele, $\mathbb{Z}_2$ topological order and the quantum spin Hall effect, Phys. Rev. Lett. **95**, 146802 (2005).

[65] L. Fu, C. L. Kane, and E. J. Mele, Topological Insulators in Three Dimensions, Phys. Rev. Lett. **98**, 106803 (2007).

[66] M. Z. Hasan and C. L. Kane, Topological Insulators, Rev. Mod. Phys. **82**, 3045 (2010).

[67] X.-L. Qi and S.-C. Zhang, Topological insulators and superconductors, Rev. Mod. Phys. **83**, 1057 (2011).

[68] B. A. Bernevig, Topological Insulators and Topological Superconductors (Princeton University Press, 2013).

[69] A. Revelli, M. M. Sala, G. Monaco, C. Hickey, P. Becker, F. Freund, A. Jesche, P. Gegenwart, T. Eschmann, F. L. Buessen, S. Trebst, P. H. M. van Loosdrecht, J. van den Brink, and M. Grüninger, Fingerprints of Kitaev physics in the magnetic excitations of honeycomb iridates, arXiv:1905.13590 .

[70] Z. Nussinov and J. van den Brink, Compass models: Theory and physical motivations, Rev. Mod. Phys. **87**, 1 (2015).

[71] K. I. Kugel and D. I. Khomskiĭ, The Jahn-Teller effect and magnetism: transition metal compounds, Soviet Physics Uspekhi **25**, 231 (1982).

[72] J. Chaloupka, G. Jackeli, and G. Khaliullin, Kitaev-Heisenberg Model on a Honeycomb Lattice: Possible Exotic Phases in Iridium Oxides $A_2\mathrm{IrO}_3$, Phys. Rev. Lett. **105**, 027204 (2010).

[73] Y. Motome, R. Sano, S. H. Jang, Y. Sugita, and Y. Kato, Materials design of Kitaev spin liquids beyond the Jackeli-Khaliullin mechanism, arXiv:2001.03731 .

[74] Y. Kasahara, T. Ohnishi, Y. Mizukami, O. Tanaka, S. Ma, K. Sugii, N. Kurita, H. Tanaka, J. Nasu, Y. Motome, and et al., Majorana quantization and half-integer thermal quantum Hall effect in a Kitaev spin liquid, Nature **559**, 227–231 (2018).

[75] T. Yokoi, S. Ma, Y. Kasahara, S. Kasahara, T. Shibauchi, N. Kurita, H. Tanaka, J. Nasu, Y. Motome, C. Hickey, S. Trebst, and Y. Matsuda, Half-integer quantized anomalous thermal Hall effect in the Kitaev material α-RuCl_3, arXiv:2001.01899 .

[76] P. Jordan and E. Wigner, Über das Paulische Äquivalenzverbot, Zeitschrift fur Physik **47**, 631 (1928).

[77] H.-D. Chen and J. Hu, Exact mapping between classical and topological orders in two-dimensional spin systems, Phys. Rev. B **76**, 193101 (2007).

[78] X.-Y. Feng, G.-M. Zhang, and T. Xiang, Topological Characterization of Quantum Phase Transitions in a Spin-$1/2$ Model, Phys. Rev. Lett. **98**, 087204 (2007).

[79] H.-D. Chen and Z. Nussinov, Exact results of the Kitaev model on a hexagonal lattice: spin states, string and brane correlators, and anyonic excitations, Journal of Physics A: Mathematical and Theoretical **41**, 075001 (2008).

[80] S. Mandal, R. Shankar, and G. Baskaran, RVB gauge theory and the topological degeneracy in the honeycomb Kitaev model, Journal of Physics A: Mathematical and Theoretical **45**, 335304 (2012).

[81] I. Kimchi, J. G. Analytis, and A. Vishwanath, Three-dimensional quantum spin liquids in models of harmonic-honeycomb iridates and phase diagram in an infinite-D approximation, Phys. Rev. B **90**, 205126 (2014).

[82] C. Wu, D. Arovas, and H.-H. Hung, Γ-matrix generalization of the Kitaev model, Phys. Rev. B **79**, 134427 (2009).

[83] V. Dwivedi, C. Hickey, T. Eschmann, and S. Trebst, Majorana corner modes in a second-order Kitaev spin liquid, Phys. Rev. B **98**, 054432 (2018).

[84] S. Chandra, K. Ramola, and D. Dhar, Classical Heisenberg spins on a hexagonal lattice with Kitaev couplings, Phys. Rev. E **82**, 031113 (2010).

[85] E. H. Lieb and M. Loss, Fluxes, Laplacians, and Kasteleyn's theorem, Duke Math. J. **71**, 337 (1993).

[86] E. H. Lieb, Flux Phase of the Half-Filled Band, Phys. Rev. Lett. **73**, 2158 (1994).

[87] N. Macris and B. Nachtergaele, On the flux phase conjecture at half-filling: An improved proof, Journal of Statistical Physics **85**, 745 (1996).

[88] A. H. Castro Neto, F. Guinea, N. M. R. Peres, K. S. Novoselov, and A. K. Geim, The electronic properties of graphene, Rev. Mod. Phys. **81**, 109 (2009).

[89] J. Fu, J. Knolle, and N. B. Perkins, Three types of representation of spin in terms of Majorana fermions and an alternative solution of the Kitaev honeycomb model, Phys. Rev. B **97**, 115142 (2018).

[90] P. A. Mishchenko, Y. Kato, K. O'Brien, T. A. Bojesen, T. Eschmann, M. Hermanns, S. Trebst, and Y. Motome, Chiral spin liquids with crystalline $\mathbb{Z}_2$ gauge order in a three-dimensional Kitaev model, Phys. Rev. B **101**, 045118 (2020).

[91] T. Takayama, A. Kato, R. Dinnebier, J. Nuss, H. Kono, L. S. I. Veiga, G. Fabbris, D. Haskel, and H. Takagi, Hyperhoneycomb Iridate $\beta-\mathrm{Li_2IrO_3}$ as a Platform for Kitaev Magnetism, Phys. Rev. Lett. **114**, 077202 (2015).

[92] K. A. Modic, T. E. Smidt, I. Kimchi, N. P. Breznay, A. Biffin, S. Choi, R. D. Johnson, R. Coldea, P. Watkins-Curry, G. T. McCandless, J. Y. Chan, F. Gandara, Z. Islam, A. Vishwanath, A. Shekhter, R. D. McDonald, and J. G. Analytis, Realization of a three-dimensional spin–anisotropic harmonic honeycomb iridate, Nature Communications **5**, 4203 (2014).

[93] M. G. Yamada, V. Dwivedi, and M. Hermanns, Crystalline Kitaev spin liquids, Phys. Rev. B **96**, 155107 (2017).

[94] A. Smith, J. Knolle, D. L. Kovrizhin, J. T. Chalker, and R. Moessner, Majorana spectroscopy of three-dimensional Kitaev spin liquids, Phys. Rev. B **93**, 235146 (2016).

[95] Y. Kato, Y. Kamiya, J. Nasu, and Y. Motome, Chiral spin liquids at finite temperature in a three-dimensional Kitaev model, Phys. Rev. B **96**, 174409 (2017).

[96] A. F. Wells et al., Three dimensional nets and polyhedra (Wiley, 1977).

[97] J. Nasu, T. Kaji, K. Matsuura, M. Udagawa, and Y. Motome, Finite-temperature phase transition to a quantum spin liquid in a three-dimensional Kitaev model on a hyperhoneycomb lattice, Phys. Rev. B **89**, 115125 (2014).

[98] J. K. Asbóth, L. Oroszlány, and A. Pályi, A Short Course on Topological Insulators (Springer International Publishing, 2016).

[99] F. D. M. Haldane, Model for a Quantum Hall Effect without Landau Levels: Condensed-Matter Realization of the "Parity Anomaly", Phys. Rev. Lett. **61**, 2015 (1988).

[100] L. Messio, B. Bernu, and C. Lhuillier, Kagome Antiferromagnet: A Chiral Topological Spin Liquid? Phys. Rev. Lett. **108**, 207204 (2012).

[101] B. Bauer, L. Cincio, B. P. Keller, M. Dolfi, G. Vidal, S. Trebst, and A. W. W. Ludwig, Chiral spin liquid and emergent anyons in a kagome lattice mott insulator, Nature Communications **5**, 5137 (2014).

[102] S.-S. Gong, W. Zhu, and D. N. Sheng, Emergent chiral spin liquid: Fractional quantum hall effect in a kagome heisenberg model, Scientific Reports **4**, 6317 (2014).

[103] A. P. Schnyder, S. Ryu, A. Furusaki, and A. W. W. Ludwig, Classification of topological insulators and superconductors in three spatial dimensions, Phys. Rev. B **78**, 195125 (2008).

[104] S. Ryu, A. P. Schnyder, A. Furusaki, and A. W. W. Ludwig, Topological insulators and superconductors: tenfold way and dimensional hierarchy, New Journal of Physics **12**, 065010 (2010).

[105] B. S. Shastry and B. Sutherland, Exact ground state of a quantum mechanical antiferromagnet, Physica B+C **108**, 1069 (1981).

[106] A. Kitaev, Periodic table for topological insulators and superconductors, AIP Conference Proceedings **1134**, 22 (2009).

[107] J. Langbehn, Y. Peng, L. Trifunovic, F. von Oppen, and P. W. Brouwer, Reflection-Symmetric Second-Order Topological Insulators and Superconductors, Phys. Rev. Lett. **119**, 246401 (2017).

[108] M. Geier, L. Trifunovic, M. Hoskam, and P. W. Brouwer, Second-order topological insulators and superconductors with an order-two crystalline symmetry, Phys. Rev. B **97**, 205135 (2018).

[109] W. A. Benalcazar, B. A. Bernevig, and T. L. Hughes, Electric multipole moments, topological multipole moment pumping, and chiral hinge states in crystalline insulators, Phys. Rev. B **96**, 245115 (2017).

[110] W. A. Benalcazar, B. A. Bernevig, and T. L. Hughes, Quantized electric multipole insulators, Science **357**, 61 (2017).

[111] F. Schindler, A. M. Cook, M. G. Vergniory, Z. Wang, S. S. P. Parkin, B. A. Bernevig, and T. Neupert, Higher-order topological insulators, Science Advances **4** (2018), 10.1126/sciadv.aat0346.

[112] D. I. Khomskii, Transition Metal Compounds (Cambridge University Press, 2014).

[113] G. Khaliullin, Orbital Order and Fluctuations in Mott Insulators, Progress of Theoretical Physics Supplement **160**, 155 (2005).

[114] S. H. Chun, J.-W. Kim, J. Kim, H. Zheng, C. C. Stoumpos, C. D. Malliakas, J. F. Mitchell, K. Mehlawat, Y. Singh, Y. Choi, T. Gog, A. Al-Zein, M. M. Sala, M. Krisch, J. Chaloupka, G. Jackeli, G. Khaliulli, and B. J. Kim, Direct evidence for dominant bond-directional interactions in a honeycomb lattice iridate Na_2IrO_3, Nature Physics **11**, 462 (2015).

[115] J. G. Rau, E. K.-H. Lee, and H.-Y. Kee, Spin-Orbit Physics Giving Rise to Novel Phases in Correlated Systems: Iridates and Related Materials, Annual Review of Condensed Matter Physics **7**, 195 (2016).

[116] J. G. Rau, E. K.-H. Lee, and H.-Y. Kee, Generic Spin Model for the Honeycomb Iridates beyond the Kitaev Limit, Phys. Rev. Lett. **112**, 077204 (2014).

[117] K. Kitagawa, T. Takayama, Y. Matsumoto, A. Kato, R. Takano, Y. Kishimoto, S. Bette, R. Dinnebier, G. Jackeli, and H. Takagi, A spin–orbital-entangled quantum liquid on a honeycomb lattice, Nature **554**, 341 (2018).

[118] R. D. Johnson, S. C. Williams, A. A. Haghighirad, J. Singleton, V. Zapf, P. Manuel, I. I. Mazin, Y. Li, H. O. Jeschke, R. Valentí, and R. Coldea,

Monoclinic crystal structure of $\alpha-\mathrm{RuCl_3}$ and the zigzag antiferromagnetic ground state, Phys. Rev. B **92**, 235119 (2015).

[119] Y. Kubota, H. Tanaka, T. Ono, Y. Narumi, and K. Kindo, Successive magnetic phase transitions in $\alpha-\mathrm{RuCl_3}$: XY-like frustrated magnet on the honeycomb lattice, Phys. Rev. B **91**, 094422 (2015).

[120] M. Majumder, M. Schmidt, H. Rosner, A. A. Tsirlin, H. Yasuoka, and M. Baenitz, Anisotropic $\mathrm{Ru^{3+}}4d^5$ magnetism in the $\alpha-\mathrm{RuCl_3}$ honeycomb system: Susceptibility, specific heat, and zero-field NMR, Phys. Rev. B **91**, 180401 (2015).

[121] J. A. Sears, Y. Zhao, Z. Xu, J. W. Lynn, and Y.-J. Kim, Phase diagram of $\alpha-\mathrm{RuCl_3}$ in an in-plane magnetic field, Phys. Rev. B **95**, 180411 (2017).

[122] D. Hirobe, M. Sato, Y. Shiomi, H. Tanaka, and E. Saitoh, Magnetic thermal conductivity far above the Néel temperature in the Kitaev-magnet candidate $\alpha-\mathrm{RuCl_3}$, Phys. Rev. B **95**, 241112 (2017).

[123] Y. Kasahara, K. Sugii, T. Ohnishi, M. Shimozawa, M. Yamashita, N. Kurita, H. Tanaka, J. Nasu, Y. Motome, T. Shibauchi, and Y. Matsuda, Unusual Thermal Hall Effect in a Kitaev Spin Liquid Candidate $\alpha-\mathrm{RuCl_3}$, Phys. Rev. Lett. **120**, 217205 (2018).

[124] A. Banerjee, P. Lampen-Kelley, J. Knolle, C. Balz, A. A. Aczel, B. Winn, Y. Liu, D. Pajerowski, J. Yan, C. A. Bridges, A. T. Savici, B. C. Chakoumakos, M. D. Lumsden, D. A. Tennant, R. Moessner, D. G. Mandrus, and S. E. Nagler, Excitations in the field-induced quantum spin liquid state of α-RuCl3, npj Quantum Materials **3**, 8 (2018).

[125] N. Janša, A. Zorko, M. Gomilšek, M. Pregelj, K. W. Krämer, D. Biner, A. Biffin, C. Rüegg, and M. Klanjšek, Observation of two types of fractional excitation in the Kitaev honeycomb magnet, Nature Physics **14**, 786 (2018).

[126] M. G. Yamada, H. Fujita, and M. Oshikawa, Designing Kitaev Spin Liquids in Metal-Organic Frameworks, Phys. Rev. Lett. **119**, 057202 (2017).

[127] M. E. J. Newman and G. T. Barkema, Monte Carlo methods in statistical physics (Clarendon Press, Oxford, 1999).

[128] J. Gubernatis, N. Kawashima, and P. Werner, Quantum Monte Carlo Methods: Algorithms for Lattice Models (Cambridge University Press, 2016).

[129] N. Metropolis, A. W. Rosenbluth, M. N. Rosenbluth, A. H. Teller, and E. Teller, Equation of State Calculations by Fast Computing Machines, The Journal of Chemical Physics **21**, 1087 (1953).

[130] D. M. Ceperley, Path integrals in the theory of condensed helium, Rev. Mod. Phys. **67**, 279 (1995).

[131] W. M. C. Foulkes, L. Mitas, R. J. Needs, and G. Rajagopal, Quantum Monte Carlo simulations of solids, Rev. Mod. Phys. **73**, 33 (2001).

[132] E. Gull, A. J. Millis, A. I. Lichtenstein, A. N. Rubtsov, M. Troyer, and P. Werner, Continuous-time Monte Carlo methods for quantum impurity models, Rev. Mod. Phys. **83**, 349 (2011).

[133] J. Carlson, S. Gandolfi, F. Pederiva, S. C. Pieper, R. Schiavilla, K. E. Schmidt, and R. B. Wiringa, Quantum Monte Carlo methods for nuclear physics, Rev. Mod. Phys. **87**, 1067 (2015).

[134] F. Assaad and H. Evertz, World-line and Determinantal Quantum Monte Carlo Methods for Spins, Phonons and Electrons, in Computational Many-Particle Physics, edited by R. Fehske, H.and Schneider and A. Weiße (Springer Berlin Heidelberg, Berlin, Heidelberg, 2008) pp. 277–356.

[135] A. W. Sandvik, Stochastic Series Expansion Methods, arXiv:1909.10591 .

[136] H. G. Evertz, G. Lana, and M. Marcu, Cluster algorithm for vertex models, Phys. Rev. Lett. **70**, 875 (1993).

[137] H. G. Evertz, The loop algorithm, Advances in Physics **52**, 1 (2003).

[138] O. F. Syljuåsen and A. W. Sandvik, Quantum Monte Carlo with directed loops, Phys. Rev. E **66**, 046701 (2002).

[139] C. Zener, Interaction between the d-Shells in the Transition Metals. II. Ferromagnetic Compounds of Manganese with Perovskite Structure, Phys. Rev. **82**, 403 (1951).

[140] S. Yunoki, J. Hu, A. L. Malvezzi, A. Moreo, N. Furukawa, and E. Dagotto, Phase Separation in Electronic Models for Manganites, Phys. Rev. Lett. **80**, 845 (1998).

[141] E. Dagotto, S. Yunoki, A. L. Malvezzi, A. Moreo, J. Hu, S. Capponi, D. Poilblanc, and N. Furukawa, Ferromagnetic Kondo model for manganites: Phase diagram, charge segregation, and influence of quantum localized spins, Phys. Rev. B **58**, 6414 (1998).

[142] Y. Motome and N. Furukawa, A Monte Carlo Method for Fermion Systems Coupled with Classical Degrees of Freedom, Journal of the Physical Society of Japan **68**, 3853 (1999).

[143] T. Eschmann, P. A. Mishchenko, T. A. Bojesen, Y. Kato, M. Hermanns, Y. Motome, and S. Trebst, Thermodynamics of a gauge-frustrated Kitaev spin liquid, Phys. Rev. Research **1**, 032011 (2019).

[144] F. L. Pedrocchi, S. Chesi, and D. Loss, Physical solutions of the Kitaev honeycomb model, Phys. Rev. B **84**, 165414 (2011).

[145] F. Zschocke and M. Vojta, Physical states and finite-size effects in Kitaev's honeycomb model: Bond disorder, spin excitations, and NMR line shape, Phys. Rev. B **92**, 014403 (2015).

[146] A. Weiße, G. Wellein, A. Alvermann, and H. Fehske, The kernel polynomial method, Rev. Mod. Phys. **78**, 275 (2006).

[147] A. Weiße, Green-Function-Based Monte Carlo Method for Classical Fields Coupled to Fermions, Phys. Rev. Lett. **102**, 150604 (2009).

[148] A. M. Ferrenberg and R. H. Swendsen, New Monte Carlo technique for studying phase transitions, Phys. Rev. Lett. **61**, 2635 (1988).

[149] A. M. Ferrenberg and R. H. Swendsen, Optimized Monte Carlo data analysis, Phys. Rev. Lett. **63**, 1195 (1989).

[150] A. M. Ferrenberg, D. P. Landau, and R. H. Swendsen, Statistical errors in histogram reweighting, Phys. Rev. E **51**, 5092 (1995).

[151] A. Weiße and H. Fehske, Exact Diagonalization Techniques, in Computational Many-Particle Physics, edited by H. Fehske, R. Schneider, and A. Weiße (Springer Berlin Heidelberg, Berlin, Heidelberg, 2008) pp. 529–544.

[152] J. J. M. Cuppen, A divide and conquer method for the symmetric tridiagonal eigenproblem, Numerische Mathematik **36**, 177 (1980).

[153] H. Q. Lin, Exact diagonalization of quantum-spin models, Phys. Rev. B **42**, 6561 (1990).

[154] A. Weiße, Divide and conquer the Hilbert space of translation-symmetric spin systems, Phys. Rev. E **87**, 043305 (2013).

[155] C. Lanczos, An iteration method for the solution of the eigenvalue problem of linear differential and integral operators, J. Res. Natl. Bur. Stand. B **45**, 255 (1950).

[156] U. Schollwöck, The density-matrix renormalization group, Rev. Mod. Phys. **77**, 259 (2005).

[157] S. R. White, Density matrix formulation for quantum renormalization groups, Phys. Rev. Lett. **69**, 2863 (1992).

[158] S. Rommer and S. Östlund, Class of ansatz wave functions for one-dimensional spin systems and their relation to the density matrix renormalization group, Phys. Rev. B **55**, 2164 (1997).

[159] M.-C. Chung and I. Peschel, Density-matrix spectra for two-dimensional quantum systems, Phys. Rev. B **62**, 4191 (2000).

[160] E. Stoudenmire and S. R. White, Studying Two-Dimensional Systems with the Density Matrix Renormalization Group, Annual Review of Condensed Matter Physics **3**, 111 (2012).

[161] T. Nishino, K. Okunishi, Y. Hieida, N. Maeshima, and Y. Akutsu, Self-consistent tensor product variational approximation for 3D classical models, Nuclear Physics B **575**, 504 (2000).

[162] F. Verstraete and J. I. Cirac, Renormalization algorithms for Quantum-Many Body Systems in two and higher dimensions, arXiv:cond-mat/0407066 .

[163] F. Verstraete, M. M. Wolf, D. Perez-Garcia, and J. I. Cirac, Criticality, the Area Law, and the Computational Power of Projected Entangled Pair States, Phys. Rev. Lett. **96**, 220601 (2006).

[164] V. Murg, F. Verstraete, and J. I. Cirac, Variational study of hard-core bosons in a two-dimensional optical lattice using projected entangled pair states, Phys. Rev. A **75**, 033605 (2007).

[165] N. Schuch, M. M. Wolf, F. Verstraete, and J. I. Cirac, Computational Complexity of Projected Entangled Pair States, Phys. Rev. Lett. **98**, 140506 (2007).

[166] G. Vidal, Entanglement Renormalization, Phys. Rev. Lett. **99**, 220405 (2007).

[167] E. Y. Loh, J. E. Gubernatis, R. T. Scalettar, S. R. White, D. J. Scalapino, and R. L. Sugar, Sign problem in the numerical simulation of many-electron systems, Phys. Rev. B **41**, 9301 (1990).

[168] P. Henelius and A. W. Sandvik, Sign problem in Monte Carlo simulations of frustrated quantum spin systems, Phys. Rev. B **62**, 1102 (2000).

[169] M. Troyer and U.-J. Wiese, Computational Complexity and Fundamental Limitations to Fermionic Quantum Monte Carlo Simulations, Phys. Rev. Lett. **94**, 170201 (2005).

[170] Z.-X. Li and H. Yao, Sign-Problem-Free Fermionic Quantum Monte Carlo: Developments and Applications, Annual Review of Condensed Matter Physics **10**, 337 (2019).

[171] N. Metropolis and S. Ulam, The Monte Carlo Method, Journal of the American Statistical Association **44**, 335 (1949).

[172] E. Ising, Beitrag zur Theorie des Ferromagnetismus, Zeitschrift fur Physik **31**, 253 (1925).

[173] D. H. Adams and S. Chandrasekharan, Chiral limit of strongly coupled lattice gauge theories, Nuclear Physics B **662**, 220 (2003).

[174] A. W. Sandvik and R. Moessner, Correlations and confinement in nonplanar two-dimensional dimer models, Phys. Rev. B **73**, 144504 (2006).

[175] F. Alet, Y. Ikhlef, J. L. Jacobsen, G. Misguich, and V. Pasquier, Classical dimers with aligning interactions on the square lattice, Phys. Rev. E **74**, 041124 (2006).

[176] H. A. Kramers and G. H. Wannier, Statistics of the Two-Dimensional Ferromagnet. Part I, Phys. Rev. **60**, 252 (1941).

[177] R. H. Swendsen and J.-S. Wang, Nonuniversal critical dynamics in Monte Carlo simulations, Phys. Rev. Lett. **58**, 86 (1987).

[178] U. Wolff, Collective Monte Carlo Updating for Spin Systems, Phys. Rev. Lett. **62**, 361 (1989).

[179] R. H. Swendsen and J.-S. Wang, Replica Monte Carlo Simulation of Spin-Glasses, Phys. Rev. Lett. **57**, 2607 (1986).

[180] C. J. Geyer, Markov Chain Monte Carlo Maximum Likelihood, Computing Science and Statistics, Proceedings of the 23rd Symposium on the Interface , 156 (1991).

[181] K. Hukushima and K. Nemoto, Exchange Monte Carlo Method and Application to Spin Glass Simulations, Journal of the Physical Society of Japan **65**, 1604 (1996).

[182] M. Falcioni and M. W. Deem, A biased Monte Carlo scheme for zeolite structure solution, The Journal of Chemical Physics **110**, 1754 (1999).

[183] D. J. Earl and M. W. Deem, Parallel tempering: Theory, applications, and new perspectives, Phys. Chem. Chem. Phys. **7**, 3910 (2005).

[184] P. Pfeuty, The one-dimensional Ising model with a transverse field, Ann. Phys. **57**, 79 (1970).

[185] R. B. Stinchcombe, Ising model in a transverse field. I. Basic theory, Journal of Physics C: Solid State Physics **6**, 2459 (1973).

[186] N. V. Prokof'ev, B. V. Svistunov, and I. S. Tupitsyn, Exact, complete, and universal continuous-time worldline Monte Carlo approach to the statistics of discrete quantum systems, Journal of Experimental and Theoretical Physics **87**, 310–321 (1998).

[187] R. Blankenbecler, D. J. Scalapino, and R. L. Sugar, Monte Carlo calculations of coupled boson-fermion systems. I, Phys. Rev. D **24**, 2278 (1981).

[188] D. J. Scalapino and R. L. Sugar, Monte Carlo calculations of coupled boson-fermion systems. II, Phys. Rev. B **24**, 4295 (1981).

[189] R. L. Stratonovich, On a Method of Calculating Quantum Distribution Functions, Soviet Physics Doklady **2**, 416 (1957).

[190] J. Hubbard, Calculation of Partition Functions, Phys. Rev. Lett. **3**, 77 (1959).

[191] W. L. McMillan, Ground State of Liquid He^4, Phys. Rev. **138**, A442 (1965).

[192] D. Ceperley, G. V. Chester, and M. H. Kalos, Monte Carlo simulation of a many-fermion study, Phys. Rev. B **16**, 3081 (1977).

[193] M. Snajdr and S. M. Rothstein, Are properties derived from variance-optimized wave functions generally more accurate? Monte Carlo study of non-energy-related properties of H2, He, and LiH, The Journal of Chemical Physics **112**, 4935 (2000).

[194] D. Bressanini, G. Morosi, and M. Mella, Robust wave function optimization procedures in quantum Monte Carlo methods, The Journal of Chemical Physics **116**, 5345–5350 (2002).

[195] C. J. Umrigar, K. G. Wilson, and J. W. Wilkins, Optimized trial wave functions for quantum Monte Carlo calculations, Phys. Rev. Lett. **60**, 1719 (1988).

[196] P. R. C. Kent, R. J. Needs, and G. Rajagopal, Monte Carlo energy and variance-minimization techniques for optimizing many-body wave functions, Phys. Rev. B **59**, 12344–12351 (1999).

[197] N. V. Prokof'ev and B. V. Svistunov, Bold diagrammatic Monte Carlo: A generic sign-problem tolerant technique for polaron models and possibly interacting many-body problems, Phys. Rev. B **77**, 125101 (2008).

[198] N. Prokof'ev and B. Svistunov, Bold Diagrammatic Monte Carlo Technique: When the Sign Problem Is Welcome, Phys. Rev. Lett. **99**, 250201 (2007).

[199] S. Pilati, E. M. Inack, and P. Pieri, Self-learning projective quantum monte carlo simulations guided by restricted boltzmann machines, Phys. Rev. E **100**, 043301 (2019).

[200] G. H. Lang, C. W. Johnson, S. E. Koonin, and W. E. Ormand, Monte carlo evaluation of path integrals for the nuclear shell model, Phys. Rev. C **48**, 1518 (1993).

[201] C. Wu, J.-p. Hu, and S.-c. Zhang, Exact so(5) symmetry in the spin-$3/2$ fermionic system, Phys. Rev. Lett. **91**, 186402 (2003).

[202] C. Wu and S.-C. Zhang, Sufficient condition for absence of the sign problem in the fermionic quantum monte carlo algorithm, Phys. Rev. B **71**, 155115 (2005).

[203] Z. C. Wei, C. Wu, Y. Li, S. Zhang, and T. Xiang, Majorana Positivity and the Fermion Sign Problem of Quantum Monte Carlo Simulations, Phys. Rev. Lett. **116**, 250601 (2016).

[204] Z.-X. Li, Y.-F. Jiang, and H. Yao, Majorana-Time-Reversal Symmetries: A Fundamental Principle for Sign-Problem-Free Quantum Monte Carlo Simulations, Phys. Rev. Lett. **117**, 267002 (2016).

[205] Z.-C. Wei, Semigroup Approach to the Sign Problem in Quantum Monte Carlo Simulations, arXiv:1712.09412 .

[206] M. Udagawa, Vison-Majorana complex zero-energy resonance in the Kitaev spin liquid, Phys. Rev. B **98**, 220404 (2018).

[207] M. Udagawa and R. Moessner, Spectroscopy of Majorana modes of non-Abelian vortices in Kitaev's chiral spin liquid, arXiv:1912.01545 .

[208] M. Troyer, B. Ammon, and E. Heeb, Parallel Object Oriented Monte Carlo Simulations, in Computing in Object-Oriented Parallel Environments, edited by D. Caromel, R. R. Oldehoeft, and M. Tholburn (Springer Berlin Heidelberg, Berlin, Heidelberg, 1998) pp. 191–198.

[209] B. Bauer, L. D. Carr, H. G. Evertz, A. Feiguin, J. Freire, S. Fuchs, L. Gamper, J. Gukelberger, E. Gull, S. Guertler, A. Hehn, R. Igarashi, S. V. Isakov, D. Koop, P. N. Ma, P. Mates, H. Matsuo, O. Parcollet, G. Pawłowski, J. D. Picon, L. Pollet, E. Santos, V. W. Scarola, U. Schollwöck, C. Silva, B. Surer, S. Todo, S. Trebst, M. Troyer, M. L. Wall, P. Werner, and S. Wessel, The ALPS project release 2.0: open source software for strongly correlated systems, Journal of Statistical Mechanics: Theory and Experiment **2011**, P05001 (2011).

[210] A. Albuquerque, F. Alet, P. Corboz, P. Dayal, A. Feiguin, S. Fuchs, L. Gamper, E. Gull, S. Gürtler, A. Honecker, R. Igarashi, M. Körner, A. Kozhevnikov, A. Läuchli, S. Manmana, M. Matsumoto, I. McCulloch, F. Michel, R. Noack, G. Pawłowski, L. Pollet, T. Pruschke, U. Schollwöck, S. Todo, S. Trebst, M. Troyer, P. Werner, and S. Wessel, The ALPS project release 1.3: Open-source software for strongly correlated systems, Journal of Magnetism and Magnetic Materials **310**, 1187 (2007).

[211] T. A. Bojesen, FerrenbergSwendsenReweighting.jl, `https://github.com/Sleort/FerrenbergSwendsenReweighting.jl` (18/01/2018).

[212] J. Bezanson, A. Edelman, S. Karpinski, and V. B. Shah, Julia: A Fresh Approach to Numerical Computing, SIAM Review **59**, 65 (2017).

[213] M. Hermanns, S. Trebst, and A. Rosch, Spin-Peierls Instability of Three-Dimensional Spin Liquids with Majorana Fermi Surfaces, Phys. Rev. Lett. **115**, 177205 (2015).

[214] T. Eschmann, P. A. Mishchenko, K. O'Brien, T. A. Bojesen, Y. Kato, M. Hermanns, Y. Motome, and S. Trebst, Thermodynamic classification of three-dimensional Kitaev spin liquids, (2020), arXiv:2006.07386 .

[215] Y. Shimomura, S. Miyahara, and N. Furukawa, Frustration-induced Dodecamer Ordering in the Double-Exchange Spin Ice Model on the Kagome Lattice, Journal of the Physical Society of Japan **74**, 661 (2005).

[216] J. T. Chalker and P. D. Coddington, Percolation, quantum tunnelling and the integer Hall effect, Journal of Physics C: Solid State Physics **21**, 2665 (1988).

[217] J. T. Chalker, N. Read, V. Kagalovsky, B. Horovitz, Y. Avishai, and A. W. W. Ludwig, Thermal metal in network models of a disordered two-dimensional superconductor, Phys. Rev. B **65**, 012506 (2001).

[218] C. R. Laumann, A. W. W. Ludwig, D. A. Huse, and S. Trebst, Disorder-induced Majorana metal in interacting non-Abelian anyon systems, Phys. Rev. B **85**, 161301 (2012).

[219] T. Eschmann, V. Dwivedi, H. F. Legg, C. Hickey, and S. Trebst, Partial flux ordering and thermal Majorana metals in (higher-order) spin liquids, (2020), arXiv:2007.04332 .

[220] A. Saket, S. R. Hassan, and R. Shankar, Manipulating unpaired Majorana fermions in a quantum spin chain, Phys. Rev. B **82**, 174409 (2010).

[221] M. V. Berry, Quantal Phase Factors Accompanying Adiabatic Changes, Proceedings of the Royal Society of London. Series A, Mathematical and Physical Sciences **392**, 45 (1984).

[222] S. shen Chern, On the Curvatura Integra in a Riemannian Manifold, Annals of Mathematics **46**, 674 (1945).

[223] T. Fukui, Y. Hatsugai, and H. Suzuki, Chern Numbers in Discretized Brillouin Zone: Efficient Method of Computing (Spin) Hall Conductances, Journal of the Physical Society of Japan **74**, 1674–1677 (2005).

[224] F. Wilczek and A. Zee, Appearance of Gauge Structure in Simple Dynamical Systems, Phys. Rev. Lett. **52**, 2111 (1984).

[225] Y. Hatsugai, Explicit Gauge Fixing for Degenerate Multiplets: A Generic Setup for Topological Orders, Journal of the Physical Society of Japan **73**, 2604 (2004).

[226] Y. Hatsugai, Characterization of Topological Insulators: Chern Numbers for Ground State Multiplet, Journal of the Physical Society of Japan **74**, 1374–1377 (2005).

[227] A. Altland and M. R. Zirnbauer, Nonstandard symmetry classes in mesoscopic normal-superconducting hybrid structures, Phys. Rev. B **55**, 1142 (1997).

[228] N. Read and A. W. W. Ludwig, Absence of a metallic phase in random-bond Ising models in two dimensions: Applications to disordered superconductors and paired quantum Hall states, Phys. Rev. B **63**, 024404 (2000).

[229] I. A. Gruzberg, N. Read, and A. W. W. Ludwig, Random-bond Ising model in two dimensions: The Nishimori line and supersymmetry, Phys. Rev. B **63**, 104422 (2001).

[230] A. Mildenberger, F. Evers, A. D. Mirlin, and J. T. Chalker, Density of quasiparticle states for a two-dimensional disordered system: Metallic, insulating, and critical behavior in the class-D thermal quantum Hall effect, Phys. Rev. B **75**, 245321 (2007).

[231] M. Aidelsburger, S. Nascimbene, and N. Goldman, Artificial gauge fields in materials and engineered systems, Comptes Rendus Physique **19**, 394 (2018).

[232] C. Schweizer, F. Grusdt, M. Berngruber, L. Barbiero, E. Demler, N. Goldman, I. Bloch, and M. Aidelsburger, Floquet approach to $\mathbb{Z}_2$ lattice gauge theories with ultracold atoms in optical lattices, Nature Physics **15**, 1168 (2019).

[233] L. W. Clark, B. M. Anderson, L. Feng, A. Gaj, K. Levin, and C. Chin, Observation of density-dependent gauge fields in a bose-einstein condensate based on micromotion control in a shaken two-dimensional lattice, Phys. Rev. Lett. **121**, 030402 (2018).

[234] B. Yang, H. Sun, R. Ott, H.-Y. Wang, T. V. Zache, J. C. Halimeh, Z.-S. Yuan, P. Hauke, and J.-W. Pan, Observation of gauge invariance in a 71-site quantum simulator, arXiv:2003.08945 .

[235] C. Hickey and S. Trebst, Emergence of a field-driven U(1) spin liquid in the Kitaev honeycomb model, Nature Communications **10**, 530 (2019).

[236] J. Yoshitake, J. Nasu, Y. Kato, and Y. Motome, Majorana-magnon crossover by a magnetic field in the Kitaev model: Continuous-time quantum Monte Carlo study, Phys. Rev. B **101**, 100408 (2020).

[237] T. A. Bojesen, Policy-guided Monte Carlo: Reinforcement-learning Markov chain dynamics, Phys. Rev. E **98**, 063303 (2018).

[238] J. Liu, Y. Qi, Z. Y. Meng, and L. Fu, Self-learning Monte Carlo method, Phys. Rev. B **95**, 041101 (2017).

[239] J. Liu, H. Shen, Y. Qi, Z. Y. Meng, and L. Fu, Self-learning Monte Carlo method and cumulative update in fermion systems, Phys. Rev. B **95**, 241104 (2017).

[240] B. Stroustrup, The C++ Programming Language, 4th ed. (Addison-Wesley Professional, 2013).

[241] C. Sanderson and R. Curtin, Armadillo: A template-based C++ library for linear algebra, Journal of Open Source Software **1**, 26 (2016).

[242] C. Sanderson and R. Curtin, A User-Friendly Hybrid Sparse Matrix Class in C++, Lecture Notes in Computer Science , 422–430 (2018).

[243] S. Trebst, D. A. Huse, and M. Troyer, Optimizing the ensemble for equilibration in broad-histogram Monte Carlo simulations, Phys. Rev. E **70**, 046701 (2004).

[244] S. Trebst, D. A. Huse, E. Gull, H. G. Katzgraber, U. H. E. Hansmann, and M. Troyer, Ensemble Optimization Techniques for the Simulation of Slowly Equilibrating Systems, in Computer Simulation Studies in Condensed-Matter Physics XIX, edited by D. P. Landau, S. P. Lewis, and H. B. Schöttler (Springer Berlin Heidelberg, Berlin, Heidelberg, 2009) pp. 33–47.

[245] W. H. Press, S. A. Teukolsky, W. T. Vetterling, and B. P. Flannery, Numerical Recipes in C (2nd Ed.): The Art of Scientific Computing (Cambridge University Press, USA, 1992).

[246] R. Barrett, M. Berry, T. F. Chan, J. Demmel, J. Donato, J. Dongarra, V. Eijkhout, R. Pozo, C. Romine, and H. V. der Vorst, Templates for the Solution of Linear Systems (SIAM, Philadelphia, PA, 1994).

Acknowledgements

First of all, I would like to thank Simon Trebst for giving me the opportunity to work on what has been a very interesting and also challenging PhD project. I feel I have received the best possible guidance and support over the years, as well as the chance to work in an excellent environment. I thank Achim Rosch and Markus Grüninger for being my second referee and chairman of the thesis committee.

This work would not have been possible without a number of excellent and very fruitful collaborations. I would like to express my gratitude to Yukitoshi Motome, Petr Mishchenko, Yasuyuki Kato, Troels Bojesen, Kevin O'Brien and Maria Hermanns for our joint work on 3D Kitaev systems. Especially, I thank Petr Mishchenko for generously sharing his expertise on the Monte Carlo method used here. Our collaboration not only included many weekly video meetings, but also my eleven-week visit at the University of Tokyo, where I have been received with the greatest hospitality. For that, I would like to thank Yukitoshi Motome and all members of his group. I also thank Vatsal Dwivedi and Ciarán Hickey for our productive collaboration on the Kitaev Shastry-Sutherland model.

My research has been part of the CRC 1238 (project C03) of the Deutsche Forschungsgemeinschaft, which not only funded my work, but also many conference travels, and, most of all, my visit to Tokyo. I thank all people involved, and, especially, Benita Schuba and Clara Berthet for their administrative support. Very special thanks go to Petra Neubauer-Günther for her great support at the Bonn-Cologne Graduate School of Physics and Astronomy, and to Andreas Sindermann at the Institute of Theoretical Physics at the University of Cologne. The numerical simulations in this work have been performed on the JUWELS cluster at the Forschungszentrum Jülich, and on the CHEOPS cluster at RRZK Cologne.

A big thank you goes to Jan Attig, Carsten Bauer, Christoph Berke, Vatsal Dwivedi, Ciarán Hickey, Martin Gembé and Dominik Kiese for being a great help in proofreading this thesis.

I thank all my friends and colleagues at the University of Cologne for the great time, especially my office mates Bahar, Dominik, Finn, Frederic, Jan, Kai, Martin, all people from the Trebst and Rosch group, and Max Goedecke for having lunch with me! Last but not least, I thank my family for all their support over the years!

Erklärung zur Dissertation

Ich versichere, dass ich die von mir vorgelegte Dissertation selbständig angefertigt, die benutzten Quellen und Hilfsmittel vollständig angegeben und die Stellen der Arbeit – einschließlich Tabellen, Karten und Abbildungen –, die anderen Werken im Wortlaut oder dem Sinn nach entnommen sind, in jedem Einzelfall als Entlehnung kenntlich gemacht habe; dass diese Dissertation noch keiner anderen Fakultät oder Universität zur Prüfung vorgelegen hat; dass sie – abgesehen von unten angegebenen Teilpublikationen – noch nicht veröffentlicht worden ist, sowie, dass ich eine solche Veröffentlichung vor Abschluss des Promotionsverfahrens nicht vornehmen werde. Die Bestimmungen der Promotionsordnung sind mir bekannt. Die von mir vorgelegte Dissertation ist von Prof. Dr. Simon Trebst betreut worden.

Köln, 27. Juli 2020 _____

Tim Eschmann

Bereits veröffentlichte Teilpublikationen sind auf der Folgeseite aufgeführt.

Publikationen

- T. Eschmann, V. Dwivedi, H. F. Legg, C. Hickey, and S. Trebst, *Partial flux ordering and thermal Majorana metals in (higher-order) spin liquids*, arXiv:2007.04332 (2020).

- T. Eschmann, P. A. Mishchenko, K. O'Brien, T. A. Bojesen, Y. Kato, M. Hermanns, Y. Motome, and S. Trebst, *Thermodynamic classification of three-dimensional Kitaev spin liquids*, arXiv:2006.07386 (2020).

- P. A. Mishchenko, Y. Kato, K. O'Brien, T. A. Bojesen, T. Eschmann, M. Hermanns, S. Trebst, and Y. Motome, *Chiral spin liquids with crystalline $\mathbb{Z}_2$ gauge order in a three-dimensional Kitaev model*, Phys. Rev. B **101**, 045118 (2020).

- A. Revelli, M.M. Sala, G. Monaco, C. Hickey, P. Becker, F. Freund, A. Jesche, P. Gegenwart, T. Eschmann, F.L. Buessen, S. Trebst, P.H.M. van Loosdrecht, J. van den Brink, and M. Grüninger, *Fingerprints of Kitaev physics in the magnetic excitations of honeycomb iridates*, arXiv:1905.13590 (2019).

- T. Eschmann, P.A. Mishchenko, T.A. Bojesen, Y. Kato, M. Hermanns, Y. Motome, and S. Trebst, *Thermodynamics of a gauge-frustrated Kitaev spin liquid*, Phys. Rev. Research **1**, 032011 (2019).

- V. Dwivedi, C. Hickey, T. Eschmann, and S. Trebst, *Majorana corner modes in a second-order Kitaev spin liquid*, Phys. Rev. B **98**, 054432 (2018).